Volume 10 No 1 2010

ISSN 1473-6691 (print)
ISSN 1742-3422 (online)

Journal of the ICRU

ICRU REPORT 83

Prescribing, Recording, and Reporting Photon-Beam Intensity-Modulated Radiation Therapy (IMRT)

OXFORD JOURNALS
OXFORD UNIVERSITY PRESS

OXFORD UNIVERSITY PRESS

INTERNATIONAL COMMISSION ON RADIATION UNITS AND MEASUREMENTS

ICRU REPORT 83

Journal of the ICRU Volume 10 No 1 2010

ICRU REPORT No. 83

PRESCRIBING, RECORDING, AND REPORTING PHOTON-BEAM INTENSITY-MODULATED RADIATION THERAPY (IMRT)

THE INTERNATIONAL COMMISSION ON RADIATION UNITS AND MEASUREMENTS

April 2010

Journal of the ICRU Volume 10 No 1 2010

PRESCRIBING, RECORDING, AND REPORTING PHOTON-BEAM INTENSITY-MODULATED RADIATION THERAPY (IMRT)

Report Committee

V. Grégoire (Co-Chair), Université Catholique de Louvain, Brussels, Belgium
T. R. Mackie (Co-Chair), University of Wisconsin, Madison, USA
W. De Neve, Academic Hospital of the University of Ghent, Ghent, Belgium
M. Gospodarowicz, Princess Margaret Hospital, Toronto, Ontario, Canada
J. A. Purdy, Mallinckrodt Institute of Radiology, St-Louis, Missouri, USA
M. van Herk, The Netherlands Cancer Institute, Amsterdam, The Netherlands
A. Niemierko, Massachusetts General Hospital, Boston, Massachusetts, USA

Commission Sponsors

P. M. DeLuca, Jr., University of Wisconsin, Madison, Wisconsin, USA
R. A. Gahbauer, Ohio State University, Columbus, Ohio, USA
D. T. L. Jones, Cape Scientific Concepts, Cape Town, South Africa
A. Wambersie, Université Catholique de Louvain, Brussels, Belgium
G. F. Whitmore, Ontario Cancer Institute, Toronto, Ontario, Canada

Consultants to the Report Committee

A. Ahnesjö, MDS Nordion, Uppsala, Sweden
M. Goitein, Ankerstrasse 1, Windisch AG, Switzerland
N. Gupta, Ohio State University, Columbus, Ohio, USA
T. Landberg, Rigshospitalet, Copenhagen, Denmark

The Commission wishes to express its appreciation to the individuals involved in the preparation of this Report, for the time and efforts which they devoted to this task and to express its appreciation to the organizations with which they are affiliated.

British Library Cataloguing in Publication Data. A Catalogue record of this book is available at the British Library.

Journal of the ICRU Vol 10 No 1 (2010) Report 83
Oxford University Press
doi:10.1093/jicru/ndq001

The International Commission on Radiation Units and Measurements

Introduction

The International Commission on Radiation Units and Measurements (ICRU), since its inception in 1925, has had as its principal objective the development of internationally acceptable recommendations regarding:

(1) quantities and units of radiation and radioactivity,
(2) procedures suitable for the measurement and application of these quantities in clinical radiology and radiobiology, and
(3) physical data needed in the application of these procedures, the use of which tends to assure uniformity in reporting.

The Commission also considers and makes similar types of recommendations for the radiation protection field. In this connection, its work is carried out in close cooperation with the International Commission on Radiological Protection (ICRP).

Policy

The ICRU endeavors to collect and evaluate the latest data and information pertinent to the problems of radiation measurement and dosimetry and to recommend the most acceptable values and techniques for current use.

The Commission's recommendations are kept under continual review in order to keep abreast of the rapidly expanding uses of radiation.

The ICRU feels that it is the responsibility of national organizations to introduce their own detailed technical procedures for the development and maintenance of standards. However, it urges that all countries adhere as closely as possible to the internationally recommended basic concepts of radiation quantities and units.

The Commission feels that its responsibility lies in developing a system of quantities and units having the widest possible range of applicability. Situations can arise from time to time for which an expedient solution of a current problem might seem advisable. Generally speaking, however, the Commission feels that action based on expediency is inadvisable from a long-term viewpoint; it endeavors to base its decisions on the long-range advantages to be expected.

The ICRU invites and welcomes constructive comments and suggestions regarding its recommendations and reports. These may be transmitted to the Chairman.

Current Program

The Commission recognizes its obligation to provide guidance and recommendations in the areas of radiation therapy, radiation protection, and the compilation of data important to these fields, and to scientific research and industrial applications of radiation. Increasingly, the Commission is focusing on the problems of protection of the patient and evaluation of image quality in diagnostic radiology. These activities do not diminish the ICRU's commitment to the provision of a rigorously defined set of quantities and units useful in a very broad range of scientific endeavors.

The Commission is currently engaged in the formulation of ICRU Reports treating the following subjects:

Approaches to the Dosimetry of Low-Dose Exposures to Ionizing Radiation
Design of a Voxel Phantom for Radiation Protection
Dose and Volume Specifications for Reporting Intra-Cavity Therapy in Gynecology
Doses from Cosmic-Ray Exposures of Aircrew
Fundamental Quantities and Units
Harmonization of Reporting Patient Diagnostic Doses
Image Quality and Patient Dose in Computed Tomography
Key Data for Measurement Standards in the Dosimetry of Ionizing Radiation
Prescribing, Recording, and Reporting Ion-Beam Therapy

The Commission continually reviews radiation science with the aim of identifying areas in which

the development of guidance and recommendations can make an important contribution.

The ICRU's Relationship with Other Organizations

In addition to its close relationship with the ICRP, the ICRU has developed relationships with other organizations interested in the problems of radiation quantities, units, and measurements. Since 1955, the ICRU has had an official relationship with the World Health Organization (WHO), whereby the ICRU is looked to for primary guidance in matters of radiation units and measurements and, in turn, the WHO assists in the worldwide dissemination of the Commission's recommendations. In 1960, the ICRU entered into consultative status with the International Atomic Energy Agency (IAEA). The Commission has a formal relationship with the United Nations Scientific Committee on the Effects of Atomic Radiation (UNSCEAR), whereby ICRU observers are invited to attend annual UNSCEAR meetings. The Commission and the International Organization for Standardization (ISO) informally exchange notifications of meetings, and the ICRU is formally designated for liaison with two of the ISO technical committees. The ICRU also enjoys a strong relationship with its sister organization, the National Council on Radiation Protection and Measurements (NCRP). In essence, these organizations were founded concurrently by the same individuals. Presently, this long-standing relationship is formally acknowledged by a special liaison agreement. The ICRU also corresponds and exchanges final reports with the following organizations:

Bureau International de Métrologie Légale
Bureau International des Poids et Mesures
European Commission
Council for International Organizations of Medical Sciences
Food and Agriculture Organization of the United Nations
International Committee of Photobiology
International Council for Science
International Electrotechnical Commission
International Labor Organization
International Organization for Medical Physics
International Radiation Protection Association
International Union of Pure and Applied Physics
United Nations Educational, Scientific and Cultural Organization

The Commission has found its relationship with all of these organizations fruitful and of substantial benefit to the ICRU program.

Operating Funds

In recent years, principal financial support has been provided by the European Commission, the National Cancer Institute of the US Department of Health and Human Services, and the International Atomic Energy Agency. In addition, during the last 10 years, financial support has been received from the following organizations:

American Association of Physicists in Medicine
Belgian Nuclear Research Centre
Electricité de France
Helmholtz Zentrum München
Hitachi, Ltd.
International Radiation Protection Association
International Society of Radiology
Ion Beam Applications, S.A.
Japanese Society of Radiological Technology
MDS Nordion
National Institute of Standards and Technology
Nederlandse Vereniging voor Radiologie
Philips Medical Systems, Incorporated
Radiological Society of North America
Siemens Medical Solutions
Varian Medical Systems

In addition to the direct monetary support provided by these organizations, many organizations provide indirect support for the Commission's program. This support is provided in many forms, including, among others, subsidies for (1) the time of individuals participating in ICRU activities, (2) travel costs involved in ICRU meetings, and (3) meeting facilities and services.

In recognition of the fact that its work is made possible by the generous support provided by all of the organizations supporting its program, the Commission expresses its deep appreciation.

Hans-Georg Menzel
Chairman, ICRU
Geneva, Switzerland

Journal of the ICRU Vol 10 No 1 (2010) Report 83
Oxford University Press
doi:10.1093/jicru/ndq002

Prescribing, Recording, and Reporting Photon-Beam Intensity-Modulated Radiation Therapy (IMRT)

Contents

Journal of the ICRU Vol 10 No 1 (2010) Report 83
Oxford University Press
doi:10.1093/jicru/ndq003

Preface

The use of radiation therapy for the eradication or control of malignant disease results in both normal and malignant tissues being irradiated and damaged. An obvious advantage results when greater amounts of radiation are delivered to diseased tissues than to normal tissues—a therapeutic gain. Not only will less radiation to normal tissue reduce complications, but it can allow the escalation of the absorbed dose to malignant tissue for the same normal tissue response—a further therapeutic advantage.

Either strategy represents a therapeutic advantage for their respective indications. Fundamental to these treatment strategies is the precise knowledge of the location in three dimensions (3D) of all irradiated normal and malignant tissues, and the ability to deliver the radiation absorbed dose with similar spatial accuracy. Further, knowledge of the radiation response of malignant tumors and of the 3D locations of microscopic disease spread is important for treatment planning. These aspects and the recent advances in imaging science are fundamental to intensity-modulated radiation therapy (IMRT).

During the last 10 years to 20 years, imaging science has advanced rapidly so that now anatomic detail with excellent resolution can be determined non-invasively, and more recently increasingly important information about tissue physiology can be provided. Modern multi-slice axial x-ray computed tomography (CT) techniques can generate 3D views of any anatomical region with superb spatial and reasonable temporal resolution. The resulting millimeter-sized pixels of anatomical information can also be directly related to tissue physical properties that embody all the radiological information of scatter, attenuation, and absorption required for adequate radiation-treatment planning. In addition to the detailed anatomical information derived from CT procedures, the combined use of CT with 3D positron-emission tomography (PET) using positron-emitting radionuclides such as ^{18}F-labeled fluorodeoxyglucose incorporated in physiological tracers yields time-dependent metabolic information with millimeter resolution. This detailed and heretofore unavailable information has great potential for disease evaluation, tumor staging, and treatment planning.

These developments in imaging science served to drive advances in radiation-treatment planning and treatment delivery in directions not anticipated a decade ago. Since absorbed-dose calculation engines are largely based on convolution/superposition techniques, current treatment-planning systems make direct use of the 3D data sets mentioned above to generate 3D representations of radiation energy deposition. For megavoltage photon beams, exceptionally accurate and high-resolution 3D dose maps are achievable. These dose-calculation tools are now coupled to sophisticated treatment-planning optimization algorithms.

The foregoing advances set the stage for the subject of this Report, namely IMRT. While there are several techniques for implementing IMRT, all use multiple, spatially small radiation beamlets, often of different intensity, administered from numerous different directions. In some cases, a fan beam, also composed of numerous beamlets of varying intensity, is administered in a cylindrically symmetric rotational manner similar to CT devices. The immediate result of these developments is the ability to create almost arbitrary 3D distributions of absorbed dose with millimeter resolution. Inherent in these distributions is the presence of very steep absorbed-dose gradients. All of this has led to the ability to deliver 3D absorbed-dose distributions of high conformity to the target volume and with concomitant avoidance of selected normal structures. In this manner, precise and accurate treatment is achievable with high ratios of doses in malignant tissues to those in normal tissues. Interestingly, these techniques usually distribute a lower absorbed dose to a larger volume of normal tissue. In some cases, the total energy deposited in normal tissue (usually called integral absorbed energy) is more than in conventional treatment techniques, raising concerns about potential carcinogenic risk.

The IMRT process, in effect, makes a very large number of free parameters available for treatment planning and can be effectively used only in conjunction with computerized optimization

treatment-planning techniques. Appropriate optimization algorithms allow the user to specify the desired absorbed-dose distribution in 3D with millimeter resolution. The optimization engine then generates a series of estimated parameter values to achieve the desired distribution with prespecified fidelity. These algorithms are now quite sophisticated and sometimes include aspects of tissue response, *e.g.*, complication and cell-killing probabilities.

The present Report broadly discusses all aspects of IMRT. A special effort is made to illustrate the path from conventional external-beam therapy to the radically different IMRT technique. Previous ICRU Reports have thoroughly discussed therapeutic approaches and treatment specifications for various radiation modalities (see, for example, ICRU Reports 52, 60, 71, and 78). However, IMRT requires new considerations for planning, prescribing, reporting, and recording due to the extraordinary control over the 3D absorbed-dose distributions with their steep dose gradients. In particular, the adoption of dose–volume histograms (DVHs) for dose specification is essential. The use of dose-at-a-point for the specification of absorbed dose is retained for historical and comparative purposes.

The implications of using complex and somewhat inscrutable optimization algorithms are discussed. The enhanced capabilities of IMRT both take account of and require extensions and expansions to past ICRU recommendations. Examples of such considerations include multiple target volumes together with new measures of dose uniformity and the degree of dose conformity in the desired target volumes. The use of DVHs in prescribing, recording, and reporting is emphasized.

This Report also includes appendices showing suggested documentation in several clinical examples and a discussion of quality assurance procedures needed for IMRT. The complex nature of IMRT requires appropriate record keeping to assess and improve clinical results. This, in part, grows out of the unknown nature of many commercial optimization systems. While the input parameter values and parameter ranges might be specified, the exact nature of the optimization process is not necessarily visible to the user. For any non-linear optimization approach, different starting conditions can easily lead to different final outcomes! Thus, record keeping and quality assurance become of paramount importance.

Finally, IMRT has and will continue to introduce dramatic changes to the treatment of malignant disease with external-beam radiation. The future will certainly include changes in treatment fractionation, absorbed-dose escalation, boost therapy, and the extension of IMRT to other radiation-therapy modalities. We anticipate that this Report will serve as a firm foundation for understanding the complexity of IMRT and for implementing future developments in IMRT.

Paul DeLuca
Dan Jones
Reinhard Gahbauer
Gordon Whitmore
André Wambersie

Journal of the ICRU Vol 10 No 1 (2010) Report 83
Oxford University Press
doi:10.1093/jicru/ndq004

Abstract

Rapid developments in imaging techniques, including functional imaging, have fueled the drive to implement new methods of delivering three-dimensional (3D) radiation therapy, such as intensity-modulated radiation therapy (IMRT), with unprecedented accuracy. In comparison with 3D conformal radiation therapy, it is now possible with IMRT to escalate the absorbed dose in the target volume for the same normal-tissue absorbed-dose and/or to reduce the normal-tissue dose for the same tumor dose, resulting in improved tumor control and/or less normal tissue complications. IMRT is accomplished by the sequential isocentric delivery of multiple small beams, typically of non-uniform intensity, that can lead to the generation of very steep dose gradients. To meet the requirements of such sophisticated beam-delivery techniques, both tumor and normal-tissue volumes must be delineated in 3D with high precision. The use of dose–volume histograms for the specification of absorbed dose is inherent to the treatment modality. The demands on treatment-planning systems to ensure accurate dose delivery necessitate the employment of complex iterative optimization processes. The stringent requirements on precision for the entire treatment process from imaging to treatment entail the implementation of rigorous commissioning and quality-assurance programs. The present Report provides the information necessary to standardize techniques and procedures and to harmonize the prescribing, recording, and reporting of IMRT where possible with those of other modalities. Applicable concepts and recommendations in other ICRU Reports concerning radiation therapy are adopted and extended where required. Clinical examples of IMRT are provided to illustrate the recommendations of prescribing, recording, and reporting that are contained in this Report. As the present Report describes in some detail the physical, technical, treatment-planning, and clinical aspects of IMRT, it should be a useful reference for current practitioners and should also provide new and potential users, as well as other interested readers, with the basic background to enable them to understand the techniques involved and the requirements for implementing IMRT.

Journal of the ICRU Vol 10 No 1 (2010) Report 83
Oxford University Press
doi:10.1093/jicru/ndq005

Executive Summary

The advent of intensity-modulated radiation therapy (IMRT) is rapidly changing the field of external-beam radiation therapy. Using computer-based optimization techniques to allow IMRT to comply with user-specified absorbed-dose and dose–volume constraints in specified target volumes as well as in normal tissues, IMRT allows a dramatic customization of the three-dimensional (3D) dose distribution. Quite often reductions of absorbed dose in critical organs at risk means that the targeted region can be exposed to escalated levels of radiation for the same level of normal-tissue toxicity. The advantages for curative treatment and even for some palliative treatments are readily apparent. Historical evidence generally indicates improved tumor control and decreased morbidity whenever an improvement of the ratio tumor-to-normal-tissue dose was achieved.

Intensity-modulated radiation therapy requires the precise selection and delineation of the various anatomic volumes based on 3D volume imaging. Moreover, treatment-planning systems must now integrate various imaging modalities, including functional imaging for planning, not only before the start of treatment, but also during treatment to allow the adaptation of the absorbed-dose distribution to the desired and possibly changing target volumes. The concepts of gross tumor volume (GTV) and clinical target volume (CTV) remain of critical importance. Gross tumor volumes are delineated on a 3D basis using clinical (*e.g.*, physical examination), anatomical (*e.g.*, CT, MRI), and/or functional-imaging modalities (*e.g.*, PET, functional MRI). Intensity-modulated radiation therapy easily accommodates the delineation and treatment of multiple GTVs. The GTVs can be delineated before the start of treatment and at various times during treatment. However, the nomenclature used should clearly reflect the possibility of having various GTVs by using unambiguous annotations. The use of terminology such as biological target volume, proliferative target volume, and hypoxic target volume is not recommended and is not discussed in this Report.

For indirectly ionizing beams such as photons, IMRT is implemented most commonly by the isocentric delivery of multiple small beams (beamlets) of non-uniform intensity. Hence, effective treatment planning for IMRT is quite demanding and is performed in 3D in an iterative manner based on 3D images of the volume to be treated. Such approaches require that traditional ICRU recommendations for prescribing, recording, and reporting of treatments be adapted and expanded. This Report discusses such recommendations in detail. A special emphasis is placed upon the use of dose–volume histograms (DVHs) in reporting and recording.

This Report recommends that a CTV should always be associated with the GTV for malignant tumors. In postoperative irradiation, often only a CTV is delineated. The selection of the CTV should be based on the knowledge of the probability of microscopic tumor infiltration into the surrounding normal tissues and/or nodes; the delineation of the CTV should result from the knowledge of the anatomical pathways for tumor infiltration and dissemination.

In IMRT, organs or structures that are not delineated can receive significant radiation absorbed doses. Contouring organs at risk (OAR) is the first step to control the dose in normal tissues, which might cause unacceptable complications. For so-called "parallel-like organs," the whole organ should be entirely delineated. For so-called "serial-like organs," those parts of the organ that could receive a high dose should be delineated in a consistent way. For tubular types of organ (*e.g.*, the rectum), delineation of the wall is preferred to whole-organ delineation. Especially for a serial-like organ, a planning organ at risk volume (PRV) should be delineated around the OAR. Tissues not included in the CTV or not delineated as dose-limiting OARs should still be specifically delineated and named the remaining volume at risk (RVR). Dose–volume constraints applied to the RVR avoid unsuspected regions of high dose. In addition, the absorbed dose to the RVR can be useful in estimating the risk of late effects, such as carcinogenesis.

Numerous recent publications note that the PTV and PRV margins should be based on clinical measurements. Not surprisingly, these results indicate

that systematic uncertainties have more impact on the accuracy of absorbed dose delivered to the patient than do random uncertainties. This Report strongly recommends that the margins not be compromised when delineating the PTV or PRV, even in those situations in which these volumes might encroach on an OAR or CTV. Moreover, the report describes optimization techniques, which can control the compromise of absorbed-dose homogeneity in the PTV with dose reduction in the PRV.

The IMRT treatment-planning process uses a complex iterative computer-based optimization process. The so-called *optimizer* serves to convert the radiation oncologist's treatment goals into a set of beamlets of specified intensities and directions for delivery of the planned treatment. This Report designates the set of treatment goals as the "planning aims" to differentiate them from the "prescription." A detailed example is used to guide this discussion.

Unlike three-dimensional conformal therapy (3D-CRT), IMRT does not deliver absorbed dose in all of the target volume concurrently. Hence, IMRT delivered to organs in motion, such as lungs, or to organs that change volume or location between fractions can generate regions of high and low absorbed dose in the CTV, even though a generous PTV margin has been established. Such challenges are more important for IMRT than for conventional irradiation techniques due to the very high dose gradients IMRT can achieve. In addition, sparing of OARs might also introduce regions of non-uniformity in the PTV. Intensity-modulated radiation therapy has gained prominence because it allows a lower dose to neighboring sensitive normal tissues even though it can sometimes result in less dose homogeneity to the tumor. Although the absorbed dose in normal tissue might be lower than in 3D-CRT, it can be distributed over larger volumes.

In this Report, recommendations concerning absorbed-dose reporting evolved from previous ICRU recommendations while attempting to retain a relationship with the previous recommendations. Dose-reporting recommendations are adapted to IMRT and to the changing technological advances, such as DVHs, and thus allow the decades of clinical experience in conventional therapy to be interpreted in the context of IMRT. The move from single-point to volume-based absorbed-dose specification is possible because of modern imaging and computer technology, and is essential for IMRT. This Report therefore recommends dose–volume-based specification of absorbed dose. This is most easily accomplished by employing the concept of DVHs. By a logical and careful choice of these reporting parameters, the connection with previous ICRU recommendations can be maintained in a fairly straightforward manner. The minimum and maximum absorbed doses are not recommended for reporting, but are replaced by the near-minimum, $D_{98\ \%}$, and near-maximum, $D_{2\ \%}$, values. The report recommends that the median absorbed dose, specified by $D_{50\ \%}$, should be reported, as it is considered to correspond best with the previously defined dose at the ICRU reference point. Three clinical examples included in the Report illustrate the use of recommendations contained within this Report.

Intensity-modulated radiation therapy places significant demands on all aspects of quality assurance, from the acquisition of appropriate 3D images, through the absorbed-dose optimization process, to beamlet delivery and verification. Appropriate quality assurance should be performed to ensure that the planning and treatment equipment is functioning within the tolerances required for IMRT. Quality assurance in IMRT is demanding and relates to or involves all aspects of the clinical situation, the clinical experience, and the goals of the treatment. Appropriate patient-specific quality control is necessary to ensure that the patient receives the prescribed dose as accurately as possible. These criteria do not replace visual inspection of the calculated dose distribution to determine if there is significantly higher or lower dose to a small fraction of the volume irradiated. Several methods of obtaining comparative absorbed-dose samples are recommended, but a clinic should employ a variety of methods and not rely on a single system of patient-specific quality control.

Finally, the previous ICRU recommendation of 5 % absorbed-dose accuracy is replaced by a statistical measure. This Report recommends that in low-gradient situations, defined as a relative change of absorbed dose that is less than 20 %/cm in any direction, that 85 % of target-volume absorbed-dose samples should be within 5 %. For high gradients, defined to be relative changes of absorbed dose that are greater than or equal to 20 %/cm, the use of distance to agreement is recommended instead of absorbed-dose accuracy. In high-gradient regions, the dose distribution should have 85 % of absorbed-dose samples within 5 mm of the intended position.

As cancer is a disease that will be a major health factor for the remaining life of the patient, it is recommended to record and retain the parameters to describe the absorbed-dose distribution in the patient for at least the life of the patient plus a minimum of 5 years or in accordance with local regulatory requirements. In addition to the requirements relevant to patient care, for clinical trials all of the parameters describing the absorbed-dose distribution in the patient should be retained as long as scientifically needed.

Journal of the ICRU Vol 10 No 1 (2010) Report 83
Oxford University Press
doi:10.1093/jicru/ndq006

1. Introduction

1.1 Overview of Intensity-Modulated Radiation Therapy

During the second half of the last century, key technological innovations in radiotherapy technology, diagnostic imaging, and computer science greatly modified the routine practice of radiotherapy, leading to substantial improvements in treatment delivery and outcome (Bernier *et al.*, 2004). Before 1950, deeply seated tumors were treated with cross-fired beams or rotation techniques (Webb, 1993) to ensure an acceptably low absorbed dose to the normal tissues, especially skin and bone. The introduction of deeply penetrating external photon beams, initially ^{60}Co in the 1950s, and eventually those from high-energy electron linear accelerators (linacs) in the 1960s, allowed the target absorbed dose to be increased without increasing normal-tissue morbidity. These megavoltage x-ray beams especially reduced the absorbed dose to the skin for simple beam-delivery configurations such as parallel-opposed beams and to the bone due to their absorption characteristics.

During the 1970s and 1980s, treatment planning based on the use of planar diagnostic x rays was widely implemented. A "simulator," a specialized imaging system for radiotherapy employing an x-ray imaging system and having the same geometry and degrees of freedom as a linac or rotational ^{60}Co unit, became a widely used tool for planning the treatment delivery. The bony anatomy was visible with planar x rays, but the location of soft tissues including tumors was difficult to ascertain and could often only be deduced from or correlated with bony landmarks, air cavities, or contrast-enhanced images. The increasing use of x-ray computed tomography (CT) in the 1980s and magnetic resonance imaging (MRI) in the 1990s enabled much more reliable three-dimensional (3D) assessment of the location and extent of the disease. With these imaging improvements and advances in treatment-planning techniques, it became practical to design treatment fields that conformed more closely to the target volume.

Conventional radiotherapy was traditionally administered using a number of coplanar beams, usually of relatively uniform or smoothly varying intensity across the field. The use of low-melting-point heavy cast-metal alloys allowed the treatment fields to be more easily custom shaped than with lead blocks. Multileaf collimators (MLCs), designed to replace molded heavy metal blocks, made it easier to use multiple complex-shaped fields even in the same treatment session. Three-dimensional treatment planning made it possible to plan and deliver non-coplanar beams, especially for brain tumors. Nevertheless, non-coplanar beams were less often used for treatments of the torso, because this strategy tended to increase the integral absorbed dose (product of mean absorbed dose and volume) to the patient.

Many linacs became equipped with electronic portal-imaging systems for verification of patient positioning, thus improving conformity between the planned and delivered absorbed doses. Digitally reconstructed radiographs (DRRs) (Sherouse *et al.*, 1990) were constructed from the CT-scan data set by digitally simulating the passage of x rays through the patient's CT representation in the same geometry as the treatment. The DRRs could be compared with x-ray images acquired at the time of treatment to verify the treatment position. Digitally reconstructed radiographs were especially valuable for non-coplanar beams as the planar-imaged anatomy would otherwise have an unfamiliar perspective. All of these technical innovations allowed more accurate treatment delivery to tumors, potentially allowing higher tumor absorbed doses and thus increased local tumor control and/or reduced absorbed doses to the surrounding normal tissues.

When 3D planning techniques and special delivery systems to shape the field are used to reduce normal-tissue damage close to the target volume, the technique is usually referred to as conformal radiotherapy (CRT) or three-dimensional conformal therapy (3D-CRT). When compared with conventional approaches, 3D-CRT tends to use more treatment fields and reduce absorbed dose to normal tissues abutting the target volume, but usually leads to an increase in the volume of tissue traversed.

The International Commission on Radiation Units and Measurements (ICRU) developed guide-

lines for prescribing, recording, and reporting absorbed dose for radiation therapy including 3D-CRT (ICRU, 1993; 1999). These documents recommended concepts and procedures for the delineation of the tumor, normal-tissue structures, and margins to take into account potential tumor invasion, organ motion, and setup error.

1.1.1 From 3D-CRT to Intensity-Modulated Radiation Therapy

In both traditional radiotherapy and 3D-CRT, wedges or compensators to account for a curved or sloping patient entrance surface (so-called missing-tissue compensators) were used to modify the beam intensity within the field to attempt to achieve absorbed-dose distributions with improved dose homogeneity. Multileaf collimators have largely replaced the use of wedges and missing-tissue compensators and have simplified attempts to make the beam shape conform to the tumor shape.

The concept of intensity-modulated radiation therapy (IMRT) arose because radiotherapy treatment-planning optimization algorithms predicted that the optimal radiation pattern from any single direction was typically non-uniform (Brahme, 1987; 1988; Brahme *et al.*, 1982; Cormack, 1987). It was shown that a set of intensity-modulated beams from multiple directions could be designed to produce dose homogeneity within the tumor similar to that from conventional radiotherapy but with superior conformality, especially for concave or other complex-shaped target volumes, thereby sparing nearby normal tissues (IMRTCWG, 2001). In addition, IMRT makes it easier to produce non-uniform absorbed-dose distributions if required for treatment of a volume within another defined volume (also called concomitant boost or simultaneous integrated boost techniques) (Brahme and Ågren, 1987; Mackie *et al.*, 1993; Weeks *et al.*, 1994). Rather than using uniform or constantly varying intensity distributions across each incident field, IMRT attempts to achieve more optimal absorbed-dose distributions by varying the beam intensity (fluence) within each incident beam, usually by subdividing the beam into a number of smaller segments and modulating each to achieve its selected fluence contribution. Modulation of the beam is greatly facilitated by the use of MLCs or of binary collimators combined with a moving couch. The latter were specifically developed for IMRT.

Calculation of the fluence required from each beam segment has only recently become practical with the use of high-performance computers using algorithms taking an iterative approach to dose calculation and now referred to as "inverse treatment planning." The word "inverse" is used in reference to the established body of mathematical inverse problem-solving techniques, which start at the final or desired result and work backwards to establish the best way to achieve it. So-called inverse treatment planning starts by describing a goal, *i.e.*, a series of descriptors characterizing the desired absorbed-dose distribution within the tumor, with additional descriptors designed to spare normal tissues. The inverse-planning process works iteratively to determine beam shapes and fluence patterns to achieve an optimal or acceptable absorbed-dose distribution. Examples of descriptors include the minimum absorbed dose to the target volume, the maximum absorbed dose to an organ at risk, and dose–volume specifications for both tumor and organs at risk (OAR) (see Section 3), together with factors describing the relative importance of each descriptor. These descriptors are incorporated into a mathematical objective function that attempts to specify with a single number the function's value or merit (also called cost or goodness of the plan). The optimization procedure, which is an iterative search for the solution that minimizes the cost or maximizes the goodness, is guided by the objective function. The treatment planner is expected to adjust the values of the descriptors throughout the process in order to achieve a compromise among different goals. Modification of the treatment descriptors effectively modifies the objective function. Because of the iterative nature of finding the solution and the need to change values of the treatment descriptors, the term "optimized planning" instead of the term "inverse planning" is adopted in the rest of this document to describe the treatment-planning process for IMRT. The term "optimized planning" is chosen despite its imprecision; the IMRT planning and delivery process does not guarantee that an objectively optimal solution is obtained. This and other characteristics of the optimized-planning technique will be further elaborated in Section 2.

1.1.2 Delivery of IMRT

There are several ways for delivering IMRT (Table 1.1). A conventional MLC, originally designed for blocking fields, delivers IMRT either by using multiple field segments (called segmental MLC, SMLC, or "step-and-shoot" IMRT), which can supply a discrete number of intensities (Bortfeld *et al.*, 1994; Siochi, 1999), or by having the leaf pairs move across the field at a varying rate (called dynamic MLC, DMLC, or "sliding-window" IMRT) to deliver the modulated fields (Convery and Rosenbloom, 1992; Dirkx *et al.*, 1998; Ling *et al.*,

Table 1.1. IMRT methods. The preferred optimization approaches for each IMRT method are described in Section 2.3.

Type of method	Intensity modulation method	Preferred optimization approach
Compensators	A beam filter designed to provide a patient-specific intensity pattern designed by an optimization procedure	Optimized beamlets
Segmental MLC (step and shoot)	Multiple MLC segments delivered from each treatment direction	Direct-aperture optimization
Dynamic MLC (sliding window)	Leaves slide across the field at different rates	Optimized beamlets
Intensity-modulated arc therapy (IMAT)	Leaves move while the gantry is rotating. Can require multiple rotation arcs	Direct-aperture optimization
Serial tomotherapy	Gantry rotates around the patient with the couch fixed. Binary leaves modulate a fan beam. Upon completion of each rotation, the couch is moved in a step-wise fashion	Optimized beamlets
Helical tomotherapy	Gantry and couch move synchronously. Binary leaves modulate a fan beam	Optimized beamlets
Robotic radiotherapy	Multiple non-coplanar pencil beams delivered by a robot	Optimized beamlets

1996; Spirou and Chui, 1994). In SMLC IMRT, the MLC is put into several different configurations, with each configuration defining a separate beam aperture (also called a segment) from the same beam direction. On the other hand, in DMLC IMRT, each pair of opposed leaves move across the field, and the time-dependent position of each leaf determines the intensity pattern delivered.

Intensity-modulated radiation therapy can be delivered with rotational therapy using intensity-modulated arc therapy (IMAT) or tomotherapy. Intensity-modulated arc therapy uses a conventional MLC and has the leaf pattern changing continuously as the gantry rotates (Yu, 1995). To deliver intensity-modulated fields, IMAT can require several rotational arcs each with different patterns of irradiation. This is because a single rotation yields only a step-wise intensity pattern (either open or blocked) from each arc segment through which the arc passes. Multiple arcs allow more intensity levels. For example, two arcs each with different monitor units delivered would allow four intensity levels from a given arc segment: (1) only Arc 1 open, (2) only Arc 2 open, (3) both Arc 1 and Arc 2 open, and (4) neither Arc 1 nor Arc 2 open. However, it has recently been shown that controlled variation of absorbed-dose rate during the gantry rotation can achieve some intensity modulation of the beam even if only a single rotation is delivered (Otto, 2008). A boost dose to part of the treatment volume can be readily delivered by using an additional rotation. Tomotherapy is intensity-modulated rotational therapy using a narrow CT-like fan beam modulated by a binary collimator. The binary collimator has multiple leaves, specifically designed to deliver IMRT for rotating fan beams (Carol, 1995; Mackie *et al.*, 1993). It is called a binary collimator because each leaf moves rapidly from the closed position to the open position across the fan beam to expose the source. The length of time a leaf is in the open position determines the intensity delivered by the sub-beam or "beamlet." The fan-beam width is collimated by a pair of jaws above the binary MLC in the same fashion as the fan-beam width is defined in a CT scanner. Serial tomotherapy, which was the first form of IMRT to treat patients, rotates a fan beam once around the patient with the couch fixed (Carol, 1995; Grant, 1996). The couch moves in successive steps to complete the treatment. In helical tomotherapy, the fan-beam rotation and couch are in simultaneous motion so that the source of radiation describes a helical pattern with respect to the patient (Mackie, 2006; Mackie *et al.*, 1993; 1999).

A robotic radiotherapy device using pencil beams delivered from a large number of directions can also be used to deliver IMRT (Webb, 1999; 2000). While these devices were designed for stereotactic radiosurgery, a large number of pencil beams from multiple non-coplanar directions when planned with optimization techniques are equivalent to multi-directional IMRT. Compensating filters, specifically designed using optimization techniques to produce intensity modulation, is a tool that can be used to produce IMRT (Djordjevich *et al.*, 1990; Jiang and Ayyangar, 1998; Renner *et al.*, 1989; Yoda and Aoki, 2003).

1.1.3 Clinical Experience with IMRT

Intensity-modulated radiation therapy can generate absorbed-dose distributions superior to 3D conformal treatments in several situations, including concave target volumes for which multiple OAR are close to the target volume, and for producing

multiple absorbed-dose levels in the target volume similar to boost therapy (IMRTCWG, 2001). Figure 1.1 is a schematic representation of a concave target volume being treated by a set of three uniform-intensity beams and one partially blocked beam when compared with a set of five beams that are all intensity modulated. Concave-shaped absorbed-dose distributions are required for tumors surrounding the spine and for treatment of prostate cancer with seminal-vesicle involvement. Multiple organs, including the parotid glands, eyes, brainstem, auditory apparatus, thyroid, and spinal cord, are commonly at risk in treating head and neck cancer. Intensity-modulated radiation therapy can lead to improved conformality of the high-dose region to the tumor.

Usually, but not always, IMRT requires greater time and resource commitment than conventional radiotherapy. Because of the resulting steeper absorbed-dose gradients, optimal IMRT requires more accurate delineation of both tumor and normal tissue than does conventional radiotherapy. Additional normal tissue often has to be delineated because tissue that is not specified can receive unexpected high absorbed doses. Iterative optimization can take more time than 3D-CRT treatment planning. The beam-on time can be longer because the delivery has a lower duty cycle. In general, the higher the degree of modulation, the longer the irradiation takes. On the other hand, compared with 3D-CRT without the use of a MLC, the overall treatment time might be less because there is no need to manually change blocks. Most IMRT programs have instituted more stringent machine quality assurance (QA) to check the performance of the IMRT delivery system (see Appendix A.2). For example, the tolerance for MLC leaf position must be smaller for IMRT than when used to provide field blocks for 3D-CRT. New procedures for patient-specific dosimetry QA are required because simple methods cannot be employed to check the calculations for the patient's treatment. However, IMRT is not necessarily always more difficult. For example, in conventional high-dose treatments of the head and neck, photon beams combined with electron beams from lateral directions must often be used to prevent the cord dose from exceeding tolerance. This greatly increases treatment complexity and the skills required, yet the photon/electron beam deliveries do not always produce homogeneous absorbed-dose distributions in the tumor. By contrast, IMRT can produce homogeneous absorbed-dose distributions in the target and spare the critical structures without use of electron beams.

The use of IMRT has been growing rapidly. In a survey performed in 2003 in the USA, among 168 radiation oncologists randomly selected, one-third was using IMRT (Mell *et al.*, 2003). In 2005, a similar survey showed that more than two-thirds of radiation oncologists were using some form of IMRT, mainly for increased normal-tissue sparing or target-dose escalation (Mell *et al.*, 2005). Among the sites treated by IMRT, head and neck malignancies and prostate cancers are by far the most common, followed by central nervous system, lung, breast, and gastro-intestinal tumors. However, thus far, few prospective randomized trials demonstrating superiority of IMRT over conventional treatments, either in terms of efficacy or morbidity reduction, have been reported. For breast cancer, a randomized study was performed comparing IMRT with standard tangential, wedged fields. Donovan *et al.* (2002) reported that apparently better absorbed-dose distributions were achieved with IMRT. In a follow-up study, using a prospective randomized clinical trial, Donovan *et al.* (2007) found

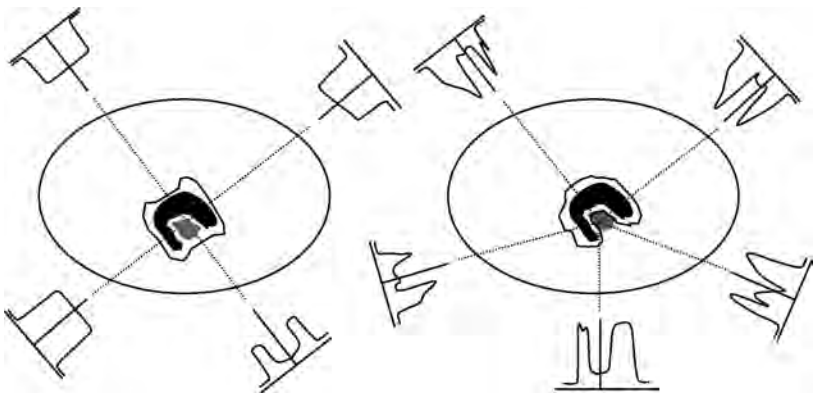

Figure 1.1. Comparison of CRT (left) and IMRT (right). The ability for CRT to alter isodose lines was limited to shaping of field boundaries with MLCs or blocks, the use of wedges or compensators for missing tissues, and central blocks for shielding critical structures. The IMRT beams can have highly non-uniform beam intensities (fluences) and are capable of producing a more concave-shaped absorbed-dose distribution. With neither conformal therapy nor IMRT can the PRV be always completely avoided, but with IMRT the concave isodose curve that includes the PTV better avoids the PRV. The black region indicates the PTV; the gray region indicates a PRV, and the line surrounding the PTV is a typical isodose contour.

statistically that the cosmetic effect was significantly worse in patients in the conventional-treatment arm when compared with the IMRT arm. Using a matched case-control methodology for head and neck cancer, Jabbari *et al.* (2005) reported that, after a decline following radiotherapy, xerostomia and quality-of-life (QOL) measures improved 6 months after therapy for the IMRT-treated patients but not for the patients treated with conventional radiotherapy. The potential benefits gained from IMRT in reducing xerostomia or improving QOL, compared with standard RT, are best reflected some time (>6 months) after therapy.

For the head and neck, the most convincing retrospective studies of the increased therapeutic gain achievable with IMRT are from tumors close to the base of the skull, such as nasopharyngeal and paranasal sinus cancers, for which a higher rate of local control and a lower incidence of complications have been reported in comparison with conventional techniques (Claus *et al.*, 2002; Lee *et al.*, 2002). A substantial reduction in late radiation-induced toxicity such as xerostomia has also been extensively documented following the use of IMRT for treating pharyngo-laryngeal squamous cell carcinomas (SCCs), without any reduction in local-regional control probability (Chao *et al.*, 2001a; Eisbruch *et al.*, 1999; 2001; Henson *et al.*, 2001). A few retrospective studies have also reported that, despite the high conformality of absorbed-dose distributions, geographical misses were rather uncommon in IMRT for pharyngo-laryngeal SCCs (Chao *et al.*, 2002; 2003; Dawson *et al.*, 2000; Eisbruch *et al.*, 2004). For prostate cancer, the largest study comes from the Memorial Sloan Kettering Cancer Center, New York, NY, which has reported over 772 patients treated using IMRT with minimum target absorbed doses in excess of 81 Gy (roughly 20 % higher than the absorbed dose used in conventional treatment). In this study, only 4.5 % of patients developed a grade 2 rectal toxicity (moderate diarrhea, excessive rectal mucus, or intermittent bleeding) and none experienced a grade 3 or greater toxicity (Zelefsky *et al.*, 2002). Recent studies have suggested that in-treatment-room imaging could increase the accuracy of absorbed-dose delivery and consequently further decrease the rate of rectal complications (see review in Bucci *et al.*, 2005).

1.2 Issues Common to Both 3D-CRT and IMRT

Many advances and emerging concerns in radiation therapy are not unique to IMRT but also impact 3D-CRT. Nevertheless, issues such as 4D imaging and adaptive radiotherapy, uncertainties, and radiation-induced secondary cancers might be more significant for IMRT.

1.2.1 Imaging and 4D Adaptive Treatment

Selecting and delineating regions of interest is one of the most technically and intellectually challenging and time-consuming aspects of modern radiotherapy. Three-dimensional CRT, in general, and IMRT, in particular, increase the need for accurate anatomic delineation. This requires an adequate specification of the tumor location and a thorough knowledge of the processes of likely infiltration and spread (see Sections 4.2 and 4.3). In IMRT, the optimization process has no ability to constrain the absorbed dose to tissue structures that are not delineated. Consequently, tissues containing tumor cells that are not delineated are very unlikely to be adequately treated, and sensitive structures not delineated might receive an unacceptably high absorbed dose. Three-dimensional imaging systems are a key to the determination of the tumor and normal-tissue volumes. Automated contouring systems can make it easier to segment images but increase the importance of verifying the accuracy of the computer delineation.

Modern image-acquisition systems are increasing the sensitivity and specificity of tumor detection. Functional and molecular imaging are emerging and provide new opportunities to understand the biology of both normal tissues and tumors (Bradbury and Hricak, 2005; Jager *et al.*, 2005). The improved capabilities of imaging systems such as magnetic resonance spectroscopy (MRS) and improved markers of physiologic activity in positron-emission tomography (PET) will help to define more accurately the extent and location of tumor where the absorbed dose should be increased. Thus the boundaries between gross tumor volumes or GTVs (see Section 4.2) and clinical target volumes or CTVs (see Section 4.3) will also become better defined. For example, MRS can detect a higher concentration of choline, which is typically found in malignant prostate adenocarcinoma, in an otherwise apparently normal sub-region of the prostate (Huzjan *et al.*, 2005). The sub-region that is so defined could potentially be prescribed a higher absorbed dose. Also, it has been shown that in head and neck tumors, ^{18}FDG-PET imaging was more accurate than CT or MR imaging for delineating the GTV of the primary tumor (Daisne *et al.*, 2004). IMRT allows for complex prescriptions for delivering higher absorbed doses to sub-volumes of the GTV suspected of having more radioresistant disease

(Bentzen, 2005; Ling *et al.*, 2000). This is sometimes referred to as a "biological target volume" that can be subjected to concomitant boosting.

New imaging studies are also able to better characterize normal tissues and normal-tissue function. For example, using functional MRI, it is now possible to locate brain structures that need to be spared, *e.g.*, motor cortex, in the treatment of brain tumors; these structures can then be delineated as an organ at risk to which dose–volume constraints can be assigned (Nair, 2005).

Over the years, it has been recognized that using imaging as a "snapshot" of the tumors and/or normal tissues is an oversimplification of reality, as location, morphology and physiology can change during treatment, *e.g.*, due to breathing during a treatment fraction, but also between fractions due to tumor response and/or patient weight loss. The ability to measure these changes and adapt the course of treatment will lead to adaptive treatment, also called 4D adaptive treatment (Ramsey *et al.*, 2006). Magnetic resonance and CT scanners are being developed to provide the capability of producing multiple 3D views of the patient with sufficient rapidity to construct a 4D view of the patient and to provide a 4D delineation that can be used for treatment planning. Computed tomographic scanners have rotational periods less than 1 s. Adequate image reconstruction requires only a gantry rotation of slightly more than 180°. This fast data-acquisition speed enables multiple images to be acquired to characterize the motion during a typical breathing cycle. A pneumatic cuff over the diaphragm or a tracking system monitors the movement of the chest to correlate the images with their corresponding breathing phase. Images acquired through several breathing cycles can then be assembled into a single 4D-imaging set. These advances might make it possible to dynamically define the position and extent of the GTV and CTV during a treatment fraction. This will add greatly to the size of the data set needing evaluation.

The availability of 4D anatomic data can revolutionize the treatment of lung cancer because now the details of lung motion can be shown (Mageras and Yorke, 2004). The planning target volume (PTV—see Section 4.5) includes the CTV and a margin to take into account uncertainty of positioning, motion, and anatomical changes. The 4D information could be used to evaluate more accurately the PTV margin required for conventional radiotherapy and IMRT. It is possible to use a 4D representation to plan the delivery of radiotherapy and deblur or sharpen the absorbed-dose gradients that typically get blurred or distorted when the patient breathes. Four-dimensional information could be used for planning the delivery of radiotherapy in which the tumor is tracked, and then either the movement of the tumor is compensated for by dynamic movements of the couch or the beam is made to follow the tracked tumor (Keall, 2004). It could be used to determine the optimal breathing phase more accurately so as to determine how much of the breathing cycle can be safely used for irradiation when the treatment is gated (Mageras and Yorke, 2004; Seppenwoolde *et al.*, 2002). The delivery of radiation could be synchronized with breathing if the patient were guided to breathe in the same way during treatment as at the time the 4D image was acquired (Zhang *et al.*, 2004). Some of these methods will require the absorbed dose to be computed in multiple phases. For those methods, the absorbed-dose distribution from each phase must be summed up and displayed on one breathing phase. The same deformable registration that would be used to transfer the contours between breathing phases could also be used to establish the one-to-one mapping required to transfer absorbed dose assigned to voxels in one breathing phase onto the same voxels in another breathing phase (Brock *et al.*, 2006; Lu *et al.*, 2004). Deformable registration creates maps showing how a mass of tissue moves during one breathing cycle. Deformable registration provides a link from these 4D representations to a corresponding set of 3D representations, each describing one of the breathing phases.

The fourth dimension in treatment delivery can allow visualization of the changes during the entire course of treatment. In head and neck tumors, it has been shown that the tumor volume can dramatically decrease during a 7-week treatment, and that re-planning, taking into account this volume change, would translate into a substantial sparing of the surrounding non-target tissues (Geets *et al.*, 2007a; 2007b). Similarly, substantial variation in normal-tissue volume has also been reported during radiotherapy of other sites (Barker *et al.*, 2004). Developments in coming years will hopefully indicate which outcomes might benefit from 4D treatment planning and adaptive changes. However, they will dramatically expand the complexity of tissue delineation (often called segmentation), absorbed-dose specification, and dose reporting.

While the size of the data set derived from different imaging modalities might grow by an order of magnitude, the time for analysis must not. In the case of contouring the GTV or CTV, tools to transfer contours from one breathing phase to another will be required before 4D data will be routinely used. Deformable registration to produce a one-to-one

mapping of the voxels from an image set acquired at one phase to another at a different phase is required. The ability to quickly review and edit the transferred contours is also required. The understanding of the nature and magnitude of motion will be fully appreciated only when the data can be viewed through time using image loops with interactive selection of geometric viewpoint and display type.

Two-dimensional images acquired with a portal image system and compared with a DRR cannot be used to precisely determine how the treatment volume is changing and, in some cases, how the PTV has to be modified (Yan *et al*., 1997). Image sets showing anatomical changes during the progress of treatment can be created by routine 3D imaging of the patient following treatment setup and prior to delivery. An in-treatment-room CT scanner, either separate from or integrated into the treatment unit, can acquire such image data and in addition evaluate the setup of a patient prior to radiotherapy (Jaffray *et al.*, 1999; Langen *et al.*, 2005; Mackie *et al.*, 1993; 2003; Uematsu *et al.*, 1996). The treatment can then be re-planned or the absorbed dose reconstructed using those image sets.

The composite absorbed-dose distribution describing the accumulated absorbed dose from all days of treatment might also employ deformable registration to map the absorbed dose from each day onto the planning CT representation (Lu *et al.*, 2004; Olivera *et al.*, 1999; Wang *et al.*, 2005). When mapped onto the planning image set, the planned and accumulated absorbed-dose distribution can be compared. In some cases, it might be possible to adjust the plan during the remaining course of radiotherapy to make up for identified deficiencies. For example, if analysis of the composite absorbed-dose distribution at some time in the course reveals that there are low-dose regions in the target volume, subsequent fractions could be re-optimized to add absorbed dose. It might even be possible to reduce the absorbed dose in a region of high absorbed dose in a selected normal tissue. This type of adaptive radiotherapy will require increased attention by the radiation oncologist throughout the course of treatment.

1.2.2 Margins and Uncertainties

The concept of a margin is described in ICRU Reports 50, 62, 71, and 78 (ICRU, 1993; 1999; 2004; 2007). A margin provides a buffer in the delineation of tissues to account for uncertainties. The CTV includes the GTV and a margin to take into account microscopic extension of the tumor. The PTV adds a margin to the CTV to account for organ motion or setup error. Margins, allowing for positioning, motion, and anatomical changes, are also required for the OAR to arrive at the planning organ-at-risk volume (PRV). The need to quantify margin requirements will be of increasing relevance for IMRT. Intensity-modulated radiation therapy tends to produce steep absorbed-dose gradients between the target volume and the OAR. Having realistic margins for both the tumor volume and any OAR allows the planning process to better compromise between an adequate absorbed dose to the PTV and a safe absorbed dose to normal tissue.

Factors affecting margin requirements to define the PTV include uncertainty of patient positioning, mechanical uncertainty of the equipment (*e.g.*, gantry sagging), dosimetric uncertainties (*e.g.*, penetration of the beam), the use of motion-management techniques such as gating, image-transfer errors from CT and simulator to the treatment unit, and human factors. These factors will vary from center to center, and, within a given center, from machine to machine and from patient to patient. The use of patient immobilization devices, the application of quality-assurance programs, and the skill and experience of the radiographers/radiotherapists are also important and must be taken into account. Additionally, the use of different image-guidance systems or other uncertainty-reduction techniques can significantly alter the size of the required margins. Standard rationales for determining the margins must be established and followed to ensure that the margins are sufficient but not excessive.

Several approaches to quantify the CTV-to-PTV margin requirements have been published (Austin-Seymour *et al.*, 1995; Balter *et al.*, 1996; Goitein and Schultheiss, 1985; Roeske *et al.*, 1995; Stroom *et al.*, 1999a; 1999b; van Herk *et al.*, 2000). Variations in setup can result for a variety of reasons. One example is the systematic error that arises if the planning CT image is not appropriately representative of the patient throughout the course of therapy. For example, if on the day of CT planning, the patient's rectum is distended by bowel gas, the position of the prostate will be offset and perhaps rotated from its average position. In addition, random variation about the average position can occur daily. Every investigation has concluded that systematic variations are more important than random variations. Daily CT guidance using an in-room CT system is becoming common practice to reduce both systematic and random position variations (Forrest *et al.*, 2004; Ma and Paskalev, 2006). However, even with the best

image-guidance systems, variations cannot be eliminated. Image-guidance systems themselves have uncertainties, and deformation of the patient's anatomy cannot be eliminated, although its extent can be estimated with deformable-registration techniques (Brock *et al.*, 2006; Lu *et al.*, 2004). Then beam delivery can perhaps be modified (Mohan *et al.*, 2005) to compensate for such effects. Imaging at the time of treatment can be used to better define the pattern of dose variability or reduce the uncertainty of setup. Image guidance can be used to define the margins for a specific protocol or treatment machine or to adjust a patient-specific margin using repeated imaging procedures. Yan *et al.* (1999) showed that such repeated imaging procedures can greatly reduce the systematic uncertainty in positioning with respect to the original planning image. When delineating a PTV, the different types of uncertainties and variations identified above should be estimated and combined.

Even if the setup uncertainty were completely eliminated, there would still be uncertainty due to organ motion and to changes in the anatomy of the patient associated with weight loss or tumor shrinkage (or growth). This contribution to the margin can be reduced with gating or tracking techniques, or replanning, but the uncertainty cannot be eliminated completely.

The margin defining the PTV is principally used to maintain the absorbed dose at or near the prescription value in the CTV. Historically, there have been limited means to make isodose surfaces conform to the PTV, but recently the degree of control over conformity has greatly improved with the advent of IMRT. However, IMRT can create absorbed-dose distributions that are difficult to evaluate with traditional approaches. Intensity-modulated radiation therapy can easily change the degree of absorbed-dose homogeneity in the target volume. For example, for prostate cancer, absorbed-dose homogeneity might not be essential and may be deliberately reduced if the absorbed dose in the rectum is of concern. Current dose-reporting specifications need to be supplemented by other figures of merit for a meaningful evaluation of absorbed-dose distributions, but this can increase the complexity of dose reporting (see Section 3.2). The dose–volume histogram (DVH) has become a critical tool to evaluate complex 3D absorbed-dose distributions, and its use is even more important for IMRT (Drzymala *et al.*, 1991). However, with a DVH alone, the location of low- and high-dose regions cannot be determined. A low-dose region in the periphery of the CTV is likely to be less important than at the center, and a high-dose region might be of less concern well inside the tumor boundary. An increasing concern is that IMRT might result in unexpected regions of high absorbed dose outside the PTV in normal tissues that have not been specified as avoidance regions or that have been specified but with insufficient importance attached to them.

1.2.3 Radiation-Induced Secondary Cancers

The risk of secondary malignancies following radiotherapy is a controversial subject. One consideration is that patients undergoing therapy for cancers might be at higher risk of secondary tumors due to their genetic predisposition, or due to their particular lifestyle and exposure to carcinogens such as tobacco and alcohol. These factors could be more dominant than the radiation risk itself. Whenever large-scale radiotherapy studies have been performed and compared with surgery, radiotherapy has been shown to be associated with a statistically significant increase in the risk of secondary malignancies, particularly in long-term survivors. In a study on radiation-induced second malignancies after prostate radiotherapy delivered with large margins before the 3D-conformal era, it was shown that patients had a 6 % increase in the relative risk of developing a solid tumor (except prostate cancer) compared with patients treated by surgery (Brenner *et al.*, 2000). In women, the ratio of observed-to-expected cases of breast cancer after radiotherapy for Hodgkin's disease was up to 2.24 times that of women at the same age in the general population (Travis *et al.*, 1996). This increased relative risk was particularly important for women irradiated before the age of 16. However, this study refers to delivery of large fields in radiotherapy planned before the era of 3D-CRT. Techniques employed with more modern radiotherapy might change the incidence of second malignancies in the future.

The transition from conventional radiotherapy to 3D-CRT involved a reduction in the volume of normal tissues receiving a high absorbed dose and perhaps an increase in absorbed dose in the target volume. As a consequence of the smaller volume of normal tissue irradiated to a high absorbed dose, a decrease in the number of radiation induced secondary cancers might be expected per unit volume irradiated. Of less certainty is whether there will be an overall decrease or increase in the number of induced secondary carcinomas (Hall and Wuu, 2003) because a larger overall normal tissue volume is irradiated to a lower dose. On the other hand, the switch from conventional radiotherapy to 3D-CRT or IMRT might result in an increased rate of secondary malignancies. IMRT typically involves a larger

volume of normal tissue being exposed to lower radiation absorbed doses than does 3D-CRT (Hall and Wuu, 2003). Even when the integral absorbed dose is approximately the same for IMRT and 3D-CRT (Aoyama *et al.*, 2006; D'Souza and Rosen, 2003), there are theoretical arguments for a potentially increased risk for carcinogenesis (Jones, 2009). Carefully conducted clinical trials with long follow-up will determine the validity of this concern.

When compared with conventional radiation therapy, an IMRT treatment plan typically results in an increase in the number of monitor units by a factor of from 2 to 3, increasing the absorbed dose outside the boundary defined by the primary collimator as a result of leakage and scattered radiation (Williams and Hounsell, 2001). As a consequence, the total body dose received can be substantially increased. In a comparison between a conventional technique and a serial tomotherapy treatment of 70 Gy for head and neck tumors, it was estimated that the effective dose from leakage radiation increased from 242 mSv to 1969 mSv (Verellen and Vanhavere, 1999) in proportion to the extra monitor units delivered. Altogether, it has been estimated that IMRT without provision for avoidance of the most carcinogenic tissues (discussed below) could potentially double the incidence of second malignancies compared with conventional radiotherapy, from about 1 % to 1.75 % for patients surviving 10 years (Hall and Wuu, 2003). However, the biological models on which these estimates are based might be questionable.

Approaches to reduce the carcinogenic potential are possible. Unwanted absorbed dose can be decreased by increased shielding in the primary collimator, and removal of the field-flattening filter. The field-flattening filter is not required if the beam is used only for IMRT (Mackie *et al.*, 1993; Vassiliev *et al.*, 2006); if necessary, the beam can be modulated to make it uniform. These improvements have been implemented in helical tomotherapy (Mackie *et al.*, 1999). Inside the volume irradiated by IMRT, it is also possible to delineate normal-tissue structures, such as the breast, thyroid, and lung, which have a high potential for the development of second malignancies, and then use the optimization process to limit their absorbed dose and thus perhaps lower the probability of carcinogenesis.

1.3 Aim of the Present Report and Relation to Existing ICRU Reports

For several decades, the ICRU has been involved in a continuous effort to improve uniformity in defining terms and concepts for reporting radiation therapy. ICRU Report 29, *Dose Specification for Reporting External Beam Therapy with Photons and Electrons*, was published in 1978 (ICRU, 1978). It was superseded in 1993 by ICRU Report 50, *Prescribing, Recording, and Reporting Photon Beam Therapy* (ICRU, 1993). A *Supplement to Report 50* (ICRU Report 62) was published in 1999 (ICRU, 1999). ICRU Reports 50 and 62 deal with conventional external photon-beam irradiation techniques, including 3D-CRT; the present Report deals with the more complex special technique, *viz*., IMRT. Reports on electron (ICRU Report 71) and proton (ICRU Report 78) beam therapy have recently been published (ICRU, 2004; 2007). The present Report conforms to the recommendations of ICRU Report 78 (ICRU, 2007).

As a general rule, the recommendations for prescribing, recording, and reporting special techniques in external photon-beam therapy such as IMRT should be consistent with previous ICRU recommendations. In particular, the same definitions of terms and concepts should be used whenever possible. However, account must be taken of the clinical and technical uniqueness of each treatment approach. The present Report is based on concepts and definitions previously introduced in ICRU Reports 50 and 62.

The processes of IMRT optimization is described in detail in Section 2. Section 3 updates the concepts for dose reporting, which has moved from single spatial point reporting (*e.g*., the ICRU Reference Point, minimum and maximum absorbed doses) to dose–volume reporting (Level 2 reporting). It also explores investigational (Level 3 reporting) concepts such as the clinical and biological metrics of tumor-control probability, normal-tissue complication probability, and equivalent uniform dose. Level 3 reporting also includes conformity and homogeneity indices, and reporting on absorbed-dose uncertainties. In Section 4 of this Report, special attention is given to the selection and delineation of target volumes, which can be defined using various imaging modalities, but which can also undergo changes in shape and nature during treatment. Section 4 also revisits the concepts of the PTV and PRV to better define the uncertainties in their specification. Section 5 updates the definition of absorbed-dose prescription by discussing the concept of planning aims based on dose–volume constraints. Appendix A.1 presents new algorithms and concepts in absorbed-dose computation and recommends that tissue heterogeneity calculations be used for IMRT. Appendix A.2 makes recommendations on machine- and patient-specific QA. These include

checks of the delivery and imaging systems, but also individual patient QA, which should not be limited to measurement at a single point. It should include QA of beam intensity, multiple point dose checks using a phantom, or independent absorbed-dose-distribution calculations, presuming that adequate QA is conducted on the treatment equipment. Finally, three clinical examples illustrating how the recommendations on reporting treatments described in the present Report can be used in routine practice are presented in Appendix B.

Journal of the ICRU Vol 10 No 1 (2010) Report 83
Oxford University Press
doi:10.1093/jicru/ndq007

2. Optimized Treatment Planning for IMRT

2.1 Introduction

Three-dimensional conformal therapy (3D-CRT) and intensity-modulated radiation therapy (IMRT) make a radical departure from conventional radiation therapy in regard to treatment planning. Conventional therapy has typically been limited to beam portals of varying size and intensity using beam-shaping devices and perhaps patient-dependent intensity modifiers. Computational algorithms provided adequate descriptions of the distributions of absorbed dose. Traditionally, the therapy team "optimized" the treatment plan using the few free parameters available. Tumor prescriptions were often selected to prevent normal-tissue injury in surrounding critical tissues. Manual optimization was a relatively straightforward process largely founded on clinical judgment, with only limited exploration of potentially better solutions and with no easily derived comparative dose-distribution metrics.

The almost simultaneous advent of high-precision three-dimensional (3D) volume imaging and 3D radiation-beam treatment planning has driven the present revolution in radiation therapy. Now the number of beam directions and intensities are essentially unlimited. Whether using multiple small individual beams delivered under computer control with arbitrary directions and intensities, or with intensity-modulated fan beams arranged in a co-planar geometry, the capability of automated optimization techniques vastly exceeds those of manual optimization processes. In this section, the current processes for computer-assisted optimized treatment planning that take advantage of modern 3D imaging and IMRT delivery are described.

2.2 Comparison of 3D-Conformal and IMRT Treatment Planning

In 3D-conformal planning, beam modification includes, for example, changing beam boundaries and directions, using beam modifiers such as wedges or compensators, or changing the absorbed-dose contribution of different fields. This process is iterative in nature. The quality of the resulting absorbed-dose distributions and the dose–volume histograms (DVHs) is highly dependent on the skill and experience of the planner. This process, in effect, mainly employs the clinical judgment and experience of the treatment team to "optimize" the therapy plan. Such judgments are made in the context of optimizing tumor control while controlling the complication risk. In 3D-CRT, the approach to optimizing the resulting distribution in absorbed dose is accomplished by iteratively modifying beam characteristics, such as direction, collimator rotation angle, beam weight, and field boundaries, which collectively describe each of the fields that make up the plan. Three-dimensional conformal therapy becomes IMRT when non-uniform-intensity sub-beams or multiple uniform-intensity beams of different dimensions are delivered from each beam direction. While 3D-CRT treatment planning was traditionally done manually, in principle this iteration process could be computerized (Xiao *et al.*, 2000). Intensity-modulated radiation therapy employs automated, iterative optimization techniques (Bortfeld, 2003; 2006; Boyer *et al.*, 1999; Mackie, 2006; Mohan, 1996; Webb, 2003). Figure 2.1 illustrates a comparison between traditional and IMRT optimization methods. In traditional optimization, beam parameters such as the direction, the presence of beam modifiers (*e.g.*, wedges), and the shapes of the beams are established; then the resulting absorbed dose is computed. The beam attributes are iteratively modified as necessary. In IMRT optimization, constraints such as those based on dose–volume considerations are chosen. The key distinctions between traditional and IMRT methods are: (1) use of mathematical objective functions and incorporation of user-defined dose–volume constraints, and (2) employment of an iterative computer-based IMRT algorithm to seek the optimal solution. The beamlet weights or the weights of a series of beam segments are determined and the absorbed-dose distribution that results is then computed. The beamlet weights and/or segment shapes or weights are iteratively modified. If necessary, the

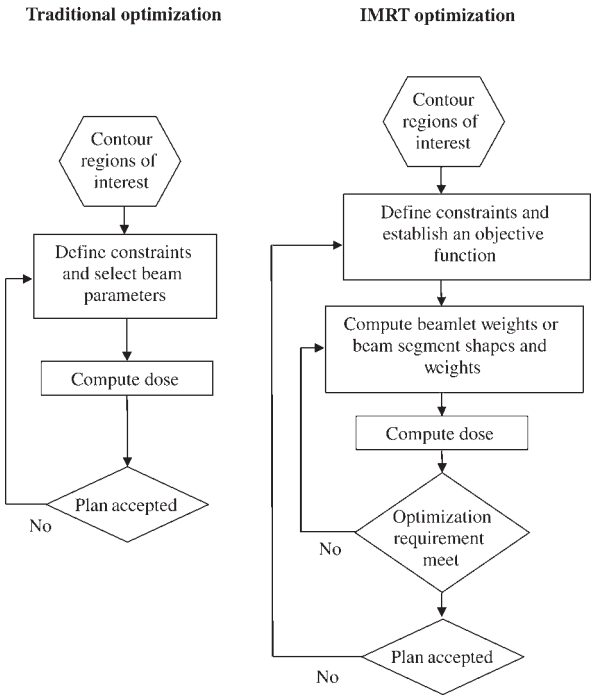

Figure 2.1. Comparison between traditional (left) and IMRT (right) optimization processes.

constraints that define the objective function can also be modified. This would lead to another round of automated iterative optimization. The radiation oncologist makes the final decision on plan acceptability. Similar optimization approaches are common to the field of operations research (Hillier and Lieberman, 2005).

2.3 Overview of the Optimization Process

The large number of degrees of freedom is a consequence of using many variable-intensity beamlets. The choice of possible intensity patterns and beam directions is enormous. Manual comparisons of all possible intensity patterns that could be delivered even from a few beam directions are not practical. The optimization process is a technique for exploring the various choices for the values of the available free parameters in the context of a desired outcome. The so-called objective function takes into account absorbed-dose constraints and weights the importance of the target and organs at risk (OAR) absorbed doses and serves as the means to arrive at an optimal intensity pattern. The term "optimization" in this context does not necessarily mean that the method will find the best intensity distribution to accomplish the stated treatment goals for any given clinical situation.

Optimization theory encompasses approaches to solving complex problems for which the solution that approaches as close as possible to the desired outcome is sought (Kelly, 1999). In the case of radiotherapy, the desired result is an absorbed-dose distribution assumed to be most appropriate for treating the tumor and sparing critical tissue. An optimization method could, in principle, establish the beam directions and beam delivery patterns from these directions on the basis of a completely specified "ideal" absorbed-dose distribution. This approach is not followed because such an ideal and physically achievable absorbed-dose distribution can rarely be conceived at the beginning of the process. Rather, a set of constraints on the absorbed dose delivered to various tissues is chosen for selected patient volumes, *e.g.*, the planning target volumes (PTVs) and the OARs. Examples of constraint descriptors of the absorbed-dose distribution common in radiotherapy optimization systems are the "minimum" absorbed dose to the PTV, the "maximum" absorbed doses to the OAR, dose–volume specifications for both the tumor and the OAR, and factors describing the relative importance of each volume. In this Report, the use of the minimum and maximum absorbed doses for reporting is not recommended and will be discussed in Section 3. There are many ways that these descriptors can be mathematically formulated as an objective function leading to a metric that quantifies the "goodness" of a particular solution. Often, guided by DVH and dose-distribution analysis, the values of the constraint descriptors are changed by the planner during the optimization process.

A computer-based algorithm can include a set of inviolable ("hard") constraints to restrict the solutions to those that are "feasible." Such constraints might include physical constraints such as forbidding negative beam intensities and restrictions on beam size or direction. Because hard constraints cannot be violated, the solution based only on hard constraints will not be the "best" or even near best; rather the solution is simply feasible as it satisfies all of the hard constraints. This situation is schematically indicated in Figure 2.2a, for which two beam weights for fixed beam directions are constrained to a region of acceptable solution values for various chosen organ absorbed doses. The interior shaded region comprises a set of solutions that all satisfy the hard constraints and are all considered feasible.

A much improved ability to reach the clinical goals is achieved if the objective function also includes "soft" constraints or objectives and uses optimization techniques to seek an optimal set of free parameters. Such objectives can be malleable and can include specifications such as dose–volume uniformity, other dose–volume criteria,

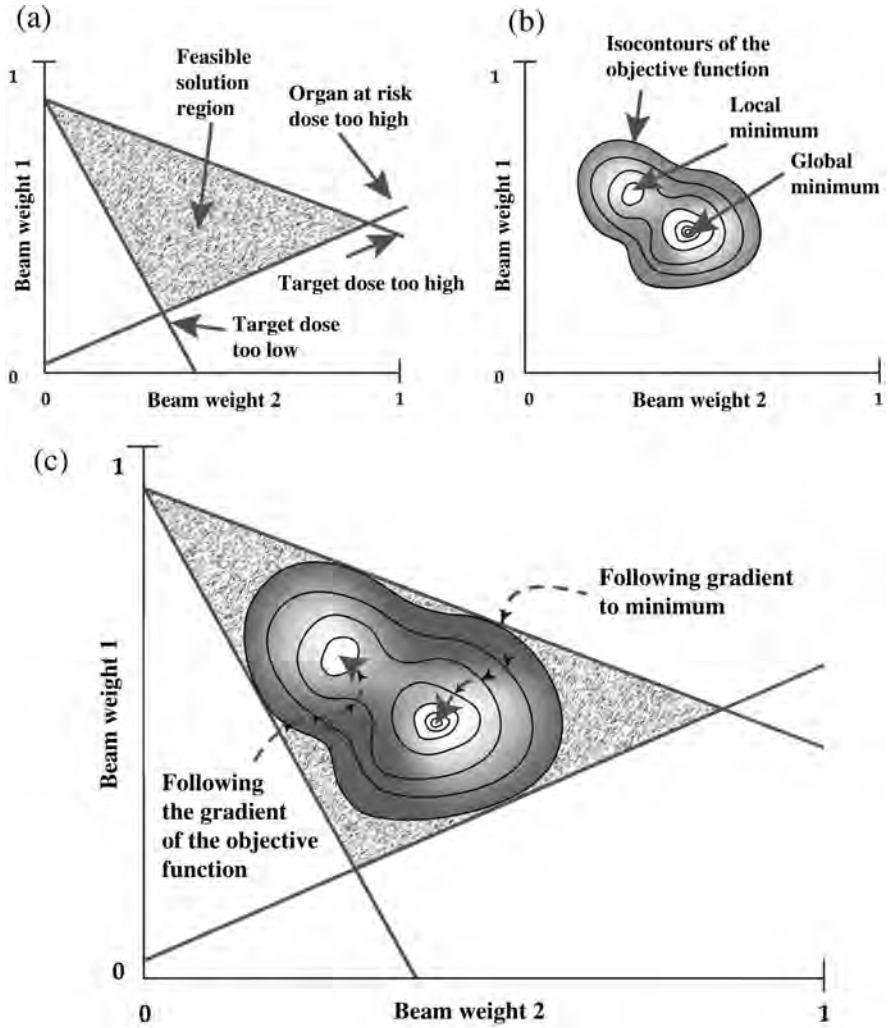

Figure 2.2. Illustration of feasible and optimal solutions for a simple case of only two beams. The weights for the two beams define a 2D solution space. In IMRT, there can be tens of thousands of beamlet weights, so the solution space has a high number of independent dimensions. In the upper left panel, a region of feasible solutions is illustrated. Absorbed-dose constraints define the boundary of the region of feasible solutions, although in general the lines defining the region of feasible solutions would not be linear. In the upper right panel, the optimal solutions resulting from the use of the objective function are superposed upon the region of feasible solutions. Two minima are indicated, only one of which is the best solution ("global minimum"). Finally, two gradient-search results are indicated in the lower panel, indicating the effect of starting the search from different initial conditions.

various absorbed-dose limits to targets and tissues, *etc*. The optimization algorithm searches the parameter space seeking to achieve an objective function (made up of soft and hard constraints) generating an optimized solution. Figure 2.2b schematically indicates such a process. Note that the hard constraints bound the solution space, while soft constraints define a global minimum or "best" solution for a given objective function. In the example provided, two minima are indicated, but only one is a global minimum.

The objective function can be quite complex with many parameters, some of which enter in a non-linear manner. Hence, a solution in closed form is not possible, and sophisticated algorithms are used (*e.g.*, gradient descent, stochastic annealing, neural networks, genetic algorithms) to search the parameter space. However, the solution space can be so large that a global minimum cannot be established in a realistic time, and a local minimum is accepted (Figure 2.2c). In fact, depending upon initial starting locations, different minima might be found from the optimization as shown in Figure 2.2c.

The free parameters searched could, in principle, include a large number of beam directions comprising specific beamlet intensities. For example, in tomotherapy, all coplanar directions are free parameters for optimization, but non-coplanar directions are not allowed. In contrast, in other forms of

IMRT beam directions are selected by the treatment planner, and non-coplanar directions may be used and optimized. Mohan and Bortfeld (2006) showed that beam directions commonly used for 3D-CRT are not necessarily optimal for IMRT. If only a few beams are employed, using beam directions as free parameters can be very useful. Conversely, if a large number of coplanar beams are used, we note that (1) an odd number of evenly spaced beams are generally used as a simple way to avoid opposed beams, and (2) optimization of beam direction provides little improvement. The Accuray Cyberknife™ employs a computer-controlled linac whose location in space and hence beam direction is completely arbitrary. In such a case, the optimization procedure includes arbitrary non-coplanar beam directions and intensities. Sternick *et al.* (1997) demonstrated that for rotational therapy, changing the beam energy has little optimization value. In fact, linac energies above 10 MV are rarely necessary and result in increased photo-neutron production, and the photon-beam penumbra increases due to the increasing lateral range of secondary electrons.

2.4 Examples of an Objective Function and the Iterative Optimization Process

The most common objective functions used for IMRT are based on soft constraints obtained from dose and volume criteria using least-squares minimization, which tends to enforce absorbed-dose homogeneity within the PTV and to reduce the absorbed dose in normal structures depending on the assigned absorbed dose. Both the target and normal structures can use the same general formulation. While many approaches are possible, the central idea is to minimize a scalar objective function that is the weighted sum, over all designated (delineated) tissues, of the squared differences between the assumed administered absorbed dose and the user-defined constraint absorbed doses in both the PTVs and normal tissues. Weighting factors that reflect the relative importance of a tissue type should be normalized to the number of voxels that make up the tissue type so that small important structures are not underrepresented. A simple objective function, $F(\vec{w})$, for a single PTV and a single PRV can be minimized to achieve a set of beamlet or segment weights $\vec{w}$ as follows:

$$\min[F(\vec{w})] = \frac{I_{\mathrm{PTV}}}{T_{\mathrm{PTV}}} \sum_{i \in T_{\mathrm{PTV}}} c^{-}_{\mathrm{PTV}} (d_i - d^{-}_{\mathrm{PTV}})^2 + \frac{I_{\mathrm{PRV}}}{T_{\mathrm{PRV}}} \sum_{i \in T_{\mathrm{PRV}}} c^{+}_{\mathrm{PRV}} (d_i - d^{+}_{\mathrm{PRV}})^2, \quad (2.1)$$

where I_{PTV} is the relative importance of the PTV and T_{PTV} the number of voxels contained within the PTV. Similarly, I_{PRV} and T_{PRV} are the relative importance and number of voxels in the planning organ at risk volume (PRV—see Section 4.7), respectively. The summations in Eq. 2.1 are over only those voxels (labeled i) that are contained within the PTV or the PRV. Voxels that have not been assigned to a structure are not included in a summation and are therefore ignored by the optimizer. The quantity d^{-}_{PTV} is the minimum constraint absorbed dose for the PTV. The quantity d^{+}_{PRV} is the maximum constraint absorbed dose for the PRV. The terms c^{-}_{PTV} and c^{-}_{PRV} are set to zero when a voxel has met the constraint and set to unity when a voxel has not met the constraint, that is

$$c^{-}_{\mathrm{PTV}} = \begin{cases} 1 & \text{if } d_i < d^{-}_{\mathrm{PTV}} \\ 0 & \text{otherwise,} \end{cases} \quad (2.2)$$

$$c^{+}_{\mathrm{PRV}} = \begin{cases} 1 & \text{if } d_i > d^{+}_{\mathrm{PRV}} \\ 0 & \text{otherwise.} \end{cases} \quad (2.3)$$

In this example of an objective function, I_{PRV}, d^{-}_{PTV}, I_{PRV}, and d^{+}_{PRV} are the optimization parameters that are chosen by the treatment planner to control the behavior of the optimizer. For the PTV, the lowest absorbed dose that would be accepted is typically assigned to d^{+}_{PTV}. Higher values assigned to the PTV importance parameter I_{PRV} will tend to prevent low absorbed dose in the target at the expense of higher absorbed dose to normal tissues. Typically, d^{+}_{PRV} would be assigned an absorbed dose lower than that which would cause complications and could also be lower than can actually be achieved to further lower the normal-tissue absorbed dose. There is a possibility that a value of d^{+}_{PRV} not set low enough will unnecessarily raise the absorbed dose to the normal-tissue structure. Therefore, it is often recommended that d^{+}_{PRV} be lowered and I_{PRV} be increased during the optimization process until there appears to be an adverse impact on the absorbed-dose distribution in the target volume or other normal tissues. A high value given to the normal-tissue importance I_{PRV} will tend to reduce the absorbed dose to all of its voxels, but might compromise dose homogeneity in the PTV. It is possible for a voxel to be a located inside both the PTV and PRV. These voxels will influence the optimization in conflicting ways; however, this will also tend to create a steep gradient. Equation 2.1 is a highly simplified example. It has terms that will be invoked when the absorbed dose in the PTV is too low, but there are no special terms that will keep the absorbed dose in the PTV from being too high.

The example objective function described in Eq. 2.1 has terms that deal with the minimum acceptable absorbed dose in the PTV and the maximum absorbed dose in the PRV. These are special examples of more general dose–volume constraints. Often d^{+}_{PTV} would be indentified with the minimum tumor absorbed dose that can be designated $D_{100\ \%}$, or perhaps with a value that is near the minimum absorbed dose, $D_{98\ \%}$. Multiple dose–volume constraints for a single structure can also be included by adding terms to Eq. 2.1. The structure-importance parameters (I_{PTV} and I_{PRV} in Eq. 2.1) define the relative importance of one structure when compared with another (for example, the importance of the prostate PTV when compared with that of the rectal-wall PRV). If there is more than one constraint for a structure, "constraint-importance" parameters need to be included as factors in the summation terms. Such parameters are the relative weights of one constraint parameter for a structure when compared with another constraint parameter for the same structure. Having multiple constraints for each structure allows some control of the shape of the cumulative DVH for that structure.

An initial set of optimization parameters, which collectively define an objective function, are needed to begin the optimization process. The second from the top box in the right-hand side of Figure 2.1 corresponds to this initialization step. In some optimized treatment-planning systems, an initial set of parameters can be selected from a pre-established library that is keyed to disease site and stage. During the course of optimization, these parameters are usually altered by the planner to steer the results toward absorbed-dose homogeneity in the tumor and/or normal-tissue avoidance. For example, planners often first seek to achieve absorbed-dose homogeneity in the PTV and then alter the constraint parameters to lower the absorbed dose to the OAR. Figure 2.3 illustrates this iterative process for a prostate case. Tables 2.1 and 2.2 list the constraint parameters used to begin the first cycle of iteration for this case. These parameters define an objective function with nine summation terms; three for the PTV in Table 2.1 (the maximum absorbed dose, the DVH constraint, and the minimum absorbed dose), and two each for three PRVs in Table 2.2. The minimum and maximum absorbed-dose constraints for the PTV are set to make as homogeneous an absorbed-dose distribution in the target as possible. The upper panels of Figure 2.3 show DVHs and absorbed-dose distributions after the first cycle of 350 iterations. The result is an acceptable absorbed-dose distribution in the PTV, bladder, and femoral heads. However, the planner decided to change the constraints to improve the absorbed dose in the rectal wall and substantially maintain the absorbed-dose distribution in the PTV. Tables 2.1 and 2.2 also list the parameter choices for a second cycle of 150 iterations. The DVH constraint for the rectal wall, $D_{35\ \%} = 35$ Gy (also expressed as $V_{35\ \mathrm{Gy}} = 35\ \%$) for

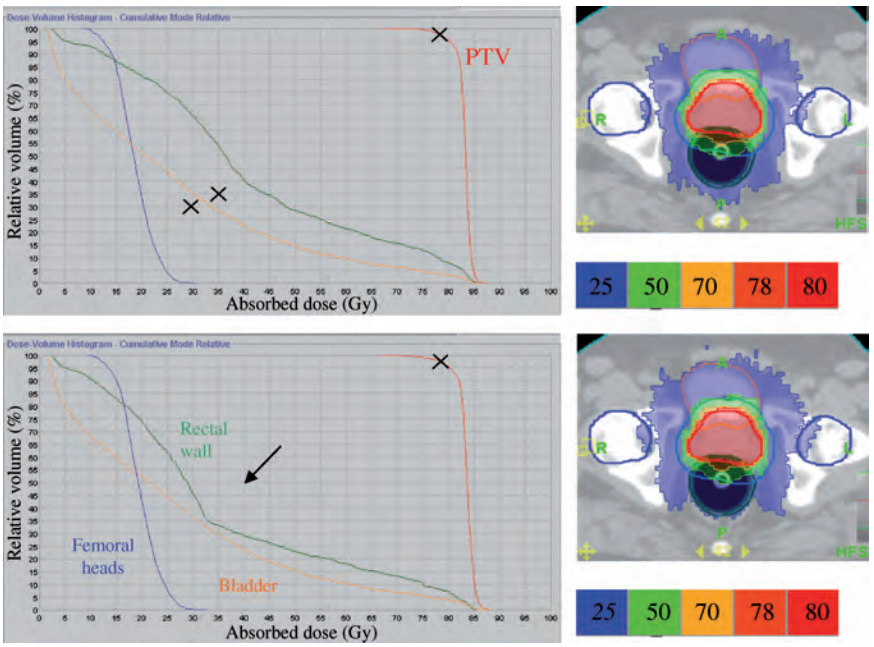

Figure 2.3. Results of constraint-parameter choices for an optimization process. Shown here are two snapshots from a treatment-planning system of the optimization process after the first and second cycles of iteration for optimized planning for prostate cancer. Relative volume is normalized to the volume of the region of interest and reported as percents. The first and second set of constraint-parameter choices are shown in both Table 2.1 (for the PTV) and Table 2.2 (for the normal tissues).

Table 2.1. Optimization parameters for the PTV as utilized in the TomoTherapy Hi-Art™ treatment-planning system for the initial and second iteration cycles of the prostate plan described in Figure 2.3. The parameters that changed between the cycles are italicized. All importance factors are dimensionless. In this example, note that the optimizer uses the minimum ($D_{100\ \%}$) and maximum ($D_{0\ \%}$) absorbed dose as optimization parameters. In Section 3, a recommendation is made instead that near-minimum ($D_{98\ \%}$) and near-maximum ($D_{2\ \%}$) absorbed doses are more useful.

	Iteration cycle	Structure importance	Max. absorbed dose (Gy)	Max. absorbed-dose importance	DVH volume (%)	DVH absorbed dose (Gy)	Min. absorbed dose (Gy)	Min. absorbed-dose importance
PTV	1	*100*	78	50	98	78	78	*50*
	2	*500*	78	50	98	78	78	*100*

Table 2.2. Optimization parameters for the OARs as utilized in the TomoTherapy Hi-Art™ treatment-planning system for the initial and second iteration cycles of the prostate plan described in Figure 2.3. The parameters that changed between the cycles are italicized. Note that these optimization parameters are not universally adopted by treatment-planning system designers. For example, many commercial optimization planning systems allow a larger number of DVH constraints to be defined for normal tissues.

	Iteration cycle	Structure importance	Max. absorbed dose (Gy)	Max. absorbed-dose importance	DVH volume (%)	DVH absorbed dose (Gy)	DVH importance
Rectal wall	1	*50*	70	*10*	*35*	*35*	*10*
	2	*100*	70	*100*	*30*	*30*	*50*
Bladder	1	5	70	10	25	25	5
	2	5	70	10	25	25	5
Femoral heads	1	5	25	5	50	15	5
	2	5	25	5	50	15	5

the first cycle is changed to $D_{30\ \%} = 30$ Gy. To guide the optimizer, the relative importance of the rectal wall is changed from 50 to 100, the penalty on the maximum absorbed dose is changed from 10 to 100, and the DVH penalty is changed from 10 to 50. At the same time, the PTV importance is changed from 100 to 500, and its minimum dose penalty is changed from 50 to 100 to prevent the absorbed-dose distribution in the PTV from changing substantively. The DVHs and the absorbed-dose distribution at the end of 150 further iterations (500 in total) are shown in the lower panels of Figure 2.3. The DVH of the PTV is almost unchanged. Note that there is a hard constraint on a prescription value of $D_{98\ \%} = 78$ Gy (indicated by the cross mark on the DVH). The rectal-wall DVH has been substantially altered. In particular, the change in the DVH constraint and the rectal-wall importance and DVH penalty has pushed the DVH curve in the direction indicated by the arrow. The constraints of the bladder and femoral heads were not altered between cycles, and the DVHs are somewhat altered negatively. Additional iteration cycles with further changes in the optimization parameters might provide overall improvements in the absorbed-dose distribution. The values at the beginning of any iteration cycle are chosen by the planner from experience, but are somewhat arbitrary as the values can be altered in a trial-and-error fashion until the radiation oncologist is satisfied with the result. The results of only two cycles of iteration are shown in Table 2.3 and Figure 2.3. This procedure can continue until any further change in parameters will not improve the result either in terms of the homogeneity of absorbed dose in the PTV or a reduction of absorbed dose in the OAR. The outer iteration loop, in the right-hand side of Figure 2.1 flowchart, corresponds to the cycles of changing optimization-parameter values.

Intensity-modulated radiation therapy optimization methods are still reliant on the experience of the treatment planner for insight on how a change in a constraint parameter affects the absorbed-dose distribution. Automated multi-criteria optimization methods have been proposed so as to enable the parameters to be more systematically selected (Lahanas *et al.*, 2003; Romeijn *et al.*, 2004).

2.5 Iterative Search for an Improved Absorbed-Dose Distribution

The optimization problem involves the search for the best beam intensities from the possible beam configurations. The search is outlined by the inner loop of the flowchart in Figure 2.1. The dimensions of the search space and the number of possible solutions are very large. The number of dimensions corresponds to the number of possible "beamlets."

Table 2.3. Evaluation criteria for the first two cycles of iteration for the prostate cancer plan shown in Figure 2.3 using the TomoTherapy Hi-Art™ treatment-planning system. The values for selected criteria for each region of interest are italicized. These results show that changing the optimization parameters as illustrated in Tables 2.1 and 2.2 improved the evaluation criteria for the rectal wall and did not substantially alter the absorbed-dose distribution in the PTV. The optimization parameters for the bladder and femoral heads did not change between iteration cycles, and the evaluation criteria are slightly worse. Further iteration cycles would be required to obtain a better plan.

	Iteration cycle	$D_{98\ \%}$ (Gy)	D_{mean} (Gy)	$D_{50\ \%}$ (Gy)	$D_{2\ \%}$ (Gy)	$V_{70\ \mathrm{Gy}}$ (%)	$V_{20\ \mathrm{Gy}}$ (%)
PTV	1	*78*	*83*	*83*	*85*	~100	100
	2	*78*	*83*	*83*	*86*	~100	100
Rectal wall	1	3	*23*	*36*	*84*	*16*	82
	2	3	*21*	*28*	*84*	*14*	75
Bladder	1	2	*20*	*21*	83	6	*51*
	2	2	*19*	*22*	84	7	*52*
Femoral head	1	12	*18*	*18*	26	0	35
	2	12	*19*	*19*	26	0	42

For example, if there are five beam directions and the field area is discretized into 40×40 beamlets each, then the search space consists of $5 \times 40 \times 40 = 8000$ dimensions. If there are 10 allowed beam intensities (or weights) for each beamlet, then the number of possible intensity patterns is 10^{8000}, and an exhaustive search is not possible. If more directions are used as is the case for Hi-Art™ helical tomotherapy, the dimensions can be even larger. This large search space cannot be visualized and requires a high-speed computing infrastructure to perform the search.

The search for the optimal intensity pattern begins by initializing the intensity for each of the possible beam configurations or beamlets (a distinction will be made in the next subsection between direct-aperture optimization and beamlet optimization). The two most common initialization approaches are either to assign the same intensity to all the beamlets that can pass through a target volume or to assign zero intensity to all of the beamlets. Ideally the initial or starting conditions for the search will not influence the result. However, this is often not true in practice (see Figure 2.2); the fluence pattern generated by different starting conditions can be somewhat different. However, the absorbed-dose distributions that are generated from the fluence patterns can still be very similar.

Regardless of the formulation of the problem, the solution to an optimization problem is found by iteratively finding the minimum of an objective function. There are two general approaches to searching for the possible solutions: deterministic and stochastic methods. In deterministic methods, given the same setup and initial conditions, the same solution will always be found. Examples of deterministic methods would be linear least squares and gradient (or methods of steepest) descent (Morse and Feshbach, 1953). At each iteration step, the gradient descent finds a value of the objective function smaller than the last (Bortfeld, 1999; Holmes and Mackie, 1994; Spirou and Chui, 1998; Xing and Chen, 1996). A commonly used gradient descent in IMRT is non-linear least-squares minimization (Bortfeld and Schlegel, 1993). In a stochastic search, randomly selected iterative steps test areas of the solution space that are less optimal than previous ones (Mageras and Mohan, 1993; Webb, 1992). An example of a stochastic search is the simulated-annealing method used with the first serial tomotherapy system (Carol, 1995). In comparing deterministic and stochastic methods, the main advantage of the gradient-descent and other deterministic approaches is speed. However, there is no assurance that the gradient-descent algorithm will find the global minimum of the objective function if there are multiple local minima (Deasy, 1997). The existence of such local minima can be demonstrated in gradient descent algorithms by starting the optimization at different points in parameter space and showing convergence to different results. Figure 2.2c shows the outcome of a hypothetical objective function constructed with only two beam weights, for which there happen to be two minima. Depending on the starting point, a deterministic gradient-decent algorithm could find either of these local minima. In principle, stochastic methods are capable of finding the global minimum if there is unlimited time to search the parameter space. In practice, time is restricted for treatment planning.

For both deterministic and stochastic algorithms, the approach to convergence to the minimum is faster at the beginning of the search than at the end. The stopping criterion for the iterative search is sometimes hard to establish. Automated methods that stop the search if progress in reducing the objective-function value has slowed are common. Some systems allow the treatment planner to stop it manually. Often the value of the

objective function is portrayed graphically to aid in choosing when to stop the search. A review by Oelfke *et al.* (2006) also provides an excellent description of optimization search methods.

2.6 Beamlet Optimization and Aperture-Based Optimization

For either stochastic or deterministic strategies, there are two general frameworks for the problem of optimization in IMRT: beamlet optimization (Bortfeld *et al.*, 1990; Holmes *et al.*, 1991; Webb, 1992) and aperture-based optimization (Shepard *et al.*, 2002). Both types use the same criteria (same constraints and same objective function).

In beamlet optimization, each field is discretized into a grid of sub-beams or beamlets each of which is characterized by a distinct intensity. The method of beamlet optimization was pioneered for serial tomotherapy and, as is shown in Table 1.1, is ideal for tomotherapy, robotic beam delivery, and designing compensators. Beamlet-based optimization is also a good approach for designing dynamic MLC IMRT because this delivery method can give quite highly modulated intensity patterns. For IMRT using conventional MLC, once the optimal intensity map is found, it must be translated into instructions for delivering the irradiation pattern according to the specified method of delivery. The process of translating from the irradiation grid to instructions for delivery is called "leaf segmentation." Depending on the method of delivery, after the process of leaf segmentation, a final absorbed-dose calculation and monitor-unit calculation can result in a significantly different absorbed-dose distribution than suggested by the optimized plan. This discrepancy is called "convergence error" (Jeraj and Keall, 2000). The cause of the discrepancy is two-fold. The optimization algorithm often uses a simpler model (usually because of speed issues) of energy deposition than is utilized for the final absorbed-dose calculation and monitor-unit calculation. Secondly, the final absorbed-dose calculation takes into account limitations in the MLC delivery that are not accounted for in the absorbed-dose calculation used by the optimizer. Examples of MLC limitations include the minimum opening distance that must be maintained between two opposing leaves (so that the leaves do not touch and cause mechanical damage) and the minimum-allowed monitor units that can be accurately delivered by a segment. Intensity-modulated radiation therapy programs should establish that there is negligible convergence error in their optimized treatment-planning system.

Aperture-based optimization avoids the leaf-segmentation step and takes into account the limitations of the MLCs during each optimization step so that the segmentation step is eliminated. Instead, the best set of aperture shapes (and their relative weights) is found to deliver the intensity pattern without explicit discretization of the field into a grid of beamlets. Apertures are often first defined to be the projection of the PTVs similar to the techniques of 3D-CRT. The apertures are iteratively modified or new aperture segments are created based on elevating the absorbed dose to regions in which the absorbed dose is too low or decreasing the absorbed dose to regions in which the absorbed dose is too high. Seeking the best apertures directly is the best approach for segmental MLC and IMAT methods of delivery. If the same dose-calculation algorithm is used for the iterative optimization of apertures as for the final absorbed-dose calculation, then this method will avoid convergence errors as well. An approach similar to direct-aperture optimization has also been used with manual planning techniques employing 3D-CRT planning systems (De Neve *et al.*, 1996; Fraass *et al.*, 1999; Galvin *et al.*, 1993) and is sometimes called "forward optimization." It is worth describing this non-automated process to gain insight into the automated techniques used in aperture-based optimization. For each beam direction, the dosimetrist or treatment planner selects a variety of beam apertures that completely encompass the target and completely avoid one or more critical structures. The absorbed-dose distributions for each of the apertures are then computed, and the segment weights are adjusted typically to make sure that the absorbed dose in critical normal tissues is acceptable. If there are critical tissues adjacent to the target, the absorbed dose in the PTV might not be acceptably homogeneous. The treatment planner will then add more beam segments (apertures) to elevate the absorbed dose in subvolumes of the target volume where the absorbed dose is too low and to re-weight the other segments to avoid critical structures. This manual process is repeated until the magnitude and homogeneity of the absorbed dose to the target is sufficient and the absorbed dose to critical structures is not excessive. The automated aperture-based optimization procedure, in addition to new segments, can modify the boundaries of previous segments to better avoid normal tissue or improve target-dose homogeneity. The process just described is additive in nature. It is also possible to begin by fully exposing the target volume from all directions and then to perform a subtractive process to avoid normal tissues. Both additive and subtractive strategies can be used in some aperture-based approaches.

2.7 Optimization Incorporating Biological Information

Currently, optimization systems typically use absorbed dose in the formulation of objective functions. The absorbed-dose distribution in an organ at risk is typically inhomogeneous. The optimization trade-off between absorbed dose and volume requires clinical understanding. With two parallel-opposed fields, critical normal tissues and tumors can receive similar absorbed doses, typically 1.8 Gy to 2 Gy per fraction. In IMRT, the absorbed dose received by normal tissues can be substantially lower than the absorbed dose received by the target. For example, in a typical head-and-neck IMRT plan, the absorbed dose per fraction to the spinal cord might be as low as 30 % to 60 % of the prescribed absorbed dose to the target volume, when compared with 60 % to 80 % of the prescribed absorbed dose in conventional parallel-opposed photon-beam radiotherapy (Lee *et al.*, 2007). A similar or even greater reduction in absorbed dose per fraction can also be obtained for the contralateral parotid gland (Chao *et al.*, 2001b). Calculations based on the linear-quadratic dose–response model and clinical experience have shown that for a similar total absorbed dose, lowering the absorbed dose per fraction will reduce the biological effect, while increasing the absorbed dose per fraction will increase that effect (Withers and Thames, 1988). In contrast to many tumor types with a high α/β ratio, late-responding normal tissues often have a low α/β ratio making them especially sensitive to this phenomenon. In essence, a lower absorbed dose per fraction to normal tissue will increase the therapeutic ratio. In addition, for the same absorbed dose to normal tissue, IMRT can allow an increased tumor absorbed dose, thus further increasing the therapeutic ratio. Biological models that can accurately incorporate the effect of absorbed dose to tumor and normal tissues might be developed in the future to explicitly optimize the trade-offs that must be made between eradication of the tumor and avoidance of normal-tissue damage. Radiobiological-response models are discussed more fully in Section 3.7.2.

The concept of equivalent uniform dose (EUD), introduced by Niemierko (1997), was originally defined to be the absorbed dose that if given uniformly would lead to the same cell kill as the actual non-uniform absorbed-dose distribution. The current definition of EUD is a generalized mean absorbed dose (Niemierko, 1999). Equivalent uniform dose is discussed in detail in Section 3.7.3. If the input parameters can be well justified, the EUD approach can, in principle, provide better protection of the critical structures and a similar or slightly better absorbed-dose distribution in the PTV than optimization based only on the physical absorbed-dose distribution. Figures 2.4 and 2.5 illustrate a comparison of optimizations based on absorbed-dose and EUD constraints (Wu *et al.*, 2002). The reliability of the EUD concept, however, depends critically on the values of the different parameters that are used to fit the dose–volume

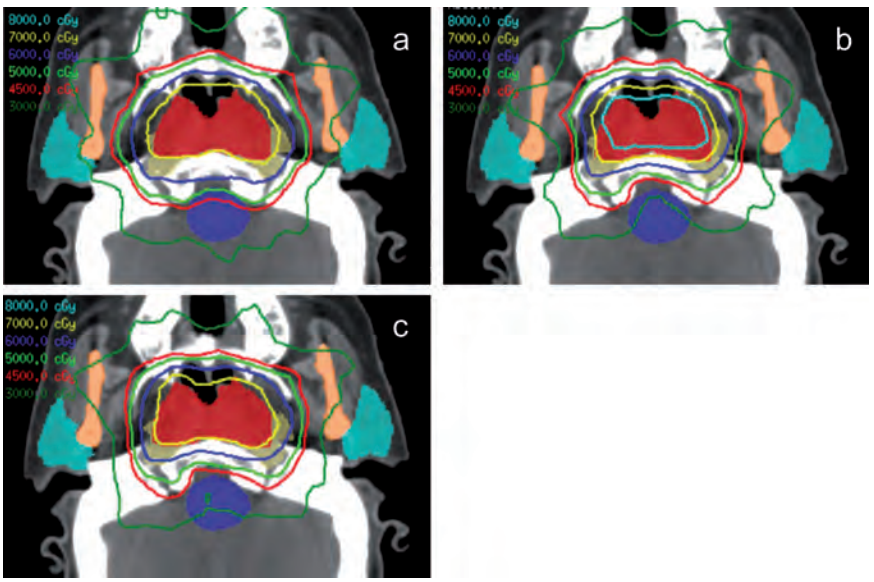

Figure 2.4. Examples of a typical head-and-neck case optimization using: (a) traditional absorbed-dose and dose–volume optimization; (b) EUD-based optimization without constraints on target absorbed-dose inhomogeneity; and (c) EUD-based optimization with constraints on target absorbed-dose inhomogeneity. The light blue lines represents the 80 Gy isodose curves, yellow the 70 Gy, dark blue the 60 Gy, inner green the 50 Gy, red the 45 Gy, and the outer green the 30 Gy isodose curves. Note that the 80 Gy isodose curve exists only in (b).

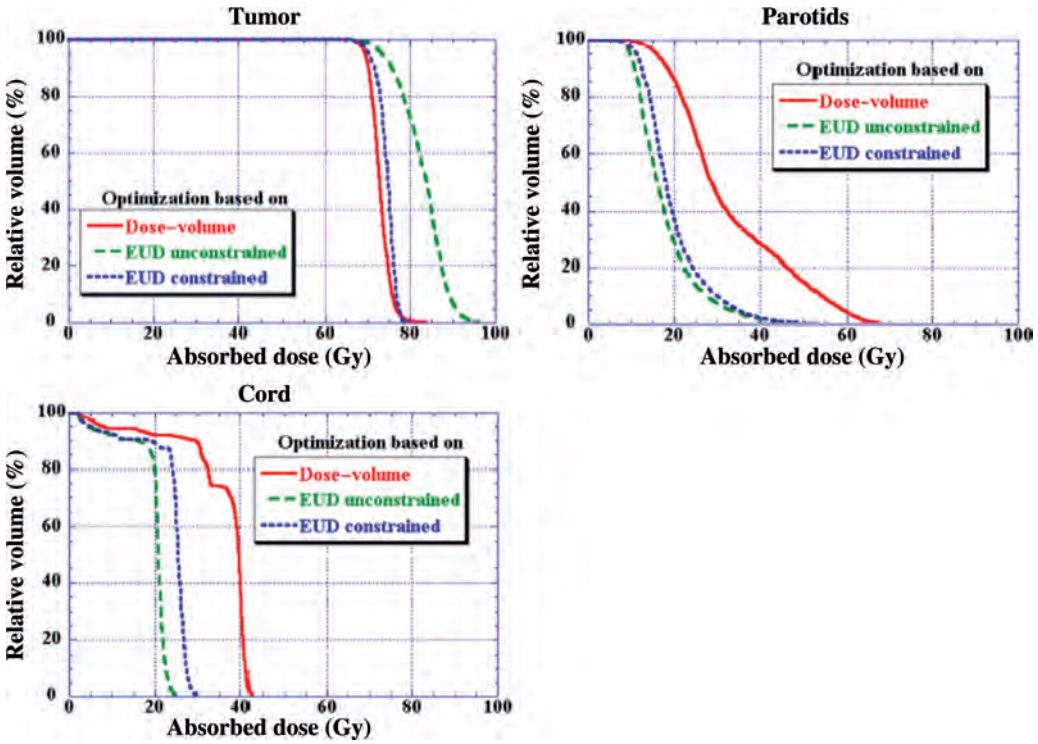

Figure 2.5. Dose–volume histograms corresponding to the absorbed-dose distributions of Figure 2.4 for the PTV, the parotid glands, and the spinal cord. The volume axis is relative to the total volume of region of interest and reported in percent. In EUD-constrained plans, absorbed-dose constraints were chosen to achieve a more homogeneous absorbed-dose distribution in the PTV.

effect. The concept of EUD has been used as one of several metrics to determine the impact of absorbed-dose heterogeneity on normal tissues and tumors (Aoyama *et al.*, 2006; Wang and Li, 2003). At this time, the use of EUD for optimization and plan evaluation should be considered as investigational.

The most useful patient-specific objective function would maximize the probability of uncomplicated control (Brahme, 1999). Such approaches proposed by several investigators usually put tight constraints on the maximum normal-tissue complication probability (Lind *et al.*, 1999; Wang *et al.*, 1995). The trade-off between competing complications is difficult to model mathematically. Radiobiological models are not yet fully validated, and might not even properly rank competing plans for a specific case. Although promising, further clinical validation of the biological optimization tools is required. In the meantime, it appears wise to restrict their use to well-designed clinical studies aimed at showing their usefulness as evaluation metrics. Examples of biological evaluation metrics that might ultimately be employed as objective functions are described in more detail in Section 3.7.3.

Journal of the ICRU Vol 10 No 1 (2010) Report 83
Oxford University Press
doi:10.1093/jicru/ndq008

3. Special Considerations Regarding Absorbed-Dose and Dose–Volume Prescribing and Reporting in IMRT

If all centers were well equipped and well staffed, it would be possible to report all information available using modern ("state-of-the-art") techniques, and the exchange of information would be improved. Unfortunately, facilities and/or medical staff are limited in some centers. On the other hand, if the ICRU recommendations for reporting are limited to those appropriate for centers with minimum technical and medical capabilities, only limited information can be exchanged and the benefit is modest. Historically, as a compromise, the ICRU (ICRU, 1993; 1999; 2004; 2007) identified three levels of prescribing and reporting.

Level 1 recommendations: minimum standards for prescribing and reporting. Prescribing and reporting at Level 1 is considered the minimum standard required in all centers, a standard below which radiotherapy should not be performed. Operating at Level 1 is sufficient for simple treatments and implies that knowledge of absorbed doses on the central beam axis is known and that simple two-dimensional (2D) absorbed-dose distributions at the central axis are available.

Level 2 recommendations: prescribing and reporting state-of-the-art techniques. Level 2 prescribing and reporting implies that the treatments are performed using computational dosimetry and 3D imaging. At this level, it is assumed that all volumes of interest, *e.g.*, gross tumor volume (GTV), clinical target volume (CTV), planning target volume (PTV), organs at risk (OAR), and planning organ-at-risk volume (PRV) (see Section 4), are defined using, for example, a series of computed tomography (CT) or magnetic resonance imaging (MRI) sections and that 3D absorbed-dose distributions are available and include heterogeneity corrections. It is expected that dose–volume histograms (DVHs) for all volumes of interest are routinely computed. It is also assumed that a complete QA program is in place to ensure that the prescribed treatment is accurately delivered.

Level 3 recommendations: optional research-and-development reporting. Reporting at Level 3 includes the development of new techniques and/or approaches for which reporting criteria are not yet established. Examples include the use of concepts such as tumor-control probability (TCP), normal-tissue complication probability (NTCP), or equivalent uniform dose (EUD) (ICRU, 2007).

It is recommended that all information required for Level 1 prescribing and reporting should be included in Level 2, and recommendations at Levels 1 and 2 should be incorporated when reporting at Level 3. It is recognized that procedures at Level 3 might be added to Level 2 in the future.

3.1 The ICRU Reference Point and ICRU Reference Dose

The ICRU has long recommended that the absorbed dose, D_{ref}, to an unambiguous point, the ICRU Reference Point, be reported to communicate absorbed doses prescribed or received (ICRU, 1978; 1993; 1999; 2004). In ICRU Report 50 (ICRU, 1993), the process for the selection of an ICRU Reference Point was specified as follows:

- the absorbed dose at the point should be clinically relevant;
- the point should be easy to define in a clear and unambiguous way;
- the point should be selected so that the absorbed dose can be accurately determined;
- the point should be in a region where there is no steep absorbed-dose gradient.

These recommendations will be fulfilled if the ICRU Reference Point is located:

- always at the center (or in a central part) of the PTV, and
- when possible, at the intersection of the (treatment) beam axes.

3.1.1 Conventional Reporting of Point Absorbed Doses

Conventional computation algorithms start with absorbed-dose distributions measured in a water

phantom and then correct these to estimate the absorbed-dose distribution in the patient. The absorbed dose at a point on the central axis in a homogeneous tissue region is reliably determined for an open (*i.e.*, unblocked) field incident normal to the surface of the patient because it is based directly on measurements of a beam incident normal to the surface of a water phantom. Examples of special situations that could influence or compromise the accuracy of point-dose calculations in a patient are: (1) Dose-correction algorithms treat separately the influence of beam modifiers, patient contours, and tissue heterogeneities as independent effects whereas, in fact, they are not necessarily independent. For example, in a lung cancer case with a block shielding the cord, all three types of absorbed-dose correction would be required. The reporting point would need to lie in the field away from the central axis in a heterogeneous tissue medium beneath a non-flat patient body contour, and therefore the reported absorbed dose would depend heavily on the ability to apply the corrections. The beam-modifier correction for the block should take into account the reduced scatter to the lung. Heterogeneity corrections would result in additional absorbed dose due to less attenuation in lung but are generally applied to the primary beam, not the beam scattered in the patient. These effects should be taken into account simultaneously. (2) Dose-at-a-point reporting is also less reliable for wedged treatments because absorbed-dose gradients can reach a sizable fraction of the prescribed absorbed dose per millimeter. (3) With some dose-calculation algorithms, the accuracy for non-uniform tissue types and densities is problematic enough that many protocols specify reporting the result of calculations assuming that all intervening tissues are composed of unit density water. ICRU Reports 50 and 62 have already suggested that Level 1 and dose-at-a-point reporting is not sufficient for complex, 3D conformal-radiation-therapy treatments (ICRU, 1993; 1999).

In previous ICRU Reports, limitations of reporting an absorbed dose at a point were recognized and some cases in which the criteria for a Reference Point cannot be fulfilled were discussed (*e.g.*, ICRU, 1999). It should be kept in mind that when these Reports were published (ICRU, 1993; 1999), it was often not possible to identify and accurately delineate all volumes of interest and to compute the absorbed-dose distributions in 3D. Heterogeneity corrections were time-consuming, inaccurate, and thus often not applied. Therefore, selection of a clinically relevant, clearly defined reference point at which the absorbed dose can be accurately determined appeared to be the best and only practical approach at that time. This approach was recognized to be reliable and has indeed successfully been used in randomized clinical trials (ICRU, 1999).

3.1.2 Dose–Volume Calculations

Today, more accurate model-based dose-calculation algorithms (see Appendix A.1) and modern 3D imaging methods make it possible to generate the whole absorbed-dose distribution to characterize the delivery and not just the absorbed dose at a single point. This allows dose–volume-based prescriptions and reporting.

In modern radiation therapy, the specification of the absorbed dose to relevant anatomic volumes rather than to single points is critical to the communication of the treatment intent. The reported absorbed dose should be descriptive of the absorbed dose in the volume. Level 1 reporting, including the reporting of absorbed dose at a point, is inadequate for three-dimensional conformal therapy (3D-CRT) and intensity-modulated radiation therapy (IMRT) for the following reasons: (1) The absorbed-dose distribution within a PTV for IMRT can be less homogeneous than in conventional radiation therapy, often with significant variations. The selection of a dose-reporting point that lies within a region of high or low absorbed dose could then significantly misrepresent the absorbed dose. A point on the central axis is not a representative point for plans that include an interior OAR. Certainly, the point at which the maximum absorbed dose occurs is unlikely to be representative. (2) Soon Monte Carlo calculations will be used routinely to compute absorbed-dose distributions for IMRT. In Monte Carlo simulation, the statistical fluctuations in the results for small volumes make it difficult and uncertain to determine an absorbed dose at a point, whereas this is reasonably achieved in a volume. (3) From a single beam direction, IMRT can produce absorbed-dose gradients within a PTV much larger than those generated by a wedge. (4) The absorbed-dose gradient at the boundary of a PTV as a result of multiple IMRT beams can be more than 10 %/mm, and a small shift in the field delivery can affect the reliability of using a single point to report the absorbed dose. (5) Modern treatment-planning systems have sufficient evaluation tools for Level 2 reporting to be the standard for use in IMRT.

3.2 Level 2 Prescribing and Reporting for IMRT

Recommendations for Level 2 reporting are based on absorbed-dose and volume information obtained

from DVHs. Dose–volume histograms have been in practical use in radiotherapy since the late 1970s and are routinely used to evaluate and report 3D-CRT, IMRT, electron, and heavier particle therapies (ICRU, 1985; 2004; 2007; Shipley *et al.*, 1979). Figure 3.1 shows an example of a DVH. A DVH represents, in a concise although simplified way, the dose–volume relationship within a volume of interest. Visual inspection of DVHs can lead to identification of clinically important characteristics of an absorbed-dose distribution, such as the presence (but not the location) of regions of high or low absorbed dose or other absorbed-dose heterogeneities, which are often difficult to assess rapidly and consistently from conventional isodose or color-wash presentations.

Cumulative DVHs are histograms of the volume elements that receive at least a given absorbed dose, and they are usually expressed as either the absolute volume or the volume relative to the total structure volume, receiving at least a given absorbed dose, D. Each point on the line of a relative cumulative DVH is described by the following:

$$DVH_{\text{rel cum}}(D) = 1 - \frac{1}{V}\int_0^{D_{\max}} \frac{\mathrm{d}\,V(D)}{\mathrm{d}\,D}\,\mathrm{d}\,D, \qquad (3.1)$$

where V is volume of the structure and $D_{\max}$ the maximum dose in the structure, and the differential DVH is defined by $\mathrm{d}V(D)/\mathrm{d}D$, which is the increment of volume per absorbed dose at absorbed dose, D (Figure 3.1).

An absolute cumulative DVH can be obtained from a relative cumulative DVH by multiplying by the volume of the structure. Dose–volume histograms can be used to determine values such as D_{median}, which is the absorbed dose received by 50 % of the volume, making it often a good choice for a representative absorbed-dose value for the PTV even though it does not provide information about where in the volume the median absorbed dose might occur and is thus less useful if the absorbed-dose distribution in the structure is highly heterogeneous.

In plotting a relative cumulative DVH, the first defined point is located at the intersection along the horizontal line representing 100 % volume and the vertical line representing the minimum calculated absorbed dose, $D_{\min}$. By convention, a horizontal line is drawn from a point representing 100 % volume and zero absorbed dose to the first defined point on the histogram. Similarly, the last point in the DVH curve is located at the intersection along the horizontal line representing 0 % volume (along the abscissa) and the point of maximum calculated absorbed dose, $D_{\max}$. The minimum and maximum absorbed doses are often obscured by the 100 % and 0 % volume grid lines, which make visual evaluation uncertain. The determination of the location of low- or high-dose regions within a structure is not possible from a DVH alone.

The usual specification for a characteristic value for a distribution within which there can be some variation is the mean. The mean absorbed dose to the PTV is equal to the amount of energy imparted to the PTV divided by the PTV mass. The mean

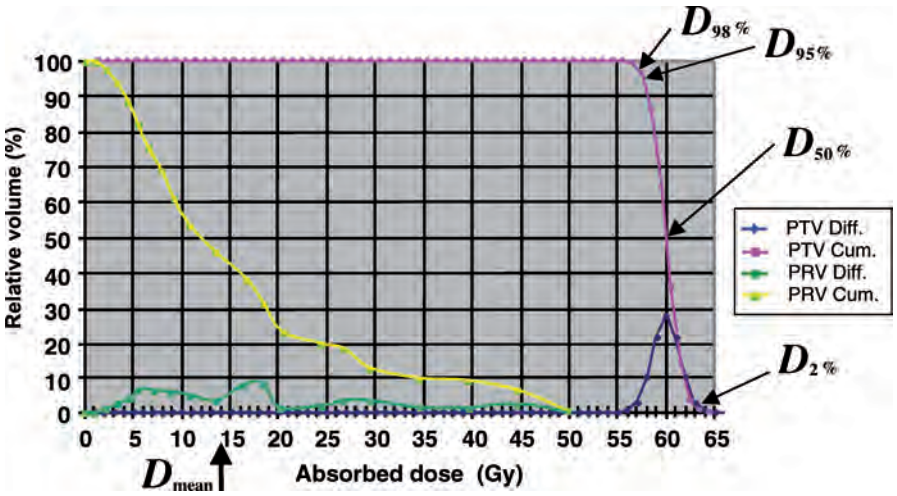

Figure 3.1. Example of differential DVHs and their corresponding cumulative DVHs. The dose–volume metrics, $D_{\text{near-min}} = D_{98\ \%}$, $D_{95\ \%}$, $D_{50\ \%}$ (median), and $D_{\text{near-max}} = D_{2\ \%}$ are indicated for the PTV. For this example, the values of $D_{98\ \%}$, $D_{95\ \%}$, $D_{50\ \%}$, and $D_{2\ \%}$ are 57 Gy, 57.5 Gy, 60 Gy, and 63 Gy, respectively. The D_{mean} for a PRV is also indicated. Notice that the mean absorbed dose for an organ at risk is generally not the same as its median absorbed dose, whereas the mean absorbed dose for the PTV is generally very close to its median absorbed dose.

absorbed dose is thus defined as:

$$D_{\text{mean}} = \frac{1}{V}\int_0^{D_{\max}} D\,\frac{\mathrm{d}V(D)}{\mathrm{d}D}\,\mathrm{d}D, \qquad (3.2)$$

and also represents the integral dose divided by the volume.

Typical differential DVHs for the PTV are often similar to that portrayed in Figure 3.1, in that they are symmetric and unimodal (*i.e.*, having only one peak), so that the median ($D_{50\ \%}$) and mean absorbed doses are nearly identical.

3.3 Impact of Modern Treatment-Planning Techniques

In recent years, and especially since the advent of IMRT, prescriptions have been specified and reported using dose–volume metrics. This was greatly facilitated by the definitions and recommendations in ICRU Reports 50 and 62 (ICRU, 1993; 1999) that encouraged the delineation of target and organ-at-risk volumes using 3D image sets. All commercial treatment-planning systems now report cumulative DVHs for the specified volumes from which a variety of metrics for reporting can be obtained. The main reason for the use of dose–volume reporting in IMRT is that the coverage of the PTV by a specific absorbed dose can be explicitly determined from a DVH, and be better controlled through optimized planning. The use of dose–volume reporting instead of reporting the absorbed dose at the ICRU Reference Point is predicated on the use of an adequate dose-calculation system. Recently, dose-calculation algorithms, such as the convolution/superposition method, have been adopted and provide accurate absorbed-dose calculations because they function well in inhomogeneous tissues (reviews on the convolution/superposition method can be found in Ahnesjö, 1994; 1995; Ahnesjö and Aspradakis, 1999; and Mackie *et al.*, 1995; 1996; 2000; 2001). Thus the absorbed dose is computed throughout the PTV, and no particular point, such as the ICRU Reference Point, is favored (see Appendix A.1). The present Report recommends that the users of treatment-planning systems ensure that these systems have the ability to compute the absorbed dose accurately for small fields, inhomogeneous tissues, and in regions in which there is electronic disequilibrium (see Appendix A.1).

There have been few studies comparing more modern dose–volume prescription and reporting with older established methods. Frank *et al.* (2003) compared traditional treatment-planning methods with modern methods. The traditional treatment-planning methods, including dose-at-a-point prescription, either calculated the absorbed-dose distribution on the basis of a homogeneous tissue density or with heterogeneity corrections. The modern method used a dose–volume prescription and calculated the absorbed-dose distribution using density obtained from CT-based treatment plans. Thirty stage I/II inoperable non-small-cell lung cancer plans were studied. They found better PTV coverage with the modern planning methods. In particular, they found that 14 of the 30 patients studied would have had less than 90 % of the PTV receiving the prescribed absorbed dose if they had used the traditional calculation and prescription methods. It is expected that the combination of heterogeneity corrections and the use of dose–volume prescriptions will improve the homogeneity of absorbed dose in the PTV also when IMRT is employed.

Donovan *et al.* (2002) found that dose-at-a-point prescribing and traditional methods of delivering the absorbed dose to the breast resulted in 96 % of patients having more than 105 % of the prescribed absorbed dose in the upper half of the breast and 70 % of the patients having more than 105 % in the lower half of the breast. Intensity-modulated radiation therapy prescriptions using dose–volume methods resulted in less than 4 % of the patients having more than 105 % of the prescribed absorbed dose in either half of the breast. They found that the use of such dose–volume prescriptions leads to a more homogeneous absorbed-dose delivery to the PTV. In a follow-up study of these patients, Donovan *et al.* (2007) found that the conventionally treated patients have significantly increased late complications when compared with the IMRT patients. In the case of breast, IMRT is capable of providing better missing-tissue compensation when compared with simple wedges. It is likely that when only tangential fields are used to irradiate the breast, custom compensators designed explicitly to compensate for missing tissue would be just as effective as IMRT planning and delivery. The study by Donovan *et al.* (2002) evaluated two techniques: standard breast radiotherapy using tangential fields with wedges employing dose-at-a-point prescription and IMRT with dose–volume prescription and reporting. Despite some indications that IMRT might improve breast radiotherapy, it should be pointed out that there are other issues related to the treatment of breast, such as the movement of the breast and a possible increased volume of low absorbed dose in other tissues, *e.g.*, the contralateral lung and breast.

The AAPM Task Group 65 Report (AAPM, 2004) reviewed all of the publications describing absorbed-

dose computations with and without the effect of tissue heterogeneities. When compared with homogeneous-tissue calculations, the review found that there can be much more than a 10 % relative difference in the computed absorbed dose when heterogeneity corrections are used. The Report concluded that modern model-based absorbed-dose computations (see Appendix A.1) are capable of calculating the absorbed dose to within a 5 % relative uncertainty if the effect of tissue heterogeneities are included, and recommended that the absorbed dose be calculated with heterogeneity corrections. The US National Cancer Institute in cooperation with the Advanced Technology Consortium (ATC) has stipulated that trials involving IMRT should use absorbed-dose algorithms that take into account the effect of tissue heterogeneities (ATC, 2006). A report, describing a stereotactic-radiotherapy clinical trial of lung cancer specified that lung-density corrections not be used, and showed that absorbed-dose distributions were affected significantly when absorbed-dose corrections were appropriately applied (Xiao *et al.*, 2007). In particular, the volume of the target receiving at least 60 Gy ($V_{60\,\mathrm{Gy}}$) was reduced by 10 % and the absorbed dose outside the target increased significantly. Unfortunately, there are still ongoing lung cancer trials in which heterogeneity corrections are not used (*e.g.*, RTOG Trial 0618, see www.rtog.org/members/protocols/0618/0618.pdf). We recommend that absorbed-dose calculations including corrections for heterogeneities are used in future trials (see Appendix A.1).

It is recommended that dose–volume specifications be used for reporting the treatment plan. The absorbed dose that covers a specified fractional volume V, D_V, should be reported. This information can be found from a cumulative DVH as the DVH absorbed-dose value specified at a percent volume V. For example, $D_{95\ \%}$ is the minimum absorbed dose that covers 95 % of the volume of the PTV. The volume, V, that D_V is based on should be reported textually or as a subscript value (*e.g.*, $D_{95\ \%} = 50$ Gy, $D_{\mathrm{median}} = 55$ Gy).

The dose–volume metric $D_{100\ \%}$ would be commonly called the minimum absorbed dose. The $D_{100\ \%}$ value is the absorbed dose at a single or a few voxels that happened to have the lowest absorbed dose. The minimum absorbed dose might not be accurately determined because it is often located in a high-gradient region at the edge of the PTV, making it highly sensitive to the resolution of the calculation and the accuracy of delineating the CTV or determining the PTV. For example, the radius of a 0.5 L spherical target volume of water is 49.2 mm, and the radius would have to change by less than 0.2 mm to produce a 1 % change in the volume of the PTV. Therefore, reporting of $D_{100\ \%}$ is not recommended because the PTV cannot be determined with sufficient accuracy to warrant constraining the absorbed dose to every voxel on the PTV periphery. Reporting of minimum absorbed dose should be replaced by the better-determined near-minimum absorbed dose, $D_{98\ \%}$, also designated as $D_{\mathrm{near\text{-}min}}$. Other dose–volume values, such as $D_{95\ \%}$, may also be reported but should not replace the reporting of $D_{98\ \%}$. The clinical relevance of the lowest PTV absorbed doses can depend on their position within the PTV. If they are close to the boundary of the PTV, a low-dose region might have less clinical relevance when compared with a position well within the PTV boundary. The location of low-dose regions within the GTV, CTV, and PTV boundaries can be of concern, but current planning tools to visualize directly the location of absorbed-dose regions identified within the DVH do not typically exist. Such regions might be identifiable using isodose contours. Hence, it is important that the radiation oncologist not rely solely on the DVH for treatment evaluation but also carefully inspect the absorbed-dose distributions slice-by-slice (or in 3D) to make sure that the PTV is being adequately irradiated.

In previous ICRU Reports, it was recommended to report as the "maximum absorbed dose" the high absorbed dose in at least a given minimum volume of the tissue (ICRU, 1993). In the present Report, another option is recommended analogous to the procedure for reporting the minimum absorbed dose, namely, to report the near-maximum absorbed dose, $D_{2\ \%}$, as a replacement for the "maximum absorbed dose". Both recommendations serve the same purpose: to report an absorbed dose that is not reliant on a single computation point. However, the radiation oncologist might judge that the "maximum absorbed dose" defined by ICRU 50 (ICRU, 1993) is clinically relevant, and this value may be reported. It is recommended that $D_{2\ \%}$ also be reported as it is simple to obtain and will add to consistency of reporting. If another dose-volume descriptor, for example D_V, where V is a small fractional volume, is felt to be clinically relevant, the fraction of the volume chosen should be reported textually or as part of a subscript.

These dose–volume values for the PTV and CTV represent the lower and upper bounds on the "actual" absorbed dose in the CTV, respectively. The DVH of the CTV would be representative of the absorbed dose to the CTV if the CTV did not change shape, did not move, and the treatment was always perfectly set up. The DVH of the PTV would be representative if the CTV moved evenly throughout the volume encompassed by the PTV.

A large separation between the DVH curves indicates that there is a steep gradient between at least a portion of the volume of the CTV and PTV boundaries. Even though the prescribed absorbed dose is identified with the PTV, the values of D_V for the CTV should be included in addition to reporting the PTV prescription. Comparing the dose–volume values of the PTV with those of the CTV will indicate the ability of the chosen margin to maintain an adequate absorbed dose to the CTV.

The report does not recommend any particular value of V in D_V for a prescription. However, the median absorbed dose, $D_{50\ \%}$, is likely to be a good measure of a typical absorbed dose in a relatively homogeneously irradiated tumor. As shown in Figure 3.2, the median absorbed dose has been shown to be computed accurately by many commercial treatment-planning systems (Das *et al.*, 2008), and its value is easy to determine from a cumulative DVH. The original rationales for reporting the absorbed dose at the ICRU Reference Point and that for reporting of $D_{50\ \%}$ are very similar, *i.e.*, reporting an absorbed dose that is largely representative of the absorbed dose in the PTV. However, numerically the values could probably differ to a small extent depending on the absorbed-dose distribution in the PTV.

Often for IMRT, the median absorbed dose is close to the mean absorbed dose for a target volume. Figure 3.3 illustrates a differential DVH with a median absorbed dose of 60 Gy and the resulting cumulative DVH obtained using Eq. 3.1. The greatest slope for the cumulative DVH is at or close to the median absorbed dose $D_{50\ \%} = 60$ Gy. For consistency, the reporting of the median absorbed dose, $D_{50\ \%}$, is recommended in addition to any other D_V that the radiation oncologist believes to be clinically relevant. The reporting of other D_V values gives a perspective on the absorbed-dose heterogeneity. A radiation oncologist might conclude that a larger (or even smaller) fractional V than 50 % is biologically more relevant, and so the freedom to prescribe any value is respected. However, $D_{50\ \%}$ should always be reported. The mean absorbed dose, which can be derived from a DVH, as indicated in Eq. 3.2, is also likely to be a good measure of the typical absorbed dose in the target volume. Treatment-planning systems should report the mean absorbed dose. When deemed clinically relevant, the mean absorbed dose is recommended for Level 2 reporting.

It is strongly recommended that if the method of prescription in a protocol or treatment aim is changed from a point-dose to a dose–volume approach, the impact on the absorbed dose received by patients should be determined. Figure 3.3 illustrates an example of the analysis that should be done. This figure assumes that the absorbed doses to the ICRU Reference Point and $D_{50\ \%}$ for the PTV are nearly identical (also see Figure 3.2 in ICRU Report 62, p. 24). This may not be always true; an evaluation of the relationship between $D_{50\ \%}$ and the absorbed dose at the ICRU Reference Point should be undertaken before any prescription methodology is changed. Suppose, using the data in Figure 3.3, that the prescription to the ICRU Reference Point was previously 60 Gy, and a $D_{50\ \%}$ of 60 Gy would be

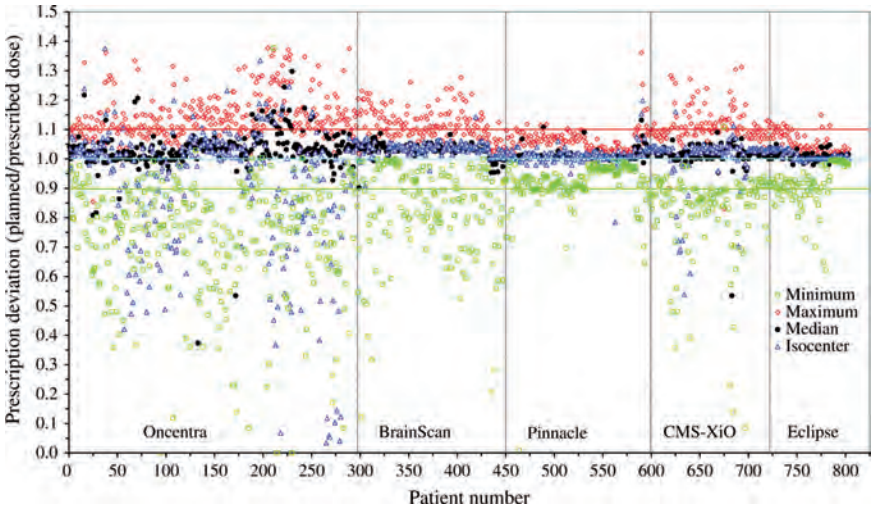

Figure 3.2. Dosimetric deviations between the prescribed and planned absorbed doses among 803 patients from five medical institutions with different treatment-planning systems. Vertical lines separate the data according to treatment-planning system (from left to right: Oncentra, BrainScan, Pinnacle, CMS-XiO, Eclipse). The horizontal line at 1.0 represents no deviation; the horizontal lines at 1.1 and 0.9 represent absorbed-dose relative variations of +10 % and −10 %, respectively, between the planned absorbed dose and the prescribed absorbed dose. There are wide variations in the minimum and the maximum absorbed doses. The median absorbed dose is the most accurate quantity computed. From Das *et al.* (2008); reproduced with permission.

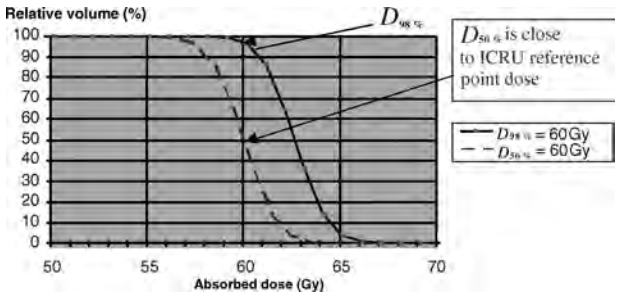

Figure 3.3. Schematic representation of DVHs resulting from two different approaches to prescribing. The dashed line is the DVH of a treatment that had been prescribed so that ICRU Reference Point received 60 Gy. The solid curve shows the DVH if the physician prescribes 60 Gy to $D_{98\,\%}$ instead. In many cases, the median absorbed dose $D_{50\,\%}$ is assumed to correspond to the ICRU Reference Point dose. The difference in all absorbed-dose metrics for the tumor for the two prescriptions is significant, differing by a common ratio of $D_{50\,\%}/D_{98\,\%}$. When comparing treatments reported using these two approaches, it is thus important to compare the numerical values and avoid introducing a systematic difference.

nearly equivalent. For a $D_{50\,\%}$ of 60 Gy, the $D_{98\,\%}$ is 57 Gy, and thus a prescription of $D_{98\,\%}$ of 57 Gy would be equivalent to a prescription of 60 Gy to the ICRU Reference Point. If instead the $D_{98\,\%}$ prescription was set at 60 Gy, this would have amounted to about a 5 % increase in the absorbed dose to a typical point in the PTV, $D_{50\,\%}$ in this example.

The PTV is a tool designed to ensure that the CTV receives an adequate absorbed dose. The CTV $D_{50\,\%}$ and $D_{2\,\%}$ should be very similar to these metrics for the PTV. However, near values of $D_{98\,\%}$ the DVHs for the CTV and PTV can diverge considerably. If it were possible to obtain the "true" DVH for the CTV, for which motion and setup uncertainties were accounted for in detail, it would be bounded by the DVHs of the CTV and PTV. In the future, absorbed-dose reconstruction to determine the actual absorbed dose delivered, taking into account setup errors, might enable a more accurate approximation to the "true" DVH of the CTV (Kapatoes *et al.*, 2001a; 2001b; McNutt *et al.*, 1996; Partridge *et al.*, 2002). Additionally, systems using MRI to determine the patient anatomy during treatment might make absorbed-dose reconstruction possible even with motion (Dempsey *et al.*, 2005; Fallone *et al.*, 2007; Raaymakers *et al.*, 2004).

Often a compromise must be made between achieving a large absorbed dose in the PTV and protecting sensitive normal structures. The clinician must be the judge of the degree of compromise, taking into account that regions of low absorbed dose in the target volume can lead to a reduced probability of tumor control. With a prescription using $D_{98\,\%}$, there will be, by definition, 2 % of the defined PTV volume with an absorbed dose less than the prescription.

3.4 Dose–Volume Reporting Specific to the OAR and PRV

The functional arrangement of normal-tissue cells has been described as parallel or serial (Withers, 1986; Withers *et al.*, 1988); see also Section 4.6. This distinction can be helpful in determining absorbed-dose limits in normal tissues (OAR) because serial-like tissues, such as the esophagus or spinal cord, can lose their function if a small region of the tissue is damaged. Parallel-like tissues, such as the lung or liver, have sufficient reserve capacity so that a sizeable amount of damage can be tolerated without a complication occurring.

For parallel-like structures, it is recommended that more than one dose–volume specification be considered for reporting. The mean absorbed dose in parallel-like structures can be a useful measure of absorbed dose in an organ at risk. Typically, because of highly non-homogeneous absorbed-dose distributions in an OAR, the mean absorbed dose and the median absorbed dose are not similar in value, and so the median absorbed dose cannot be used as an accurate substitute for the mean. Treatment-planning systems should present the mean absorbed dose for purposes of reporting, as this might be an especially useful metric for parallel-like normal structures. For parallel-like normal tissues, dose–volume reporting specifying V_D, which is a volume that receives at least the absorbed dose D, is a concept that has been commonly used. For example, Graham *et al.* (1995) found that the incidence and severity of lung pneumonitis was well correlated with $V_{20\,\mathrm{Gy}}$, the volume of normal lung receiving more than 20 Gy. It is recommended that both D_{mean} and V_D be reported, where the subscript D is an absorbed dose that if exceeded within some volume has a high probability of causing a serious complication. Typically, V_D would be reported using the absolute value of D and V as a fraction (percent) of the volume of the organ. An example would be $V_{20\,\mathrm{Gy}} = 30$ %. It is also recommended for parallel-like organs that the entire organ be contoured so that meaningful values of D_{mean} and V_D can be determined (see Section 2.6).

The maximum absorbed dose as specified by a single calculation point (D_{max} or $D_{0\,\%}$) has often been reported for serial-like organs or structures even though such a reported maximum absorbed dose was considered relevant only if the involved tissue volume had a minimum dimension of at least 15 mm. However, an even smaller dimension was considered

appropriate for some organs such as the spinal cord, eye, optical nerve, or larynx (ICRU, 1993). The minimum dimension for the maximum absorbed-dose region in a structure is not easy to establish, and so this Report recommends that $D_{2\ \%}$ be reported. To obtain a true value of $D_{2\ \%}$ the entire organ should be delineated, and it is recommended that this be done whenever possible (see Section 4.6). However, a high estimate of $D_{2\ \%}$ will result if only those portions of the organ that receive a high absorbed dose are delineated. This is because delineating large volumes that have low absorbed dose will lower the $D_{2\ \%}$ value when compared with only delineating the high-dose region. For the case of incomplete delineation, the anatomic description of the delineated regions should be described when reporting the $D_{2\ \%}$. The "maximum absorbed dose" may still be specified in terms of the absorbed dose in a minimum volume as recommended in ICRU Report 50, but if this or another maximum-like specification is used to describe the treatment protocol their values should be reported together with the value of $D_{2\ \%}$.

Care should be taken in changing from a maximum absorbed dose, $D_{0\ \%}$, or other maximum-like dose–volume specification to the near-maximum absorbed dose, $D_{2\ \%}$. For example, the Radiation Therapy Oncology Group (RTOG) Protocol 0615 (www.rtog.org/members/protocols/0615/0615.pdf) for nasopharyngeal cancer set the $D_{1\ \%}$ at 50 Gy for the spinal cord PRV but placed a constraint such that the spinal cord itself would have a maximum absorbed dose ($D_{0\ \%}$) of 45 Gy. Replacing $D_{1\ \%}$ or $D_{0\ \%}$ in this protocol by $D_{2\ \%}$ might require $D_{2\ \%}$ dose to be significantly reduced compared with $D_{1\ \%}$ or $D_{0\ \%}$ depending on the gradient of the DVH curve for the spinal cord at high absorbed doses.

Because most organs are not clearly a serial-like or parallel-like structure, at least three dose–volume specifications should be reported. These would include D_{mean}, $D_{2\ \%}$, and a third specification, V_D, that correlates well with an absorbed dose D, which if exceeded within some volume has a known high probability of causing a serious complication. Other specifications of risk, as deemed by the radiation oncologist to be relevant, may also be reported. When feasible, the whole organ should be delineated. When not feasible, a clear description of the delineation criteria should be reported.

3.5 Reporting of Treatment Fields Delivered per Fraction

For any type of low linear energy transfer radiotherapy, there is sound radiobiological rationale for the delivery of all treatment segments and fields in every fraction. In IMRT, if all of the fields are not delivered each day, the daily absorbed dose to the treatment volume could be inhomogeneous, and—since the biological effect varies with absorbed dose per fraction—this could produce a very different biological effect. It is recommended that all fields be delivered on all days, but if this is not possible then the exact nature of the treatment delivery should be clearly reported.

3.6 Reporting of Software Versions for Treatment Planning and Delivery

In the last decade, dose-calculation algorithms have changed dramatically. This is expected to continue for the foreseeable future as Monte Carlo dose-calculation algorithms become more accessible. In addition, beam characterization (*i.e.*, parameters describing the beam model used; see Appendix A.1 for more details) and algorithms to account for collimator-leaf shape and extrafocal radiation (scatter from the head of the treatment unit) are under development. As part of Level 2 reporting, it is important to note the make, model, and software version of the treatment-planning system used. The reporting should also include information on the optimizer software used. It is usually relevant to report details of the treatment-delivery software in addition to the treatment-planning system.

3.7 Level 3 Reporting: Reporting Developmental Techniques and Concepts

Level 3 reporting describes techniques and concepts that are under development, and have not yet reached a stage at which they are sufficiently established to recommend their use in routine practice. However, their continued investigation is encouraged, and some such concepts and developments are described below.

3.7.1 Dose Homogeneity and Dose Conformity

Dose homogeneity and dose conformity are independent specifications of the quality of the absorbed-dose distribution. Dose homogeneity characterizes the uniformity of the absorbed-dose distribution within the target volume. Dose conformity characterizes the degree to which the high-dose region conforms to the target volume, usually the PTV. Figure 3.4 illustrates examples of dose homogeneity and dose conformity.

Dose homogeneity and the uniformity of the absorbed-dose distribution are synonymous terms.

A perfectly homogeneous dose to the PTV would be characterized by a spike (a delta function) in the differential DVH or a vertical drop of the cumulative DVH line for the PTV at that absorbed dose. Typically, the differential DVH for a PTV for a reasonable treatment plan has a near Gaussian shape tightly distributed around the mean absorbed dose. A useful measure for such a distribution is the standard deviation of the mean. Therefore, in the best circumstances both the mean absorbed dose to the PTV and the standard deviation of the mean would be reported. Unfortunately, some current treatment-planning systems do not report either the mean or the standard deviation of the mean. The reporting of both the mean absorbed dose to the PTV and the standard deviation of the mean is a recommendation to vendors.

Several definitions of a homogeneity index have been proposed, and some individuals favor one over another often depending on the radiotherapy modality. For example, in radiosurgery for which dose homogeneity is characteristically low and the prescription can be 50 % of the maximum absorbed dose, the ratio of the maximum absorbed dose to the prescription absorbed dose has been used (Khoo, 1999; Murphy *et al.*, 2001). This definition indicates only the magnitude of overdosing but, perhaps more importantly, does not indicate if there is underdosing within the target volume. This definition would give a homogeneity index of unity if the maximum absorbed dose was equal to the prescription absorbed dose but part of the target was missed. This definition cannot be recommended. As another example, Thilmann *et al.* (2003) defined the homogeneity index, $HI_{95\ \%/107\ \%}$, as the fraction of the CTV with an absorbed dose higher than 95 % and lower than 107 % of the ICRU-prescribed absorbed dose. This definition does not indicate the magnitude of underdosage or overdosage. For 3D-CRT and IMRT, another definition sometimes cited is the maximum-minus-minimum absorbed dose normalized to the ICRU prescription absorbed dose (Wu *et al.*, 2004). Because the use of the minimum, the maximum, and ICRU Reference Point doses is no longer recommended, instead the following definition for homogeneity index is suggested:

$$HI = \frac{D_{2\ \%} - D_{98\ \%}}{D_{50\ \%}}. \tag{3.3}$$

An *HI* of zero indicates that the absorbed-dose distribution is almost homogeneous. $D_{50\ \%}$ is suggested as the normalization value because reporting of $D_{50\ \%}$ is strongly recommended in Level 2 reporting. In Figure 3.1, for example, $D_{2\ \%}$ is 63 Gy, $D_{50\ \%}$ is 60 Gy, and $D_{98\ \%}$ is 57 Gy, so the *HI* is equal to 0.1.

Even though, as we have seen in Section 3.3 for breast radiotherapy (Donovan *et al.*, 2002; 2007), the target might have better dose homogeneity

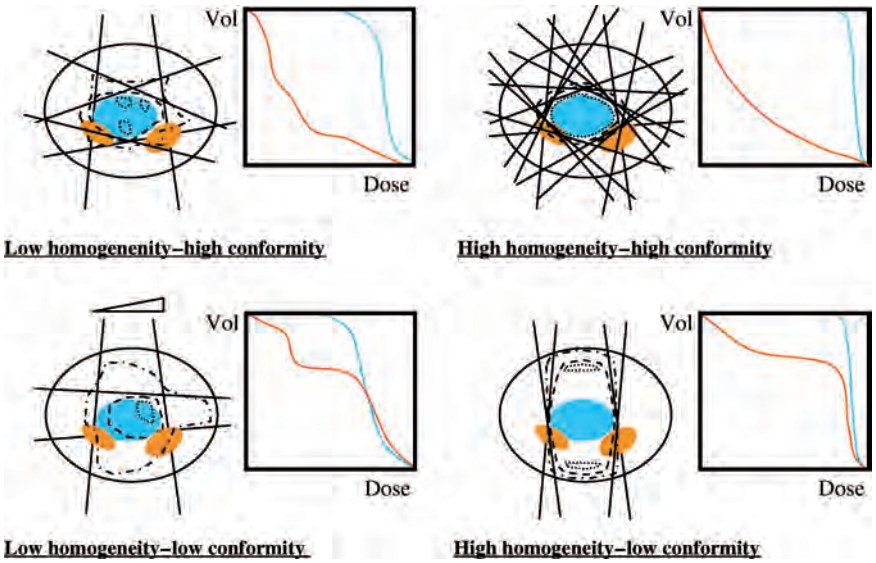

Figure 3.4. Examples of low and high dose homogeneity and dose conformity. The PTV is in blue and the PRV is in orange. Dashed lines indicate isodose lines. Homogeneity is a measure of the uniformity of absorbed dose in the PTV indicated by the "squareness" of the DVH. Conformity is a measure of the overlap between the isodose surface defining a significantly large absorbed dose and the surface of the PTV. Upper left panel shows the effect of unequal beam weighting to protect OARs. Lower left panel shows the effect of unequal beam weighting and use of a wedge. Upper right panel shows the effect of many beam portal angles with variable weighting. Lower right panel indicates the effect of 180° portal separation and lack of avoidance of the OARs.

with IMRT than with conventional radiotherapy delivery, small regions of high or low absorbed dose inside the target volume can develop in IMRT when avoidance of neighboring sensitive structures is considered more important than PTV-dose homogeneity. The ICRU previously recommended that the absorbed dose in the PTV be confined within from 95 % to 107 % of the prescribed absorbed dose (ICRU, 1999). With IMRT, these constraints can be unnecessarily confining if the avoidance of normal tissue is more important than target-dose homogeneity. In the present Report, it is recommended that the extent of high- and low-dose regions is specified using dose–volume quantities such as $D_{2\ \%}$ and $D_{98\ \%}$ for regions of high and low absorbed dose, respectively. For clinical trials, the average values of these quantities for all patients could be reported together with confidence intervals of the specified value. For the tumor, the equivalent uniform dose, EUD (see Section 3.7.3), also has potential as part of a dose-homogeneity specification, such as the ratio of EUD to D_V. As indicated, several approaches for reporting homogeneity indices have been suggested, but—whatever index is chosen for reporting—it must be clearly specified.

One of the hallmarks of 3D-CRT and IMRT is the conformity that can be achieved between the high-dose volume and the PTV. Indeed, the term 3D-CRT received its name from this property. The difference between the level of conformity achievable with conventional 3D-CRT and IMRT is most evident for concave target regions (see Figure 1.1).

A variety of indices have been proposed to characterize the degree of dose conformity of the treated volume (TV) to the PTV using a single parameter. These include the conformity index (ICRU, 1999; Knöös *et al.*, 1998), another index proposed by Paddick (2000), and the Dice similarity coefficient (Dice, 1945; Zhang *et al.*, 2007). In using any of these index formulations, with the exception of the conformity index, for which there is a requirement that the TV include the entire PTV, it is recommended that $D_{98\ \%}$ be used for delineating the TV. However, because of the increasing availability and use of DVH formats for reporting absorbed-dose information, the applicability of any of the above indices for reporting results of IMRT is likely to be limited.

3.7.2 Clinical and Biological Evaluation Metrics

Biological-based evaluation metrics are interesting research quantities, but clinically they should be used with caution. They are based not only on absorbed dose and volume, both of which can be physically defined, but also to some extent on clinical observations and/or biological models. In principle, such models are an important addition to a purely physical quantity because they relate to the aims of radiation therapy to provide improved tumor control and/or to reduce the probability of damaging healthy tissue. A complete and accurate biological model of radiation oncology response would be extremely useful, especially if used as an objective function on which to base the search for the IMRT delivery pattern. All biological models have uncertainties in the values of the parameters chosen. As biological models become more utilized in research studies as prescription and evaluation quantities, their possible role will become better defined. Eventually, the models might be used directly as objective functions in IMRT treatment planning, but these models will not entirely supplant the clinical judgment of a radiation oncologist. We recommend that biologically based quantities be explored as evaluation metrics to provide additional quantitative tools for radiation oncology. If biologically based metrics are to be reported, the assumptions used in the models, their parameters, and the model itself must be unambiguously specified.

In animal experiments and in clinical practice, local tumor-control probability (TCP) follows a sigmoid curve from zero control at some low absorbed dose to certain local control at high absorbed doses. There are simple phenomenological models based on clinical observations. For example, the logistic function can approximate the TCP:

$$TCP = \frac{1}{1 + (d_{50\,\%}/D)^{4\gamma_{50\,\%}}}, \tag{3.4}$$

where $d_{50\ \%}$ is the absorbed dose at which the *TCP* is 50 %, $\gamma_{50\ \%}$ the slope at the point of 50 % tumor control, and D the absorbed dose administered (Bentzen and Tucker, 1997; Suit *et al.*, 1965). The use of the logistic function assumes an approximate uniform response in those cells that determine the final outcome (*e.g.*, hypoxic cells) and a uniform absorbed-dose distribution, and so its use in IMRT is limited.

Mechanistic models of the TCP usually assume that local control is achieved if and only if all clonogenic tumor cells are inactivated. Based on a Poisson distribution, the probability of no clonogenic cells surviving following treatment, *TCP*, is in this case given by:

$$TCP = \exp(-N\,SF), \tag{3.5}$$

where N is the number of clonogens and SF the surviving fraction of clonogens (Munro and Gilbert, 1961). Assuming that *in vivo* tumor cells behave according to the linear-quadratic model (Barendsen, 1982; Chadwick and Leehouts, 1973; Douglas and Fowler, 1976; Kellerer and Rossi, 1972; Lea, 1947; Thames *et al.*, 1982), the surviving fraction is given by

$$SF = \exp\left[-n(\alpha d + \beta d^2)\right], \tag{3.6}$$

where n is the number of fractions of equal absorbed dose d. The parameters α and β are obtained by fitting the linear-quadratic relationship to clinical data (Steel, 1993). Equation 3.6 requires uniform absorbed dose and cell sensitivity.

All parts of the tumor might not be irradiated to the same absorbed dose and parts might have a different clonogen density and/or clonogen sensitivity. Assuming that within each of several parts of a tumor, the cellular radiation sensitivity, absorbed dose per fraction d_i, and total absorbed dose D_i are uniform and each part behaves independently of each other part, it is possible to generalize Eq. 3.5 by formulating the probability of eradication of the whole tumor in terms of eradication of its parts (Goitein, 1987; Yorke, 2003):

$$TCP = \prod_i \exp[-n_i\, SF(D_i, d_i)], \tag{3.7}$$

where n_i is the number of clonogens in part i and is given by the density of clonogens and the volume of that part of the tumor. TCP is then interpreted as the probability of tumor clonogens not surviving anywhere in the tumor. Generally, the difficulty with modeling the TCP is assigning parameter values to describe the tumor. The validity of TCP values using Eq. 3.7 is highly dependent on knowledge of the absorbed-dose uniformity and cell sensitivity.

The response of normal tissue to injury has all of the complexity of tumor-tissue response with respect to its dependence on cell type, absorbed dose, and absorbed dose per fraction. In addition, the functional relationship among cells is also important (Withers, 1986; Withers *et al.*, 1988). Serial-like tissues, such as the esophagus or spinal cord, can lose their function if a small circumferential region of the tissue is damaged (Poltinnikov *et al.*, 2005). Parallel-like tissues, such as the lung or liver, have sufficient reserve capacity so that a sizeable amount of damage can be done without a complication occurring. This means that normal-tissue-complication probability (NTCP) has an organ-specific dependence on the volume of damage. Phenomenologically, the volume dependence of the tolerance absorbed dose TD_v for a normal tissue can be modeled according to a power law (Kutcher and Burman, 1991; Lyman, 1985; Lyman and Wolbarst, 1989):

$$TD_v = TD_{v=1} v^{-s}, \tag{3.8}$$

where $TD_{v=1}$ is the tolerance absorbed dose when the whole organ or tissue structure is irradiated, v the fraction of the volume receiving a selected absorbed dose, and s a tissue-dependent exponent that depends on the tissue structure. The TD_v is the tolerance absorbed dose if only a portion of its volume were irradiated. A parallel-like structure has an exponent close to unity implying that the probability of harm at a given absorbed dose is proportional to the volume irradiated. For serial-like structures, the exponent is significantly less than unity. If the exponent is close to zero, the tolerance absorbed dose for any volume irradiated is equal to the tolerance absorbed dose for the structure as a whole, and so irradiating only a portion is nearly equivalent to irradiating the whole structure to the same absorbed dose. So tissues such as the spinal cord can fail because of inactivation of a small portion, whereas tissues such as the kidney or lung can lose a substantial portion of their functional units with little clinical impact (Steel, 1993). This formula is based on the assumption that none of the remaining volume, $(1 - v)$, receives any absorbed dose, but generally normal tissues are typically irradiated to a wide range of absorbed doses. Emami *et al.* (1991) published values of tolerance-absorbed-dose estimates for several partial organ volumes, and Burman *et al.* (1991) provided fits to determine the exponent s for these organs. Updates to the original Emami *et al.* (1991) and Burman *et al.* (1991) estimates have been given for radiation myelitis in the spinal cord (Schultheiss *et al.*, 1995), radiation pneumonitis in the lung (Martel *et al.*, 1994), xerostomia due to parotid damage (Eisbruch *et al.*, 2001), and radiation-induced liver disease (Dawson *et al.*, 2001). A joint ASTRO/AAPM initiative, called Quantitative Analyses of Normal Tissue Effects in the Clinic (QUANTEC), to update Emami *et al.* (1991) is underway. QUANTEC will compile models and model parameters for normal-tissue complication (Bentzen *et al.*, 2010) for a number of treatment sites. The use of IMRT itself will undoubtedly force a re-examination of the tolerance limits. For example, Ozyigit and Chao (2002) found that after IMRT only from 17 % to 30 % of head-and-neck patients had grade 2 xerostomia when compared with approximately 75 % of those treated with conformal radiotherapy.

The Lyman (1985) model for the NTCP explicitly used a volume-dependent power law and assumed that the probability of complication follows a sigmoid curve described by the error function. Other publications deal with ways of using a DVH to take into account the range of absorbed doses (Kutcher and Burman, 1991; Lyman and Wolbarst, 1989; Moiseenko *et al.*, 2000).

Niemierko and Goitein developed separate models for serial-like (Niemierko and Goitein, 1991) and parallel-like (Niemierko and Goitein, 1993) organs. The critical-element model, for serial-like tissue structures, assumes that the damage to a single functional sub-unit (FSU) will damage the structure. The NTCP for serial-like organs is given by

$$NTCP = 1 - [1 - p(D)]^N, \tag{3.9}$$

where $p(D)$ is the probability of damaging any FSU with absorbed dose D, and N the number of FSUs. This formulation assumes that all FSUs receive the same absorbed dose.

The probability of uncomplicated control is the combined probability that the tumor is controlled and there are no adverse complications. It is thus not realistic to assume that TCP is independent of NTCP. That is because an individual who is genetically more sensitive to a complication, and therefore has a higher NTCP, might have a tumor that is also more sensitive to radiation and therefore also have a higher TCP. As long as the NTCP is smaller than the TCP, and the correlation, c, between *TCP* and *NTCP* can be determined, the probability of uncomplicated control, PUC, can be written as

$$\begin{aligned} PUC = {} & c(TCP - NTCP) + (1 + c) \\ & TCP(1 - NTCP). \end{aligned} \tag{3.10}$$

Radiation therapy is typically given only if the TCP is much larger than the NTCP, so the utility of this equation to rationalize competing values of the TCP and the NTCP is severely limited.

3.7.3 Equivalent Uniform Dose

The concept of the equivalent uniform dose (EUD) was proposed by Niemierko (1997). It is meant to be that homogeneous or uniform absorbed dose that would give the same biological response or clinical effect as the absorbed-dose distribution actually delivered. It allows a distribution to be replaced by a single scalar value. It was originally a biologically based quantity defined by

$$EUD = 2\,\mathrm{Gy}\frac{\ln\left[\frac{1}{N}\sum_{i=1}^{N}\left(SF_{2\,\mathrm{Gy}}\right)^{D_i/2\,\mathrm{Gy}}\right]}{\ln\left(SF_{2\,\mathrm{Gy}}\right)}, \tag{3.11}$$

where $SF_{2\,\mathrm{Gy}}$ is the surviving fraction at 2 Gy, D_i the absorbed dose at the ith calculation point, and N the number of calculation points.

More recently, Niemierko (1999) redefined the concept of EUD to be the generalized mean for normal-tissue complications as follows (also see Yorke, 2003):

$$EUD = \left(\sum_i v_i D_i^a\right)^{1/a}, \tag{3.12}$$

where v_i is the volume of the dose–volume bin with absorbed dose D_i, and the exponent a is a complication-specific parameter. There are no recommended publications documenting values for a. However, serial-like tissues have large positive values of a, and values are close to 1 for parallel-like structures. The same formalism can be used for tumors, with a being large and negative.

The EUD, as with all biological metrics, should be used with caution if the parameters are not well known. Figure 3.5 illustrates that the EUD formula can favor either of two plans depending on the value of the parameter a. For the reporting of EUD metrics, all of the assumptions including parameter values should be carefully and explicitly reported.

3.8 Reporting of Confidence Intervals

Although estimations of uncertainty are difficult, confidence intervals should be reported whenever possible. For example, rather than simply reporting $D_{50\ \%}$ for an individual or the average value of $D_{50\ \%}$ for patients in a trial, it would be useful to report the confidence intervals for those values. If quality-assurance measurements verified the absorbed doses delivered to patients in the trial, the population-averaged deviation of the measurements from the expected result, normalized to the expected result, would be a useful measure, as would the confidence interval of the population deviation. Confidence intervals are presently considered to be part of Level 2 or Level 3 reporting whenever possible.

The PTV is designed largely to accommodate alignment and motion uncertainties, and the treatment plan is frequently designed such that the PTV receives a lower absorbed dose at its boundaries than in its interior. As the CTV is unlikely always to be located near the edge of the PTV, the absorbed dose actually delivered to the CTV is likely to be closer to the desired distribution than the DVH of the PTV would suggest. Thus, the DVH of the PTV will tend to exaggerate the dose heterogeneity of the CTV. Similarly, the DVH of the CTV will tend to indicate more homogeneity than is actually the case. It is therefore useful to show the PTV and the CTV

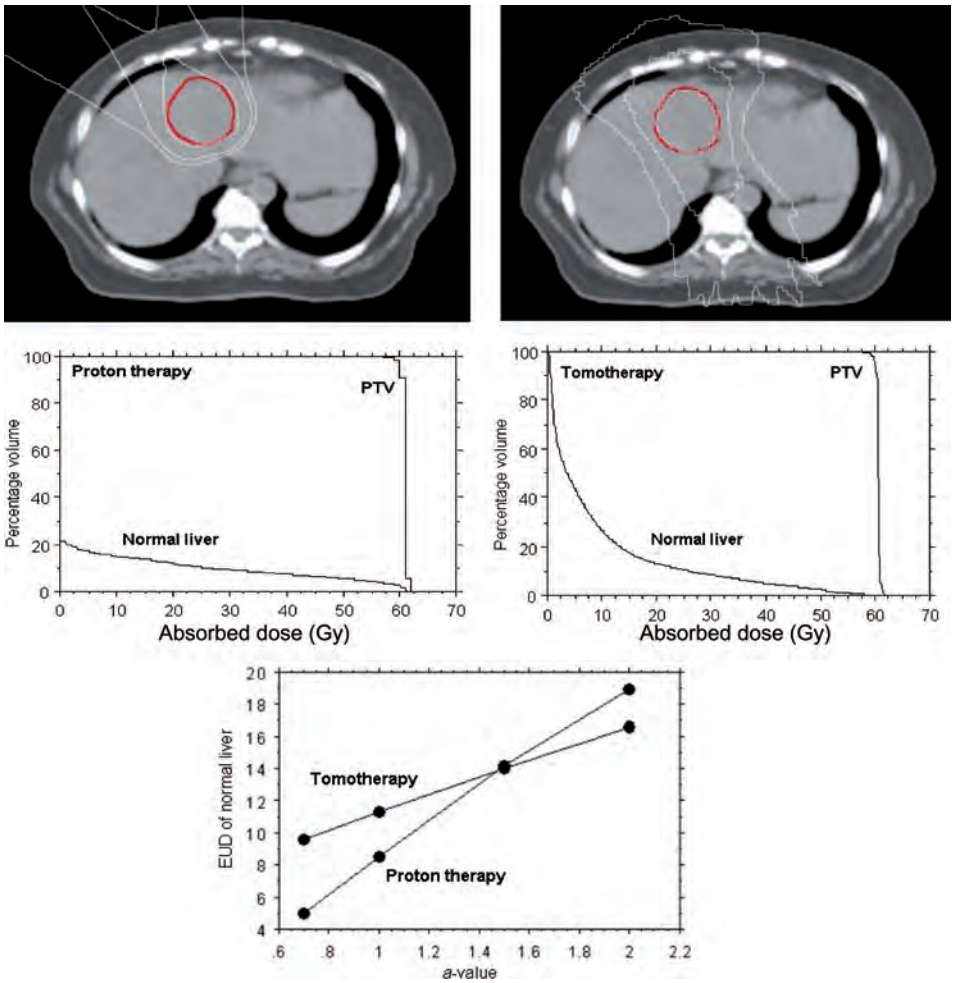

Figure 3.5. Example of a comparison of EUDs between two modalities for a liver treatment. Upper left panel shows the 60 Gy, 30 Gy, and 15 Gy isodose lines for a two-field proton-therapy treatment. Upper right panel shows the same isodose lines for a helical tomotherapy plan. Middle left panel shows the DVH for the proton plan. Middle right panel shows the DVH for the tomotherapy plan. Lower panel shows the EUD for normal liver as a function of parameter a in the general EUD formula of Eq. 3.12. The two-field proton case has a lower integral absorbed dose than for tomotherapy. However, the tomotherapy case is more conformal with a lower volume at the higher absorbed dose levels. The calculated EUD can be higher in the normal liver for either plan depending on the value of the parameter a. (Figure courtesy of Thomas Mackie, University of Wisconsin, and Hide Aoyama, Sapporo University.)

DVHs on the same graph, as these define the envelope of possible values of the DVH of the CTV, depending on actual motion or setup uncertainty and assuming a correct absorbed-dose distribution and accurate contouring of volume.

Without a statement of the confidence level, an uncertainty estimate is meaningless. Goitein (1983) argued that, for many metrics in radiation therapy that follow normal distributions, one standard deviation is not restrictive enough, and two standard deviations is too restrictive, and that an 85 % confidence interval, corresponding approximately to 1.5 standard deviations, is a more useful accuracy constraint for many applications. Medical physicists need to make quality-assurance measurements to ensure that accuracy can be determined and maintained.

Treatment-planning systems must make an effort to make available new capabilities to report the uncertainty or confidence intervals for their calculated absorbed-dose distributions. This should involve a determination of the systematic (Type B) and random (Type A) uncertainties of the planning-system calculations by comparing the planning results with the results of measurement after estimating the measurement uncertainty, including the uncertainty in the delivery. The mean of a set of measurements when compared with the computation represents the Type B uncertainty and the spread within the set of measurements represents the Type A uncertainty. In the case of Monte Carlo methods, the uncertainty in the random sampling is relatively easy to determine on the basis of sampling theory. Detailed

comparisons of computation with measurement could be done with a set of expert users, coordinated by vendors of treatment-planning systems, and published in the peer-reviewed literature. Once uncertainty information is available, treatment planners need a graphical user interface so that uncertainty can be presented along with absorbed-dose information.

Journal of the ICRU Vol 10 No 1 (2010) Report 83
Oxford University Press
doi:10.1093/jicru/ndq009

4. Definition of Volumes

4.1 Introduction

As introduced in ICRU Reports 50, 62, 71, and 78 (ICRU, 1993; 1999; 2004; 2007), several volumes related to both tumor and normal tissues have been defined for use in the treatment-planning and reporting processes. Delineation of these volumes is an obligatory step in the planning process, as absorbed dose cannot be prescribed, recorded, and reported without specification of target volumes and volumes of normal tissue at risk.

The defined volumes were:

- Gross tumor volume or GTV
- Clinical target volume or CTV
- Planning target volume or PTV
- Organ at risk or OAR
- Planning organ-at-risk volume or PRV
- Internal target volume or ITV
- Treated volume or TV
- Remaining volume at risk or RVR

The GTV, CTV, and OAR correspond, respectively, to volumes of known (GTV), and/or suspected (CTV) tumor infiltration, and volumes of normal tissues that might be irradiated and affect the treatment prescription (OAR). These volumes have an anatomical/physiological basis, in contrast to the ITV, the PTV, and the PRV, which are concepts introduced to ensure that the absorbed dose delivered to the corresponding CTV and OAR match the prescription constraints. The GTV is delineated using various diagnostic modalities. The selection and delineation of the CTV and the OAR is a medical decision, which results from a clinical judgment involving many factors. Unlike the ITV, the PTV, and the PRV, the delineation of the GTV and the CTV should be independent of the irradiation techniques, and influenced only by oncological considerations. For the delineation of volumes, and in their use, it is irrelevant whether photons, electrons, protons, or any other radiation is to be employed. Indeed, it is important not to let the intended modality affect how these volumes are delineated as one might wish to combine, compare, or retrospectively analyze treatment plans for more than one radiation modality.

Three-dimensional imaging and the selection and delineation of the GTV, CTV, and OAR are crucial steps in a chain starting with the decision to treat the patient with radiotherapy and ending with the response evaluation and the follow-up in search of recurrence and treatment-induced morbidity (see Figure 4.1).

It should be understood that even though the GTV, CTV, and OAR are purely oncological or anatomical concepts, a representation of these volumes is used in the planning process, *e.g.*, outlines on a computed tomography (CT) scan. These representations (volumes) should be considered a snapshot

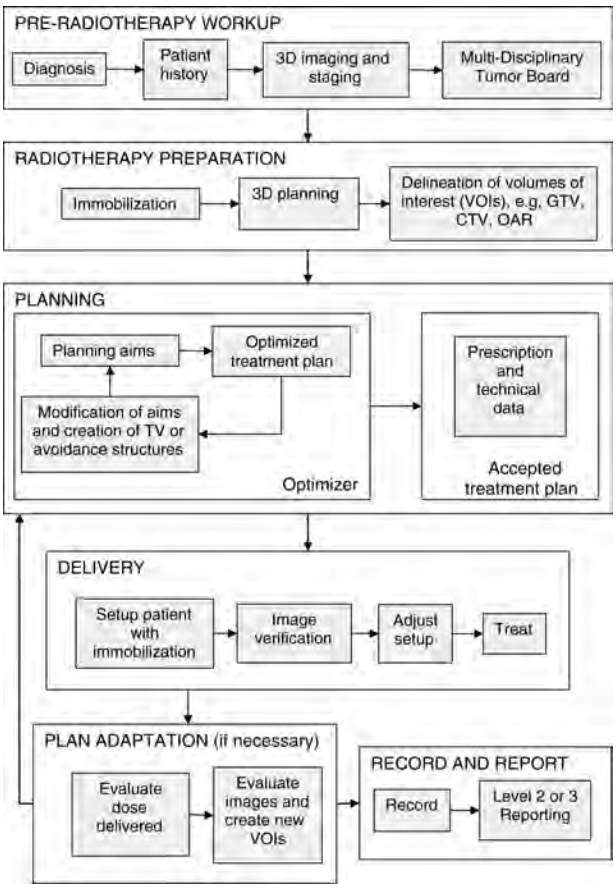

Figure 4.1. Flowchart of a typical course of radiotherapy.

of the anatomy at a given time. All volumes should be a representation of the patient's anatomy in treatment conditions. Movement or anatomical changes in the patient can be visualized by using a time-series (four-dimensional) representation, *e.g.*, daily-repeated or respiration-correlated CT scans, in which the fourth dimension (*i.e.*, time) allows visualization of time-dependent changes in morphology. Future planning systems will be able to handle four-dimensional scans, for instance, by displaying a cine loop on the screen. In principle, this technology will make it possible to generate four-dimensional representations of a patient. Four-dimensional CT technology is being used more and more, *e.g.* for lung-tumor treatment.

4.2 Gross Tumor Volume

The GTV is the gross demonstrable extent and location of the tumor.

The GTV may consist of a primary tumor (primary tumor GTV or GTV-T), metastatic regional node(s) (nodal GTV or GTV-N), or distant metastasis (metastatic GTV, or GTV-M). Typically, different GTVs are defined for the primary tumor and the regional node(s). But in some particular clinical situations, it might well be that the metastatic node cannot be distinguished from the primary tumor, *e.g.*, a nasopharyngeal undifferentiated carcinoma infiltrating postero-laterally into the retropharyngeal space, including possible infiltrated nodes. In such situations, a single GTV encompassing both the primary tumor and the node(s) may be delineated.

In case of post-operative irradiation after assumed complete surgical resection (R0 or R1 resection), there is no GTV to define, and only a CTV needs to be delineated (see Section 4.3). Although in the vast majority of cases the GTV refers to a malignant tumor, the terminology may also be used for non-malignant lesions treated with ionizing radiation (*e.g.*, glomus tumor of the carotid body, arteriovenous malformation, and pituitary adenoma).

There are several reasons to describe and report the GTV in a complete and accurate way. First, it is required for staging, *e.g.*, according to the TNM system (see below). Secondly, an adequate absorbed dose must be delivered to the whole GTV to obtain local tumor control. Thirdly, evaluation of the regression of the GTV might be needed for redefining the CTV and the PTV (see Section 4.5) during the course of treatment. Fourthly, changes of the GTV during treatment might be predictive of treatment outcome.

When reporting a GTV, several items need to be specified:

- First, the location and tumor extent according to the TNM/AJCC or UICC (AJCC, 2002; UICC, 2002) cancer-staging systems and the WHO International Code for Disease in Oncology (ICD-O) (WHO, 2000).
- Second, the methods used to delineate the GTV. For three-dimensional conformal therapy (3D-CRT) and intensity-modulated radiation therapy (IMRT), in addition to the clinical examination, various imaging modalities are used. Until recently, anatomic imaging with CT or magnetic resonance (MR) scans was typically the most commonly used technique to define the extent of the GTV. The use of functional imaging with positron emission tomography (PET) using various tracers (such as shown in Table 4.1), or with functional MRI, can reveal some key biological factors (*e.g.*, metabolic status, hypoxia, cellular proliferation) that are likely to impact on the treatment outcome. Functional information can be used to define sub-GTVs that are to receive some additional absorbed dose (Ling *et al.*, 2000). It is therefore recommended that the method used to evaluate the size of the GTV be specified. Figures 4.2 and 4.3 present two clinical examples in which several clinical and imaging methods were used to delineate the GTVs before and during treatment. These examples illustrate the increasing need to specify how the GTV was delineated.
- Last, any changes occurring in the GTV during treatment can be quantified with anatomic- and/or functional-imaging techniques, allowing the definition of a modified GTV that might be used to adjust the absorbed-dose distribution (Geets *et al.*, 2006; 2007b). It is therefore recommended

Table 4.1. Tracers for image-guided radiotherapy using PET. ^{18}F has a physical half-life of 110 min, and ^{11}C has a half-life of 20 min. See review by Grégoire *et al.* (2009).

Tracer name	Accepted abbreviation	Function
^{18}F-fluoro-2-deoxy-D-glucose[a]	^{18}F-FDG	Glucose metabolism
^{18}F-fluoro-ethyl-tyrosine[a,b]	^{18}F-FET	Protein synthesis
^{18}F-3′-deoxy-3′-fluoro-thymidine	^{18}F-FLT	Cell proliferation
^{18}F-fluoro-methyl-D-tyrosine	^{18}F-FMT	Protein synthesis
^{11}C-methionine[a]	^{11}C-MET	Protein synthesis
^{11}C-acetate		Fatty-acid metabolism
^{18}F-fluoro-misonidazole	^{18}F-FMISO	Hypoxia

[a]Already used in IMRT clinical studies.
[b]Alternative is the SPECT tracer ^{123}I-α-methyltyrosine (^{123}I-IMT).

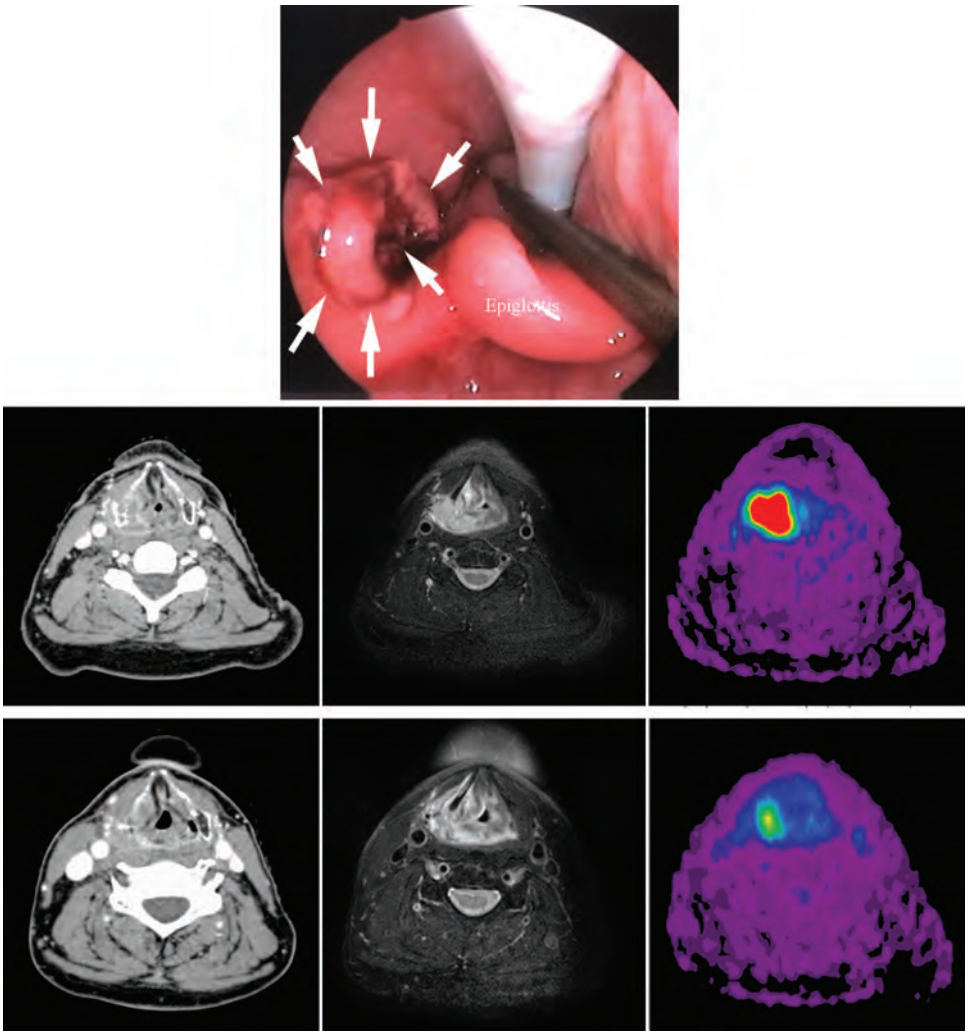

Figure 4.2. Comparison among various modalities for the definition of the primary head-and-neck tumor GTV. *Upper panel*: view from a laryngoscope under general anesthesia, which shows an exophytic tumor (see arrows) of the right lateral oropharyngeal wall extending into the right piriform sinus.
Middle panel: GTV-T imaged prior to any treatment

- Left: primary-tumor GTV imaged with a contrast-enhanced CT: GTV-T (CT, 0 Gy): volume of 25.8 ml.
- Middle: primary-tumor GTV imaged with a fat-saturated T2-weighted MRI: GTV-T (MRI T2, fat sat, 0 Gy): volume of 28.5 ml.
- Right: primary-tumor GTV imaged with a FDG-PET: GTV-T (FDG-PET, 0 Gy): volume of 22.2 ml.

Lower panel: GTV imaged after an absorbed dose of 20 Gy.

- Left: primary-tumor GTV imaged with a contrast-enhanced CT: GTV-T (CT, 20 Gy): volume of 16.3 ml.
- Middle: primary-tumor GTV imaged with a fat-saturated T2-weighted MRI: GTV-T (MRI T2, fat sat, 20 Gy): volume of 19.8 ml.
- Right: primary-tumor GTV imaged with a FDG-PET: GTV-T (FDG-PET, 20 Gy): volume of 12.5 ml.

At 20 Gy, the GTV as determined by all techniques has already substantially decreased. This is particularly visible with FDG-PET.

that the absorbed dose and/or the time when the GTV is evaluated or measured with respect to the start of treatment be indicated.

Because delineation of a GTV can vary according to the diagnostic modality (*e.g.*, clinical examination, anatomic imaging, functional imaging) used, a clear annotation is required. For example:

- GTV-T (clin, 0 Gy): tumor GTV evaluated clinically before the start of the radiotherapy.
- GTV-T (MRI-T2, 30 Gy): tumor GTV evaluated with a T2-weighted MRI scan after an absorbed dose of 30 Gy of external beam irradiation.

This approach avoids the introduction of new or potentially confusing terminology, *e.g.*, biological target volume, proliferative target volume, hypoxic target volume, and is able to cover all the different situations that might be encountered. The annotations described above are meant only as examples.

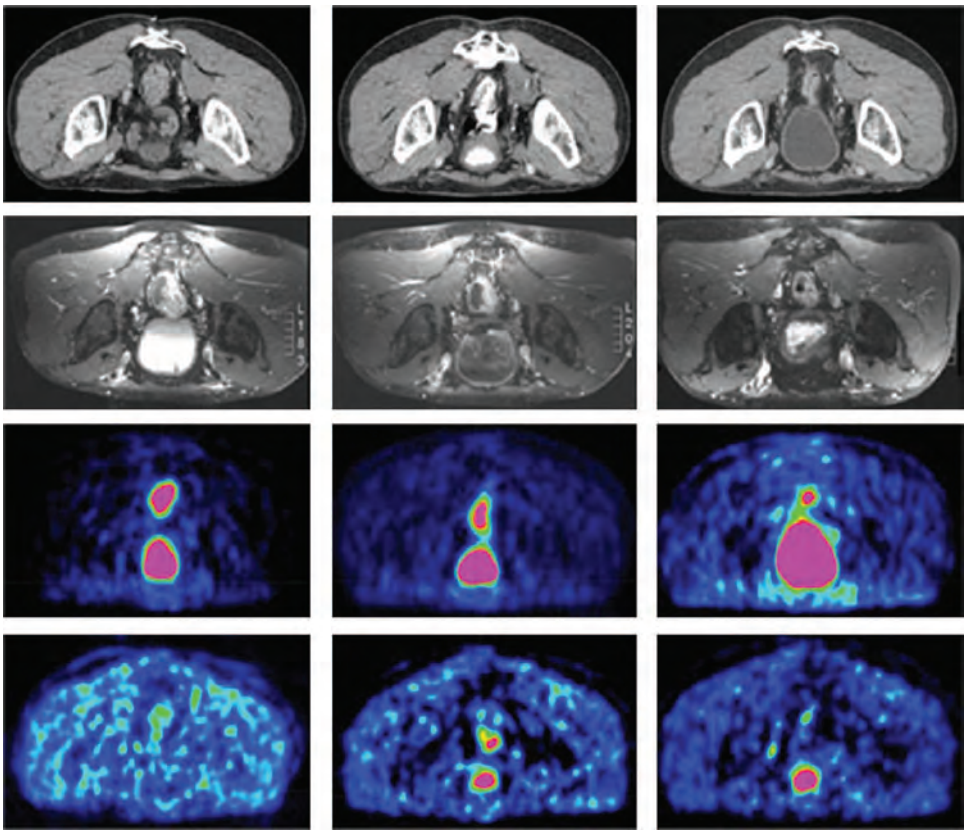

Figure 4.3. Comparison among various modalities for the definition of a primary-rectal-tumor GTV before (left), during concomitant chemoradiotherapy (center), and after radiation therapy (right). Positron emission tomography–computed tomographic acquisitions were performed in a prone position using a belly board; MRI acquisitions were performed in a supine position. (Figure courtesy of Prof. K. Haustermans, Katholieke Universiteit Leuven, Belgium.)

Left column: GTV delineated prior to any treatment.

- First row: primary-tumor GTV delineated with a contrast-enhanced CT: GTV-T (CT, 0 Gy).
- Second row: primary-tumor GTV delineated with a fat-saturated T1-weighted turbo spin-echo MRI: GTV-T (MRI T1, fat sat, 0 Gy).
- Third row: primary-tumor GTV delineated with a FDG-PET: GTV-T (FDG-PET, 0 Gy).
- Fourth row: primary-tumor GTV delineated with a F-Misonidazole PET: GTV-T (F-Miso-PET, 0 Gy).

Middle column: GTV delineated during treatment (average absorbed dose of 19 Gy).

- First row: primary-tumor GTV delineated with a contrast-enhanced CT: GTV-T (CT, 19 Gy).
- Second row: primary-tumor GTV delineated with a fat-saturated T1-weighed turbo spin-echo MRI: GTV-T (MRI T1, fat sat, 19 Gy).
- Third row: primary-tumor GTV delineated with a FDG-PET: GTV-T (FDG-PET, 19 Gy).
- Fourth row: primary-tumor GTV delineated with a F-Miso PET: GTV-T (F-Miso-PET, 19 Gy).

Right column: GTV evaluated 27 days after treatment.

- First row: primary-tumor GTV delineated with a contrast-enhanced CT: GTV-T (CT, 46 Gy).
- Second row: primary-tumor GTV delineated with a fat-saturated T1-weighted turbo spin-echo MRI: GTV-T (MRI T1, fat sat, 46 Gy).
- Third row: primary-tumor GTV delineated with a FDG-PET: GTV-T (FDG-PET, 46 Gy).
- Fourth row: primary-tumor GTV delineated with a F-Miso PET: GTV-T (F-Miso-PET, 46 Gy).

Other styles could be equally valid and unambiguous.

When using various imaging modalities to delineate the GTV, the need for image registration adds uncertainty in the GTV delineation. Uncertainties in GTV delineation generally propagate to CTV delineation. Such uncertainties, together with other geometric uncertainties, are taken into account in the CTV-to-PTV margin (see Section 4.5).

4.3 Clinical Target Volume

The CTV is a volume of tissue that contains a demonstrable GTV and/or subclinical malignant disease with a certain probability of occurrence considered relevant for therapy. There is no general consensus on what probability is considered relevant for therapy, but typically a probability of occult disease higher than from 5 % to 10 % is assumed to require treatment. This remains a

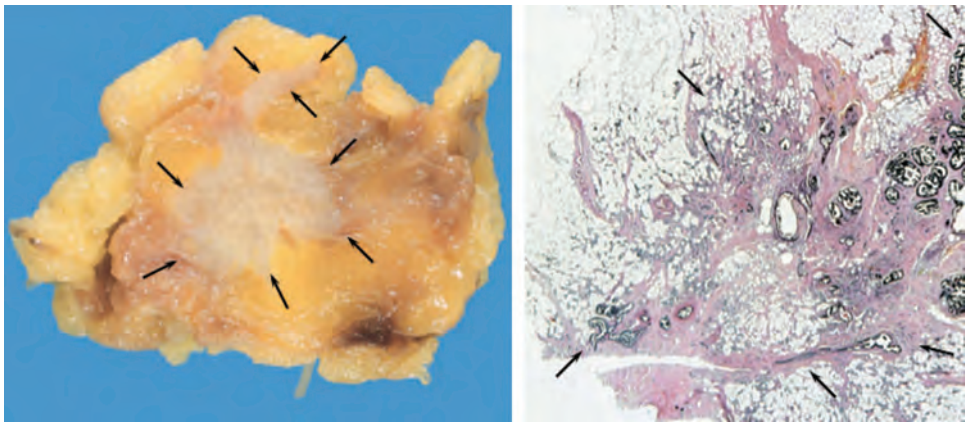

Figure 4.4. Macroscopic section (left) and microscopic view (right) of a breast carcinoma after surgical removal. Tumor-cell projections into the surrounding fatty tissue are marked with arrows. (Figure courtesy of Prof. B. Weynand, Université Catholique de Louvain, St. Luc University Hospital, Brussels, Belgium.)

clinical judgment in which the type of malignancy, the consequence of failure, and the expected feasibility of salvage treatment need to be considered.

The notion of subclinical malignant disease includes the microscopic tumor spread at the boundary of the primary-tumor GTV (thus outside of what can be observed, palpated, or visualized in a particular imaging modality), the possible regional infiltration into lymph nodes, and the potential metastatic involvement of other organs (*e.g.*, brain), despite their normal appearance on clinical and radiological examinations. In Figure 4.4, the comparison between the macroscopic and the microscopic sections of a breast carcinoma illustrates the lack of clear boundaries and the tumor infiltration in the surrounding fatty tissues.

There might not be a CTV associated with a benign-tumor GTV because there is no risk of microscopic or metastatic tumor infiltration into the regional nodes (see Figure 4.5). In the case of post-operative irradiation (after R0 or R1 resection), there is no GTV. In such a case, only a CTV will be selected and delineated.

The selection of the tissues that bear risk for microscopic infiltration outside of the GTV is a probabilistic assessment integrating the biological and clinical behavior of the various tumor entities and the knowledge of the surrounding anatomy, including structures that are barriers to tissue infiltration (*e.g.*, muscular fascia, bone cortex), or—on the contrary—structures that are easy conduits for tumor dissemination (*e.g.*, fatty space). Different tumors can exhibit a variety of spread patterns. For instance, the vast majority of sarcomas do not bear risk of lymph-node infiltration, and thus the post-operative CTV will typically include only the post-operative tumor bed using the principle of "fascia containment" (O'Sullivan *et al.*, 2003). On the contrary, in head-and-neck squamous-cell carcinoma, the probability of pathologic lymph-node involvement has been well described, and the distribution follows a predictable pattern allowing clinicians to tailor the CTV to the primary-tumor location and extent (see Table 4.2) (Grégoire *et al.*, 2000; 2003a; 2003b; 2003c; 2006). Similar observations have been reported for other tumor types and sites as well (see Table 4.3) (see review in Grégoire *et al.*, 2003d). At the primary-tumor site, the selection of the CTV should be guided by the general principle that the microscopic spread of tumor cells follows anatomical compartments (*e.g.*, para-laryngeal, para-pharyngeal, pre-epiglottic spaces in the head-and-neck area) bounded by anatomical barriers (*e.g.*, bone cortex, muscular fascia, ligaments) (Grégoire *et al.*, 2003a). Unless transgressed, such barriers would limit the local primary-tumor spread. Over the last few years, recommendations for CTV selection have been proposed for various primary-tumor sites (see review in Grégoire *et al.*, 2003d).

The delineation of the CTV is currently based on clinical experience. For quantitative margin definition and future research, it would be advantageous to introduce a probabilistic definition, *e.g.*, to choose the CTV based on a defined probability of containing clonogenic cells that need to be treated.

The three-dimensional delineation of the CTV for both the primary-tumor GTV and the nodal GTV should be guided by published recommendations, which aim to translate the regions at risk for microscopic dissemination (both around the primary tumor and at lymph-node areas) into boundaries easily identifiable on planning CT or MRI (see reviews in Grégoire *et al.*, 2003d). Examples of 3D-CTV delineation are given in Figure 4.6.

By definition, each malignant-tumor GTV should be associated with a CTV. However, several contiguous GTVs could be associated with a common CTV.

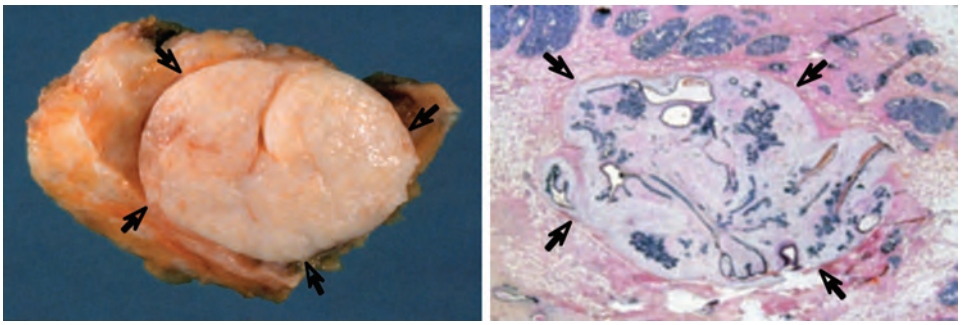

Figure 4.5. Macroscopic section (left) and microscopic close view (right) of a breast fibroadenoma after surgical removal. This well-defined tumor is surrounded by a fibrous capsule (see arrows). (Figure courtesy of Prof. B. Weynand, Université Catholique de Louvain, St. Luc University Hospital, Brussels, Belgium.)

A typical example is multiple contiguous metastatic nodes at Levels II and III in the neck, which will be associated with a single CTV covering the whole of Levels II and III. Similarly, when sub-GTVs are delineated, for example by a GTV-T (F-Miso-PET) to detect hypoxia, the whole anatomic GTV, for example a GTV-T (CT), is typically surrounded by a common CTV.

When several CTVs are used, it is recommended that an unambiguous terminology corresponding to the GTV denomination be used. For example:

- CTV-T (0 Gy) corresponds to the CTV including the primary-tumor GTV and assumed regions of infiltration as defined before the start of the treatment.
- CTV-T + N (MRI-T2, 30 Gy) corresponds to the CTV for the primary tumor and regional nodes evaluated with a T2-weighted MRI scan after an absorbed dose of 30 Gy. It should be remembered that the CTV does not describe the range of motion of internal anatomy. Knowledge of the CTV motion (and all other geometrical uncertainties) must be taken into account in the PTV delineation (see Section 4.5).

4.4 Internal Target Volume

In ICRU Report 62 (ICRU, 1999), the ITV was defined as the CTV plus a margin taking into account uncertainties in size, shape, and position of the CTV within the patient. Such a margin was called the *internal margin* as opposed to the *set-up margin*. In ICRU Report 62, it was recommended that internal and external margins be added quadratically, but often in practice they are instead added linearly, which can lead to an unacceptably large margin. The ITV might be useful only in clinical situations in which uncertainty concerning the CTV location dominates setup uncertainties and/or when they are independent. The ITV is considered an optional tool in helping to delineate the PTV.

4.5 Planning Target Volume

The concept of PTV was introduced in ICRU Report 50 (ICRU, 1993) and restated in ICRU Reports 62, 71, and 78 (ICRU, 1999; 2004; 2007).

The PTV is a geometrical concept introduced for treatment planning and evaluation. It is the recommended tool to shape absorbed-dose distributions to ensure that the prescribed absorbed dose will actually be delivered to all parts of the CTV with a clinically acceptable probability, despite geometrical uncertainties such as organ motion and setup variations. It is also used for absorbed-dose prescription and reporting. It surrounds the representation of the CTV with a margin such that the planned absorbed dose is delivered to the CTV. This margin takes into account both the internal and the setup uncertainties. The setup margin accounts specifically for uncertainties in patient positioning and alignment of the therapeutic beams during the treatment planning, and through all treatment sessions.

The delineation of the PTV utilizes knowledge of the presence and impact of uncertainties and variations in both the tumor location and machine parameters. In earlier ICRU documents, the possibility of compromising the margins of the PTV if they encroached on OAR was suggested (ICRU, 1999; 2004; 2007), but is no longer recommended. To reduce the CTV-to-PTV margin has always been a temptation. As an example, the CTV-to-PTV margin between the prostate and rectum is often 1 cm, except in the anterior–posterior direction for which it is reduced to spare the rectum (Zelefsky, 1999). It is understandable why one might want to shrink the anterior–posterior margins. In an IMRT planning study, Zhang *et al.* (2006) found that while keeping the absorbed dose to the rectum essentially the same, the prescription absorbed dose could be escalated from 70 Gy to 78 Gy in 2 Gy fractions by reducing the 3D PTV margin from 10 mm to 5 mm. Most of the benefit of rectal

Table 4.2. Selection of the nodal CTV for oropharyngeal squamous-cell carcinoma (Grégoire *et al.*, 2000).

Nodal stage (AJCC, 1997)	Levels to be included in the CTV	
	Ipsilateral neck	Contralateral neck
N0–N1 (in Levels II, III, or IV)	II–III–IV + RP[a] for post-pharyngeal wall tumor	II–III–IV + RP for post-pharyngeal wall tumor
N2a–N2b	Ib, II, III, IV, V + RP	II–III–IV + RP for post-pharyngeal wall tumor
N2c	According to N stage on each side of the neck	According to N stage on each side of the neck
N3	I, II, III, IV, V + RP ± adjacent structures according to clinical and radiological data	II–III–IV + RP for post-pharyngeal wall tumor

[a]Retropharyngeal nodes.
Notes: *Inclusion of level Ib*: any tumor with extension to the oral cavity, *e.g.*, retromolar trigone, mobile tongue, inferior gum, oral side of anterior tonsilar pillar.
Unilateral neck treatment: localized tumor of the tonsil without frank involvement of the soft palate (*i.e.*, tumor extension beyond the intersection of the tonsilar pillars) or the base of tongue.
Retropharyngeal irradiation: systematic irradiation of retropharyngeal lymph nodes irrespective of the N stage for transfixing soft-palate tumors is warranted.
Limit of validity: *T stage*: there are no data to support any adaptation of the recommendations as a function of the stage of the primary tumor.
Post-operative setting: In principle, similar recommendations apply in the post-operative setting, with amendments recently described (Grégoire *et al.*, 2006). This would allow a unilateral neck treatment in case of pN0 on the contralateral side after bilateral neck dissection. However, overall quality control of the neck-node dissection and the pathological examination of the specimen will have to be taken into consideration.

Table 4.3. Selection of the CTV for rectal carcinoma according to T–N stage (recompiled from Gunderson, 2003, in Grégoire *et al.*, 2003d).

T–N stage	Organ or site of adherence or invasion	Tumor or tumor-bed volumes	Nodal volumes
T1–3N1–2	Not applicable	Rectum/rectal bed[a]	Internal iliac, pre-sacral
T4N0	Anterior or posterior	Rectum/rectal bed plus organ/structure involved	Internal iliac, pre-sacral; optional: external/common iliac if anterior adherence
T4N1-2 (anterior adherence or invasion)	Prostate, bladder, uterus, vagina (proximal 2/3)[b]	Rectum/rectal bed plus organ/structure involved	Internal iliac, pre-sacral, external/common iliac[b]
T4N1-2 (posterior/lateral adherence or invasion)	Presacrum or pelvic side-walls	Rectum/rectal bed plus organ/structure involved	Internal iliac, pre-sacral

[a]Primary tumor plus from 3 cm to 5 cm margin.
[b]Inguinal nodes should be included if the distal vagina or anus is involved by direct extension of primary or recurrent tumor.

sparing comes about by reducing the margin in the anterior–posterior direction. The benefit will, however, be real only if the margin reduction is substantiated by experience. However, most evidence indicates that the setup uncertainty in the anterior–posterior direction is larger than in the superior–inferior and lateral directions (Lattanzi *et al.*, 2000; Schubert *et al.*, 2009; Wong *et al.*, 2005). If anything, the margins should be larger in the anterior–posterior direction.

To ensure accurate reporting of absorbed dose to the PTV in cases for which the PTV encroaches or overlaps another PTV, OAR, or PRV, it is now recommended that the delineation of the primary PTV margins should not be compromised. Developments in treatment-planning software now make it possible to achieve sufficient dose sparing of the OAR by using priority rules in optimizer planning systems (see Section 2). Alternatively, subdivision of the PTV into regions with different prescribed absorbed doses (so-called PTV-subvolumes, PTV_{SV}) may be used as indicated in Figure 4.7. Similar methods may also be used in case of overlapping PTVs. The dose reporting should, however, be done for the whole PTV (see Section 3.3). Doing so ensures that reporting underdosage to the PTV adequately reflects a lower probability of adequate absorbed-dose coverage to the CTV.

Although the delineation of the GTV and the CTV is independent of the irradiation technique, the delineation of the PTV is dependent on the technique and is part of the treatment prescription. To avoid significant deviation from the prescribed absorbed dose in any part of the CTV(s), a margin

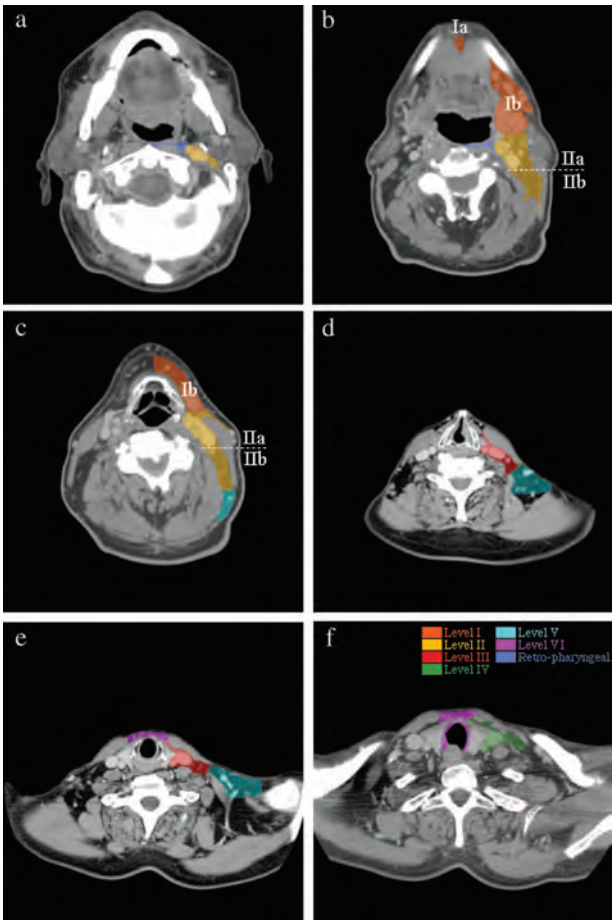

Figure 4.6. Three-dimensional delineation of neck nodes at different levels for head-and-neck squamous-cell carcinoma (SSC). Computed tomographic imaging of a patient with a T1N0M0 glottic SCC (see tumor in panel d). The examination was performed on a dual-detector spiral CT (Elscint Twin, Haifa, Israel) using a slice thickness of 2.7 mm, a reconstruction interval of 2 mm, and a pitch of 0.7 mm. Contrast medium was injected intravenously at a rate of 2 ml/s to a total of 100 ml. Sections were taken at the level of the bottom edge of C1 (panel a), the upper edge of C3 (panel b), mid-C4 (panel c), the bottom edge of C6 (panel d), the bottom edge of C7 (panel e), and mid-D1 (panel f). Neck nodes at each level were drawn on the CT slice using the radiological boundaries published by Grégoire *et al.* (2003c).

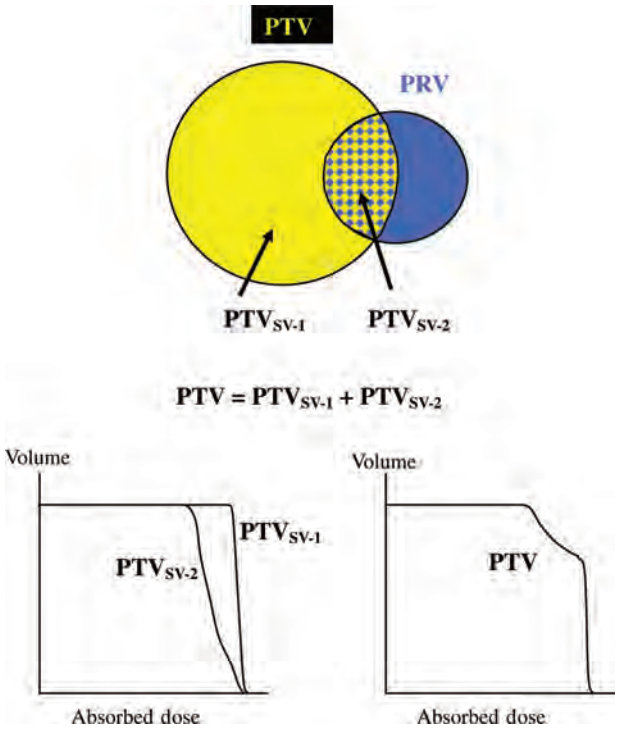

Figure 4.7. Schematic description of the PTV subvolume delineated in case of overlap between the PTV and the PRV (see Section 5.2). This subvolume PTV can be used for planning purposes (beam arrangement and absorbed-dose prescription), but the absorbed dose should be reported for the whole PTV (right DVH). In the case of absorbed-dose compromise in the overlapping region between the PTV and the PRV, reporting the absorbed dose in the sub-PTV, PTV_{SV-1}, (left DVH) can incorrectly represent the absorbed dose to the underlying CTV.

must be added to the CTV taking into account uncertainties and variations in (1) position, size, and shape of the CTV (internal variations), and (2) patient and beam positioning (external variations). These variations occur during a given radiation-treatment fraction, between successive fractions, and between planning and treatment. Figure 4.8 illustrates the movements of the prostate CTV due to changes in rectum filling. Factors affecting internal variations are anatomical site, protocols (*e.g.*, bowel preparations), and patient-specific differences. Factors affecting external variations are methods of patient positioning, mechanical uncertainty of the equipment (*e.g.*, sagging of gantry, collimators, and couch), dosimetric uncertainties (*e.g.*, penetration of the beam), transfer errors from CT and simulator to the treatment unit, and human factors.

The importance of these factors will vary from center to center and within a given center from machine to machine, protocol to protocol, and patient to patient. The use of patient-immobilization devices, the application of quality-assurance programs, and the skill and experience of the radiation therapy technologists or radiation therapy nurses are important and must be taken into account. Also, the use of image-guidance systems or other uncertainty-reduction techniques can significantly alter the size of the required margins.

The PTV concept, which was introduced to deal with geometric variation assuming a relatively static beam, might not adequately address the issue of the interplay between organ motion and intensity modulation. With an intestinal-crypt-cell assay, Gueulette *et al.* (2005) elegantly showed that in using a scanning proton beam to irradiate mice, movement of the small intestine in relation to movement of the pencil beam could result in regions of

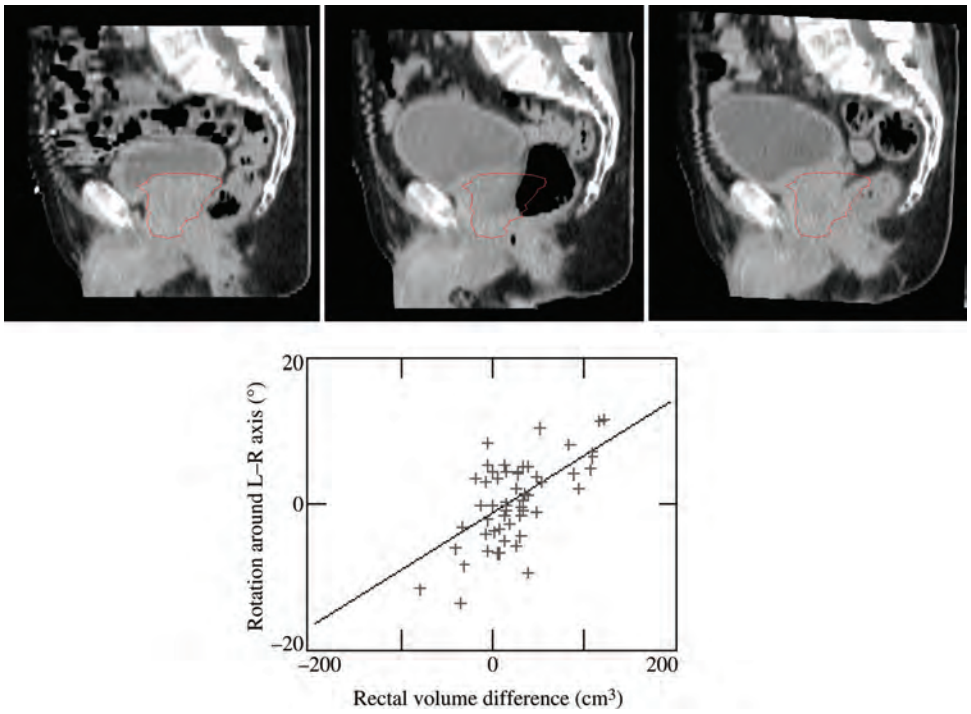

Figure 4.8. Illustration of the impact of rectal volume on prostate CTV displacement. Top row: Sagittal reconstructions of a planning CT (left) and two repeat CT scans (middle and right, matched on the pelvic bone) with the prostate as delineated on the planning CT overlaid in red. Clearly, the prostate rotates in an anterior direction around its apex due to the increased rectal volume: either gas (middle) or stool (right). Bottom row: Correlation between rectal-volume difference and prostate rotation around the left–right axis measured in 11 patients. (Modified from van Herk *et al.*, 1995; reproduced with permission.)

the intestine being significantly under irradiated or over irradiated. Without correction for organ motion, the use of IMRT increases the probability of the interplay effect, in which regions of high or low absorbed dose occur within the PTV (Bortfeld *et al.*, 2004; Gueulette *et al.*, 2005; Kissick *et al.*, 2005).

The PTV margin surrounding the CTV should be three-dimensional. The margin could be defined in any number of directions, but most treatment-planning systems only allow margins to be defined differently in each of the Cartesian dimensions. To determine the CTV–PTV margin, the net effect of all geometrical errors as described earlier should be taken into account. Requiring 100 % confidence for adequately treating the CTV would result in unreasonably large margins. Many authors have proposed approaches to calculate the margins on the basis of systematic and random uncertainties (see Table 4.4).

In some clinical situations (*e.g.*, breast cancer, head-and-neck cancer), the PTV extends close to or even outside the patient's skin because of invasion of tumor or because of the application of a margin. Most dose-computation algorithms cannot accurately compute absorbed dose in buildup regions, which will lead to convergence errors when such algorithms are used in optimization (Jeraj and Keall, 2000). Methods to overcome this limitation, such as PTV sub-division and relaxation of the absorbed-dose objectives for planning, will be discussed in Section 5.

In the future, the concept of a PTV might be utilized in unconventional ways to ensure that the prescribed absorbed dose is delivered to the CTV. Planning systems might include evaluation of the effect of geometrical uncertainties in the objectives and constraints, making the PTV unnecessary for absorbed-dose shaping (Baum *et al.*, 2005). While the PTV might then not necessarily be useful for dose optimization, it should still be delineated and used for the purpose of dose reporting.

4.6 Organ at Risk

The OAR or critical normal structures are tissues that if irradiated could suffer significant morbidity and thus might influence the treatment planning and/or the absorbed-dose prescription.

In principle, all non-target tissues could be OARs. However, normal tissues considered as OARs typically depend on the location of the CTV and/or the prescribed absorbed dose. For example, in the post-operative irradiation of a lower-limb soft-tissue sarcoma, the muscles that are not included in the compartment at risk for microscopic

Table 4.4. Summary of various published recommendations for margins around target volumes (CTV) and OAR (modified from van Herk, 2004).

Author	Region	Recipe	Comments
Bel *et al.* (1996)	PTV	0.7σ	Statistical uncertainties only (linear approximation)—Monte Carlo.
Antolak and Rosen (1999)	PTV	1.65σ	Statistical uncertainties only, block margin?
Stroom *et al.* (1999a)	PTV	$2\,\Sigma + 0.7\sigma$	95 % absorbed dose to on average 99 % of CTV tested in realistic plans.
van Herk *et al.* (2000)	PTV	$2.5\,\Sigma + 0.7\,\sigma$ (or more correctly): $2.5\Sigma + 1.64$ $(\sigma - \sigma_e)$	Minimum absorbed dose to CTV is 95 % for 90% of patients. Analytical solution for perfect conformation.
McKenzie (2000)	PTV	$2.5\,\Sigma + \beta + (\sigma - \sigma_e)$	Extension of van Herk *et al.* (2000) for fringe dose due to limited number of beams. The factor β depends on the beam organization.
Parker *et al.* (2002)	PTV	$\Sigma + \sqrt{(\sigma^2 + \Sigma^2)}$	95 % minimum absorbed dose and 100 % absorbed dose for 95 % of volume. Probability levels not specified.
van Herk *et al.* (2002)	PTV	$2.5 + \Sigma + 0.7\sigma + 3$ mm (or more correctly): $\sqrt{2.7^2\Sigma^2 + 1.6^2\sigma^2} - 2.8$ mm	Monte Carlo based test of 1 % TCP loss due to geometrical errors for prostate patients, fitted for various σ and Σ.
Ten Haken *et al.* (1997), Engelsman *et al.* (2001a, 2001b)	PRV (liver and lung)	0	No margin for respiration, but compensation by absorbed-dose escalation to iso-NTCP, reducing target-dose homogeneity constraints.
McKenzie *et al.* (2000)	PRV	A	Margin for respiration on top of other margins when respiration dominates other uncertainties.
van Herk *et al.* (2003)	PRV (lung)	$0.25\,A$ (caudally); $0.45\,A$ (cranially)	Margin for (random) respiration combined with random setup error of 3 mm SD, when respiration dominates other uncertainties ($A > 1$ cm).
McKenzie *et al.* (2002)	PRV	$1.3\,\Sigma \pm 0.5\,\sigma$	Margins for small and/or serial organs at risk in low (+) or high (−) absorbed-dose region.

Symbols: Σ, standard deviation of systematic uncertainties; σ, standard deviation of statistical (random) uncertainties; σ_e, describes width of beam penumbra fitted with a Gaussian function; A, peak-to-peak amplitude of respiration.

infiltration are considered as OARs, and thus will influence the beam delivery. Fibrosis and edema induced by absorbed dose in these muscles might indeed have a major impact on the treatment morbidity. In contrast, in the head-and-neck area, the paraspinal muscles or the muscles of the posterior neck are typically not considered as OARs, and then would not influence the beam delivery. In some conventional head-and-neck treatments, the mandible and much of the oral mucosa are well outside the field and do not need to be delineated. With IMRT, the mandible and large volumes of mucosa relatively far from target volumes might sometimes receive high absorbed doses. Delineating these volumes has become more common in order to control the absorbed-dose distribution to these tissue structures. The criteria for defining and prescribing absorbed-dose limitations to the OARs will no doubt evolve with time.

From a functional point of view, tissue organization has been conceptually divided into "serial," "parallel," or "serial–parallel" (ICRU, 1993; Withers *et al.*, 1988). Serial organs, or serial-like organs (*e.g.*, spinal cord, nerve, the gastro-intestinal tract), consist of a chain of functional units, which all need to be preserved to guarantee the functionality of the tissue. For instance, in the spinal cord, destruction of a specific nerve bundle will affect all nerve functions downstream from the level of injury. Parallel organs, or parallel-like organs (*e.g.*, lung, parotid), consist of functional units acting independently of each other. For instance, in the lung, destruction of a limited number of alveolar structures will not greatly affect the overall organ function. Breathing capacity will be significantly impaired only when a threshold lung volume has been destroyed. Some organs such as the kidney have a mixed serial and parallel organization. The glomerulus has a more

parallel organization, whereas the distal tubules are more serially organized.

The concept of tissue organization is operationally useful for determining dose–volume constraints and for the evaluation of the dose–volume histograms (DVHs). Indeed, for serial-like organs showing a threshold-binary response, the absorbed dose at or close to the maximum absorbed dose to a given volume is typically the best predictor of loss of function. In contrast, for parallel-like organs showing graded absorbed-dose responses, the mean absorbed dose or the volume that receives an absorbed dose in excess of some defined value have been used as predictors of loss of function.

This concept of tissue organization is also useful for the delineation of OARs. For instance, for the retina or tubular-type organs such as the rectum, it is preferred (but more time consuming) to delineate the wall or surface rather than the full organ. For serial-like organs, as the volume irradiated can have less impact on the assessment of the organ tolerance, the extent to which these organs are delineated will probably have a lesser importance for the patient's treatment (see Figure 4.9). However, to allow comparison between centers, it is very useful to follow guidelines, *e.g.*, to delineate the spinal cord for head-and-neck tumors from its junction with the brain stem to the first dorsal vertebra, and for prostate cancer to delineate the rectum starting at the anus up to the position at which the rectum turns horizontally into the sigmoid colon. In contrast, for parallel-like organs, the volume assessment is crucial, and complete organ delineation is required (see Figure 4.10). In all instances, the volume of the organ delineated should be recorded. This is particularly important when DVHs are reported in terms of relative volumes.

Intensity-modulated radiation therapy treatments result in more heterogeneous absorbed-dose distributions in normal tissues and larger volumes of normal tissues irradiated, each tissue presenting with different responses. Thus the optimization process requires enhanced consideration of biological response of normal tissues. Dose–volume constraints for OARs are mainly derived from retrospective clinical observations, which have been translated into normal-tissue complication probability (NTCP) curves (see Section 3.7.2) (Burman *et al.*, 1991; Emami *et al.*, 1991; Kutcher *et al.*, 1991). The majority of the data come from clinical literature of the 1970s and 1980s, *i.e.*, from the pre-3D-imaging era and therefore with less reliable dose and volume information. It is only more recently that prospective studies have systematically looked at the relationship between absorbed dose, volume, and normal-tissue complications for patients treated with 3D-CRT or IMRT (Adkison *et al.*, 2008; De Ruysscher *et al.*, 2008). More data would greatly improve our confidence in setting dose–volume constraints before running the dose optimizer. As an example, it has been reported for the parotid glands that after receiving a mean absorbed dose of from 26 Gy to 39 Gy, the secretion return to near normal 1 year after treatment (Eisbruch *et al.*, 1999). In conventional fractionation schemes (*i.e.*, 2 Gy per fraction per day) for the whole liver, a mean absorbed dose less than 30 Gy appears tolerable, and no absorbed-dose limit has been defined when less than 25 % of the liver is irradiated (Dawson *et al.*, 2002). Additional

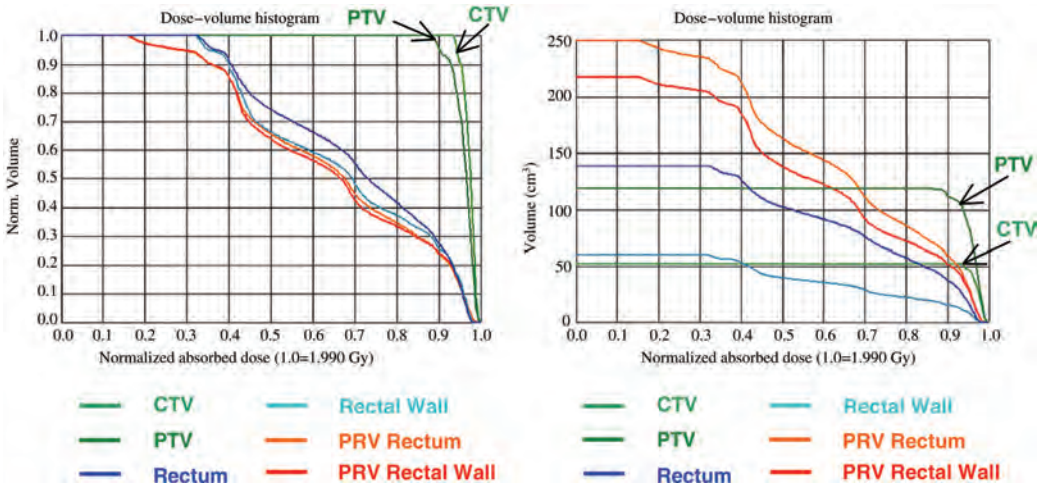

Figure 4.9. Relative (left) and absolute (right) cumulative DVHs for a prostate-cancer case. The rectum and the rectal wall were delineated 3 cm more caudally and cranially than the prostate. The volumes were normalized separately. The DVHs for the rectum and rectal wall are different, although the difference is minimal for their respective PRVs. The margin on the PRV was 0.5 cm as was the margin between the PTV and the CTV. The PRV margin for the rectal wall was applied only on the outside of the rectal OAR.

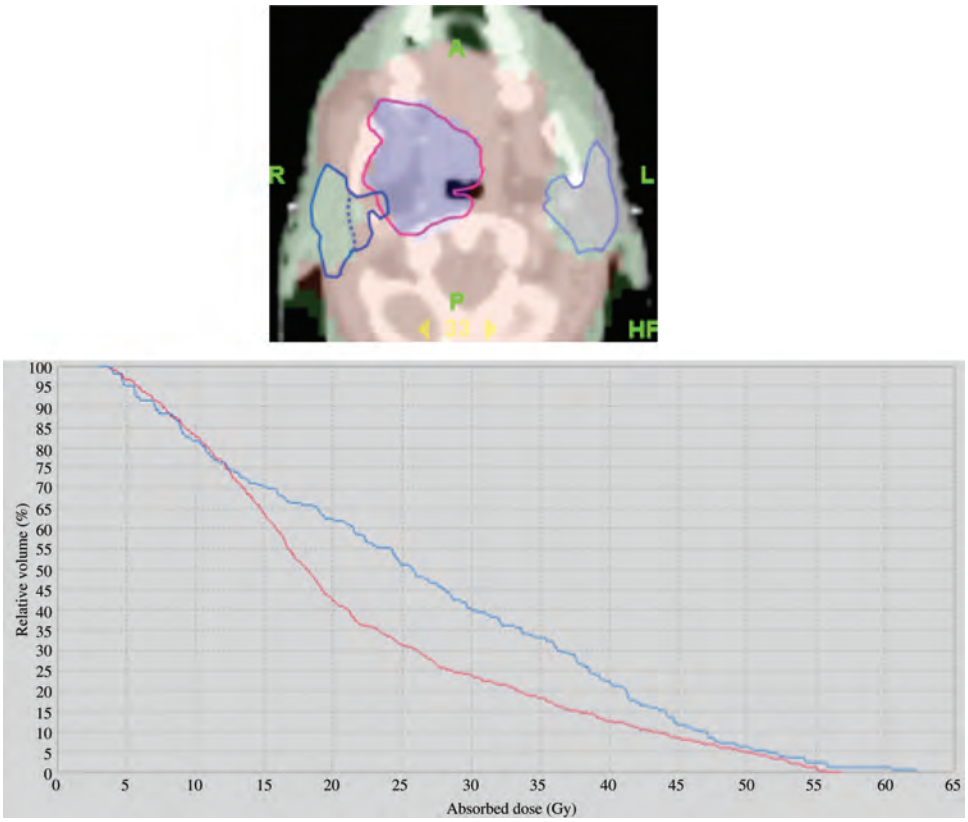

Figure 4.10. Comparison of the absorbed-dose distribution in the whole right parotid gland and the superficial lobe for a T2–N0–M0 squamous-cell carcinoma of the right tonsillar fossa. The relative volume is normalized to the volume of the region of interest and expressed as a percent. Top panel: the PTV associated with the primary-tumor CTV is delineated in red. The right and left parotid glands are delineated in dark and light blue, respectively. The dashed line in the right parotid gland separates the superficial lobe from the deep lobe. The patient was treated with a Hi-Art Tomotherapy system. A median absorbed dose ($D_{50\ \%}$) of 65 Gy was prescribed to the PTVs associated with the primary tumor. The blue, pink, and green areas represent the 62.5 Gy, 35 Gy, and 25 Gy isodose curves, respectively. Bottom panel: DVH of the whole right parotid gland (blue curve) and of the superficial lobe (red curve). The mean absorbed doses reached 26.5 Gy and 21.8 Gy for the whole parotid and the superficial lobe, respectively.

data have been derived for the brain, heart, rectum, and lung (Gagliardi *et al.*, 2001; Levegrün *et al.*, 2001; Rancati *et al.*, 2003; Seppenwoolde and Lebesque, 2001). If the absorbed dose per fraction or the total number of fractions is significantly changed from conventional schedules (form 1.8 Gy to 2 Gy per fraction, ≈35 fractions), the tolerance absorbed doses might have to be re-evaluated (Timmerman, 2008).

4.7 Planning Organ at Risk Volume

As is the case with the PTV, uncertainties and variations in the position of the OAR during treatment must be considered to avoid serious complications. For this reason, margins have to be added to the OARs to compensate for these uncertainties and variations, using similar principles as for the PTV. This leads, in analogy with the PTV, to the concept of PRV.

A margin around an OAR with a serial-like structure *(e.g.*, spinal cord) is more clinically relevant than that around an OAR with a parallel-like structure (*e.g.*, liver, lung, parotid). Note that delineation of the PTV and the PRV will often result in one or more overlap regions. It is recommended that the margins not be compromised for the PTV or PRV even if overlaps occur. To ensure sufficient normal-tissue sparing, priority rules in the planning system can be used or the PTV or PRV can be subdivided into regions with different absorbed-dose constraints. In any case, it is recommended that the absorbed dose be reported in the full PRV and PTV.

For reporting, it is recommended that, as for the PTV, the PRV be described by including the size of the margins applied to the OAR in different directions. As for the PTV, many authors have proposed approaches to calculate the OAR–PRV margins on the basis of systematic and random uncertainties (see Table 4.4).

4.8 Treated Volume

Because of the limitations of irradiation techniques, the volume receiving the prescribed absorbed dose might be different than the PTV; it might be larger (sometimes much larger) or smaller, and in general more simply shaped (less so with IMRT than with conventional or three-dimensional radiation therapy). This leads to the concept of the TV (ICRU, 1999). The TV is the volume of tissue enclosed within a specific isodose envelope, with the absorbed dose specified by the radiation oncology team as appropriate to achieve tumor eradication or palliation, within the bounds of acceptable complications. As proposed in proton therapy (ICRU, 2007), $D_{98\ \%}$ could be selected to determine the TV in photon therapy. When reported, the value of the isodose selected to define the TV should be quoted either relative to the prescribed absorbed dose or in absolute terms. It is important to identify the shape, size, and position of the TV in relation to the PTV for several reasons. One reason is to provide information to evaluate causes for local recurrences (inside or outside the TV).

4.9 Remaining Volume at Risk

Ideally when delineating the OAR, especially for IMRT, all normal tissues that could potentially be irradiated should be outlined. The imaged volume within the patient, excluding any delineated OAR and the CTV(s), should be identified as the RVR. The RVR is operationally defined by the difference between the volume enclosed by the external contour of the patient and that of the CTVs and OARs on the slices that have been imaged.

The RVR is of importance in evaluating plans as it will be affected by the absorbed dose it receives and, if it not specifically evaluated, there could be unsuspected regions of high absorbed dose within the patient that would otherwise go undetected. In addition, the absorbed dose in the RVR might be useful in estimating the risk of late effects, such as carcinogenesis. Therefore, contouring the RVR is especially important for younger patients who can expect a long life span. Looking for high-dose regions using a DVH of the RVR is, however, no substitute for a thorough analysis, on a slice-by-slice basis, to examine the absorbed-dose distribution for all beam paths.

Journal of the ICRU Vol 10 No 1 (2010) Report 83
Oxford University Press
doi:10.1093/jicru/ndq010

5. Planning Aims, Prescription, and Technical Data

5.1 Introduction

Earlier ICRU Reports 50, 62, 71, and 78 (ICRU, 1993; 1999; 2004; 2007) described the process of treatment specification and treatment "prescription" for external-beam therapy. Generally, the process starts with a specification of the desired absorbed dose to various delineated volumes of interest. This was often referred to as the "prescription." When the treatment techniques were simple and easily defined, and the anticipated distributions of absorbed dose similarly simplistic, the prescription was often easily achieved. With the introduction of IMRT and developments in treatment planning, the distribution of absorbed dose to multiple volumes could be prioritized and tailored through an iterative process, referred to as optimization. The prescription is the finally accepted set of values of the modified planning aims in the treatment plan after an optimization process.

This process of developing a treatment plan is shown schematically in Figure 4.1. As shown in this figure, the process consists of three major components: (1) the definition and description of the "planning aims" using image-based information from which all of the volumes of interest are delineated and the desired absorbed-dose levels are specified; (2) a complex beam delivery "optimization" process to achieve and, if needed, modify the initial "planning aims"; and (3) a complete set of finally accepted values, which becomes the "prescription" and, together with the required "technical data" represent the "accepted treatment plan." This process is the responsibility of the treating physician. Hence, in this report and as shown in Figure 4.1, the accepted treatment plan now comprises the final treatment prescription, plus all of the technical data needed to achieve it.

5.2 Planning Aims

The planning aims are dosimetric goals used to develop the treatment plan (see, *e.g.*, Figure 5.1.). Goals can be defined for any specified volume including the planning target volumes (PTVs) and the planning organ-at-risk volumes (PRVs), for which constraints might be needed. Often data on desired absorbed doses and planning constraints to begin the planning process are described in planning protocols.

The use of multiple dose–volume constraints (*e.g.*, D_{mean}, $D_{98\ \%}$, $D_{95\ \%}$, $D_{2\ \%}$, ...) (see Sections 3.2 and 3.3) for each defined volume leads to more precision in the planning aims and is therefore recommended. Analysis of treatment outcome in terms of tumor control and normal-tissue toxicity as a function of absorbed dose and absorbed-dose distribution provides values for desirable dose–volume indices, such as D_V (absorbed dose in fraction V of the volume) and V_D (volume receiving at least an absorbed dose D). These are useful parameters that can be used for planning aims. For example, in treating prostate carcinoma, Boersma *et al.* (1998) suggest a set of dose–volume constraints to avoid damage to the rectum wall: no more than 40 % of the PRV should exceed 65 Gy, and no more than 30 % should exceed 70 Gy, and no more than 5 % should exceed 75 Gy. For study purposes, biological metrics (*e.g.*, tumor-control probability, normal-tissue-complication probability, and equivalent uniform dose) might be used as additional constraints to help in achieving a more desirable absorbed-dose distribution. However, it must be borne in mind that these models are inherently a simplification of the biological reality and remain to be validated on a large scale. Presently, their use should probably be restricted to dose reporting instead of absorbed-dose prescription. A more comprehensive description of these models is presented in Sections 3.7.2 and 3.7.3.

In the process of optimization, the priority of one constraint over another and/or the priority of one volume over another are specified by parameters that quantitatively weight the set of priorities (see Section 2.3). The priority ranking is a clinical decision that might be described in a clinical protocol. To initiate the planning process, planners sometimes use so-called artificial dose–volume

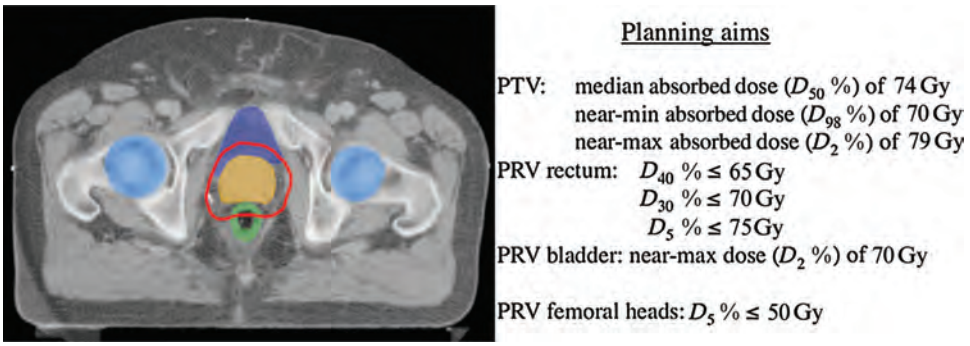

Figure 5.1. Planning aims for treatment of a prostate adenocarcinoma. Color legend is: the CTV in orange, the PTV in red, the PRV rectum in green, the PRV bladder in dark blue, and the PRV femoral heads in light blue. The PTV overlaps with the PRV rectum and the PRV bladder giving rise to conflicts in the planning aims. Resolution of these conflicts is achieved by selecting various sets of priorities for the PTV and the PRV and/or by using different dose-constraints on the overlapping region between the PTV and the PRVs. D_V is defined as the absorbed dose in fraction V of the volume.

constraints, which can be different from the desired ones or from clinically relevant absorbed-dose constraints. The dose–volume constraints are modified iteratively to achieve the best plan. For example, to encourage absorbed-dose homogeneity in the target volume, planners can initially set the same numerical value, different from the desired prescribed absorbed dose, for the minimum, median, and maximum absorbed doses to the PTV to initiate the planning process, and concentrate on lowering the absorbed dose to the organs at risks. Thereafter, the treatment planners typically modify the objective-function parameters to steer the solution toward a clinically acceptable one (see Figure 2.3).

In practice, the initial planning aims (which should always be recorded) might be physically impossible to achieve, *e.g.*, absorbed-dose gradients that are too steep, a PTV region that extends into air (outside the body contours), or internal conflicts, such as absorbed doses delivered in an intersection volume between the PTV and the PRV. Thus, the set of constraints and objectives are not fixed but can evolve to achieve an acceptable plan in accordance with the treatment aims.

5.3 Special Situations Illustrating the Use of Planning Aims

The clinical situations described below illustrate the application of the concept of planning aims when the desired absorbed dose might be difficult to achieve:

1. Planned absorbed dose in the buildup region and in a PTV extending outside the body contour.
2. Overlapping volumes and conflicting absorbed-dose objectives.
3. Unexpected high absorbed dose to part of the remaining volume at risk (RVR).

5.3.1 Dose Planning in the Buildup Region and in a PTV Extending Outside the Body Contour

In cases for which the tumor or clinical target volume (CTV)-to-PTV margin approaches the surface of the skin, part of the PTV can extend into the buildup region of incident photon beams or even into the surrounding air (so-called in-air PTV). Most dose-computation algorithms cannot accurately compute absorbed dose in buildup regions. This will lead to a convergence error, *i.e.*, the optimizer does not reach a global minimum for the objective function (Jeraj and Keall, 2000). Pursuing a planning aim in air outside the skin contour is clinically relevant if sufficient fluence in the surrounding air is needed to prevent the CTV from extending outside the beam edge either by movement or by virtue of setup error. In tangential breast irradiation, the region of the beam that has been deliberately planned to bypass the skin surface has been called the "flash region" (Evans *et al.*, 2000). The term “flash” can also be used for other sites for which extension of the PTV outside the skin surface requires sufficient fluence in surrounding air.

In planning optimization, at least three problems must be considered regarding buildup and in-air PTV regions. First, it might be difficult to achieve the desired absorbed dose in the regions of the PTV close to or outside the patient’s outline, in buildup areas or in air. Second, the optimization algorithm might attempt to increase the absorbed dose in these PTV regions by creating fluence peaks in beams with suitable directions. This often leads to unacceptably inhomogeneous PTV absorbed-dose distributions or regions of high absorbed dose elsewhere. Third, removing the part of the PTV in air or bounding the PTV expansion by the skin contour (for which some planning systems have automated algorithms) avoids irrelevant optimizing of

absorbed dose in air, but is not a solution as a "flash region" will not be created during optimization. Two solutions can be envisaged to allow the PTV concept to be modified:

- *Planning-target-volume subdivision and relaxation of the planning aims*: If underdosage of the CTV near the skin is clinically unacceptable, a bolus needs to be applied as would be done in conventional radiotherapy. If underdosage in the buildup region is clinically acceptable, two different planning strategies could be followed. One method is based on subdivision of the PTV into a number of subvolumes (SVs) (see Figure 5.2.), while in the other method the acceptable absorbed-dose range of the PTV planning aim is relaxed. In the subdivision method, the PTV is divided into two or more SVs so that a region and a degree of acceptable underdosage can be described in that region. The second method, increasing the acceptable absorbed-dose range for the whole PTV, has the drawback of lacking spatial control over the underdosed region.
- *Flash region*: PTV subdivision or relaxed absorbed-dose objectives for planning do not solve the problem of fluence peaks extending beyond the treatment area. In breast IMRT, for example, various methods based on manual definition of beam apertures and beam intensities have been proposed for adequate treatment of the flash region (Evans *et al.*, 2000; Hong *et al.*, 1999; Kestin *et al.*, 2000). It is beyond the scope of this report to discuss these methods in detail. Figure 5.3. presents an example of a treatment of breast cancer with tangential fields, in which intensity values from the breast periphery are extrapolated to the regions of the PTV outside the beam's eye view of the breast.

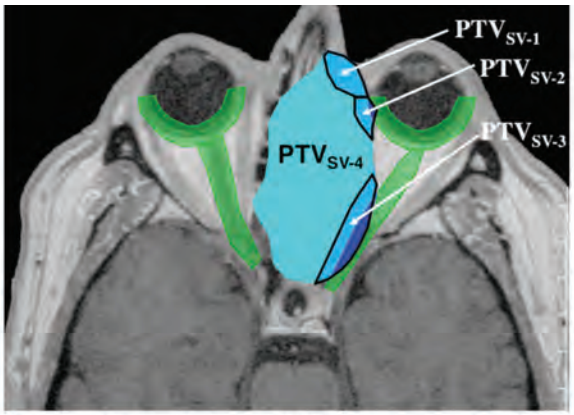

Planning aims		Modification to planning aims	
PTV		PTV	
median dose (D_{50} %):	70.0 Gy	PTV_{SV-1}	
near-min dose (D_{98} %):	≥ 66.5 Gy	near-max dose (D_2 %):	≤ 74.9 Gy
near-max dose (D_2 %):	≤ 74.9 Gy	near-min dose (D_{98} %):	≥ 66.5 Gy
Optic nerves		PTV_{SV-2}	
near-max dose (D_2 %):	≤ 60.0 Gy	near-max dose (D_2 %):	≤ 50.0 Gy
Retina		near-min dose (D_{98} %):	≥ 49.0 Gy
near-max dose (D_2 %):	≤ 50.0 Gy	PTV_{SV-3}	
		near-max dose (D_2 %):	≤ 60.0 Gy
		near-min dose (D_{98} %):	≥ 58.0 Gy
		PTV_{SV-4}	
		median dose (D_{50} %):	70.0 Gy
		near-max dose (D_2 %):	≤ 74.9 Gy
		near-min dose (D_{98} %):	≥ 66.5 Gy
		PRV optic nerves	
		near-max dose (D_2 %):	≤ 60.0 Gy
		PRV retina	
		near-max dose (D_2 %):	≤ 50.0 Gy

Figure 5.2. Planning process for the treatment of an ethmoid-sinus adenocarcinoma. Color legend is: the PTV in blue, and the PRV for optic nerve and retina (retina and optic nerves + 2 mm margin) in green. The planning aim leads to a conflict between the near-maximum absorbed dose ($D_{2\ \%}$) to the PRV (50 Gy for the retina and 60 Gy for the optic nerves) and the near-minimum absorbed dose ($D_{98\ \%}$) to the PTV (66.5 Gy). To resolve these conflicts, the PTV was subdivided in four SVs (PTV_{SV-1} to PTV_{SV-4}) to which different dose–volume constraints were applied. The PTV_{SV-1} consists of the parts of the PTV that are within 5 mm of the skin or extend outside the skin in air. The planner should secure sufficient fluence in PTV_{SV-1} to prevent the CTV from being underdosed by movements or setup error. The PTV_{SV-2} consists of the parts of the PTV that overlap with or are closer than 3 mm to the PRV of the retina. A $D_{near\text{-}max}$ of 50 Gy was given to the PTV_{SV-2} to prevent overdosage to the retina. The PTV_{SV-3} consists of the parts of the PTV that overlap or are closer than 3 mm from the PRV of the left optic nerve. A $D_{near\text{-}max}$ of 60 Gy was given to the PTV_{SV-3} to prevent over-dosage to the optic nerve. The PTV_{SV-4} is not subject to any specific constraints, and the original planning aim can be applied. To achieve a minimum absorbed dose of 66.5 Gy in PTV_{SV-4} while respecting the 50 Gy and 60 Gy absorbed-dose constraints of the PRVs of retina and optic nerves, respectively, the optimizer must generate a sharp absorbed-dose gradient between the PRVs and PTV_{SV-4}.

5.3.2 Overlapping Volumes and Conflicting Planning Aims

As discussed in Section 4.5 and shown in Figure 4.7, overlap between different PTVs, between the PTV and the PRV, and between different PRVs leads to a volume that is shared by two or more contoured volumes. A conflict can occur if the planning aims of the overlapping contoured volumes lack a common desired absorbed-dose range. To ensure that the conflict does not occur in the planning aims, at least two different methods can be applied. One method is based on subdivision of the volumes (see Figure 5.2.). Absorbed-dose objectives are set for the individual segments, some of which contain the overlapping volumes (PTV_{SV-2} and PTV_{SV-3} in Figure 5.2.) while others contain non-overlapping volumes (PTV_{SV-4} in Figure 5.2.). In the other method, the absorbed-dose objectives for planning are relaxed for one or more of the contoured volumes that exhibit overlap regions. Both methods aim for the same result, namely a controlled

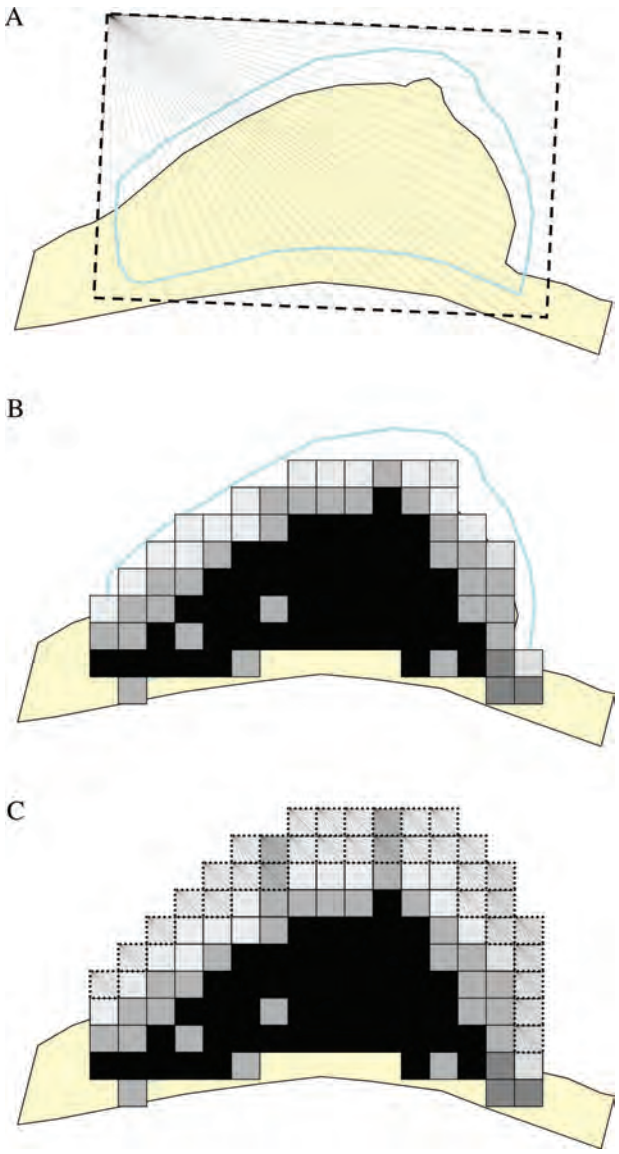

Figure 5.3. Securing the "flash region" in IMRT. (A) Beam's eye view (BEV) of a conventional tangential field (dashed outline). The blue contour shows the PTV extending outside the breast to secure flash; (B) IMRT optimization is performed on the part of the PTV a few millimeter inside the skin surface to avoid (unwanted) absorbed-dose compensation in the build-up region by the optimizer. No intensity is assigned to beamlets projecting outside the BEV of the breast into the PTV; thus flash is not secured; (C) Creation of flash by extending the same intensity values from the breast periphery to the regions of the PTV outside the breast BEV.

underdosage of a volume inside the PTV, a controlled overdosage of a volume inside the PRV, or both. By changing the importance of the constraints, it is possible to go from an underdosage in the PTV to an overdosage in the PRV, or any result between these extremes. Both methods can be used simultaneously in the same planning case. Both methods require priority ranking, a clinical decision that should, ideally, be specified in the planning protocols. These methods enable the PTV and PRV delineation to be maintained without compromise. Whatever the method used, treatment-planning systems should be able to deal with voxels belonging to two different volumes of interest.

5.3.4 Unexpected High Absorbed Dose to the RVR

When absorbed-dose objectives for planning are imposed for PTVs and PRVs only, an unacceptably high absorbed dose can occur in the RVR (for a discussion of RVR, see Section 4.9). Because IMRT planning systems exploit many degrees of freedom to optimize an absorbed-dose distribution according to the planning aims, if the absorbed dose to the RVR is unconstrained, it is even possible that the maximum absorbed dose of the plan can be found in it. The problem and some solutions have been described in the literature (Claus *et al.*, 2001; Dogan *et al.*, 2002; Esthappan *et al.*, 2004). The absence of an absorbed-dose prescription to the RVR can result in two types of problems, namely regions of high absorbed dose and/or gentle absorbed-dose gradients between the PTV and the RVR. To avoid these difficulties, planning aims should be applied as recommended for the PRV, as the RVR is analogous to an additional PRV.

5.4 Treatment Plan

5.4.1 Prescription

When the optimized absorbed-dose distribution is accepted by the physician, the prescription and technical data are finalized. The treatment plan includes the final prescription as well as all technical data required for treatment delivery. The prescription is a description of the volumes of interest, the absorbed dose and/or dose–volume requirements for the PTV, the fractionation scheme, the normal-tissue constraints, and the absorbed-dose distribution(s) planned. The choice between plan improvement and plan acceptance is often based on trade-offs among conflicting aims. The prescription, while considered acceptable, can be different from the original planning aim (see Figure 4.1). Regarding the absorbed-dose prescription to the PTVs, it is recommended here that the same metrics used for reporting be used for prescribing, *e.g.*, to prescribe a given D_{median} or a given D_V (see Sections 3.2 and 3.3).

5.4.2 Technical Data

When a plan is accepted, the technical data needed to execute the treatment are established. The technical data consist of an electronic

instruction file (*e.g.*, control-point sequence) to control the treatment machine and written instructions on how to treat the patient. Examples of technical data are:

- the number of beams and their directions, the number of beam segments and their intensity distributions, *etc.*;
- the aperture shapes or multileaf-collimator settings, *etc.*;
- the number of monitor units per beam segment, *etc.*;
- the positioning and immobilization parameters for the patients on the couch, *etc.*

Physician approval of a given plan implies approval of the technical aspects of the treatment. This is the case because if the technical factors were altered the treatment would almost certainly no longer fulfill the prescription. The technical factors can include extensive data files, which cannot be effectively inspected by the eye. It is recommended that the format for the electronic recording of data is standardized, *e.g.*, the DICOM-RT protocol (DICOM is managed by the Medical Imaging and Technology Alliance—a division of NEMA, the Association of Electrical and Medical Imaging Equipment Manufacturers, Rosslyn, VA, USA). Extensive quality-assurance measures are thus needed to ensure that the technical factors linked with the plan are indeed used for the treatment. These aspects are discussed in Appendix A.2.

Local and national laws and regulations might require that additional personnel (*e.g.*, a medical physicist) as well as the treating physician approve (with the date) the technical component of the prescription.

Journal of the ICRU Vol 10 No 1 (2010) Report 83
Oxford University Press
doi:10.1093/jicru/ndq011

Appendix A: Physical Aspects of IMRT

A.1 Absorbed-Dose Computation

A.1.1 Photon Interactions and Energy-Deposition Processes

When compared with conventional radiotherapy, intensity-modulated radiation therapy (IMRT) requires more attention to several aspects of dose-computation models. The processes of beam generation and shaping in the treatment machine and the subsequent energy-deposition in the patient are quite complex. Some confusion in discussions of photon-beam absorbed-dose calculations comes from the use of terms that are not unambiguously defined. An illustrative example is "scatter," which can refer to any quantity related to scattered radiation, not distinguishing whether the scattering takes place in the beam-delivery system or in the patient. For clarity, it is beneficial to separate the description into what takes place in the beam-delivery system and what results from interactions within the patient (see Figure A1.1). In this Report, the term direct radiation is used to denote radiation generated in the x-ray target that reaches the patient directly without further interaction in the head of the treatment unit; the term indirect, or extrafocal, radiation denotes radiation that has a history of interaction/scattering in the head of the treatment unit. Inevitably photon interactions in the treatment head yield an electron-contamination component. The direct and indirect radiation, together with the electron contamination, constitutes the incident beam.

Photons that have interacted in the head of the treatment unit yield two major absorbed-dose components in the patient: absorbed dose from indirect photons and absorbed dose from electron contamination. Absorbed dose from indirect photons originating in the head, depending on beam energy and head design, accounts for from 2 % to 15 % of the total absorbed dose in the patient (Ahnesjö, 1994; 1995; Liu *et al.*, 1997a; 1997b). The indirect sources act as extended sources causing the penumbra of the field to be substantially broader than the direct-beam penumbra. A conventional jaw or custom-made radiation block usually has faces oriented parallel with a line from the effective source of direct radiation and therefore reduces the production of indirect photons. Some multileaf collimator (MLC) vendors do not use leaf ends that diverge from the effective source position but instead curve the leaf ends. This design prevents a sharp discontinuity of the correspondence between the light and radiation field and is simpler to implement mechanically. Compared with divergent leaves, the curved leaves have increased photon transmission, give rise to a blurred field boundary, and produce indirect photons and charged-particle (mainly electrons) contamination. The dose-computation algorithm has to be able to accurately calculate the absorbed dose under these curved leaf ends. Such calculations can be done in a number of ways, including having the energy fluence description appropriately blurred to account for the unsharp penumbra. In IMRT, a typical field is made up of a large number of smaller segments or sub-fields. The more sub-fields or aperture segments that are added together, the more important becomes the modeling of the direct-beam penumbra, leakage through the collimator system, and the indirect photons.

The amount of charged-particle contamination is very sensitive to the presence of scattering material. The charged-particle component has a limited penetration depth and thus contributes to absorbed dose only in the buildup region and slightly deeper. Therefore, dosimetry protocols state that beams should be calibrated at a depth beyond the range of charged-particle contamination (Almond *et al.*, 1999; IAEA, 2000).

Photons are indirectly ionizing particles that deposit most of their energy through secondary charged particles liberated in photon interactions with the exposed medium. The energy imparted by charged particles released from first interactions in the patient of photons from the incident beam constitutes the primary absorbed dose. For photon beams used in radiation therapy, the effective range in water of the released charged particles is approximately from 0.3 cm to 2.5 cm, causing the primary absorbed-dose distribution to resemble a blurred

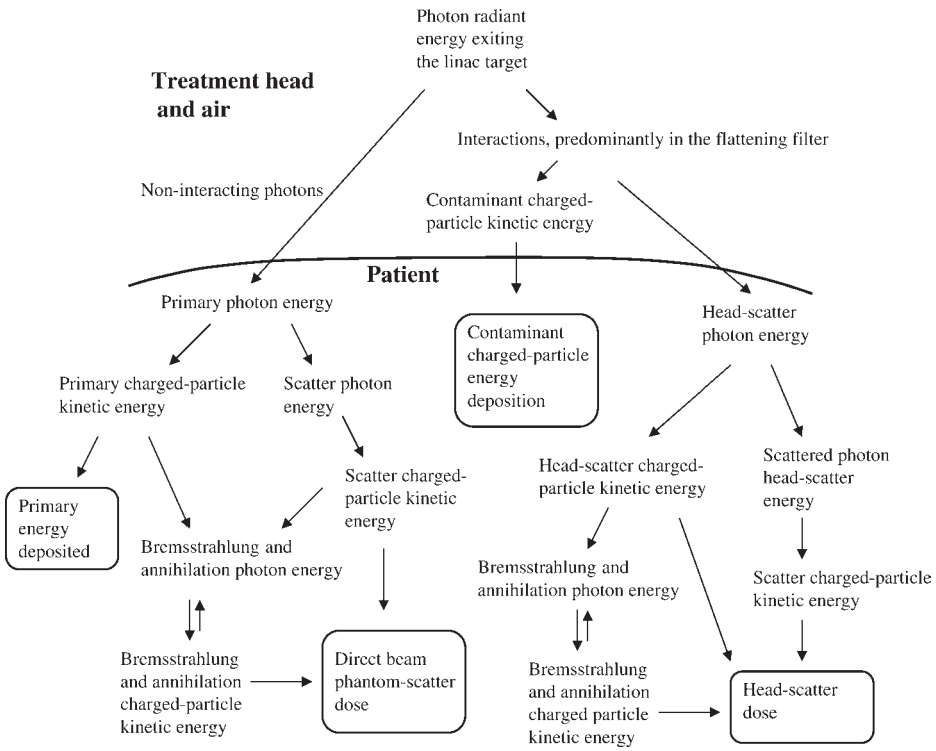

Figure A.1.1. Outline of the interaction history for the two main categories commonly referred to in absorbed-dose calculations for treatment planning: direct and indirect radiation. The direct absorbed dose can be divided into primary-beam absorbed dose and primary-beam phantom-scatter absorbed dose. The indirect radiation can be divided into contaminant charged-particle and indirect-photon absorbed dose. The particle nature of photons is assumed. (Adapted from Ahnesjö and Aspradakis, 1999; Mackie *et al.*, 1988; reproduced with permission.)

image of the incident beam fluence. A drastic change in absorbed dose for small changes in field size occurs when the field size is as small as those encountered in IMRT. In low-density material, the range of the charged particles can be many times longer than in water thereby exacerbating the effect. Figure A1.2 compares absorbed-dose distributions from a parallel x-ray field from a 4 MV linac in a heterogeneous slab phantom for a variety of circular field sizes. More significant perturbations in absorbed dose would result at small field sizes for higher energy beams because the range of charged particles would be even longer. Intensity-modulated radiation therapy demands the ability to determine the absorbed dose accurately for small fields, especially for heterogeneous tissues.

The photons scattered in the patient add, through the secondary charged particles, a smoothly varying patient- or phantom-scatter absorbed-dose component reaching laterally well outside the beam edge. The mean free path of a scattered photon in the patient is of the order of from 10 cm to 25 cm; hence there is a substantial absorbed dose at a considerable distance from the beam edge. The ratio of phantom-scatter to primary absorbed dose increases with depth. However, at therapeutic depths the primary absorbed dose is at least two to five times higher than the phantom-scatter absorbed dose. The phantom-scatter absorbed dose increases with field size.

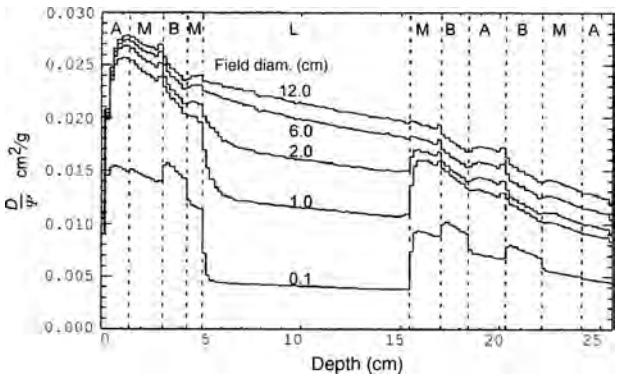

Figure A.1.2. Influence of field size on the depth-dose in a heterogeneous phantom. Shown is absorbed dose per energy fluence along the central axis of a 4 MV parallel beam as a function of depth and beam diameter computed using the convolution/superposition algorithm. The phantom is a slab phantom comprising adipose tissue (A), muscle (M), bone (B), and lung (L). The absorbed-dose reduction in the lung (L), more pronounced at smaller field sizes, is due to the transport of electrons out of the irradiated region in the low-density material. (From Ahnesjö and Aspradakis, 1999; reproduced with permission.)

A.1.2 Modeling the Beam

There are two general classes of dose-calculation algorithms: correction-based and model-based. In the correction-based approach, the absorbed dose in a water phantom from a rectangular beam incident normally on the surface of the phantom is first measured and parameterized into absorbed-dose distributions as functions of the distance from the source to the surface of the phantom, field size, depth, and lateral position. This parameterization is then corrected for plan-specific perturbations of the ideal water phantom measurements. The corrections are necessitated by the presence of beam blocks, wedges, or compensators, and because the beam may not be incident normally on a flat surface and the tissues are not well simulated by water. In a model-based algorithm, measurements of the absorbed-dose distributions for a variety of situations are used to develop parameters for a model that describes the attenuation of incident photons and the production of secondary radiation (Ahnesjö and Aspradakis, 1999; Liu *et al.*, 1998; Mackie *et al.*, 1995; 1996; 2000; 2001). A growing number of authors have addressed the importance of relevant beam modeling for accurate absorbed-dose calculations (Ahnesjö, 1994; 1995; Fippel *et al.*, 2003; Jeraj *et al.*, 2004; Kim *et al.*, 2001; Libby *et al.*, 1999; Liu *et al.*, 1997a; 1997b; Lovelock *et al.*, 1995; Mohan *et al.*, 1985). A useful beam model should be simple enough to understand and implement, and should have only a small number of free parameters. It should be possible to determine the model parameters by practical measurements, and the model should be sophisticated enough to validate all clinically relevant benchmarking measurements in accordance with accuracy requirements (Fippel *et al.*, 2003). The simplest possible beam model is a point source located at the beam target. This approach implicitly provides inverse-square corrections for source-to-surface distance shifts, and was the basis for most early treatment-planning systems whose absorbed-dose calculations were based on a library of measured data.

To model more complex properties (*i.e.*, output factors, profile changes, penumbra variations, *etc.*), a simple single-source model is insufficient. Hence, multi-source models have been developed that consider multiple sources of photons such as scatter from any field-flattening filter and partial blocking of extended sources (Liu *et al.*, 1997a; 1997b). Typically, the primary-beam source is treated as a Gaussian distribution from two sources. The first source has a full width at half maximum (FWHM) of a few millimetres to take into account the production of direct photons in the target. A secondary low-intensity source, with a FWHM equal to that of the flattening filter, takes into account the scatter from the primary collimator and flattening filter. The shape of, and hence the attenuation by, the flattening filter determines fluence-output variations across the filter due to indirect photons arising from it. Intensity-modulated radiation therapy absorbed-dose calculations could be simplified and there would be less scatter from the head if the field-flattening filter were removed (Mackie *et al.*, 1993; Vassiliev *et al.*, 2006). The location and nature (conventional jaws *versus* curved-leaf-end collimators) of the primary-beam collimation determines the beam width and the penumbra. Advanced refinements in the dose-computation algorithm must include the effects of monitor backscatter, collimator scatter, collimator leakage, and charged-particle contamination.

Monte Carlo codes, such as the BEAM code, enable detailed simulations of the treatment head (Liu *et al.*, 2000; Rogers *et al.*, 1995). The result of such Monte Carlo simulations is typically a "phase space," *i.e.*, a data set providing a listing of energy and direction of millions of emitted particles. The phase-space data are often parameterized for convenience. An example is provided in Figure A1.3 (Chaney *et al.*, 1994), which shows the origin of photons derived from the phase-space data projected onto a plane through the beam axis. The role of measured data can be for verification of the Monte Carlo models, or the complete basis for source parameterization, or a combination of the two. Hence, different routes for constructing beam models can be designed as summarized in Figure A1.4.

Instead of deriving beam-data models for every individual machine, a more convenient approach is to have generic parameterizations for each machine type from a given manufacturer, shifting the QA focus toward machine performance, and reducing the commissioning requirements for treatment planning. Several manufacturers supply optimal beam-commissioning measurements and commit to keeping the beam characteristics within a specified accuracy in a maintenance contract. Routine quality assurance (QA) of the commissioning measurements must be a part of the clinic's QA program (see Appendix A.2). Table A1.1 is an overview of how the most important beam- and dose-model components influence absorbed-dose characteristics for typical treatment machines.

A.1.3 Dose-Calculation Algorithms

Absorbed dose per monitor unit calculated by the treatment-planning system forms the basis for both

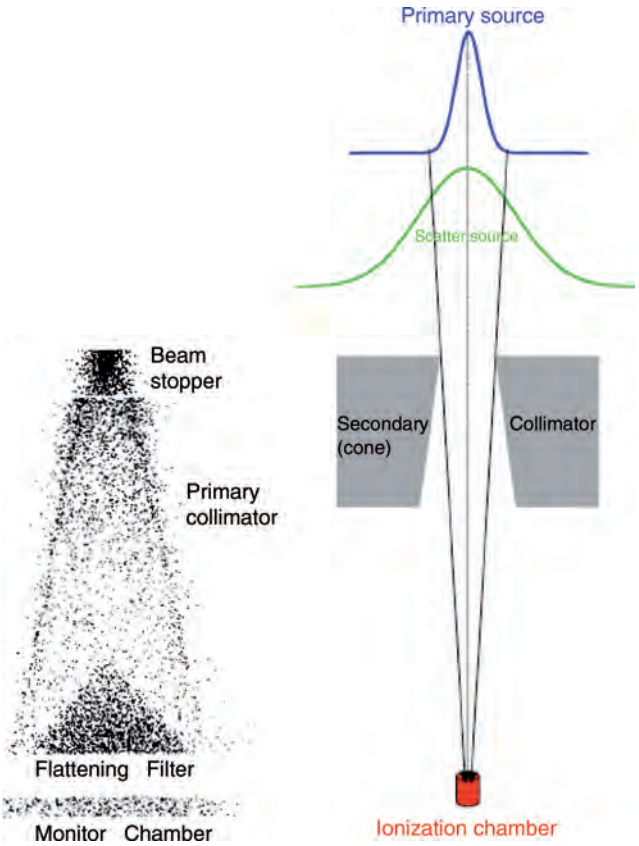

Figure A.1.3. Left: Scatter plot showing the location of photon-scattering events in the treatment head (from Chaney *et al.*, 1994; reproduced with permission). Right: Dual extended-(non-point-)source model used to describe the fluence at the detector position. The narrow primary-source width is due to the spread of bremsstrahlung production in the target and beam stopper backing the target. The scatter source is indirect (extrafocal) radiation produced mainly by Compton scatter in the field-flattening filter and the primary collimator. (From Deng *et al.*, 2004; reproduced with permission.)

prescription and reporting of delivered absorbed doses. Dose-calculation models and approximations are the most important component in data accuracy and integrity. Early dose-calculation models essentially applied absorbed-dose distributions measured in water phantoms to the patient by means of simple scaling laws. The need for fast and accurate absorbed-dose calculations together with the increasing capacity of computer hardware motivated the development of methods that allow for more explicit representations of beam characteristics and related energy-deposition phenomena (Ahnesjö and Aspradakis, 1999; Mackie *et al.*, 1995; 1996; 2000; 2001). The iterative search used in the optimization phase of treatment planning makes it tempting to introduce approximations to make the calculations for IMRT faster. However, before the treatment is executed and absorbed dose reported, the absorbed dose should be calculated as accurately as possible.

The traditional approach to absorbed-dose calculations in treatment planning has been the use of algorithms based on corrections to absorbed-dose distributions measured in water, *i.e.*, absorbed-dose reporting based on absorbed dose in water has been an implicit *de facto* standard. Although approximate, most of these correction-based algorithms considered the variation in absorbed caused by the difference in attenuation as a result of passage of the beam through heterogeneous tissues upstream of the absorbed-dose calculation point. Systems for three-dimensional (3D) treatment planning of conformal and fluence- ("intensity-") modulated therapy were first used in the early 1990s. Limitations in the traditional approach to effectively account for absorbed-dose variations due to varying field geometries and tissue heterogeneities stimulated the introduction of newer model-based algorithms. These algorithms were based on convolution or superposition methods (Ahnesjö *et al.*,1987; Aspradakis *et al.*, 2003; Boyer and Mok, 1985; Mackie *et al.*, 1985; Papanikolaou *et al.*,

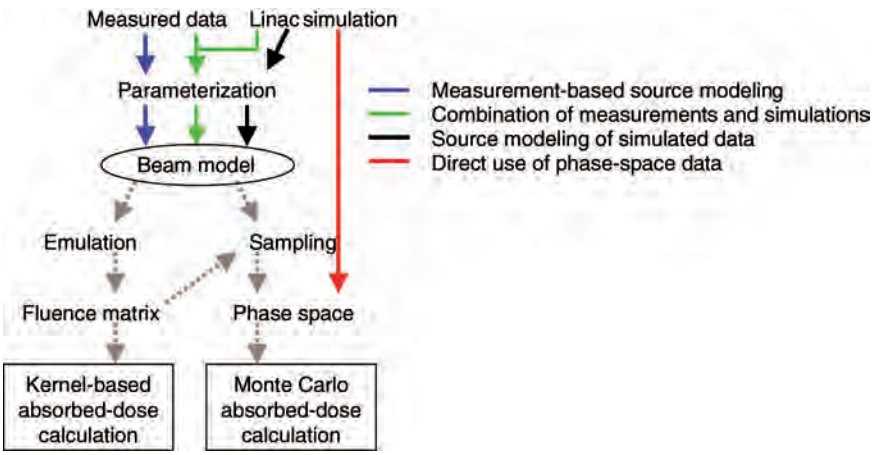

Figure A.1.4. Different beam-data characterization routes for absorbed-dose calculations.

Table A.1.1. Overview of how the model components influence absorbed-dose characteristics and measured-data requirements for typical treatment machines (MLC-equipped linacs). The right-most eight columns show the type of measured data that can be used for derivation or verification of beam and absorbed-dose model data.

	Dose characteristics								Measured data							
	Total absorbed dose	Segment output	Depth-dose shape	Buildup, d_{max}, depth	Heterogeneity impact	Lateral shape	Penumbra shape and width	Absorbed dose outside field	Beam calibration	Head-scatter factors	Output factors	Depth-dose curves	Open-beam profiles	Penumbra profiles	Small-field output	Small-field profiles
Beam-model components	–	–	–	–	–	–	–	–	–	–	–	–	–	–	–	–
Treatment-head geometry	–	–	–	–	–	–	–	–	–	–	–	–	–	–	–	–
Source-isocenter distance	–	–	X	–	–	–	–	–	–	–	–	–	–	–	–	–
Flattening-filter location	–	–	–	–	–	–	–	X	–	–	–	–	–	–	–	–
Multileaf collimator location	–	–	–	–	–	–	X	–	–	–	–	–	–	–	–	–
Primary source:	–	–	–	–	–	–	–	–	–	–	–	–	–	–	–	–
Width/shape	–	–	–	–	–	–	X	–	–	–	–	–	–	X	X	X
Energy spectrum	–	–	X	X	–	–	X	–	–	–	X	X	–	–	–	–
Primary collimator	–	–	–	–	–	–	–	–	–	–	–	–	–	–	–	–
Collimation	–	–	–	–	–	X	–	–	–	X	X	–	X	–	–	–
Scattering	–	X	–	–	–	–	–	–	–	X	–	–	–	–	–	–
Flattening filter	–	–	–	–	–	–	–	–	–	–	–	–	–	–	–	–
Spectral changes	–	–	X	–	–	X	–	–	–	–	–	X	–	–	–	–
Transmission	–	–	–	–	–	X	–	–	–	–	–	–	X	–	–	–
Scattering	–	X	–	–	–	X	–	X	–	X	–	–	–	–	X	–
Monitor	–	–	–	–	–	–	–	–	–	–	–	–	–	–	–	–
Fluence response	X	X	–	–	–	–	–	–	X	–	–	–	–	–	–	–
Backscatter	X	X	–	–	–	–	–	–	–	–	–	–	–	–	–	–
Multileaf collimator	–	–	–	–	–	–	–	–	–	–	–	–	–	–	–	–
Leaf settings	–	–	X	–	–	–	–	–	–	–	–	–	–	–	–	–
Rounded leaf-end	–	–	–	–	–	–	X	–	–	–	–	–	–	X	X	X
Focused leaf-end leak	–	–	–	–	–	–	X	–	–	–	–	–	–	X	X	X
Intra-leaf leakage	X	–	–	–	–	–	–	X	–	–	–	–	–	X	–	X
Inter-leaf leakage	X	–	–	–	–	–	–	X	–	–	–	–	–	X	–	X
Scattering	X	X	–	–	–	–	–	X	–	–	–	–	–	–	–	–
Dose-model components																
Photon transport	–	–	–	–	–	–	–	–	–	–	–	–	–	–	–	–
Attenuation	X	–	X	–	X	–	–	X	–	–	–	X	–	–	–	–
Scattering	X	X	X	–	X	X	–	X	–	–	X	X	–	–	–	–
Depth hardening	X	–	X	–	–	–	–	–	–	–	–	X	–	–	–	–
Off-axis softening	X	X	X	–	–	X	–	–	–	–	–	–	–	X	–	–
Electron transport	–	–	–	–	–	–	–	–	–	–	–	–	–	–	–	–
Lateral diffusion	X	–	–	–	X	–	X	–	–	–	–	–	–	X	X	X
Longitudinal transport	X	–	X	X	X	–	–	–	–	–	–	–	–	–	–	–
Charged-particle contamination	–	–	X	X	–	–	–	–	–	–	–	–	–	–	–	–
Monitor-units calculation	X	–	–	–	–	–	–	–	X	–	–	–	–	–	X	–

1993) in which the transport kernels are generated by Monte Carlo simulation (Ahnesjö, 1989; Mackie *et al.*, 1988) or direct Monte Carlo simulation of the particle transport (Deng *et al.*, 2004; Difilippo, 1998; Fippel *et al.*, 2003; Hartmann-Siantar *et al.*, 1996; Jeraj and Keall, 1999; Ma *et al.*, 1999; Mackie, 1990; Rogers *et al.*, 1995). Rather than correcting absorbed-dose distributions measured for normally incident beams in a water phantom for the effects of patient-specific conditions such as beam modifiers, surface contour, or tissue heterogeneities, the model-based methods directly compute the absorbed dose per energy fluence in the patient. Knöös *et al.* (2006) compared several commercial treatment-planning systems for a variety of treatment sites with the results of Monte Carlo calculations. They found that treatment-planning algorithms that consider changes in photon scattering and electron transport were more in agreement with Monte Carlo modeling, especially for small treatment volumes in which low tissue densities were present. Davidson *et al.* (2007) showed that a convolution/superposition algorithm was more accurate than a finite-pencil-beam algorithm for computing the absorbed dose in inhomogeneous tissue.

The new Monte Carlo-based algorithms can calculate absorbed dose per energy fluence in water-equivalent materials of any density from first principles. For neutron, heavy ion, and possibly proton beams, it is necessary to calculate the absorbed dose in the actual tissue using its molecular composition. For photon beams, the difference between the absorbed dose in soft tissue and water is small, but considerable deviations exist for bone and also to some degree for phantom materials. The main sensitive volume for radiation impact is living cells, which are largely composed of water. Nahum (2007) suggests that, even though it is now possible to compute the absorbed dose from photon beams in a specific tissue type, including the effect of density and elemental composition, the absorbed dose in a small mass of water in the tissue be used for prescription and reporting. It is recommended that the absorbed dose for photon beams be reported as the absorbed dose in a small mass of water in tissue and include realistic estimates for photon scattering, electron transport, and photon attenuation.

Since direct Monte Carlo absorbed-dose computations will soon be commonplace, a special note is in order regarding calculating the absorbed dose in a small mass of water. In Monte Carlo calculations, it is convenient to compute the absorbed dose in the specific material from first principles. Much as is done in cavity theory to compute the absorbed dose inside a cavity, the absorbed dose computed in the specific tissue by Monte Carlo techniques must be converted to the absorbed dose in a small mass of water in the tissue. Based on Bragg–Gray cavity theory, Siebers *et al.* (2000) described how a simple Bragg–Gray stopping power ratio could be applied to the results after the Monte Carlo simulation process. For example, although the absorbed dose in bone would be based on transport properties in the specific bone material, at the end of the simulation, the absorbed dose in a small mass of water in the bone (simulating the soft-tissue structures in the trabecular tissue) would be computed. As in cavity theory (Attix, 1986), the correction is made by a scalar multiplication using a ratio of average mass collision stopping powers of water to bone. Siebers *et al.* (2000) showed that the correction for ICRU Cortical Bone could be as high as from 11 % to 12 % for 6 MV photon beams. For ICRU soft tissue, the correction was only 1 % to obtain the absorbed dose in a small imbedded mass of water. In the case of absorbed-dose computations for the lung, the Monte Carlo transport properties should be for the lung material with the density-effect parameter in the mass collision stopping power evaluated for unit-density water (simulating the capillaries surrounding air-filled alveolus cavities) and not for the average lung density. Siebers *et al.* (2000) found that at 6 MV, the correction of absorbed dose in the lung to absorbed dose in a small mass of water was unity.

A.1.4 Calculation of Absorbed Dose per Monitor Unit

Monitor units that refer to the integrated current ("ionization reading") from a linear accelerator's coaxial parallel-plate ionization chamber have been traditionally used in place of exposure time (used for ^{60}Co radiation). The monitor ionization chamber used for photon beams is normally sealed so that it is immune to the effects of temperature and pressure. Its reading is proportional to the average intensity across the beam. The absorbed dose per monitor unit is normally calibrated with respect to the absorbed dose measured in a phantom under standard irradiation conditions specified by national or international protocols. In traditional radiotherapy, part of the planning process is to determine the number of monitor units to deliver for each field.

For IMRT, the meaning of "monitor units to be delivered" differs slightly depending on the type of beam delivery. In segmented-MLC IMRT delivery, the monitor units for each segment of a field must take into account the relative output of the field as

well as the contributions from indirect sources of radiation and backscattered radiation from the collimation system. In dynamic-MLC IMRT delivery, the monitor units to be delivered refer to the total ionization signal accumulated during the dynamic treatment, requiring careful synchrony of the leaves so that the leaf pattern is completed exactly when the total monitor units have been delivered. The monitor-unit ionization signal can also be used to shut down the treatment unit if the absorbed-dose rate varies appreciably as a function of time. For a binary collimator, the fluence delivered when a leaf is open is nearly proportional to the time that that leaf is retracted. This fluence might not be exactly proportional to the retracted time because indirect photons can be transmitted through a neighboring open leaf. The transit time of the leaves of a binary collimator leaf is taken into account by correcting the programmed open time to the measured effective open time. This correction will be illustrated later in Figure A2.7.

To achieve generality and flexibility, modern methods of absorbed-dose calculation commonly distinguish between the distinct processes of absorbed-dose calculation and beam modeling. Correction-based absorbed-dose calculations have traditionally determined only relative absorbed-dose distributions, assuming monitor-unit settings for a planned beam setup to be calculated independently. With increasing complexity in treatment delivery, and because model-based absorbed-dose calculations are able to do so, there has been a trend to compute absolute absorbed dose in calibration conditions to simplify the calculation of monitor units to be delivered. Depending on circumstances, absorbed-dose distributions can be modeled with varying degrees of explicitness in the description of the underlying phenomena.

For a conventional linac, the absorbed dose per monitor unit D/M is given by

$$\frac{D(A,r)}{M} = \frac{\Psi_0}{M}[1 + b(A)]^{-1}\frac{D(A,r)}{\Psi_0}, \qquad \text{(A.1.1)}$$

where the energy fluence per monitor unit is Ψ_0/M and is determined by Eq. A.1.2. The absorbed dose per unit energy fluence in the patient is $D(A,r)/\Psi_0$ for a field size A at depth r. The monitor unit M is composed only of forward energy fluence through the monitor. The factor $[1 + b(A)]$ corrects for variations in photon backscatter into the monitor chamber and is applied for conventional linacs because they use the monitor signal as feedback to provide output stability to the linac (see Figure A1.5). The value of the $b(A)$ correction is typically a few percent (Liu *et al.*, 2000). This feedback correction does not need to be applied for the Hi-Art™ or the CyberKnife™ systems because the monitor signal is not used to provide feedback for stabilizing their linac outputs.

As shown by the following equation, the energy fluence per monitor unit Ψ_0/M is obtained by measuring the absorbed dose per monitor unit under calibration conditions and dividing it by the absorbed dose per energy fluence calculated by the treatment-planning system under the same

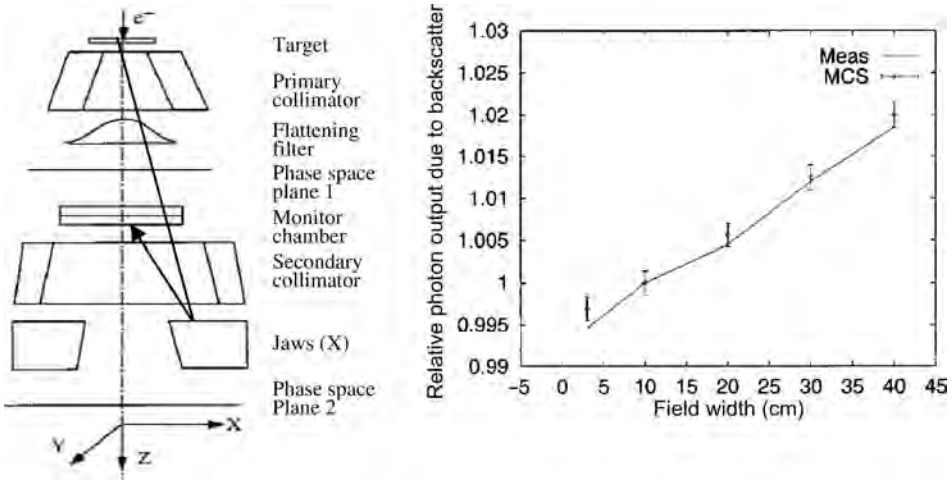

Figure A.1.5. The effect of photon backscatter into the monitor chamber for a Varian 10 MV photon beam. Monitor chambers can provide feedback to stabilize the output of a linear accelerator. When the field size is changed by moving the collimators defining the field (jaws), the backscatter into the monitor chamber changes (see left panel). Increasing backscatter lowers the output per unit monitor unit of the linac correspondingly. The amount of backscatter as a function of square-field size is a few percent (see right panel). This effect should be included in the monitor-unit calculations. (Adapted from Liu *et al.*, 2000; reproduced with permission.)

calibration conditions:

$$\frac{\Psi_0}{M} = \frac{[D(A_{\text{cal}},r_{\text{cal}})/M]_{\text{measured}}}{[D(A_{\text{cal}},r_{\text{cal}}/\Psi_0]_{\text{calculated}}}\left[1 + b(A_{\text{cal}})\right], \quad \text{(A.1.2)}$$

where the subscript "cal" denotes that the respective variable is for the beam-calibration geometry (normally in a water phantom with the isocenter at 10 cm depth for a 10 cm × 10 cm square field). A_{cal} is the calibration field size and r_{cal} the reference depth, and the term $[1 + b(A_{\text{cal}})]$ corrects for backscatter into the monitor chamber at calibration. The effect of backscatter into the monitor chamber is shown in Figure A1.5.

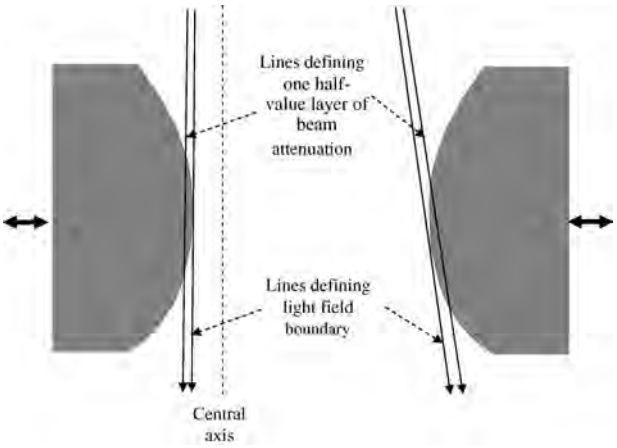

Figure A.2.1. The effect of curved leaf ends. For reasons of mechanical simplicity, most conventional MLCs use simple linear motion (as indicated by the bold double arrows). Here, one leaf is shown close to the central axis and the other farther from the central axis. If the leaves were not curved, there would be a sharp transition in crossing the central axis where the light field would be defined first at the top and then at the bottom of the collimator. The use of curved leaf ends causes the edge of the light field to differ from to the edge of the radiation field, which is typically defined by one half-value layer of attenuation. The discrepancy between the boundary defined by the light field and the radiation field is not constant with leaf position, but varies with position across the field. There is also significant leakage through the leaves when the leaves are in the "closed" position. In the "closed" position, opposed leaves might not touch because there is usually a small gap between the leaves. Curved leaf ends also degrade the penumbra of the field and make beam modeling in this region more difficult.

A.2 Commissioning and QA

A.2.1 Commissioning of Treatment-Planning Systems

Treatment-planning commissioning for IMRT is different in some regards from methods used for more traditional three-dimensional conformal radiotherapy (3D-CRT), which are well documented by the American Association of Physicists in Medicine (AAPM) (Fraass *et al.*, 1998), by the International Atomic Energy Agency (IAEA, 2004; 2007), and in the review by Williamson and Thomadson (2007). This appendix will largely focus on the differences between QA processes in 3D-CRT and IMRT.

It is not practical to do IMRT calculations by hand; computer-based methods are required. It is possible to perform IMRT calculations using so-called "forward" methods, whereby treatments with multiple fields for specified beam directions are planned using more traditional computer-based methods. However, most IMRT treatment-planning systems use formal optimization algorithms that involve iterative calculations, and even iterative definitions of planning aims, to produce acceptable results. Intensity-modulated radiation therapy can produce steep gradients between the target and organs at risk, and testing during commissioning is critical in assuring accurate results from the treatment-planning systems. The summing of multiple small fields or beamlets makes the modeling of the penumbra and low-dose region outside each of these fields very important. The calculation or determination of the leakage through the leaves, especially if they have curved ends, is very important in producing an accurate penumbra model (Cadman *et al.*, 2002; Graves *et al.*, 2001). Figure A2.1 illustrates the shape of the leaf ends for a pair of leaves in conventional MLCs. Because IMRT will result in from a 2- to a 10-fold increase in the number of monitor units when compared with conventional therapy, the leakage through leaf ends and between the leaves is extremely important (Hardcastle *et al.*, 2007). Similarly, the ratio of leakage-to-primary fluence increases when very small fields, typical of IMRT, are used.

The goal of commissioning any treatment-planning system is to ensure that the system computes the absorbed-dose distributions in patients as accurately as possible. The initial acceptance procedures by the vendor to test the quality of the treatment-planning system for IMRT might be different from those for 3D-CRT and can require different specifications and procedures. For example, the acceptance testing should reflect the special requirements for small fields, and assure an accurate description of the penumbra and leakage outside the field. Preparing an existing treatment-planning system for IMRT requires re-commissioning, including additional measurements, and the provision of other information to the planning system. For example, some MLCs have been designed so that opposing leaves cannot be in close proximity to one another, preventing full closure of the gap between

the leaves. These machine-imposed constraints on leaf motion affect the capabilities of the delivery system and need to be provided for in the planning system. Leaf tolerances sufficient for using the MLC for blocking in 3D-CRT are not sufficiently accurate when the MLCs are used for IMRT. Accuracy of from 1 mm to 2 mm in positioning a leaf to provide blocking, while adequate for 3D-CRT, is not sufficient with the small fields employed in IMRT. Figure A2.2 illustrates the possible error in the intensity that can result from an error in leaf position.

Often the QA data comprise a comparison of results of absorbed-dose computation with those of measurements under well-controlled conditions. Van Dyk *et al.* (1993) suggested that the accuracy depended on the absorbed-dose gradient. In a low-gradient region, the relative difference between computed and measured absorbed doses is important, but in a high-gradient region, the distance to agreement of isodose values is more important. The distance to agreement is the absolute distance between isodose representations of two absorbed-dose distributions. Van Dyk *et al.* (1993) suggested that commissioning measurements should be accurate within 3 % everywhere in high-dose regions (>80 % of the maximum absorbed dose) with gradients less than 20 %/cm, within 4 % in low-dose regions, and within 4 mm in high-gradient regions. Van Dyk's proposal might be too restrictive in high-dose regions and insufficiently restrictive in low-dose regions when applied to small-beam measurements used for commissioning IMRT equipment. This is because small absorbed-dose errors outside the field tend to add up to large errors when the small fields are summed together to produce a larger IMRT field. Additionally, it is very difficult to measure the absorbed dose accurately for small fields. End-to-end testing that comprises testing of the entire process from data collection, beam representation, treatment planning and delivery, and QA of the delivered absorbed dose is integral to the beam-commissioning process.

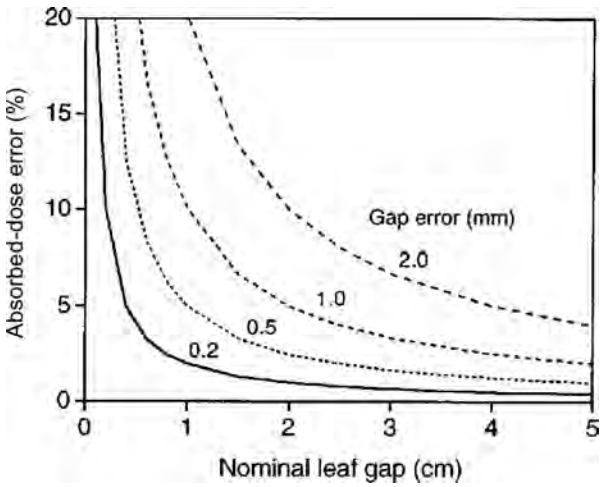

Figure A.2.2. Curves showing the increasing absorbed-dose error with decreasing nominal leaf gap (leaf-gap setting). The nominal leaf gap is the spacing between pairs of leaves that form the moving aperture of a dynamic MLC delivery. (From LoSasso *et al.*, 1998; reproduced with permission.)

A.2.2 QA of IMRT Delivery Systems

A.2.2.1 Conventional-MLC Delivery Systems. Consensus as to what QA tests should be performed for conventional MLC IMRT systems (and their frequency) is still evolving. There are several publications addressing this issue (Ezzell *et al.*, 2003; Galvin *et al.*, 1993; IMRTCWG, 2001; Williams, 2003), but there is as yet nothing definitive. Moran and Xia (2006) and De Wagter (2006) provide explicit recommendations from the US and European perspectives, respectively. What is clear is that any QA program implemented must verify the proper functioning of both the planning and the delivery systems and the transfer of data between the components of the two systems. A full description of all accelerator QA procedures is beyond the scope of this Report. A thorough review of QA for conventional linacs was published by the AAPM Task Group 142 (Klein, 2009) and replaces the recommendations of the earlier Task Group 40 (Kutcher *et al.*, 1994) for IMRT. The Klein *et al.* (2009) report has very detailed recommendations for the accuracy of linac specifications for IMRT. Only the specialized procedures specific to IMRT will be addressed here.

For most forms of IMRT, fields are composed of multiple small segments superimposed during delivery at a fixed gantry angle. The calculation of the absorbed dose delivered by these segments depends on the measured small-field data and the various modeling-parameter values used in the IMRT planning system including: (1) small-field penumbra measurement/modeling; (2) small-field output factors; (3) the leaf-gap offset factor to correct discrepancies between the light field and radiation field; (4) MLC leakage/transmission factors; and (5) leaf-sequencer accuracy. These are discussed briefly here.

Modeling of a small-field penumbra requires input of measured data. Inadequate input data produces modeling inaccuracies in the penumbra of each small field and will significantly affect the absorbed-dose distribution resulting from the application of multiple segments to the irradiated volume. Ezzell *et al.* (2003) have reported that a beam model based on beam profiles obtained with a relatively large ionization chamber having an inner

diameter larger than 0.3 cm can produce erroneous results in IMRT calculations. This is because an ionization chamber of this dimension has a coarse resolution that over-estimates the penumbra width (Laub and Wong, 2003; Low *et al.*, 1998a). Therefore, it is recommended that profile measurements be made using either radiochromic film or other detectors with high spatial resolution, such as a pinpoint ionization chamber (Ezzell *et al.*, 2003; Martens *et al.*, 2000), a small diode, or a diamond detector. Due to extended measurement times for IMRT, all ionization-chamber measurements must include consideration of chamber and cable leakage, which generally becomes more important for small chambers (Leybovich *et al.*, 2003). Film must also be used with care. For example, Kodak EDR2 radiographic film has a significantly non-linear dependence on absorbed dose (Zhu *et al.*, 2002). In addition, all radiographic film is strongly dependent on beam energy (Muench *et al.*, 1991). GafChromic® radiochromic film exhibits a small energy dependence but a strong dependence on the time between exposure and sensitometric evaluation (Soares *et al.*, 2009). Similarly, the calibration of both diodes and diamond detectors can drift with time (Das, 2009; Zhu and Saini, 2009).

Sharpe *et al.* (2000) have shown that beam output factors vary rapidly as a function of field size, and this can lead to variability in IMRT absorbed-dose distributions because small segments make up MLC IMRT fields. The output factor decreases sharply due mainly to obscuration of the primary source but due also to lack of lateral charged-particle equilibrium, less head and phantom scatter, and more backscatter into the monitor chamber when the segment field size decreases to less than 3 cm × 3 cm (Azcona *et al.*, 2002; Sharpe *et al.*, 2000). Thus, it is essential to verify the IMRT absorbed-dose-calculation algorithm against measurements for the IMRT accelerator in question using a suitable small-field detector (Martens *et al.*, 2000). In addition, it is absolutely essential for leaf-positioning accuracy to be verified. The AAPM TG-142 protocol (Klein *et al.*, 2009) recommends that a leaf should be positioned with an accuracy of 1.0 mm. Sharpe *et al.* (2000) showed that a 2 mm deviation in field size changes the output factor by 2 % for a 2×2 cm^2 field and by 15 % for a 1×1 cm^2 field of a 6 MV photon beam. In some cases, it can be necessary to restrict the lower limit of field size that can be used by the IMRT treatment-planning system in order to obtain satisfactory QA and treatment results. Sharpe *et al.* (2000) also pointed out the importance of accounting for off-axis beam softening of the photon energy spectrum for small off-axis fields.

The need for a leaf-gap offset arises when curved-end leaves are used, because there is a mismatch between the field defined by the light field and the field defined by the radiation field. Figure A2.3 illustrates a test to determine the leaf-gap offset. The leaf-gap offset is measured by joining a series of strip fields that form, as well as possible, a broad field. The leaf-gap offset is the distance that the leaf has to move away from its light-field image to match the radiation field.

Leaf leakage (due to gaps between leaves) and transmission (due to photon passage through leaves) are important issues, and include contributions from inter-leaf leakage, intra-leaf transmission, and transmission between opposed leaf ends. The effects of inter-leaf leakage are shown in Figure A2.3 The amount of leakage that contributes to each IMRT field depends on the beamlet intensities that make up the field and also on the leaf-sequencing algorithm (LSA) used. Other user-adjustable numerical values include a parameter called the dosimetric leaf gap (DLG), which is a dosimetric measure of the effective gap that results from transmission through curved leaf ends of a pair of abutting leaves (Arnfield *et al.*, 2000; LoSasso *et al.*, 2001). The dosimetric leaf offset is the amount that a leaf would need to be retracted to add the same fluence as is transmitted through the rounded leaf end. Results of a dosimetric leaf-gap test are shown in Figure A2.4 (LoSasso *et al.*, 2001) for a variety of MLC designs, off-axis positions, and energies. The gaps between leaf ends that are typically employed for dynamic MLC delivery are from 1 cm to 3 cm, so the DLG illustrated in Figure A2.4 corresponds to effective leakages of up to several percent. This must be taken into account in treatment planning for accurate absorbed-dose calculations and should, ideally, not change as a function of time.

Huq *et al.* (2002) reported a dosimetric study on the three major conventional MLCs available commercially. Their study showed that transmission values are greatly dependent on the MLC design, particularly in regard to the leaf thickness, position of the MLC in the treatment head, and whether or not the leaf ends are double-focused and move in an arc with respect to the beam, or have curved ends and move linearly across the field. Inadequate modeling of the penumbra of curved leaf ends leads to inaccuracies in IMRT treatment planning (Cadman *et al.*, 2002; Ibbott, 2009). For example, Hardcastle *et al.* (2007) reported that leaf-end leakage for a Varian Millennium MLC could result in an additional absorbed dose of 2 Gy to 3 Gy delivered over a course of treatment. It is

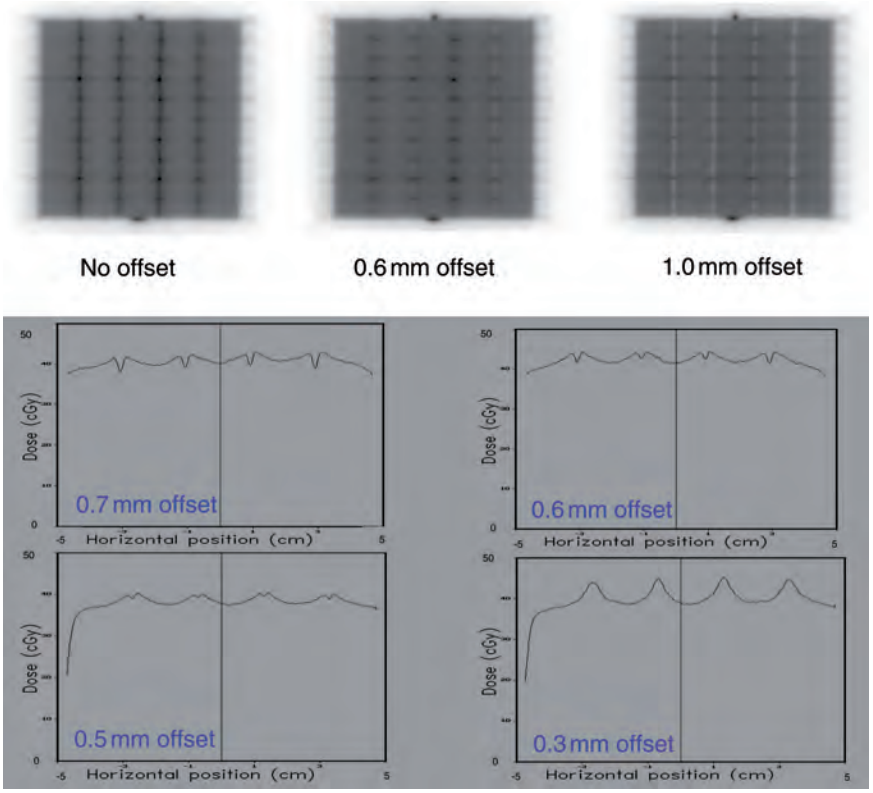

Figure A.2.3. Test to determine the optimal leaf-gap offset due to the curved leaf ends on a conventional MLC. A 10 cm $\times$ 10 cm field is formed by five successive irradiations of 2 cm $\times$ 10 cm field strips as shown in the upper panel, where the thin horizontal stripes are due to inter-leaf leakage. With zero offset between the strips, there is a hot junction (due to leaf leakage through the curved leaf ends) between the strips as indicated by the vertical black stripes between the strips. With a 1.0 mm offset, there is a cold junction between the strips as indicated by the vertical white stripes. In the lower panel, the offset is varied between strips to minimize both the hot and cold spots. The ideal offset is between 0.5 mm and 0.7 mm, which implies that the accuracy of the test is about ± 0.1 mm.

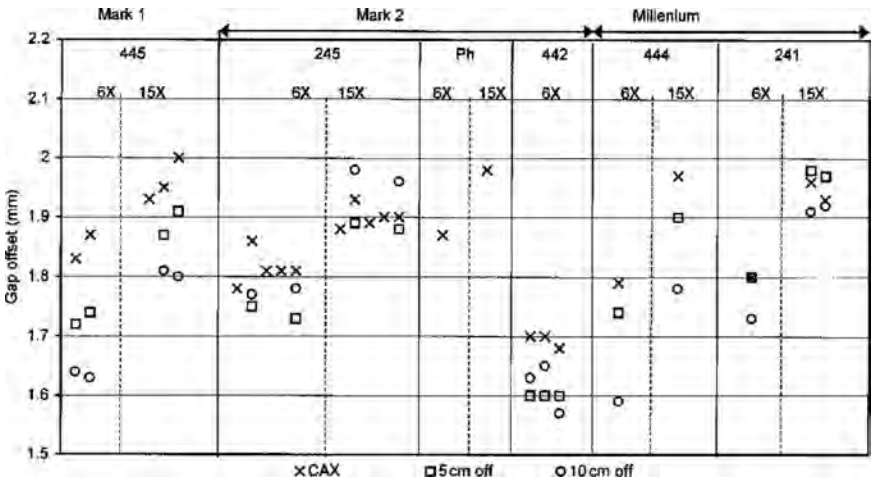

Figure A.2.4. Examples of dosimetric leaf-gap offsets chosen for a variety of Varian MLC collimators, position in the field, and beam energy. Each of these values is the result of a test similar to that described in the text. Repeat measurements indicate excellent reproducibility. In general, the leaf gap is less for low-energy accelerators, but there is no clear trend for the influence of position in the field or type of MLC. The two energies tested are 6 MV (6X) and 15 MV (15X). CAX refers to the central axis values, and 5 cm off and 10 cm off refer to off-axis distances at which measurements of the leaf-gap offset were made. Mark 1, Mark 2, and Millenium are different MLCs manufactured by the Varian Corporation. The numbers 445, 245, *etc.*, in the top row of the figure indicate individual linac designations. (From LoSasso *et al.*, 2001; reproduced with permission.)

recommended that users measure their machine's MLC transmission values and compare their results with published values (Hardcastle *et al.*, 2007; Huq *et al.*, 2002).

In implementing a conventional-MLC IMRT QA program, the physicist must also appreciate the effects on the delivered absorbed-dose distribution caused by the LSA used to convert the treatment-planning-system-derived intensity maps into a deliverable set of MLC leaf sequences. Such effects are dependent on leaf width, leaf-travel distance, interdigitation of leaves, and maximum field size. Typically, the physicist can adjust the number of intensity levels and MLC step size used by the LSA for each patient or for each disease site. These choices affect the differences seen between the planned and delivered profiles, as well as the overall delivery time. Using a smaller MLC step size and a larger number of intensity levels can result in many segments with small field sizes, which places greater importance on MLC positioning accuracy, monitor linearity and resolution, and accelerator stability, as well as on potential limitations in absorbed-dose modeling for these small segments (Ezzell and Chungbin, 2001; Low *et al.*, 2001). Figure A2.5 illustrates measurement of the error that can result when segments are delivered with a very small number of monitor units (MUs) (Palta *et al.*, 2003). The error arises because of the time required for a linear accelerator to reach stable operating characteristics after being switched on. The error is measured by comparing the absorbed dose received from multiple irradiations with beams each delivering a fraction of 1000 MU with that from a single beam calibrated to be accurate when delivering the entire 1000 MU. The error increases as the absorbed-dose rate increases (Palta *et al.*, 2003).

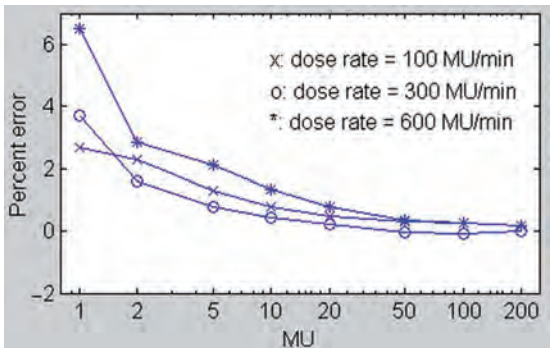

Figure A.2.5. Measurement of the error that can result when a small number of monitor units (MUs) are delivered multiple times. The abscissa represents MU per delivery. After each delivery, the beam is turned off. In all tests, a total of 1000 MU was delivered. Unlike conventional radiotherapy, small numbers of MUs are often delivered for different segments in IMRT. The error is generally larger for small numbers of MUs delivered at high absorbed-dose rates. (From Palta *et al.*, 2003; reproduced with permission.)

As indicated previously, there are no national or international standards yet for a QA program for conventional-MLC IMRT delivery. Specific QA tests depend largely on the design of the MLC (Ting, 2006; Xia and Verhey, 2001). Maintaining MLC calibration to within the tolerances determined during the IMRT commissioning test is a critical component of any IMRT QA program. Tests should verify the correct alignment and positioning of the MLC carriage and leaves. LoSasso *et al.* (2001) describe examples of QA tests to detect carriage-misalignment effects using film and the gap between leaves using feeler gauges. Figure A2.6 gives an example of typical film test patterns used to check MLC leaf-position calibration. This figure shows leaf errors that have been purposely introduced to illustrate the sensitivity of the test. Similar tests should be repeated at routine intervals and also following servicing of the MLC (Bayouth *et al.*, 2003). Chui *et al.* (1996) describe a series of five procedures for MLC QA including testing (1) the stability of leaf speed, (2) the effect of lateral disequilibrium on absorbed-dose profiles

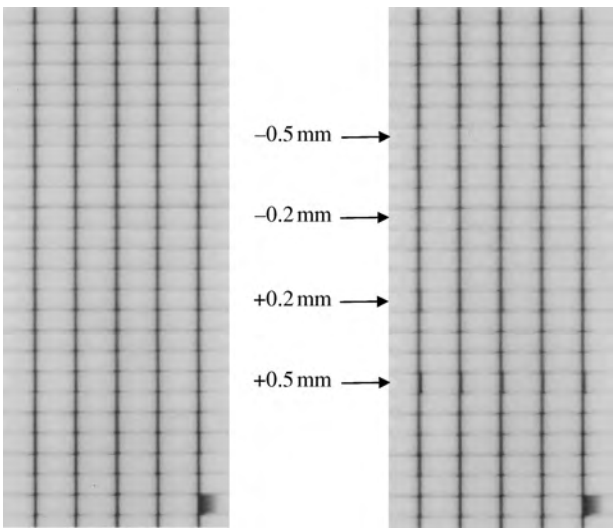

Figure A.2.6. Illustration of a test to determine correct leaf calibration. A series of 1 mm wide leaf irradiations are delivered to radiographic film at multiple positions across a field. On the left is an illustration of correct leaf-position calibration. On the right is an illustration of purposely set leaf errors to illustrate the sensitivity of the test. Leaves that are offset by 0.5 mm can be detected, but offsets of 0.2 mm cannot be detected with this test. The leaf on the right, second from bottom, has been purposefully offset halfway across the gap to mark the film with respect to orientation, and it is possible to see the differential transmission through the curved leaf end with more leakage through the left part of the gap and less transmission through the right part.

across adjacent leaves in the direction perpendicular to leaf motion, (3) the effect of acceleration and deceleration of leaf motion, (4) the effect of positional accuracy, and (5) the effect of round-ended leaves. In addition, these authors provide examples of simple test-pattern QA checks. Litzenberg *et al.* (2002) have reported the use of machine log files to check leaf acceleration and deceleration.

Finally, it must be emphasized that, just as for conventional 3D-CRT, the integrity of data transfer through the entire system (CT-simulator, treatment-planning system, record-and-verify system, and IMRT accelerator-control system) must be scrutinized rigorously, and the entire treatment team must remain vigilant when patients are treated with conventional MLC IMRT, staying alert for data corruption or failure of the software to perform correctly.

A.2.2.2 Binary MLC Delivery Systems. Binary MLC systems were designed specifically for IMRT delivery. The leaves move quickly into and out of a narrow fan beam (Carol, 1995; Mackie *et al.*, 1993) that is between 1 cm and 5 cm wide. The length of time that the leaves are outside the fan beam determines the intensity incident on the patient through that portion of the fan beam. Verification of the position of the leaves is relatively simple in that the leaves at any instant in time can have only four states: open, closed, opening, and closing. The length of time it takes the leaves to move across the field gap is tens of milliseconds (Mackie *et al.*, 2003). Light-interruption switches are used to verify the correct state of the leaves. Binary collimators have been used for tomotherapy, in which the fan beam rotates around the patient. In an example of serial tomotherapy (Best International, Pittsburg, PA, USA), two independent sets of binary leaves modulate two adjacent slices (transverse cross-section of the patient) while the couch remains stationary. The couch must be carefully translated after each rotation to treat the next two slices. In helical tomotherapy, akin to helical CT, the couch translates continuously with the rotating fan beam.

The types of QA procedures for binary MLC systems are significantly different from those of conventional MLCs, because the way in which intensity is modulated is quite different. The rotational delivery is broken up into a series of short arcs each called a projection. Typically, the time to deliver a projection is from 300 ms to 1000 ms depending on the gantry-rotation rate. In the Hi-Art™ helical tomotherapy system, the 360° rotation is subdivided into 51 arcs each of slightly over 7° (Mackie *et al.*, 2003). If a high intensity is to be delivered in a projection, the leaf is opened at the beginning of the arc defining that projection and closed at the end. If a low intensity is to be delivered, the leaf is opened near the mid-point in the time of the projection and closed just after the mid-point. In conventional IMRT delivery, the leaf speed is relatively slow and the position of the MLC is checked periodically, but the leaf velocity is not a critical parameter as the beam will not be delivered if the leaf is not in the correct position. However, in binary MLC delivery, the transition time from open to closed and from closed to open is about 20 ms and must be consistent. A change in air pressure used to drive the pistons or the wearing of the pistons or leaves can change the transition time and therefore the intensity delivered. One way to test for changes in transition time is to compare the requested open time and the actual open time for each leaf. Typical results of such a test are shown in Figure A2.7, where the requested relative opening time for a projection is compared with the actual relative opening time.

The influence of neighboring open leaves on the intensity through a particular open leaf must be measured. This "cross-talk" behavior of one leaf with its neighbor is due to the finite size of the source and the tongue-and-groove profile of the leaves. Figure A2.8 illustrates the measured increase in energy fluence through a leaf, called the fluence-output factor (FOF), when both neighboring leaves are open for the TomoTherapy Hi-Art™ system. Although both are related to the influence of transmission and extrafocal radiation from the head of the unit, the FOF differs from a conventional output factor in that FOF measures an increase in energy fluence when both neighboring leaves are open and an output factor measures the absorbed dose in a patient as a function of field size. If only one of the neighboring leaves is open, the increased fluence is half the FOF. There is very little influence on the intensity through a particular leaf from non-neighboring leaves. These test results are used in the monitor-unit calculations to improve the accuracy of delivery. The test should therefore be routinely performed and whenever the MLC is serviced or removed for inspection. As with a conventional MLC, the leakage through the leaves of a binary MLC should also be measured.

Both serial and helical tomotherapy use the same mechanical-alignment tests. The Peacock™ (Carol, 1995) serial-tomotherapy system was designed to be an add-on to a conventional linear accelerator. As such, QA for the mechanical alignment should be performed whenever it is mounted on the linac (Low *et al.*, 1998a; Saw *et al.*, 2001). One simple test for alignment is to place a film some distance

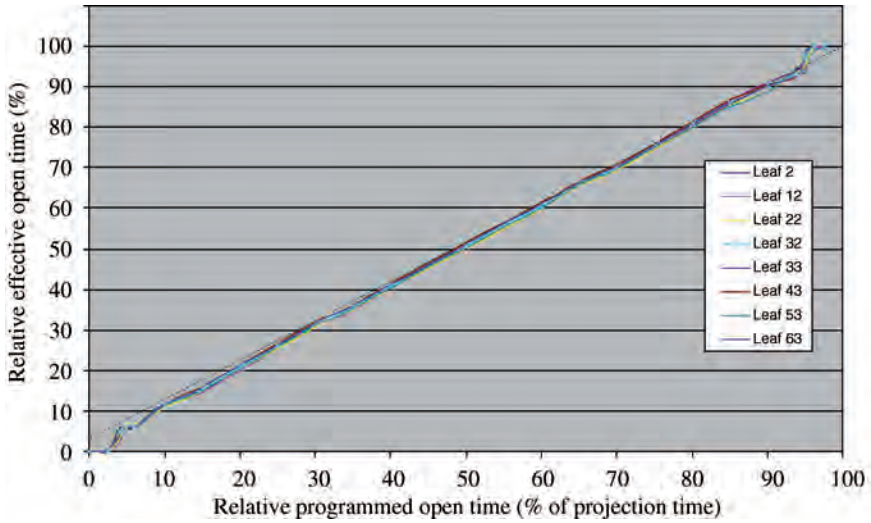

Figure A.2.7. Binary collimator leaf-performance information used for monitor-unit calculations on the Hi-Art™ helical tomotherapy unit. This figure shows the effective open time as a percentage of the time for one projection, here 500 ms long, for binary leaves when compared with their programmed open-time request. In helical tomotherapy, a single rotation is divided into 51 arc segments called projections; a projection lasts a time equal to the time for one complete rotation divided by 51. The programmed relative open time (%) is varied from very small values to the full projection time of 500 ms, and the time that the leaf is actually open is determined by processing of the megavoltage x-ray detector signal. The x-ray detector acquires a reading for every channel for every linac pulse, allowing a temporal resolution of about 3 ms or about 0.6 % of the projection time to determine when the leaves are opened or closed. The control of the leaves is such that all of the leaves at the beginning of a projection are closed. The finite leaf opening and closing time prevents a leaf from achieving a relative opening time greater than about 95 %. To deliver a very small opening time, a leaf has to begin to open and, then before it is fully open, it must start to close. It can be seen that relative opening times less than about 5 % are not possible. The dynamic range of modulation for a binary collimator controlled in this manner is continuous but with a range smaller than the projection time. The curves, one for each leaf listed, are nearly superimposed indicating similar opening and closing times. A dashed line indicates a line defining equal requested and effective open times. This measured performance of individual leaves is used in the monitor-unit calculation to determine what the leaf opening times should be. (Figure courtesy of TomoTherapy Inc., Madison, WI, USA; reproduced with permission.)

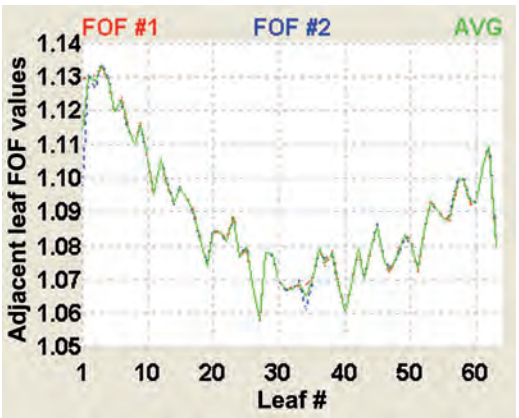

Figure A.2.8. The fluence-output factor (FOF) as a function of leaf number for the TomoTherapy Hi-Art™ system. The measured increase in energy fluence when both neighboring leaves are open is called the FOF. The figure shows the variation in FOF as a function of leaf number. Two runs of the test, listed as FOF1 and FOF2, are shown together with the average results. If only one neighboring leaf is open, the increase in energy fluence is half of the increase shown. The variation from leaf to leaf is due to small (of the order of 25 μm) variations in mechanical precision of the fixture holding the leaves. The asymmetry is due to a lateral offset in the MLC. Calibration of the FOF enables the MLC to operate with wider mechanical tolerances. (Figure courtesy TomoTherapy Inc., Madison, WI, USA; reproduced with permission.)

vertically away from the central axis. The same test is used for helical-tomotherapy systems. Figure A2.9 shows the results of the alignment test. Two exposures are made: one with the beam pointed down and the other with the beam pointed up. The double exposure reveals if one exposure was enclosed symmetrically within the other. If it is not, the MLC is misaligned in the longitudinal (in–out direction along the leaf motion) direction. The lateral (left–right) alignment can be tested on the Hi-Art™ system by using the CT detector that is also mounted on the system. With a film placed on the central axis, the odd-numbered leaves can be retracted and then restored to block the beam. Then the procedure is repeated with even-numbered leaves. These procedures permit the observation of inter-leaf leakage. The symmetry of inter-leaf leakage is a very sensitive measure of the mechanical alignment of the MLC to the beam in the lateral direction.

The Hi-Art™ tomotherapy and the Cyber Knife™ systems do not have field-flattening filters in their beams. The same arrangement has been proposed by Vassiliev *et al.* (2006) for IMRT delivery with conventional MLCs. In this case, the

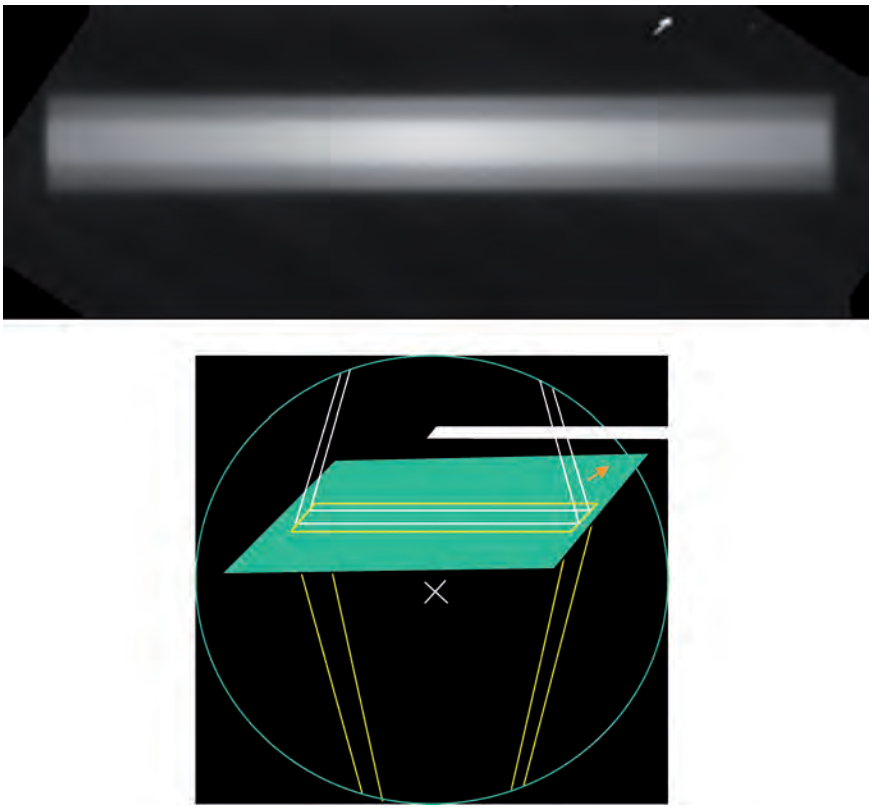

Figure A.2.9. Alignment test to determine if a tomotherapy slit beam is aligned perpendicularly to the axis of rotation. As shown in the lower panel, a film (indicated by the green plane) is placed well off the rotation axis (the axis is marked by the cross). The slit beam arriving from the near side of the film plane (indicated by white lines) will make an image within the image of a slit beam (indicated by yellow lines) that is produced farther from the film plane. In the upper panel, an image of the irradiated film indicates that the smaller image of the beam from above (indicated by the solid white area in the lower panel) is symmetrically nested within the larger image of the beam from below (indicated by the yellow lines in the lower panel). The film indicates that the beamline is aligned properly. It is possible to see on the film that the beam is produced without a field-flattening filter because the centers of the beams have a higher intensity than their edges. The small arrow on the film is used to provide orientation for the film after it has been processed. (Figure courtesy of TomoTherapy Inc., Madison, WI, USA; reproduced with permission.)

absorbed-dose profile for an unmodulated beam is approximately triangular in shape with the center of the beam having a higher intensity than the edge. The intensity pattern will become steeper if the energy is higher and shallower if the energy is lower. If the optimizer requires a uniform beam, the MLC can modulate the beam to yield a uniform intensity. The advantages of not having a field-flattening filter are an increase in intensity for smaller fields, less scatter outside the field, and less variance in the energy spectrum across the field, which simplify beam modeling. The definition of beam uniformity or flatness of the beam has to be replaced by a definition that measures the consistency of the profile. The AAPM TG-142 protocol (Klein *et al.*, 2009) recommends that for IMRT the field flatness be within 1 % for a conventional linac. To be consistent, the off-axis profile should be within 1 % of the baseline profile everywhere within the field for the Hi-Art™ and CyberKnife™ systems.

A completely different aspect of QA required for helical tomotherapy is the synchrony of the leaves and the gantry and of the couch and the gantry (Fenwick *et al.*, 2004). For example, a loss of synchrony of the couch and the gantry will mean that the absorbed-dose distribution would become angularly misaligned or twisted with respect to the planned distribution. The accuracy of the movement of the couch can be checked with a stopwatch and a camera used to monitor the patient. Alternatively, the leaves can be programmed to open for a specified distance of couch travel and angle of gantry rotation. The resulting radiation pattern can be recorded on film.

A.2.3 Patient-Specific QA

One of the first IMRT QA publications for conventional MLC systems (Burman *et al.*, 1997) described a six-step methodology for patient-specific QA: (1) verification that the intensity-

modulated field boundary matches the planning boundary, which is commonly done for 3D-CRT; (2) through an independent calculation, verification that the machine instructions driving the leaves produce the planned absorbed-dose distribution; (3) comparison of the absorbed-dose distribution in a phantom with that calculated by the treatment-planning computer for the same irradiation condition; (4) comparison of the planned leaf motions with that recorded on the MLC log files; (5) confirmation of the initial and final positions of the MLC for each field by a record-and-verify system: and (6) *in vivo* absorbed-dose measurements. Except for initiating an IMRT program, this number of QA procedures would rarely be repeated. Typically, for patient-specific QA one or more of the following methods is used to verify that the intensity pattern will deliver the desired absorbed dose:

- Measurement of the intensity pattern from individual beams for a specific patient.
- Measurements of absorbed dose in phantom of the beam-intensity pattern planned for a specific patient.
- Independent absorbed-dose calculations for the patient-specific beam intensity pattern.
- *In vivo* dosimetry.

Ibbott (2009) reported that the Radiation Physics Center at the M.D. Anderson Hospital in Houston, TX, USA, has found that the dosimetry for IMRT at many treatment centers is not as accurate as for other types of external-beam radiation therapy. Ibbott (2009) strongly recommends that patient-specific QA be performed for all patients having IMRT. Adherence to this policy is recommended.

Patient-specific QA methods will be further elaborated in the following sections. It is recommended that patient-specific QA not rely on a single method exclusively for all patients, as each method has its own strength. Additionally, patient-specific QA is no substitute for treatment-planning and machine-specific QA intended to test the commissioning and specifications of the planning and delivery systems. On the other hand, correlation of the results of patient-specific QA in a set of patients can reveal issues in planning or delivery systems that should be investigated with specific tests of the planning or delivery systems.

A.2.3.1 Measurements of Intensity from Individual Beams. Individual beam intensities can be determined by directing the beam normally onto a phantom with a flat surface and measuring the absorbed dose received. A dosimeter system, consisting of calibrated film or an array of suitable detectors, is placed at a convenient location such as at the block-tray position on the gantry or on the couch at the isocenter. The dosimeter system is then irradiated using the planned beams all delivered from a single downward-directed gantry angle. The incident irradiation pattern from each beam is generated by the planning system and compared with the measurement. Typically, the comparisons are made for each field delivered. If all of the intensity patterns are acceptable, it is assumed that the absorbed dose in the patient will be correct. Gross delivery or planning errors would likely be detected. However, if subtle errors in the intensity pattern for an individual field are detected, it can be difficult to determine the impact on the absorbed dose in the patient from the summed beams.

Traditionally film-based measurements using densitometric systems have been used to determine beam characteristics such as uniformity, symmetry, and flatness, but with suitable care film-based dosimetry can also determine the beam intensity (Childress *et al.*, 2002; Winkler *et al.*, 2005). Multipoint planar dosimeters such as electronic portal-imaging devices and diode systems (*e.g.*, MapCheck™, Sun Nuclear) that can greatly assist in the QA process have been developed (Baker *et al.*, 2005; Chang *et al.*, 2003; 2004; Jursinic and Nelms, 2003; Létourneau *et al.*, 2004; McCurdy *et al.*, 2001; Van Esch *et al.*, 2001; 2004; Warkentin *et al.*, 2003; Wiezorek *et al.*, 2005).

One of the greatest challenges of beam-intensity measurements with a planar detector is the selection of pass–fail acceptance criteria for the agreement between the measured and expected intensity. This is because the absorbed dose in these planar dosimeters does not reflect the 3D absorbed-dose distribution that will be produced in the patient. The user must compare the measured planar absorbed dose with the corresponding calculated planning absorbed-dose distribution, for the same beam and measurement depth using a 2D overlay comparison of calculated and measured absorbed-dose profiles, or using the "gamma value" introduced by Low and co-workers (Low and Dempsey, 2003; Low *et al.*, 1998b). The gamma value is a measure of a two-component user-selected criterion consisting of distance-to-agreement (DTA) and dose-difference (see Section A.2.3.4). As yet there is no agreement on pass–fail criteria for the gamma value.

A.2.3.2 Measurements of Absorbed Dose in Phantoms. The absorbed-dose distributions from all of the beams to be used to treat a patient can be measured in a phantom and compared with the computed absorbed dose with the patient replaced

by a phantom. There is no single dosimetry system that conveniently measures all the absorbed-dose information necessary for patient-specific QA. Systems that balance thorough dosimetric measurements with labor requirements and complexity have been developed in many academic centers (Agazaryan *et al.*, 2004; Chao, 2002; Higgins *et al.*, 2003; Klein *et al.*, 1998; Létourneau *et al.*, 2004; Moran *et al.*, 2005; Olch, 2002; Saw *et al.*, 2001; Wiezorek *et al.*, 2005; Winkler *et al.*, 2005; Yan *et al.*, 2005). These exploit the optimal characteristics of point dosimeters (*e.g.*, ionization chambers) and planar dosimeters. Radiographic or radiochromic film is typically used to measure the spatial position of the irradiated area (by aligning the steep-dose-gradient regions), and ionization chambers are used to measure the absorbed dose in regions with relatively low-dose gradients.

Careful dosimetry-phantom design is important for IMRT system commissioning and QA procedures. Anthropomorphic phantoms offer the advantage that they are of similar shape and size to the patients to be treated. Intensity-modulated radiation therapy QA audits that use anthropomorphic phantoms have been reported (Ibbott *et al.*, 2006; Tomsej *et al.*, 2005). Ibbot *et al.* (2006) reported that about one-third of the irradiations audited failed to meet accuracies of 7 % in a low-gradient region and that deviations of greater than 20 % occurred. Figure A2.10 shows the GORTEC (Groupe Oncologie Radiothérapie Tête et Cou) audit phantom and the results of comparing treatment-planning calculations with measurements with this phantom in 18 centers (Tomsej *et al.*, 2005). The results for QA of IMRT head-and-neck treatments indicate that the ICRU-recommended dosimetric accuracy of 5 % (ICRU, 1993) is not being achieved at many centers.

The calibration of a reference field is now highly reliable for external-beam radiotherapy. Results using the IAEA TRS-398 and the AAPM TG-51 dosimetry protocols often agree to within 1 % or less for reference-field conditions (measured at the center of 10 cm $\times$ 10 cm unmodulated open fields in water at 10 cm depth when the surface of water is 100 cm from the source). Intensity-modulated radiation therapy produces absorbed-dose distributions that are very dissimilar from those in reference-field conditions because the irradiation patterns consist of a large number of small fields. The accuracy of IMRT dosimetry depends critically on how well small fields are modeled in the planning system, including the effect of occlusion of the source by the closest jaw to the source and perturbation of the collimation system. Figure A2.11 shows results of multi-institutional IMRT audits that indicate that the discrepancy between Monte Carlo computed and measured absorbed-dose distributions is much larger for actual IMRT conditions when compared with reference conditions. This study revealed that much of the dosimetry uncertainty is due to the use of ionization chambers in clinical situations far different from the conditions used for calibration.

The type of delivery also impacts this effect. In particular, some of the dynamic field deliveries required the use of narrow-field slits traversing across the detector leading to significant partial-volume effects (Sánchez-Doblado *et al.*, 2007). Sánchez-Doblado *et al.* (2007) concluded that the uncertainty in ionization-chamber dosimetry alone was about 2.5 %.

If the treatment-planning system does not consider internal heterogeneities, determination of the cause of discrepancies between measured and calculated absorbed doses can be difficult, especially within and near bony anatomy. The spacing between locations for TLD chips might be larger than desired. Film preparation is also made more difficult with anthropomorphic phantoms due to the irregular external contours. Preparation of the film requires careful cutting in the darkroom to conform to the phantom outline. However, cuboid and cylindrical phantoms of sufficient size might accept the sheets of film with no need for cutting.

A.2.3.3 Independent Absorbed-Dose Calculations. Hand calculations of the absorbed dose at the ICRU Reference Point are common for 3D-CRT. For IMRT, it is not practical to do hand calculations. Because a single reference point is insufficient for reporting absorbed dose, a single absorbed-dose calculation point is logically also not sufficient for performing patient-specific quality assurancer. An independent method must be used to determine the distribution of absorbed dose in the patient, not merely the absorbed dose at a point. The number of points calculated must be statistically sufficient to ensure that the dose–volume prescription is being delivered according to plan. Whereas it is not always practical to make measurements in 3D, it has been practical for more than a decade to calculate absorbed dose in 3D.

Often absorbed-dose calculations less accurate than those originally employed are used for QA. This is justified to find large errors in the operation or interpretation of the treatment-planning system. However, ideally, QA procedures should have standards equivalent to or higher than the original procedures being tested. The use of inferior standards

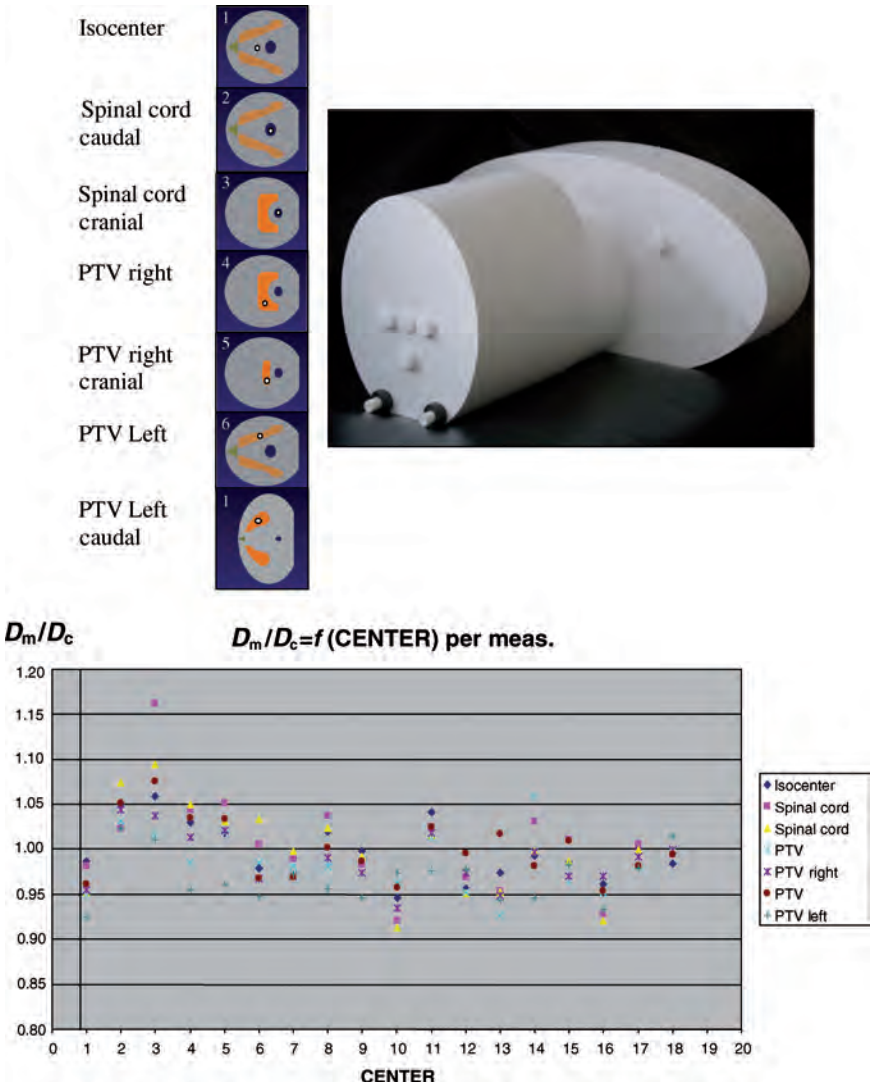

Figure A.2.10. Upper panel is the phantom developed by the GORTEC to compare the ratio of the measured absorbed dose to the computed absorbed dose at several positions for head-and-neck radiotherapy. The orange regions of interest indicate the target volume on each of the slices. About 20 % of the 126 TLD measurements from 18 centers did not agree within 5 % of the treatment-planning calculations. The spread of measurements within a center was much less than the spread of measurements between centers. (Figure courtesy of Milan Tomsej, St. Luc University Hospital, Brussels, Belgium.)

for QA procedures might lead to an unacceptable false-positive or false-negative rate. Therefore, the accuracy of the 3D absorbed-dose calculation used to test the IMRT algorithm should at least be equivalent to that of the treatment-planning system. For example, if a convolution/superposition algorithm is used for the original absorbed-dose calculation, the use of a Clarkson–Cunningham algorithm without heterogeneity corrections for comparison is acceptable for many sites in the body (Kung *et al.*, 2000). A Monte Carlo algorithm would also be acceptable for determining the absorbed dose in the presence of heterogeneous tissue densities if the Monte Carlo code had been tested sufficiently (Aaronson *et al.*, 2002; Heath *et al.*, 2004).

Therefore, as an alternative to a set of measured absorbed-dose distributions, it is acceptable to use an independent absorbed-dose calculation that is at least as accurate as the absorbed-dose calculation being tested as previously verified against commissioning measurements. The independent absorbed-dose calculation must be able to compute the absorbed dose in 3D so that the calculation can be tested at a statistically relevant number of points.

A.2.3.4 *In vivo* Dosimetry. *In vivo* absorbed-dose measurements have been often used in 3D-CRT, and these methods have also been applied to IMRT (Higgins *et al.*, 2003). The detectors used include TLDs, diodes, and MOSFET dosimeters.

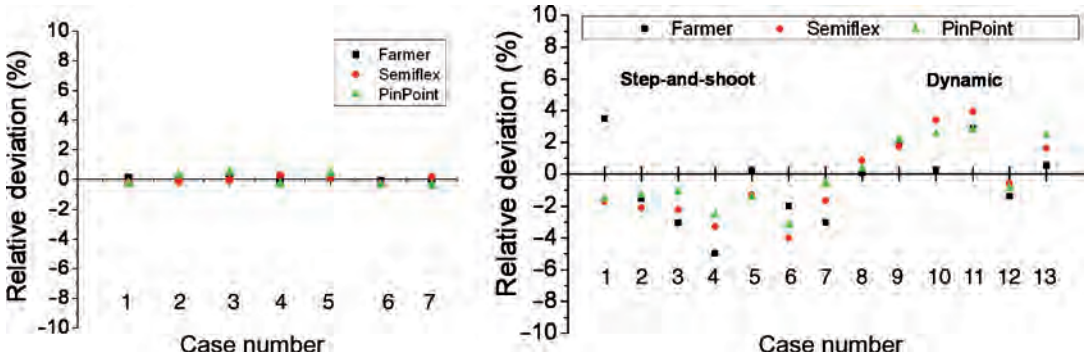

Figure A.2.11. Results of an IAEA dosimetry audit at multiple cancer centers. The left panel shows excellent agreement between the expected (derived from Monte Carlo simulation) and actual absorbed dose for reference calibrations (IAEA TRS-398 protocol) for several types of ionization chambers. The right panel shows the results for the same ionization chambers when used to validate the expected absorbed dose for IMRT. Clearly, the absorbed-dose uncertainty for IMRT is much larger than for calibration conditions. There is evidence of a difference in results depending on whether step-and-shoot IMRT (static IMRT) or dynamic IMRT is used. (From Sánchez-Doblado *et al.*, 2007; reproduced with permission.)

The absorbed dose is always integrated throughout the length of time that the IMRT irradiation takes place. The dosimetry system should be checked to make sure that it has negligible absorbed-dose-rate or time dependence. The method is particularly valuable for determining the absorbed dose near a sensitive normal-tissue structure such as the skin over the parotid gland. The limitation of *in vivo* dosimetry is that the absorbed dose at only one or a few points is determined and the irradiation of any of the measurement points may not be typical of the target volume. In IMRT, there can also be significant gradients at the measurement point that make the reading more uncertain.

It is possible to use a multi-element exit detector to determine the actual absorbed dose delivered in the patient. McNutt *et al.* (1996) first demonstrated the reconstruction of the absorbed dose delivered based on a CT scan of the patient obtained at the time of treatment and using a multi-element ion-chamber-based portal-imaging system to measure the exit absorbed dose. Since then this has been an active area of investigation (Kapatoes *et al.*, 1999; 2001a; 2001b; Partridge *et al.*, 2002; Pasma *et al.*, 1999; Yan *et al.*, 1999). There are two day-to-day variations that must be considered in absorbed-dose reconstruction: the variation of the patient anatomy or setup, and the variation of the incident intensity pattern. Of these two variations, the patient-related one is the more critical because a setup error, weight gain or loss, and tumor shrinkage or growth can greatly perturb the planned absorbed-dose distribution (Kapatoes *et al.*, 2001b). The TomoTherapy Hi-Art™ system recomputes the actual absorbed dose to the patient and superimposes it on the CT scan taken during treatment (Mackie and Tomé, 2008). This information can be used to determine if the plan should be modified for subsequent fractions.

A.2.3.5 Recommendations for Accuracy of Absorbed-Dose Delivery. Van Dyk *et al.* (1993) first proposed that the choice of metrics to specify the accuracy of absorbed-dose distributions should depend on whether the absorbed dose is being measured in a low-gradient or in a high-gradient region (see Figure A2.12). Their work described accuracy criteria for measurements related to the commissioning of dosimetry equipment, and not for measuring complex absorbed-dose distributions produced by IMRT; although the same principles still apply.

An algorithm and software tool that examines both absorbed-dose difference and DTA of absorbed dose was developed by Harms *et al.* (1998). With this method, a calculated absorbed-dose distribution is compared with a measured absorbed-dose distribution using threshold absorbed-dose difference and DTA criteria, ΔD_M and Δd_M, respectively. The calculated absorbed dose is evaluated at points within the measured absorbed-dose distribution. If either the absorbed-dose difference or the distance to agreement of absorbed dose criteria mentioned above is not met, further investigation can be warranted. In low-gradient regions, a large DTA will likely be mitigated by a small absorbed-dose difference, while in high-gradient regions a large absorbed-dose difference will likely be mitigated by a small DTA. The method proposed by Harms *et al.* (1998) is a binary, pass–fail test, the results of which are difficult to display meaningfully. A binary display does not indicate the degree of failure, so rather the absorbed-dose difference in regions of failure is sometimes displayed.

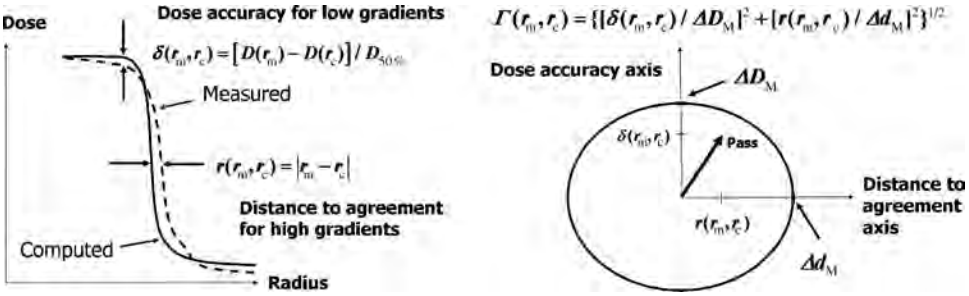

Figure A.2.12. The distinction between absorbed-dose accuracy and DTA and their application to computing the gamma function. The left panel defines the absorbed-dose accuracy and indicates that it is more relevant for points in low-gradient regions, whereas distance to agreement is more relevant for points in high-gradient regions. For each point in a absorbed-dose distribution, gamma is a function of both the absorbed-dose accuracy and distance to agreement without any distinction made about the magnitude of the absorbed-dose gradient at the point. A gamma value is used as the criterion to determine if sufficient accuracy of absorbed-dose delivery is achieved at the point. On the right panel, the pair of values $[r(r_m, r_c), \delta(r_m, r_c)]$ for a point in the absorbed-dose distribution falls within an ellipse with major axes defined by ΔD_M, the metric for absorbed-dose agreement, and Δd_M, the metric for DTA accuracy, so this point passes the criterion. It can be seen that it is possible for each criterion to separately pass, but the combination of both criteria to fail (with the vector outside the ellipse). The gamma-function test is therefore more difficult to pass than each of the metrics of absorbed-dose accuracy or distance to agreement in isolation, with a distinction based on the magnitude of the absorbed-dose gradient. The gamma function is calculated for each point in the absorbed-dose distribution and can be used to create a gamma map, which is a distribution of accuracy for the absorbed-dose distributions or can be compiled into a histogram (see Figure A2.13).

As an extension to the above technique, Low *et al.* (1998c) and Depuydt *et al.* (2002) proposed a metric called a gamma value that combines absorbed-dose difference and DTA criteria in a continuous distribution. The gamma value is a measure of how closely the calculated distribution matches the measured distribution, at a given measurement point. The gamma value will increase with (1) DTA and (2) absorbed-dose difference between measured and calculated values. Following the criteria of Harms *et al.* (1998), a calculation point at the same location as the measurement but with an absorbed-dose difference of ΔD_M will receive a penalty of 1, as will a calculation point indicating the same absorbed dose as the measurement point but being a distance Δd_M away. Using a quadrature sum, all calculation points will receive a penalty value Γ given by

$$\Gamma(r_m, r_c) = \left[\frac{r^2(r_m, r_c)}{\Delta d_M^2} + \frac{\delta^2(r_m, r_c)}{\Delta D_M^2}\right]^{1/2}, \qquad (A.2.1)$$

where this equation describes an orthogonal space defined by a DTA dimension and an absorbed-dose-error dimension with

$$r(r_m, r_c) = |r_m - r_c|, \qquad (A.2.2)$$

and

$$\delta(r_m, r_c) = \frac{D(r_m) - D(r_c)}{D_{\text{prescription}}}, \qquad (A.2.3)$$

where r_m is the position of the measured absorbed-dose voxel, r_c the position of the calculated absorbed dose, and $D(r_m)$ and $D(r_c)$ are the absorbed doses at locations r_m and r_c, respectively. For example, a calculation point that is a distance $\Delta d_M/2$ from the measurement point and indicates an absorbed-dose difference of $\Delta D_M/2$, will receive a Γ value of $1/\sqrt{2}$ or 0.707. Note that here the absorbed-dose-difference criteria are normalized to the prescription absorbed dose, which is also the median absorbed dose, $D_{50\ \%}$.

One can imagine a plane of points r_c, also containing the point r_m, against which is plotted an absorbed-dose-difference surface $\delta(r_m,r_c)$. Figure A2.12 shows an ellipsoid centered on r_m, with major axes of length Δd_M and ΔD_M, within which $\Gamma < 1$. If the criterion point falls within the ellipse, it passes. Once a set of Γ values is determined for all points r_c, the minimum can be found and assigned to the final gamma value for point r_m:

$$\gamma(r_m) = \min[\Gamma(r_m, r_c)] \quad \forall r_c. \qquad (A.2.4)$$

These values can be plotted on a continuous color scale, for example, or could be converted to a threshold and plotted as a binary function (Depuydt *et al.*, 2002). Agazaryan *et al.* (2003) plotted the gamma function $\gamma(r_m)$ along the trajectory of a selected isodose line. The gamma function is often turned into a histogram or a map. Figure A2.13 illustrates a gamma map.

The accuracy of IMRT delivery has been tested by many groups (Adams *et al.*, 2004; Clark *et al.*, 2002; Dong *et al.*, 2003; Ibbott, 2009; Ibbot *et al.*, 2008; Tomsej *et al.*, 2005; Winkler *et al.*, 2005; Zefkili *et al.*, 2004). Mature institution-specific QA programs generally provide better dosimetry QA.

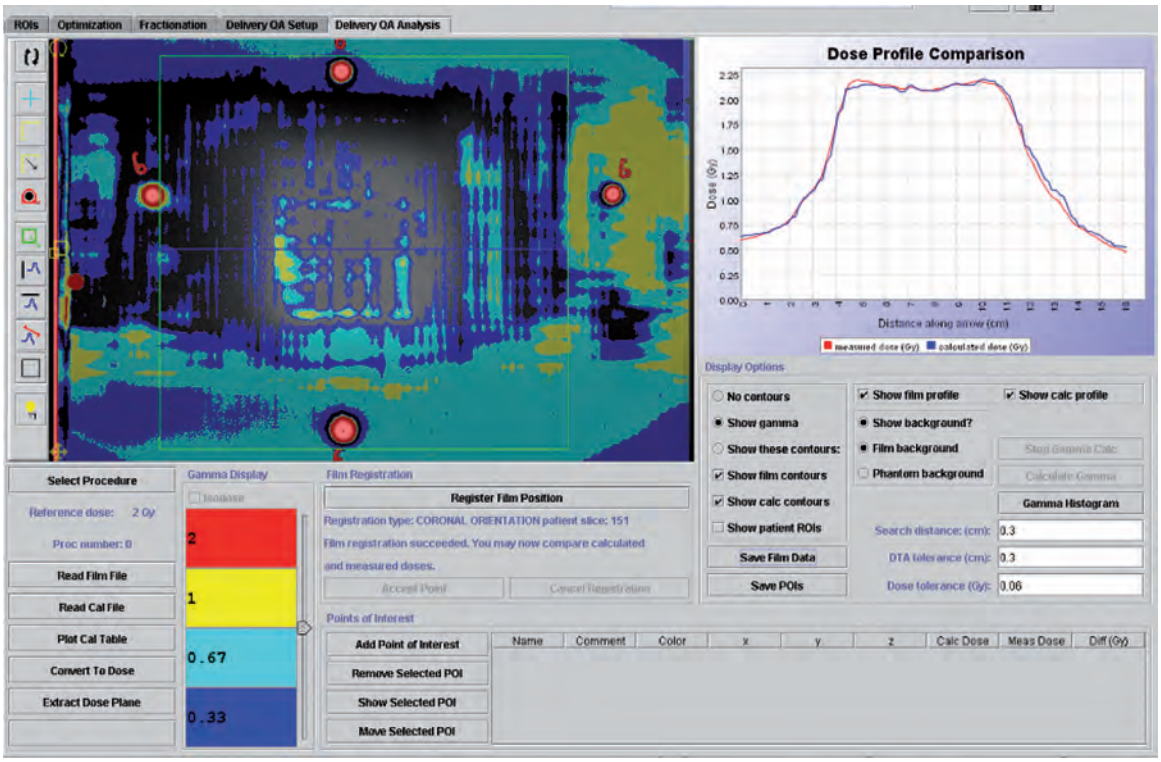

Figure A.2.13. A gamma map of a comparison between a computed absorbed-dose distribution and film measurements for a helical tomotherapy absorbed-dose distribution in a cylindrical phantom. The criteria selected were $\Delta d_M = 3$ mm (DTA) and $\Delta D_M = 3$ % (absorbed-dose difference), which corresponded to a 0.0006 Gy absorbed-dose difference. The color scale indicates the relative gamma values. Black corresponds to a gamma value below 0.33; dark blue corresponds to a gamma value above 0.33 but less than 0.67; light blue corresponds to a gamma value above 0.67 and below or equal to 1; yellow corresponds to gamma values above 1 but below or equal to 2; red corresponds to gamma values greater than 2. An absorbed-dose profile comparing the calculated and measured values is also shown. The profile indicates that the calculated and measured values agree well inside the field except near the left boundary, which has a gamma value above 1. The four circular regions are due to pin marks placed on the film for purposes of alignment.

For example, Clark *et al.* (2002) and Winkler *et al.* (2005) found relative agreement typically of 2 % between single-point measurements and calculations. Dong *et al.* (2003) reported, for 1591 irradiations performed at M.D. Anderson Hospital in Houston, TX, USA, that they were able to control the absorbed dose to within an average of 0.5 % (systematic uncertainty) with a standard deviation of 2.5 % (random uncertainty). Adams *et al.* (2004) found that in 50 % of cases measurements and calculations agreed to within 2 % in low-gradient regions and to within 3 % in high-gradient areas. Multi-institutional audits revealed more uncertainty. The Radiation Physics Center (RPC) at M.D. Anderson Hospital in Houston, TX, USA, is responsible for credentialing the dosimetry of Radiation Therapy Oncology Group (RTOG) trials at member institutions. Using specially designed anthropomorphic phantoms RPC determined that agreement between calculation and measurement is often not reached for many sites when the criteria are set at 7 % for low-gradient points and 4 mm for high-gradient points (Ibbott, 2009). In a sample of 472 institutions using 632 irradiations of head-and-neck sites, only 75 % of the irradiations met the 7 %/4 mm criteria. The passing rate for head-and-neck fell to 58 % when the criteria were tightened to 5 %/4 mm. Their results were similar to those reported by the GORTEC consortium for head-and-neck dosimetry (see Figure A2.10). For a multi-institutional audit of pelvic irradiations, the pass rate was better; 82 % passed for the 7 %/4 mm criteria. A nine-institution end-to-end planning and delivery QA intercomparison was described in the AAPM TG-119 Report (Ezzell *et al.*, 2009). All of these centers were credentialed for IMRT delivery by the RPC. Collectively, they tested most of the IMRT systems in widespread use and used a 3 mm DTA and 3 % absorbed-dose accuracy for their gamma criteria. All but one of these institutions had 95 % or more points pass the gamma test with these criteria.

The uncertainty criteria should be based on differentiating between high and low gradients. The criteria values for uncertainty chosen should be somewhat better than has been reported in multi-

institutional audits, but it is unreasonable to expect that they can be as accurate as those reported for large single institutions with an established QA program. In addition, Sánchez-Doblado *et al.* (2007) concluded that the one-standard-deviation uncertainty for ionization-chamber dosimetry alone was about 2.5 % for IMRT. AAPM TG-142 (Klein *et al.*, 2009) recommends weekly checks to ensure that the linac output is within 3 %. With these considerations, it is recommended that for a low-gradient (<20 %/cm) region, the difference between the measured (or independently computed) absorbed dose and the treatment-planning absorbed dose, normalized to the absorbed-dose prescription (*e.g.*, $D_{50\ \%}$) should be no more than 3.5 %. If the differential (absorbed-dose-deviation)-volume histogram is approximately a normal distribution with a standard deviation of about 3.5 %, with respect to the prescription absorbed dose, it means that about 85 % of points should be within 5 % of the desired value (normalized to the prescription absorbed dose). For comparison, the value of 5 % was the original ICRU requirement for accuracy of delivery at the ICRU Reference Point (ICRU, 1993). For high-gradient (>20 %/cm) regions, the accuracy of DTA should be 3.5 mm, which if the DTA histogram is normally distributed, means that 85 % of the samples should be within a 5 mm DTA. Setting the gamma criterion to the same values would result in a more conservative test than the above criteria (see Figure A2.12). There would be fewer points passing a gamma-function criterion than passing our recommended criteria in which a separate criterion is set for high gradients and low gradients.

In the future, the recommended accuracy criteria might be made more stringent. Reductions in absorbed-dose-calculation uncertainty are possible with the use of direct Monte Carlo simulations. More clinically relevant ionization-chamber dosimetry protocols are under development (Alfonso *et al.*, 2008) that should improve dosimetry accuracy for IMRT. Smaller, more tissue-equivalent dosimeters that require fewer corrections for absolute dosimetry might also become available. Finally, future audits might reveal that a significant fraction of treatment centers can achieve accuracies much better than the recommended criteria. However, it is unclear if setting tighter constraints will produce a significant change in clinical outcome as long as rigorous patient-specific QA is maintained and deviations from the recommended accuracy are addressed on a case-by-case and clinic-by-clinic basis.

Investigative action that should be taken if a significant number of points fail to meet either DTA or absorbed-dose agreement depends on the institution and treatment site. Additional measurements might confirm an inability to accurately compute the absorbed-dose distribution to a particular patient, or perhaps machine QA problems. Issues with machine QA would not be revealed if the comparison of the planning-absorbed-dose calculation was with an independent absorbed-dose calculation instead of a measurement. It might be that the absorbed-dose-difference map or gamma map revealed that the planning absorbed dose agreed with the measurement or independent calculation at some locations but not at others. The location of the disagreement should be discussed with the radiation oncologist to see if it is of clinical concern. Falsely inaccurate results such as a measurement error due to setting up a phantom incorrectly might also be discovered. If it is a concern and if additional analysis does not improve the agreement, a new treatment plan, perhaps using non-IMRT techniques should be considered. The process of resolving issues of accuracy should be fully discussed and well documented.

Journal of the ICRU Vol 10 No 1 (2010) Report 83
Oxford University Press
doi:10.1093/jicru/ndq012

Appendix B: Clinical Examples

B.1 Case Number B1. Squamous-Cell Carcinoma of the Supra-Glottic Larynx

B.1.1 Clinical Situation

A 59-year-old man with a long history of smoking presented with a 3-month history of progressive hoarseness. The patient had a good performance status with a Karnofsky index of 90 (ECOG 1). A fiberoptic examination and endoscopy under general anesthesia revealed an exophytic lesion of the right endolarynx extending from the right ary-epiglotic fold to the level of the right false vocal cord, which was infiltrated (see Figure B.1.1). The right hemi-larynx was fixed. A biopsy showed a moderately differentiated squamous-cell carcinoma (ICD-O histopathologic code 8070/3). No lymph node was palpated in the neck. Magnetic resonance imaging (MRI) showed an infiltration of the pre-epiglottic space (see Figure B.1.2). No lymph node was visualized. A computed tomographic (CT) scan of the chest did not find any metastasis or second primary. An endoscopy of the esophagus did not show any primary esophageal tumor.

The clinical classification was: T3–N0–M0, stage 3 of the supraglottic larynx (ICD-O 10: C32.1).

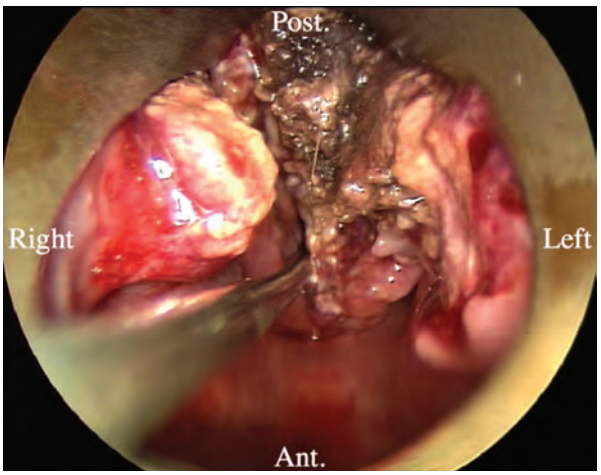

Figure B.1.1. Superior view showing the exophytic tumor of the right hemi-larynx.

B.1.2 Treatment Intent

After discussion at the head-and-neck tumor board, it was decided to treat this patient with curative intent by radiotherapy using simultaneous integrated-boost intensive-modulated radiation therapy (SIB-IMRT).

B.1.3 Patient Positioning and Image Acquisition

The patient was immobilized with a thermoplastic mask (head, neck, shoulder) in a supine position. The patient underwent a planning CT with contrast enhancement on a dual-detector spiral CT (120 kV, 330 mAs) using a slice thickness of 2.7 mm, a reconstruction interval of 2 mm, hence a pitch of 0.7. A volume of 60 ml of contrast medium was injected intravenously at a rate of 1 ml/s, followed after a rest period of 3 min by a bolus injection of 50 ml. Image acquisition started just after the end of the second injection. Slices were acquired from the level of the frontal sinus to the sternoclavicular junction.

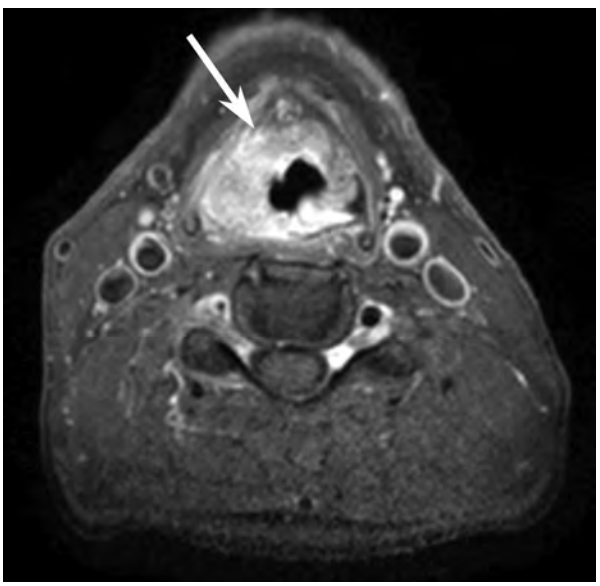

Figure B.1.2. Transverse T1-weighted MR image with fat saturation. The infiltration of the pre-epiglottic space is indicated by the arrow.

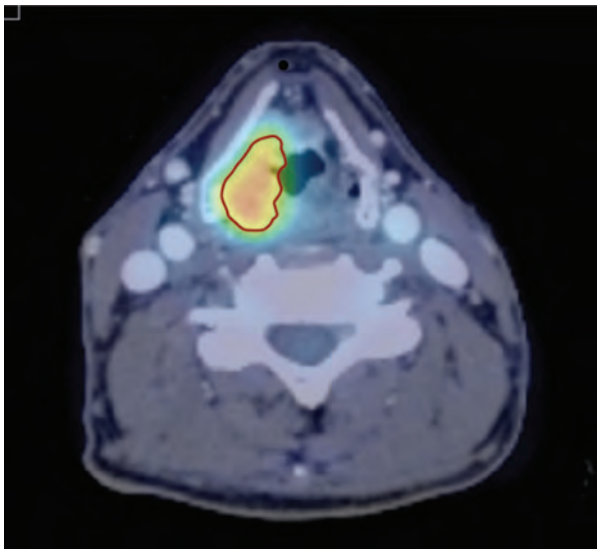

Figure B.1.3. Fusion of the FDG-PET image on the planning CT (axial view). The GTV (red contour) has been automatically delineated using a gradient-based method.

The patient also underwent a planning FDG-PET scan. After fasting for 6 h, the patient was immobilized with a thermoplastic mask on a flat tabletop. A 2 min transmission scan with a Germanium source was first performed. A total of 370 MBq (10 mCi) of FDG was injected intravenously, and the emission acquisition started 60 min later. Images were reconstructed and segmented after deblurring and denoising (Lee *et al.*, 2008).

B.1.4 Target Volumes

B.1.4.1 Gross Tumor Volume. The primary-tumor gross tumor volume (GTV) was automatically delineated from the FDG-PET scan, GTV-T (FDG-PET, 0 Gy), using a gradient-based method (Geets *et al.*, 2007a) (Figure B.1.3).

B.1.4.2 Clinical Target Volume. For the lymph nodes, the bilateral levels II to IV were selected as clinical target volume (CTV)-N according to the recommendations of Grégoire *et al.* (2003c).

For the primary tumor, two different CTVs were delineated: a CTV-T1 encompassing the entire mucosa of the larynx (sub-glottic, glottis, and supra-glottic), the pre-epiglottic space, the para-laryngeal space, and the thyroid cartilage; a CTV-T2 was delineated as a 5 mm extension of the GTV-T (FDG-PET, 0 Gy).

B.1.4.3 Planning Target Volume. A 4 mm margin was automatically added to all CTVs to define the planning target volumes (PTVs). In the direction of the skin, only a 1 mm margin was added to the CTVs-N.

B.1.4.4 Organs at Risk and Planning Organ-at-Risk Volume. The following organs at risk (OAR) were delineated:

- the spinal cord down to the first thoracic vertebra including C7;
- the brain stem;
- both parotid glands.

A 4 mm margin was added around the spinal cord to define the planning organ-at-risk volume (PRV) of the spinal cord. For the brain stem and the parotid glands, the PRVs were equal to the OARs.

Table B.1.1. Dose–volume constraints for the PTVs, PRVs, and OARs for Case B1.

Target volume (OAR/PRV)	$D^{a}_{95\ \%}$	$D_{\text{near-min}}$ or $D_{98\ \%}$	$D_{\text{near-max}}$ or $D_{2\ \%}$	Median absorbed dose or $D_{50\ \%}$	Mean absorbed dose
PTV-N and PTV-T1	≥95 % of planned absorbed dose	≥90 % of planned absorbed dose	≤107 % of planned absorbed dose	55.5 Gy	—
PTV-T2	≥95 % of planned absorbed dose	≥90 % of planned absorbed dose	≤107 % of planned absorbed dose	69 Gy	—
PRV spinal cord	—	—	≤50 Gy	—	—
Spinal cord	—	—	≤48 Gy	—	
PRV contralateral parotid[b]	—	—	—	—	≤26 Gy
PRV ipsilateral parotid[b]	—	—	—	—	≤40 Gy

[a] D_V: absorbed dose in fraction V of the volume.
[b] The PRV was defined as the parotid gland.

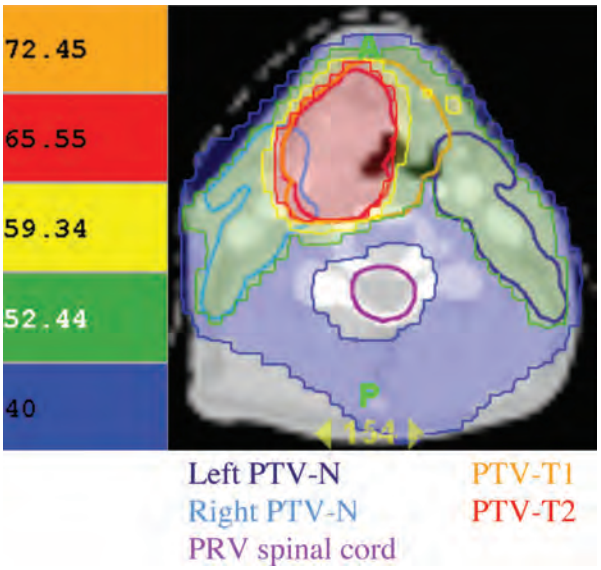

Figure B.1.4. Color wash of the absorbed-dose distributions (in Gy) for the various PTVs. An absorbed dose of 55.5 Gy (30 × 1.85 Gy, in 6 weeks) was prescribed to the PTV-T1 (FDG-PET, 0 Gy) and the PTV-N (CT, 0 Gy,), whereas an absorbed dose of 69 Gy (30 × 2.3 Gy, in 6 weeks) was prescribed to the PTV-T2 (FDG-PET, 0 Gy). The 72.4 Gy and 65.6 Gy isodoses correspond to 107 % and the 95 % of prescribed absorbed dose to the PTV-T2, respectively; the 59.3 Gy and 52.4 Gy isodoses correspond to 107 % and the 95 % of prescribed absorbed dose to PTV-T1 and PTV-N, respectively.

B.1.5 Planning Aim

The following planning median absorbed-dose ($D_{50\ \%}$) prescriptions were selected for the various PTVs. An SIB-IMRT technique was used (*i.e.*, all PTVs were simultaneously treated).

- PTV-N: 55.5 Gy in 30 fractions of 1.85 Gy in 6 weeks.
- PTV-T1: 55.5 Gy in 30 fractions of 1.85 Gy in 6 weeks.
- PTV-T2: 69 Gy in 30 fractions of 2.3 Gy in 6 weeks.

The planning absorbed-dose constraints used are listed in Table B.1.1.

B.1.6 Treatment-Planning System and Treatment Unit

The patient was planned and treated with IMRT using a HiArt unit (Tomotherapy Inc., Madison, WI, USA). A collimator width of 2.5 cm, a pitch of 0.215, and a modulation factor (defined as the ratio of the maximum opening time for any leaf divided by the mean opening time for all leaves used) of 2 were selected (Mackie *et al.*, 2003). Absorbed-dose calculations were performed using convolution/superposition and collapsed-cone algorithms with heterogeneity corrections.

B.1.7 Prescription

The plans and all associated technical data were approved by the treating physician, *i.e.*, to deliver a median absorbed dose ($D_{50\ \%}$) per fraction of 2.3 Gy to a total absorbed dose of 69 Gy to PTV-T2 according to the absorbed-dose

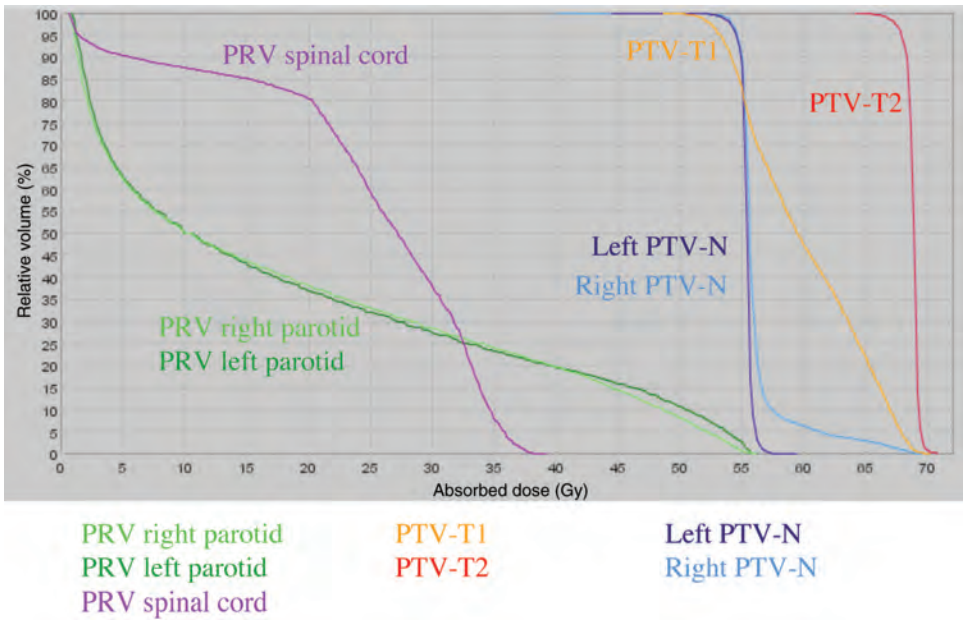

Figure B.1.5. Comparison of dose–volume histograms (DVHs) for the various PTVs and PRVs for Case B1. The relative volumes are normalized to the total volumes of the region of interests and expressed as percent. The various absorbed-dose metrics derived from these DVHs are reported in Table B.1.2. The large difference between the DVH for PTV-T2 and PTV-T1 is not so apparent in the section presented in Figure B.1.4. The section refers to an absorbed-dose distribution in a plane and does not necessarily reflect the absorbed-dose distribution in a volume.

Table B.1.2. Planned and reported absorbed-dose metrics for the CTVs, PTVs, OARs, and PRVs for Case B1.

	$D_{\text{mean}} \pm$ SD (Gy)	D_{median} or $D_{50\ \%}$ (Gy)	$D_{\text{near-min}}$ or $D_{98\ \%}$ (Gy)	$D_{95\ \%}$ (Gy)	$D_{\text{near-max}}$ or $D_{2\ \%}$ (Gy)
PTV-T2	68.9 ± 0.5	69.0 (69.0)[a]	67.0 ($\geq$62.1)	67.3 ($\geq$66.5)	69.6 ($\leq$73.7)
CTV-T2	69.4 ± 0.6	69.3	68.1	68.5	70.6
PTV-T1	60.9 ± 4.8	61.1 (55.5)	52.4 ($\geq$49.9)	53.4 ($\geq$52.7)	68.5 ($\leq$59.4)
CTV-T1	65.7 ± 4.0	66.9	55.2	56.0	70.4
Left PTV-N	55.4 ± 0.6	55.5 (55.5)	53.7 ($\geq$49.9)	54.3 ($\geq$52.7)	56.5 ($\leq$59.4)
Left CTV-N	55.7 ± 0.5	55.7	54.2	55.0	56.5
Right PTV-N	56.4 ± 2.6	55.7 (55.5)	53.7 ($\geq$49.9)	53.8 ($\geq$52.7)	66.7 ($\leq$59.4)
Right CTV-N	56.3 ± 2.2	55.8	54.0	54.5	65.2
PRV spinal cord	24.2	25.7	0.9	—	36.7 ($\leq$50.0)
Spinal cord	23.1	23.4	0.9	—	36.8 ($\leq$48)
PRV right parotid	18.5 (40)	10.2	1.1	—	54.9
PRV left parotid	18.3 (26)	10.5	0.9	—	53.8

[a]The planning-aim absorbed doses are given in parentheses.

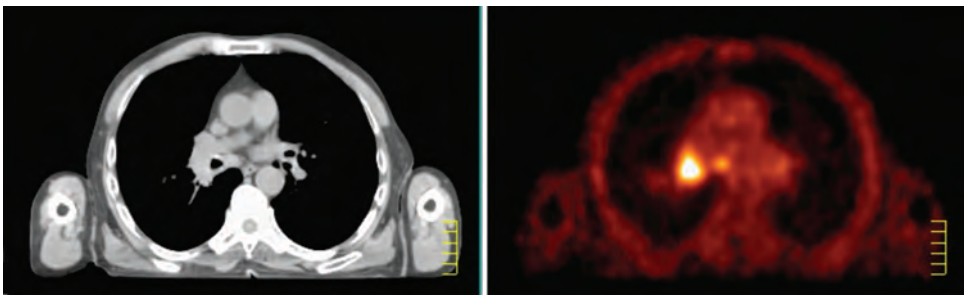

Figure B.2.1. Transverse CT (left) and FDG-PET (right) slices showing tumor in the left hilus with a lymph node in region VII.

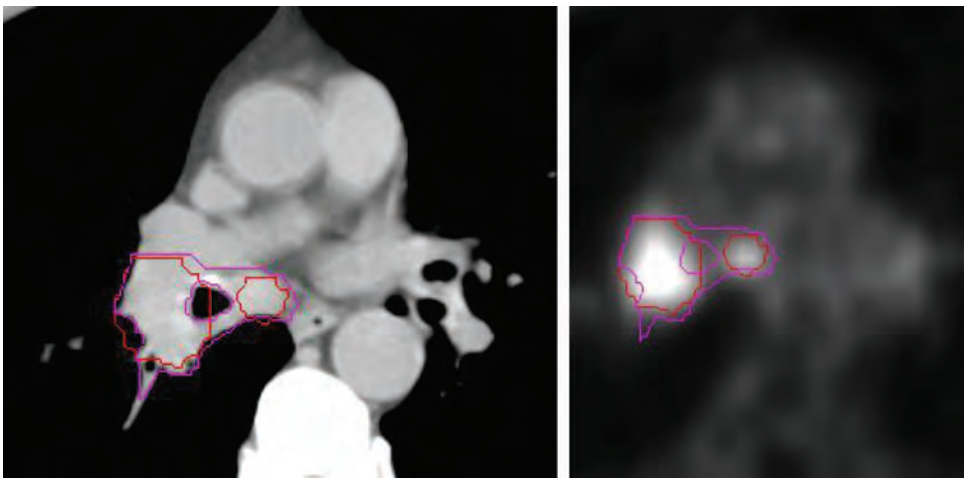

Figure B.2.2. Gross tumor volume delineated on CT (left panel) using an automatic gradient-based delineation of the FDG-PET images (right panel). The GTV-T (FDG-PET, 0 Gy) and GTV-N (FDG-PET, 0 Gy) are displayed in red; the GTV T + N (FDG-PET + CT, 0 Gy) is displayed in pink in both panels.

distributions presented in Figures B.1.4 and B.1.5, and in Table B.1.2. Prescribing PTV-T2 to 69 Gy did not allow the planning aims of 55.5 Gy to the right PTV-N and to the PTV-T1; therefore, total median absorbed doses of 55.7 Gy and 61.1 Gy were prescribed to the right PTV-N and the PTV-T1, respectively.

B.1.8 Quality Assurance

An individualized patient quality assurance (QA) was performed on a dedicated phantom before the start of treatment. All measurements were within 5 % of the expected absorbed-dose distributions. Before each fraction, the patient underwent a

Table B.2.1. Dose–volume constraints the PTVs, PRVs, and OARs for Case B2.

Target volume (OAR/PRV)	D_{median} or $D_{50\ \%}$	$D_{\text{near-min}}$ or $D_{98\ \%}$	$D_{\text{near-max}}$ or $D_{2\ \%}$	$D_{33\ \%}$	$D_{67\ \%}$	$V_{20\ \text{Gy}}$	$V_{30\ \text{Gy}}$
PTV-T + N (FDG-PET + CT, 0 Gy)	70 Gy	≥95 % of planned absorbed dose	≤107 % of planned absorbed dose				
PRV spinal cord	—	—	<55 Gy				
Lungs	—	—	—			<30 %	<20 %
PRV esophagus	—	—	—	<60 Gy	<54 Gy		
Heart	—	—	<62 Gy				
Liver	<30 Gy						

Table B.2.2. Beam directions used for IMRT planning of centrally located lung tumor.

Equipment	Beam number								
	1	2	3	4	5	6	7	8	9
Couch[a]	0	0	0	45	45	45	315	315	315
Gantry[a]	0	155	205	315	30	60	300	330	45
Collimator[a]	0	0	0	325	319	333	27	41	35

[a]Couch, gantry, and collimator rotation are in degrees.

megavoltage CT (MVCT) allowing for daily repositioning.

B.1.9 Dose Reporting

The composite absorbed-dose distributions, DVHs, and the various dose metrics are reported in Figures B.1.4 and B.1.5, and in Table B.1.2.

B.2 Case Number B2. Squamous-Cell Carcinoma of the Lung

B.2.1 Clinical Situation

A 70-year-old man stopped smoking 15 years previously after an exposure of 20 pack-years. His medical history was a cholecystectomy 7 years prior and coronary stenting 3 years prior. He takes cardio-aspirin. Following a bronchopneumonia not resolved after 2 weeks of antibiotics, a chest x ray showed a right para-hilar mass. The patient had a good performance status with a Karnofsky index of 90 (ECOG 1). A CT scan showed the tumor, located in the apex of the lower lobe of the right lung and an enlarged infra-carinal (region 7) node. The tumor extended between the pulmonary vessels and the right main bronchus. Fiberoptic bronchoscopy showed an endoluminal mass in the right lower lobar bronchus. Histological examination of biopsies indicated a squamous-cell carcinoma grade-II. A full-body PET-CT showed FDG-avid regions at the location of the lung tumor and the sub-carinal node (see Figure B.2.1). No distant metastasis was found in the bone, liver, or brain. Trans-esophageal ultrasound-guided needle aspiration of the node in region 7 showed carcinoma cells. Respiratory function parameters showed that the patient was fit for combined treatment by chemo- and radiotherapy.

The clinical classification was: T3–N2–M0, stage IIIa carcinoma of the lower lobe of the right lung (ICD-O 10: C34.3).

B.2.2 Treatment Intent

The treatment intent was curative. After discussion at the lung cancer board, induction chemotherapy, including cisplatin and gemcitabin, followed by radiotherapy (IMRT) was proposed. Re-evaluation after two cycles of chemotherapy showed stable disease. A third cycle was given, followed by radiotherapy.

B.2.3 Patient Positioning and Image Acquisition

Imaging for planning consisted of FDG-PET and CT scans on an integrated PET-CT scanner with the patient lying on a flat couch in the supine position, the arms alongside the body, using a neck support and a knee rest. The patient was instructed to breathe quietly. Two sequential sets of 5 mm CT slices were acquired (120 kV, 250 mAs) covering the region from the vertex to the upper iliac spine. The first set was acquired with a field of view (FOV) of 60 cm and without intravenous contrast medium. It was used for attenuation correction of PET images and for absorbed-dose computations. The second set, acquired with intravenous contrast medium, was used for delineation of target volumes and OARs. A volume of 75 ml of contrast medium was injected intravenously at a rate of 1 ml/s. The acquisition of the second CT image set (50 cm FOV) started after 60 ml of contrast medium had been injected.

For the PET scan, 3.7 MBq (0.1 mCi) of FDG per kilogram was injected intravenously, and the emission acquisitions (5 min per bed position) started 50 min later. All images were transferred through a

Table B.2.3. Planned and reported absorbed-dose metrics for CTVs, PTVs, OARs, and PRVs for Case B2.

Target volume (OAR/PRV)	D_{median} or $D_{50\ \%}$ (Gy)	$D_{near\text{-}min}$ or $D_{98\ \%}$ (Gy)	$D_{near\text{-}max}$ or $D_{2\ \%}$ (Gy)	$D_{33\ \%}$ (Gy)	$D_{67\ \%}$ (Gy)	$V_{20\ Gy}$ (%)	$V_{30\ Gy}$ (%)
PTV-T + N (FDG-PET + CT, 0 Gy)	70.3 (70.0)[a]	67.4 (≥66.5)	72.8 (≤74.9)				
CTV-T + N (FDG-PET + CT, 0 Gy)		68.2					
GTV-T + N (FDG-PET + CT, 0 Gy)		68.2					
PRV spinal cord			23.7 (<55.0)				
Lungs			-			27.4 (<30.0)	17.7 (<20.0)
PRV esophagus			72.1	50.3 (<60.0)	1.9 (<54.0)		
Heart			12.8 (<62.0)		0.6		
Liver	0.4 (<30.0)						
Left kidney			2.0				
Right kidney			5.0				

[a] The planning-aim absorbed doses or percentages are given in parentheses.

local network to the Version 6.2b Pinnacle treatment-planning system (Philips Medical Systems, Andover, MA, USA).

B.2.4 Target Volumes

B.2.4.1 Gross Tumor Volume. The GTV was delineated using a two-step procedure. The first step involved an automatic delineation of the FDG-avid primary tumor and lymph node using the signal-to-background approach reported by Daisne *et al.* (2003). The PET scan was acquired during quiet breathing and thus included internal motion. The auto-delineated lesions from the PET scan were defined as GTV-T (FDG-PET, 0 Gy) and GTV-N (FDG-PET, 0 Gy) (see Figure B.2.2). In a second step, the GTV-T + N (FDG-PET + CT, 0 Gy), which is the GTV delineation based on the information from both imaging modalities, was defined by overlaying the GTV-T (FDG-PET, 0 Gy) and the GTV-N (FDG-PET, 0 Gy) on the CT scan and by modifying the auto-delineated volume where the CT scan information was considered contributory. Lung-window setting was used to study the edge between lung tissue and tumor; mediastinal-window setting was selected to help in defining the edge of tumor and mediastinal tissues.

B.2.4.2 Clinical Target Volume. Elective nodal irradiation was not considered. CTV-T + N (FDG-PET+ CT, 0 Gy) resulted from a 5 mm expansion of GTV-T + N (FDG-PET + CT, 0 Gy) with restrictions on the expansion at anatomical boundaries such as air cavities or apparently normal structures such as the bone, cartilage, or blood vessels.

B.2.4.3 Planning Target Volume. A 5 mm isotropic margin was automatically added to the CTV-T + N (FDG-PET + CT, 0 Gy) to create the PTV-T + N (FDG-PET + CT, 0 Gy).

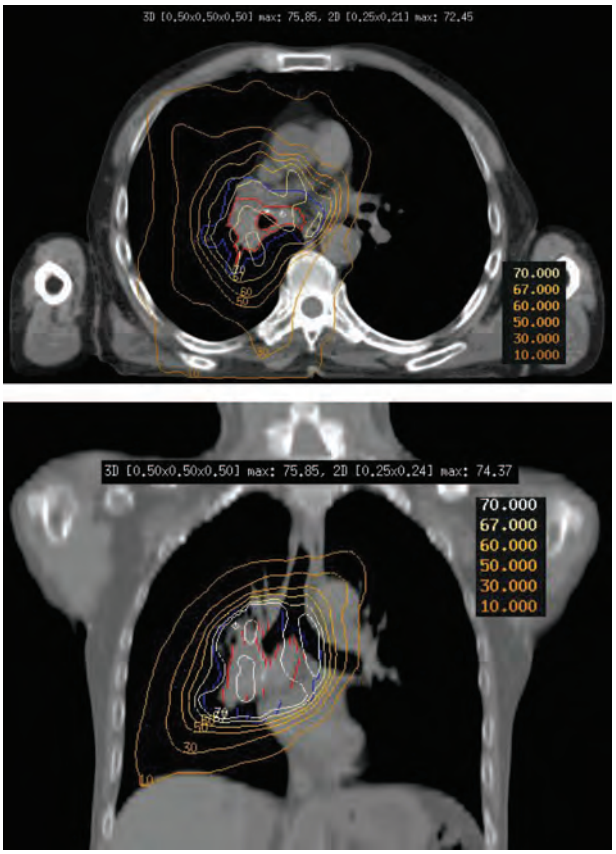

Figure B.2.3. Isodose distribution on transverse (top panel) and coronal (bottom panel) sections. The GTV-T + N (FDG-PET + CT, 0 Gy) is delineated in red; the PTV-T + N (FDG-PET + CT, 0 Gy) is delineated in blue.

B.2.4.4 Organs at Risk and Planning Organ-at-Risk Volume. The following OAR were delineated: spinal cord, left and right lungs, esophagus, heart, liver, left and right kidney.

Planning organ-at-Risk volumes were created for the spinal cord and esophagus by adding a 5 mm margin and a 3 mm margin around each organ,

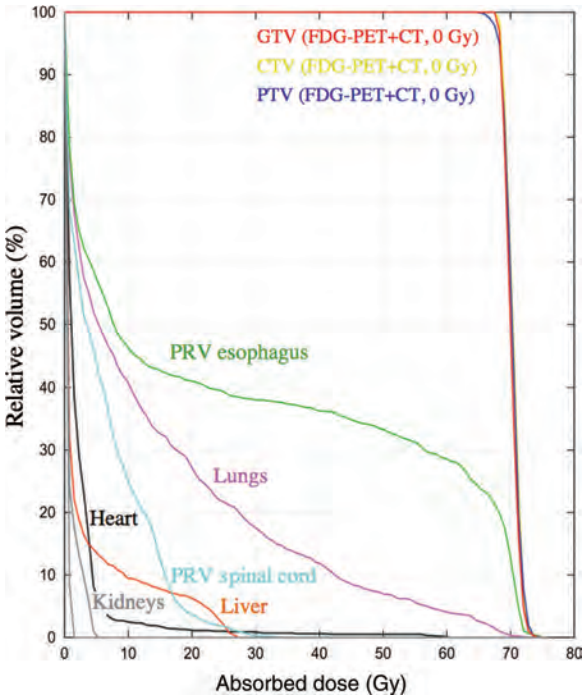

Figure B.2.4. Cumulative DVHs for the PTV, CTV, GTV, OARs, and PRVs for Case B2. The various absorbed-dose metrics derived from these DVHs are reported in Table B.2.3.

respectively, and denoted PRV spinal cord and PRV esophagus. Kidneys and the liver were also delineated because exit trajectories of non-coplanar beam directions might traverse these organs.

B.2.5 Planning Aim

The planning aim for PTV-T + N (FDG-PET + CT, 0 Gy) was a planned median absorbed dose, D_{median}, of 70 Gy in 35 fractions of 2.0 Gy in 7 weeks. The dose–volume constraints used are listed in Table B.2.1.

B.2.6 Treatment-Planning System and Treatment Unit

An IMRT treatment plan for step-and-shoot delivery on an Elekta Sli-plus linear accelerator was made using an in-house-developed extension of the GRATIS (version 12.6.3) software package (Sherouse *et al.*, 1989) that allows automatic creation of initial beam directions and segment outlines (Table B.2.2) (De Gersem *et al.*, 2001a), followed by direct optimization of MLC-leaf positions and monitor-unit (MU) counts of the segments (De Gersem *et al.*, 2001b). Segments that

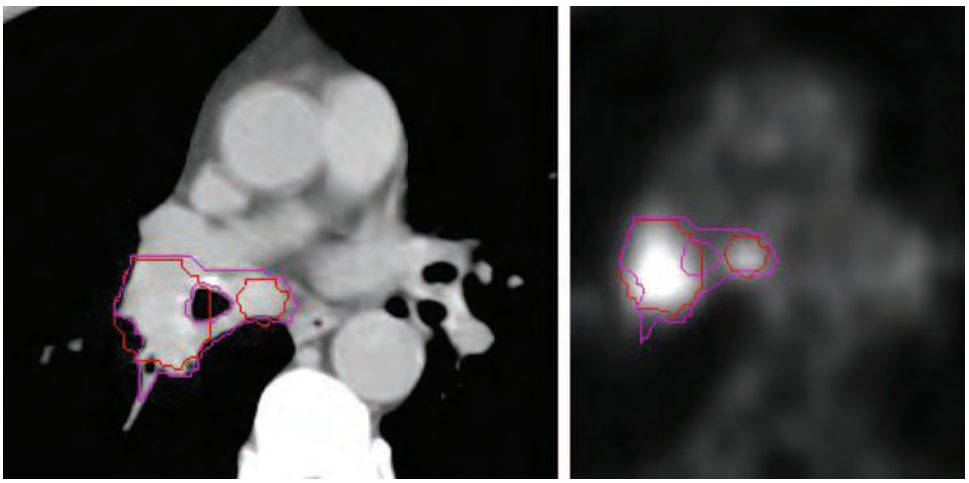

Figure B.3.1. Axial and sagittal CT images for Case B3.

Table B.3.1. Dose–volume constraints for the PTVs, PRVs, and OARs for Case B3.

$D_{\text{near-min}}$ or $D_{98\ \%}$	$D^{\text{a}}_{50\ \%}$		$D^{\text{a}}_{30\ \%}$	$D_{\text{near-max}}$ or $D_{2\ \%}$
≥95 % of planned absorbed dose	78 Gy		—	<107 % of planned absorbed dose
PRV rectal wall[b]	—	≤55 Gy	≤70 Gy	≤79 Gy
PRV bladder wall[b]	—	≤55 Gy	≤70 Gy	≤79 Gy
PRV femurs[b]	—	—	—	≤53 Gy

[a] D_V: absorbed dose in fraction V of the volume.
[b] The PRV was defined as the OAR.

receive less than 2 MU after a cycle of optimization were locked to zero MU (by the planner) for the subsequent cycles. This procedure led to a reduction of the number of beams if all segments are discarded for one or more beam directions. When the planning aims were reached after one or more cycles, optimization was stopped. Otherwise, optimization was stopped when the planner saw that, after many cycles, the planning aims could not be achieved. The absorbed-dose computations between optimization cycles, as well as the final absorbed-dose computation, were performed by the convolution/superposition algorithm in the Version 6.2b Pinnacle planning system (Philips Medical Systems).

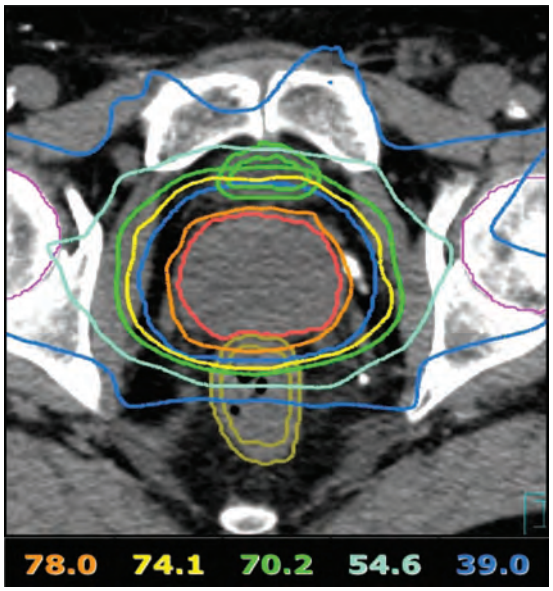

Figure B.3.2. Axial image at the center of the PTV, with isodose distributions (in Gy).

B.2.7 Prescription

The treatment plan (Tables B.2.2 and B.2.3), including all associated technical data, was approved by the treating physician. The absorbed-dose prescription was a median absorbed dose ($D_{50\ \%}$) of 2 Gy per fraction for a total absorbed dose of 70 Gy on the PTV-T + N (FDG-PET + CT, 0 Gy).

B.2.8 Quality Assurance

Quality assurance of the plan was performed by a fully automated procedure using a different

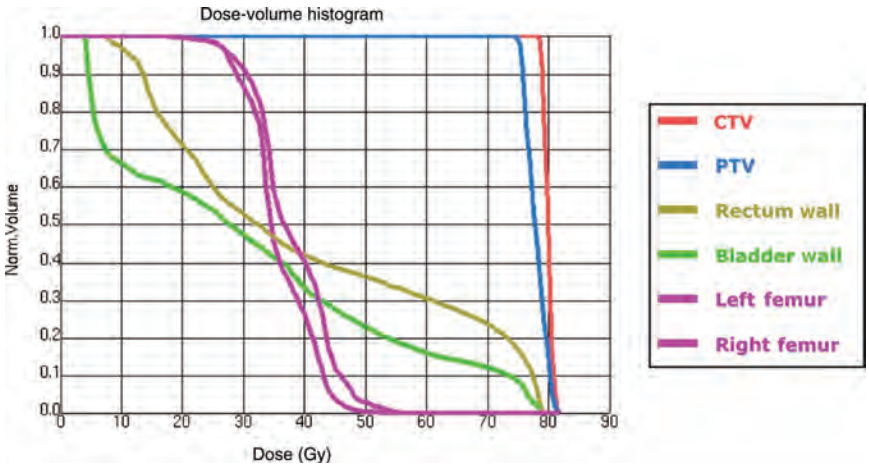

Figure B.3.3. Comparison of DVHs for the PTV and OARs for Case B3. The various absorbed-dose metrics derived from these DVHs are reported in Table B.3.2.

Table B.3.2. Planned and reported absorbed-dose metrics for CTVs, PTVs, OARs, and PRVs for Case B3.

Volume	$D_{\text{near-min}}$ or $D_{98\ \%}$ (Gy)	$D_{50\ \%}$ (Gy)	$D_{30\ \%}$ (Gy)	$D_{\text{near-max}}$ or $D_{2\ \%}$ (Gy)
PTV	74.1 ($\geq$74.1)[a]	78.0	—	81.5 ($<$81.9)
CTV	78.6	—	—	81.5
PRV rectal wall	—	32.2 (55.0)	60.5 (70.0)	78.7 (79.0)
PRV bladder wall	—	27.6 (55.0)	42.5 (70.0)	78.1 (79.0)
PRV left femur	—	—	—	46.5 (53.0)
PRV right femur	—	—	—	51.3 (53.0)

[a]The planning-aim absorbed doses are given in parenthesis.

absorbed-dose computation algorithm (developed in-house). During the first week, orthogonal portal-image sets were acquired daily. Errors of more than 5 mm were corrected on-line. From the images acquired during the first week, the $x-y-z$ coordinates of the systematic set-up error were estimated and were used to correct the set-up for following fractions. Less than daily frequency of portal imaging was accepted if set-up errors remained repeatedly below 5 mm.

B.2.9 Dose Reporting and Plan Evaluation

Absorbed-dose-distribution plots on selected slices (see Figure B.2.3), cumulative DVHs (see Figure B.2.4), and a summary table (Table B.2.3) were used for plan evaluation and dose reporting. Absorbed doses reported were the $D_{2\ \%}$, $D_{95\ \%}$, $D_{98\ \%}$, and D_{median} for all target structures, *i.e.*, the GTV, CTV, PTV; $D_{2\ \%}$, $D_{33\ \%}$, and $D_{67\ \%}$ were assessed for the heart, and PRV esophagus; $D_{2\ \%}$ for the spinal cord and PRV spinal cord; $V_{20\,\text{Gy}}$ and $V_{30\ \text{Gy}}$ for the lungs.

B.3 Case Number B3. Adenocarcinoma of the Prostate

B.3.1 Clinical Situation

A 72-year-old man presented with a prostate-specific antigen of 8.68 ng/ml. Readings of 4.7 ng/ml and 7.1 ng/ml were recorded, respectively, 3 years and 1 year previously. He had no urinary symptoms, and his past history was significant only for hypertension, which was controlled with medication. Digital rectal examination demonstrated an enlarged gland, with no discreet palpable nodule. Transrectal ultrasound showed a 47 cm^3 prostate with marked hyperplasia, and a suspicious hypoechoic nodule ($10 \times 6 \times 16\ mm^3$) within the left median peripheral zone.

Double-sextant core biopsies revealed adenocarcinoma at the right base, right mid, right apex, left mid, and left apical areas. Overall, there were 7/10 positive sites and 9/13 positive cores, with overall involvement of 5 % to 10 %. Gleason score was $3 + 4 = 7$ at the left base, and $3 + 3 = 6$ at other sites.

Final clinical classification was T1c–N0–M0, stage 2 carcinoma of the prostate (ICD-0 10: C61.9).

B.3.2 Treatment Intent

Treatment options were discussed with the patient, and he opted for radical radiotherapy. Treatment was to be delivered to the prostate only using an intensity-modulated technique.

B.3.3 Patient Positioning and Image Acquisition

Prior to simulation, the patient consented to have three gold seeds implanted in the prostate under ultrasound guidance to serve as fiducial markers for radiographic localization. The pelvis and upper legs were immobilized with a vacuum cushion in the supine position. The patient underwent a planning CT scan without contrast enhancement. The examination was performed on a four-detector spiral CT scanner (120 kV, 300 mAs) using a slice thickness of 2.5 mm, a reconstruction interval of 2 mm, and a pitch of 0.75 (see Figure B.3.1). Slices were acquired from the level of L5 to 3 cm below the lesser trochanter.

B.3.4 Target Volumes

B.3.4.1 Gross Tumor Volume. The GTV was not visible on CT images and was not defined.

B.3.4.2 Clinical Target Volume. The CTV-T was defined as the entire prostate gland.

B.3.4.3 Planning Target Volume. The PTV-T was defined by adding an anisotropic margin to the CTV. This margin was 7 mm posteriorly, and 10 mm in all other directions.

B.3.4.4 Organs at Risk and Planning Organ-at-Risk Volume. The following OARs were delineated:

- rectal wall;
- bladder wall;
- left and right femoral head and neck.

No margin was added to the OARs to define the PRVs.

B.3.5 Planning Aim

The following absorbed dose was aimed for in the PTV:

- PTV-T: median absorbed dose of 78.0 Gy in 39 fractions of 2 Gy in 8 weeks.

The dose–volume constraints used are listed in Table B.3.1.

B.3.6 Treatment-Planning System and Treatment Unit

The patient was planned with the Pinnacle treatment-planning system (Philips Medical Systems), and treated with IMRT using a Synergy-S unit (Elekta AB). Planning and treatment were completed with 6 MV x rays using seven coplanar

fields spaced at approximately equal gantry angles (40°, 80°, 110°, 250°, 280°, 310°, and 355°). Absorbed-dose calculations were performed using the standard convolution/superposition algorithm and included CT-based heterogeneity corrections.

B.3.7 Prescription

The treatment plan and all the associated technical data were approved by the treating physician. The absorbed-dose prescription was a median absorbed dose of 78 Gy according to the absorbed-dose distributions presented in Figures B.3.2 and B.3.3, and in Table B.3.2.

B.3.8 Quality Assurance

An individualized patient QA was performed before the start of treatment. Dosimetric accuracy was assessed to be within 3 % using third-party software (RadCalc Version 4.3, Build 12, Lifeline Software). Using a megavoltage portal-imaging device calibrated to produce images for absolute dosimetry, images of the absorbed-dose distributions were acquired for all fields and compared with the planned absorbed-dose distributions. Before each fraction, orthogonal portal images were used to localize the implanted fiducial markers. The patient was repositioned if the center of mass of the three markers was displaced by more than 3 mm along any axis.

B.3.9 Dose Reporting

The absorbed-dose distribution and the various absorbed-dose metrics are reported in Figures B.3.2 and B.3.3, and in Table B.3.2.

Journal of the ICRU Vol 10 No 1 (2010) Report 83
Oxford University Press
doi:10.1093/jicru/ndq013

References

AAPM (2004). American Association of Physicists in Medicine. *Tissue Inhomogeneity Corrections for Megavoltage Photon Beams.* Task Group 65 (American Association of Physicists in Medicine, College Park, MD).

Aaronson, R. F., DeMarco, J. J., Chetty, I. J., and Solberg, T. D. (2002). "A Monte Carlo based phase space model for quality assurance of intensity modulated radiotherapy incorporating leaf specific characteristics," *Med. Phys*. **29,** 2952–2958.

ACT (2006). Advanced Technology Consortium. *ATC Guidelines for the Use of IMRT (including Intra-Thoracic Treatments)*. http://www3.cancer.gov/rrp/imrt.doc.

Adams, E. J., Convery, D. J., Cosgrove, V. P., McNair, H. A., Staffurth, J. N., Vaarkamp, J., Nutting, C. M., Warrington, A. P., Webb, S., Balyckyi, J., and Dearnaley, D. P. (2004). "Clinical implementation of dynamic and step-and-shoot IMRT to treat prostate cancer with high risk of pelvic lymph node involvement," *Radiother. Oncol*. **70,** 1–10.

Adkison, J. B., Khuntia, D., Bentzen, S. M., Cannon, M., Tomé, W. A., Jaradat, H., Walker, W., Traynor, A. M., Weigel, T., and Mehta, M. P. (2008). "Dose escalated, hypofractionated radiotherapy using helical tomotherapy for inoperable non-small cell lung cancer: preliminary results of a risk-stratified phase I dose escalation study," *Technol. Cancer Res. Treat.* **7,** 441–447.

Agazaryan, N., Solberg, T. D., and DeMarco, J. J. (2003). "Patient specific quality assurance for the delivery of intensity modulated radiotherapy," *J. Appl. Clin. Med. Phys.* **4,** 40–50.

Agazaryan, N., Ullrich, W., Lee, S. P., and Solberg, T. D. (2004). "A methodology for verification of radiotherapy dose calculation," *J. Neurosurg.* **101,** 356–361.

Ahnesjö, A. (1989). "Collapsed cone convolution of radiant energy for photon dose calculation in heterogeneous media," *Med. Phys*. **16,** 577–592.

Ahnesjö, A. (1994). "Analytic modeling of photon scatter from flattening filters in photon therapy beams," *Med. Phys*. **21,** 1227–1235.

Ahnesjö, A. (1995). "Collimator scatter in photon therapy beams," *Med. Phys*. **22,** 267–278.

Ahnesjö, A., and Aspradakis, M. M. (1999). "Dose calculations for external photon beams in radiotherapy," *Phys. Med. Biol*. **44,** R99–R155.

Ahnesjö, A., Andreo, P., and Brahme, A. (1987). "Calculation and application of point spread functions for treatment planning with high energy photon beams," *Acta Oncol*. **26**, 49–56.

AJCC (1997). American Joint Committee on Cancer. *Cancer Staging Handbook*, 5th ed. (Springer, New York, Berlin, Heidelberg).

AJCC (2002). *American Joint Committee on Cancer. Cancer Staging Handbook*, 6th ed. (Springer, New York, Berlin, Heidelberg).

Alfonso, R., Andreo, P., Capote, R., Huq, M. S., Kilby, W., Kjäll, P., Mackie, T. R., Palmans, H., Rosser, K., Seuntjens, J., Ullrich, W., and Vanitsky, S. (2008). "A new formalism for reference dosimetry of small and nonstandard fields," *Med. Phys*. **35,** 5179–5186.

Almond, P. R., Biggs, P. J., Coursey, B. M., Hanson, W. F., Huq, M. S., Nath, R., and Rogers, D. W. O. (1999). "AAPM's TG-51 protocol for clinical reference dosimetry of high-energy photon and electron beams," *Med. Phys*. **26,** 1847–1870.

Antolak, J. A., and Rosen, I. I. (1999). "Planning target volumes for radiotherapy: How much margin is needed?" *Int. J. Radiat. Oncol. Biol. Phys.* **44,** 1165–1170.

Arnfield, M. R., Siebers, J. V., Kim, J. O., Wu, Q., Keall, P. J., and Mohan, R. (2000). "A method for determining multileaf collimator transmission and scatter for dynamic intensity modulated radiotherapy," *Med. Phys.* **27,** 2231–2241.

Aspradakis, M. M., Morrison, R. H., Richmond, N. D., and Steele, A. (2003). "Experimental verification of convolution/superposition photon dose calculations for radiotherapy treatment planning," *Phys. Med. Biol*. **48,** 2873–2893.

Attix, F. H. (1986). *Introduction to Radiological Physics and Radiation Dosimetry* (Wiley Interscience, New York).

Aoyama, H., Westerly, D. C., Mackie, T. R., Olivera, G. H., Bentzen, S. M., Patel, R. R., Jaradat, H., Tomé, W. A., Ritter, M. A., and Mehta, M. P. (2006). "Integral radiation dose to normal structures with conformal external beam radiation," *Int. J. Radiat. Oncol. Biol. Phys.* **64,** 962–967.

Austin-Seymour, M., Kalet, I., McDonald, J., Kromhout-Schiro, S., Jacky, J., Humel, R. T. T., and Unger, J. (1995). "Three dimensional planning target volumes: a model and a software tool," *Int. J. Radiat. Oncol. Biol. Phys*. **33,** 1073–1080.

Azcona, J. D., Siochi, R. A. C., and Azinovic, I. (2002). "Quality assurance in IMRT: Importance of the transmission through the jaws for an accurate calculation of

absolute doses and relative distributions," *Med. Phys*. **29,** 269–274.

Baker, S. J. K., Budgell, G. J., and MacKay, R. I. (2005). "Use of an amorphous silicon electronic portal imaging device for multileaf collimator quality control and calibration," *Phys. Med. Biol.* **50,** 1377–1392.

Balter, J. M., Ten Haken, R. K., Lawrence, T. S., Lam, K. L., and Robertson, J. M. (1996). "Uncertainties in CT-based radiation therapy treatment planning associated with patient breathing," *Int. J. Radiat. Oncol. Biol. Phys.* **36,** 167–174.

Barendsen, G. W. (1982). "Dose fractionation, dose rate and iso-effect relationships for normal tissue responses," *Int. J. Radiat. Oncol. Biol. Phys*. **8,** 1981–1997.

Barker, J. L., Jr., Garden, A. S., Ang, K. K., O'Daniel, J. C., Wang, H., Court, L. E., Morrison, W. H., Rosenthal, D. I., Chao, K. S. C., Tucker, S. L., Mohan, R., and Dong, L. (2004). "Quantification of volumetric and geometric changes occurring during fractionated radiotherapy for head-and-neck cancer using an integrated CT/linear accelerator system," *Int. J. Radiat. Oncol. Biol. Phys*. **59,** 960–970.

Baum, C., Birkner, M., Alber, M., Paulsen, F., and Nüsslin, F. (2005). "Dosimetric consequences of the application of off-line setup error correction protocols and a hull-volume definition strategy for intensity modulated radiotherapy of prostate cancer," *Radiother Oncol*. **7,** 35–42.

Bayouth, J. E., Wendt, D., and Morrill, S. M. (2003). "MLC quality assurance techniques for IMRT applications," *Med. Phys*. **30,** 743–750.

Bel, A., van Herk, M., and Lebesque, J. V. (1996). "Target margins for random geometrical treatment uncertainties in conformal radiotherapy," *Med. Phys*. **23,** 1537–1545.

Bentzen, S. M. (2005). "Theragnostic imaging for radiation oncology: dose-painting by numbers," *Lancet Oncol*. **6,** 112–117.

Bentzen, S. M., and Tucker, S. L. (1997). "Quantifying the position and steepness of radiation dose-response curves," *Int. J. Radiat. Oncol. Biol. Phys*. **71,** 531–542.

Bentzen, S. M., Constine, L. S., Deasy, J. O., Eisbruch, A., Jackson, A., Marks, L. B., Ten Haken, R. K., and Yorke, E. D. (2010). "Quantitative analyses of normal tissue effects in the clinic (QUANTEC): an introduction to the scientific issues," *Int. J. Radiat. Oncol. Biol. Phys*. **76,** S3–S9.

Bernier, J., Hall, E. J., and Giaccia, A. (2004). "Radiation oncology: A century of achievements," *Nat. Rev. Cancer* **4,** 737–747.

Boersma, L. J., van den Brink, M., Bruce, A. M., Shouman, T., Gras, L., te Velde, A., and Lebesque, J. V. (1998). "Estimation of the incidence of late bladder and rectum complications after high-dose (70–78 Gy) conformal radiotherapy for prostate cancer, using dose–volume histograms," *Int. J. Radiat. Oncol. Biol. Phys.* **41,** 83–92.

Bortfeld, T. (1999). "Optimized planning using physical objectives and constraints," *Semin. Radiat. Oncol.* **9,** 20–34.

Bortfeld, T. (2003). "Physical optimization," in *Intensity Modulated Radiation Therapy: A State of the Art*. Palta, J., and Mackie, T. R., Eds. (American Association of Physicists in Medicine, College Park, MD).

Bortfeld, T. (2006). "IMRT: a review and preview," *Phys. Med. Biol*. **51,** R363–R379.

Bortfeld, T., and Chen, G. T. Y. (2004). "Introduction: intrafractional organ motion and its management," *Semin. Radiat. Oncol.* **14,** 1 (abstract).

Bortfeld, T., and Schlegel, W. (1993). "Optimization of beam orientations in radiation therapy: some theoretical considerations," *Phys. Med. Biol*. **38,** 291–304.

Bortfeld, T., Bürkelbach, J., Boesecke, R., and Schlegel, W. (1990). "Methods of image reconstruction from projections applied to conformation radiotherapy," *Phys. Med. Biol.* **35,** 1423–1434.

Bortfeld, T. R., Kahler, D. L., Waldron, T. J., and Boyer, A. L. (1994). "X-ray field compensation with multileaf collimators," *Int. J. Radiat. Oncol. Biol. Phys*. **28,** 723–730.

Boyer, A., and Mok, E. (1985). "A photon dose distribution model employing convolution calculations," *Med. Phys*. **12,** 169–177.

Boyer, A. L., Xing, L., and Xia, P. (1999). "Beam shaping and modulation," in *The Modern Technology of Radiation Oncology: A Compendium for Medical Physicists and Radiation Oncologists*, Van Dyk, J., Ed. (Medical Physics Publishing, Madison, WI).

Bradbury, M., and Hricak, H. (2005). "Molecular MR imaging in oncology," *Magn. Reson. Imaging Clin. N. Am.* **13,** 225–240.

Brahme, A. (1987). "Design principles and clinical possibilities with a new generation of radiation therapy equipment: a review," *Acta Oncol.* **26,** 403–412.

Brahme, A. (1988). "Optimization of stationary and moving beam radiation therapy techniques," *Radiother. Oncol*. **12,** 129–140.

Brahme, A. (1999). "Biologically based treatment planning," *Acta Oncol*. **38,** 61–68.

Brahme, A., and Ågren, A. K. (1987). "Optimal dose distribution for eradiation of heterogenous tumors," *Acta Oncol.* **26,** 377–385.

Brahme, A., Roos, J. E., and Lax, I. (1982). "Solution of an integral equation encountered in rotation therapy," *Phys. Med. Biol*. **27,** 1221–1229.

Brenner, D. J., Curtis, R. E., Hall, E. J., and Ron, E. (2000). "Second malignancies in prostate carcinoma patients after radiotherapy compared with surgery," *Cancer* **88,** 398–406.

Brock, K. K., Dawson, L. A., Sharpe, M. B., Moseley, D. J., and Jaffray, D. A. (2006). "Feasibility of a novel deformable image registration technique to facilitate classification, targeting, and monitoring of tumor and normal tissue," *Int. J. Radiat. Oncol. Biol. Phys*. **64,** 1245–1254.

Bucci, M. K., Bevan, A., and Roach, M., III. (2005). "Advances in radiation therapy: Conventional to 3D, to IMRT, to 4D, and beyond," *CA Cancer J. Clin*. **55,** 117–134.

Burman, C., Kutcher, G. J., Emami, B., and Goitein, M. (1991). "Fitting of normal tissue tolerance data to an analytic function," *Int. J. Radiat. Oncol. Biol. Phys.* **21,** 123–135.

Burman, C., Chui, C. S., Kutcher, G., Leibel, S., Zelefsky, M., LoSasso, T., Spirou, S., Wu, Q., Yang, J., Stein, J., Mohan, R., Fuks, Z., and Ling, C. C. (1997). "Planning, delivery, and quality assurance of intensity-modulated radiotherapy using dynamic multileaf collimator: a strategy for large-scale implementation for the treatment of carcinoma of the prostate," *Int. J. Radiat. Oncol. Biol. Phys*. **39,** 863–873.

Cadman, P., Bassalow, R., Sidhu, N. P. S., Ibbott, G., and Nelson, A. (2002). "Dosimetric considerations for validation of a sequential IMRT process with a commercial treatment planning system," *Phys. Med. Biol.* **47,** 3001–3010.

Carol, M. P. (1995). "A system for planning and rotational delivery of intensity-modulated fields," *Int. J. Imaging Syst. Technol.* **6,** 56–61.

Chadwick, K. H., and Leehouts, H. P. (1973). "A molecular theory of cell survival," *Phys. Med. Biol.* **18,** 78–87.

Chaney, E. L., Cullip, T. J., and Gabriel, T. A. (1994). "A Monte Carlo study of accelerator head scatter," *Med. Phys*. **21,** 1383–1390.

Chang, J., Mageras, G. S., and Ling, C. C. (2003). "Evaluation of rapid dose map acquisition of a scanning liquid-filled ionization chamber electronic portal imaging device," *Int. J. Radiat. Oncol. Biol. Phys.* **55,** 1432–1445.

Chang, J., Obcemea, C. H., Sillanpaa, J., Mechalakos, J., and Burman, C. (2004). "Use of EPID for leaf position accuracy QA of dynamic multi-leaf collimator (DMLC) treatment," *Med. Phys.* **31,** 2091–2096.

Chao, K. S. C. (2002). "Protection of salivary function by intensity-modulated radiation therapy in patients with head and neck cancer," *Semin. Radiat. Oncol.* **12,** 20–25.

Chao, K. S., Deasy, J. O., Markman, J., Haynie, J., Perez, C. A., Purdy, J. A., and Low, D. A. (2001a). "A prospective study of salivary function sparing in patients with head-and-neck cancers receiving intensity-modulated or three-dimensional radiation therapy: Initial results," *Int. J. Radiat. Oncol. Biol. Phys.* **49,** 907–916.

Chao, K. S. C., Majhail, N., Huang, C. J., Simpson, J. R., Perez, C. A., Haughey, B., and Spector, G. (2001b). "Intensity-modulated radiation therapy reduces late salivary toxicity without compromising tumor control in patients with oropharyngeal carcinoma: a comparison with conventional techniques," *Radiother. Oncol*. **61,** 275–280.

Chao, K. S. C., Wippold, F. J., II, Ozyigit, G., Tran, B. N., and Dempsey, J. F. (2002). "Determination and delineation of nodal target volumes for head-and-neck cancer based on patterns of failure in patients receiving definitive and postoperative IMRT," *Int. J. Radiat. Oncol. Biol. Phys*. **53,** 1174–1184.

Chao, K. S. C., Ozyigit, G., Tran, B. N., Cengiz, M., Dempsey, J. F., and Low, D. A. (2003). "Patterns of failure in patients receiving definitive and postoperative IMRT for head-and-neck cancer," *Int. J. Radiat. Oncol. Biol. Phys*. **55,** 312–321.

Childress, N. L., Dong, L., and Rosen, I. I. (2002). "Rapid radiographic film calibration for IMRT verification using automated MLC fields," *Med. Phys*. **29,** 2384–2390.

Chui, C. S., Spirou, S., and LoSasso, T. (1996). "Testing of dynamic multileaf collimation," *Med. Phys.* **23,** 635–641.

Clark, C. H., Mubata, C. D., Meehan, C. A., Bidmead, A. M., Staffurth, J., Humphreys, M. E., and Dearnaley, D. P. (2002). "IMRT clinical implementation: Prostate and pelvic node irradiation using Helios and 120-leaf multileaf collimator," *J. Appl. Clin. Med. Phys*. **3,** 273–284.

Claus, F., De Gersem, W., De Wagter, C., Van Severen, R., Vanhoutte, I., Duthoy, W., Remouchamps, V., Van Duyse, B., Vakaet, L., Lemmerling, M., Vermeersch, H., and De Neve, W. (2001). "An implementation strategy for IMRT of ethmoid sinus cancer with bilateral sparing of the optic pathways," *Int. J. Radiat. Oncol. Biol. Phys.* **51,** 318–331.

Claus, F., Boterberg, T., Ost, P., and De Neve, W. (2002). "Short term toxicity profile for 32 sinonasal cancer patients treated with IMRT. Can we avoid dry eye syndrome?" *Radiother. Oncol.* **64,** 205–208.

Convery, D. J., and Rosenbloom, M. E. (1992). "The generation of intensity-modulated fields for conformal radiotherapy by dynamic collimation," *Phys. Med. Biol*. **37,** 1359–1374.

Cormack, A. M. (1987). "A problem in rotation therapy with x rays," *Int. J. Radiat. Oncol. Biol. Phys*. **13,** 623–630.

Daisne, J. F., Sibomana, M., Bol, A., Doumont, T., Lonneux, M., and Grégoire, V. (2003). "Tri-dimensional automatic segmentation of PET volumes based on measured source-to-background ratios: influence of reconstruction algorithms," *Radiother. Oncol.* **69,** 247–250.

Daisne, J. F., Duprez, T., Weynand, B., Lonneux, M., Hamoir, M., Reychler, H., and Grégoire, V. (2004). "Tumor volume in pharyngolaryngeal squamous cell carcinoma: Comparison at CT, MR imaging, and FDG PET and validation with surgical specimen," *Radiology* **233,** 93–100. Erratum in *Radiology* **235,** 1086 (2005).

Das, I. J. (2009). "Diamond detectors," pp. 895–912 in *Clinical Dosimetry Measurements in Radiotherapy*, Rogers, D. W. O., and Cygler, J. E., Eds. (American Association of Physicists in Medicine, College Park, MD).

Das, I. J., Cheng, C. W., Chopra, K. L., Mitra, R. K., Srivastava, S. P., and Glatstein, E. (2008). "Intensity-modulated radiation therapy dose prescription, recording, and delivery: Patterns of variability among institutions and treatment planning systems," *J. Natl. Cancer Inst.* **100,** 300–307.

Davidson, S. E., Ibbott, G. S., Prado, K. L., Dong, L., Liao, Z., and Followill, D. S. (2007). "Accuracy of two hetereogeneity dose calculation algorithms for IMRT

in treatment plans designed using an anthropomorphic thorax phantom," *Med. Phys*. **34,** 1850–1857.

Dawson, L. A., Anzai, Y., Marsh, L., Martel, M. K., Paulino, A., Ship, J. A., and Eisbruch, A. (2000). "Patterns of local-regional recurrence following parotid-sparing conformal and segmental intensity-modulated radiotherapy for head and neck cancer," *Int. J. Radiat. Oncol. Biol. Phys*. **46,** 1117–1126.

Dawson, L. A., Ten Haken, R. K., and Lawrence, T. S. (2001). "Partial irradiation of the liver," *Semin. Radiat. Oncol.* **11,** 240–246.

Dawson, L. A., Normolle, D., Balter, J. M., McGinn, C. J., Lawrence, T. S., and Ten Haken, R. K. (2002). "Analysis of radiation-induced liver disease using the Lyman NTCP model," *Int. J. Radiat. Oncol. Biol. Phys.* **53,** 810–821.

Deasy, J. O. (1997). "Multiple local minima in radiotherapy optimization problems with dose–volume constraints," *Med. Phys.* **24,** 1157–1161.

De Gersem, W., Claus, F., De Wagter, C., and De Neve, W. (2001a). "An anatomy-based beam segmentation tool for intensity-modulated radiation therapy and its application to head-and-neck cancer," *Int. J. Radiat. Oncol. Biol. Phys*. **51,** 849–859.

De Gersem, W., Claus, F., De Wagter, C., Van Duyse, B., and De Neve, W. (2001b). "Leaf position optimization for step-and-shoot IMRT," *Int. J. Radiat. Oncol. Biol. Phys*. **51,** 1371–1388.

Dempsey, J., Benoit, D., Fitzsimmons, J., Haghighat, A., Li, J., Low, D., Mutic, S., Palta, J., Romeijn, H., and Sjoden, G. (2005). "A device for realtime 3D image-guided IMRT," *Int. J. Radiat. Oncol. Biol. Phys*. **63,** S202.

Deng, J., Ma, C.-M., Hai, J., and Nath, R. (2004). "Commissioning 6 MV photon beams of a stereotactic radiosurgery system for Monte Carlo treatment planning," *Med. Phys*. **30,** 3124–3134.

De Neve, W., De Wagter, C., De Jaeger, K., Thienpont, M., Colle, C., Derycke, S., and Schelfhout, J. (1996). "Planning and delivering high doses to targets surrounding the spinal cord at the lower neck and upper mediastinal levels: static beam-segmentation technique executed with a multileaf collimator," *Radiother. Oncol*. **40,** 271–279.

Depuydt, T., Van Esch, A., and Huyskens, D. P. (2002). "A quantitative evaluation of IMRT dose distributions: refinement and clinical evaluation of the gamma evaluation," *Radiother. Oncol*. **62,** 309–319.

De Ruysscher, D., Wanders, R., van Haren, E., Hochstenbag, M., Geraedts, W., Pitz, C., Simons, J., Boersma, L., Verschueren, T., Minken, A., Bentzen, S. M., and Lambin, P. (2008). "HI-CHART: a phase I/II study on the feasibility of high-dose continuous hyperfractionated accelerated radiotherapy in patients with inoperable non-small-cell lung cancer," *Int. J. Radiat. Oncol. Biol. Phys*. **71,** 132–138.

De Wagter, C. (2006). "QA-QC of IMRT: European perspective," pp. 178–128 in *Image-Guided IMRT*, Bortfeld, T., Schmidt-Ullrich, R., DeNeve, W., and Wazer, D. E., Eds. (Springer, Berlin).

Dice, L. R. (1945). "Measures of the amount of ecologic association between species," *Ecology* **26,** 297–302.

Difilippo, F. C. (1998). "Forward and adjoint methods for radiotherapy planning," *Med. Phys*. **25,** 1702–1710.

Dirkx, M. L. P., Heijmen, B. J. M., and Santvoort, J. P. C. (1998). "Leaf trajectory calculation for dynamic multileaf collimation to realize optimized fluence profiles," *Phys. Med. Biol.* **43,** 1171–1184.

Djordjevich, A., Bonham, D. J., Hussein, E. M. A., Andrew, J. W., and Hale, M. E. (1990). "Optimal design of radiation compensators," *Med. Phys*. **17,** 397–404.

Dogan, N., Leybovich, L. B., King, S., Sethi, A., and Emami, B. (2002). "Improvement of treatment plans developed with intensity-modulated radiation therapy for concave-shaped head and neck tumors," *Radiology* **223,** 57–64.

Dong, L., Antolak, J., Salehpour, M., Forster, K., O'Neill, L., Kendall, R., and Rosen, I. (2003). "Patient-specific point dose measurement for IMRT monitor unit verification," *Int. J. Radiat. Oncol. Biol. Phys*. **56,** 867–877.

Donovan, E. M., Bleackley, N. J., Evans, P. M., Reise, S. F., and Yarnold, J. R. (2002). "Dose–position and dose–volume histogram analysis of standard wedged and intensity modulated treatments in breast radiotherapy," *Br. J. Radiol*. **75,** 967–973.

Donovan, E., Bleakley, N., Denholm, E., Evans, P., Gothard, L., Hanson, J., Peckitt, C., Reise, S., Ross, G., Sharp, G., Symonds-Tayler, R., Tait, D., and Yarnold, D. (2007). "Randomised trial of standard 2D radiotherapy (RT) versus intensity modulated radiotherapy (IMRT) in patients prescribed breast radiotherapy," *Radiother. Oncol*. **82,** 254–264.

D'Souza, W. D., and Rosen, I. I. (2003). "Nontumor integral dose variation in conventional radiotherapy treatment planning," *Med. Phys.* **30,** 2065–2071.

Douglas, B. G., and Fowler, J. F. (1976). "The effect of multiple small doses of x-rays on skin reactions in the mouse and a basic interpretation," *Radiat. Res*. **66,** 401–426.

Drzymala, R., Mohan, R., Brewster, L., Chu, J., Goitein, M., Harms, W., and Urie, M. (1991). "Dose–volume histograms," *Int. J. Radiat. Oncol. Biol. Phys.* **21,** 71–78.

Eisbruch, A., Ten Haken, R. K., Kim, H. M., Marsh, L. H., and Ship, J. A. (1999). "Dose, volume, and function relationships in parotid salivary glands following conformal and intensity-modulated irradiation of head and neck cancer," *Int. J. Radiat. Oncol. Biol. Phys.* **45,** 577–587.

Eisbruch, A., Ship, J. A., Kim, H. M., and Ten Haken, R. K. (2001). "Partial irradiation of the parotid gland," *Semin. Radiat. Oncol.* **11,** 234–239.

Eisbruch, A., Marsh, L. H., Dawson, L. A., Bradford, C. R., Teknos, T. N., Chepeha, D. B., Worden, F. P., Urba, S., Lin, A., Schipper, M. J., and Wolf, G. T. (2004). "Recurrences near the base of the skull following IMRT of head and neck cancer: implications for target delineation in the high neck, and for parotid sparing," *Int. J. Radiat. Oncol. Biol. Phys*. **59,** 28–42.

Engelsman, M., Damen, E. M., De Jaeger, K., van Ingen, K. M., and Mijnheer, B. J. (2001a). "The effect of breathing and set-up errors on the cumulative dose to a lung tumor," *Radiother. Oncol.* **60,** 95–105.

Engelsman, M., Remeijer, P., van Herk, M., Lebesque, J. V., Mijnheer, B. J., and Damen, E. M. (2001b). "Field size reduction enables iso-NTCP escalation of tumor control probability for irradiation of lung tumors," *Int. J. Radiat. Oncol. Biol. Phys.* **51,** 1290–1298.

Emami, B., Lyman, J., Brown, A., Coia, L., Goitein, M., Munzenrider, J. E., Shank, B., Solin, L. J., and Wesson, M. (1991). "Tolerance of normal tissue to therapeutic irradiation," *Int. J. Radiat. Oncol. Biol. Phys.* **21,** 109–122.

Esthappan, J., Mutic, S., Malyapa, R. S., Grigsby, P. W., Zoberi, I., Dehdashti, F., Miller, T. R., Bosch, W. R., and Low, D. A. (2004). "Treatment planning guidelines regarding the use of CT/PET-guided IMRT for cervical carcinoma with positive paraaortic lymph nodes," *Int. J. Radiat. Oncol. Biol. Phys.* **58,** 1289–1297.

Evans, P. M., Donovan, E. M., Partridge, M., Childs, P. J., Convery, D. J., Eagle, S., Hansen, V. N., Suter, B. L., and Yarnold, J. R. (2000). "The delivery of intensity modulated radiotherapy to the breast using multiple static fields," *Radiother. Oncol.* **57,** 79–89.

Ezzell, G. A., and Chungbin, S. (2001). "The overshoot phenomenon in step-and-shoot IMRT delivery," *J. Appl. Clin. Med. Phys*. **2,** 138–148.

Ezzell, G. A., Galvin, J. M., Low, D., Palta, J. R., Rosen, I., Sharpe, M. B., Xia, P., Xiao, Y., Xing, L., and Yu, C. X. (2003). "Guidance document on delivery, treatment planning, and clinical implementation of IMRT: report of the IMRT Subcommittee of the AAPM Radiation Therapy Committee," *Med. Phys.* **30,** 2089–2115.

Ezzell, G. A., Burmeister, J. W., Dogan, N., LoSasso, T. J., Mechalakos, J. G., Mihailidis, D., Molineu, A., Palta, J. R., Ramsey, C. R., Salter, B. J., Shi, J., Xia, P., Yue, N. J., and Xiao, Y. (2009). "IMRT commissioning: Multiple institution planning and dosimetry comparisons, a report from AAPM Task Group 119," *Med. Phys*. **36,** 5359–5373.

Fallone, G., Carlone, M., Murray, B., Rathee, S., and Steciw, S. (2007). "Investigations in the design of a novel linac-MRI system," *Int. J. Radiat. Oncol. Biol. Phys.* **69,** S19 (abstract).

Fenwick, J. D., Tomé, W., Jaradat, H. A., Hui, S. K., James, J. A., Balog, J. P., DeSouza, C. N., Lucas, D. B., Olivera, G. H., Mackie, T. R., and Paliwal, B. R. (2004). "Quality assurance of a helical tomotherapy machine," *Phys. Med. Biol*. **49,** 2933–2953.

Feshbach, H., and Morse, P. (1953). *Methods of Theoretical Physics*. (Cambridge University Press).

Fippel, M., Haryanto, F., Dohm, O., Nüsslin, F., and Kriesen, S. (2003). "A virtual photon energy fluence model for Monte Carlo dose calculation," *Med. Phys*. **30,** 301–311.

Forrest, L. J., Mackie, T. R., Ruchala, K., Turek, M., Kapatoes, J., Jaradat, H., Hui, S., Balog, J., Vail, D. M., and Mehta, M. P. (2004). "The utility of megavoltage computed tomography images from a helical tomotherapy system for setup verification purposes," *Int. J. Radiat. Oncol. Biol. Phys*. **60,** 1639–1644.

Fraass, B., Doppke, K., Hunt, M., Kutcher, G., Starkschall, G., Stern, R., and Van Dyk, J. (1998). "Quality assurance for clinical radiotherapy treatment planning: report of the AAPM Radiation Therapy Committee Task Group 53," *Med. Phys.* **25,** 1773–1829.

Fraass, B. A., Kessler, M. L., McShan, D. L., Marsh, L. H., Watson, B. A., Dusseau, W. J., Eisbruch, A., Sandler, H. M., and Lichter, A. S. (1999). "Optimization and clinical use of multisegment intensity-modulated radiation therapy for high dose conformal therapy," *Semin. Radiat. Oncol*. **9,** 60–77.

Frank, S. J., Forster, K. M., Stevens, C. W., Cox, J. D., Komaki, R., Liao, Z., Tucker, S., Wang, X., Steadham, R. E., Brooks, C., and Starkschall, G. (2003). "Treatment planning for lung cancer: traditional homogeneous point-dose prescription compared with heterogeneity-corrected dose–volume prescription," *Int. J. Radiat. Oncol. Biol. Phys*. **56,** 1308–1318.

Gagliardi, G., Lax, I., and Rutqvist, L. E. (2001). "Partial irradiation of the heart," *Semin. Radiat. Oncol.* **11,** 224–233.

Galvin, J. M., Smith, A. R., and Lally, B. (1993). "Characterization of a multileaf collimator system," *Int. J. Radiat. Oncol. Biol. Phys.* **25,** 181–192.

Geets, X., Daisne, J. F., Tomsej, M., Duprez, T., Lonneux, M., and Grégoire, V. (2006). "Impact of the type of imaging modality on target volumes delineation and dose distribution in pharyngo-laryngeal squamous cell carcinoma: Comparison between pre- and pertreatment studies," *Radiother Oncol*. **78,** 291–297.

Geets, X., Lee, J. A., Bol, A., Lonneux, M., and Grégoire, V. (2007a). "A gradient-based method for segmenting FDG-PET images: Methodology and validation," *Eur. J. Nucl. Med. Mol. Imaging* **34,** 1427–1438.

Geets, X., Tomsej, M., Lee, J. A., Duprez, T., Coche, E., Cosnard, G., Lonneux, M., and Grégoire, V. (2007b). "Adaptive biological image-guided IMRT with anatomic and functional imaging in pharyngo-laryngeal tumors: Impact on target volume delineation and dose distribution using helical tomotherapy," *Radiother. Oncol.* **85,** 105–115.

Goitein, M., and Schultheiss, T. E. (1985). "Strategies for treating possible tumor extension: Some theoretical considerations," *Int. J. Radiat .Oncol. Biol. Phys.* **11,** 1519–1528.

Graham, M. V., Purdy, J. A., Emami, B., Matthews, J. W., and Harms, W. B. (1995). "Preliminary results of a prospective trial using three dimensional radiotherapy for lung cancer," *Int. J. Radiat. Oncol. Biol. Phys.* **33,** 993–1000.

Grant, W., III (1996). "Experience with intensity modulated beam delivery," pp. 793–804 in *Teletherapy: Present and Future*, Palta, J., and Mackie, T. R., Eds. (Advanced Medical Publishing, Madison, WI).

Graves, M. N., Thompson, A. V., Martel, M. K., McShan, D. L., and Fraass, B. A. (2001). "Calibration and quality assurance for rounded leaf-end MLC systems," *Med. Phys*. **28,** 2227–2233.

Grégoire, V., Coche, E., Cosnard, G., Hamoir, M., and Reychler, H. (2000). "Selection and delineation of

lymph node target volumes in head and neck conformal radiotherapy. Proposal for standardizing terminology and procedure based on the surgical experience," *Radiother. Oncol.* **56,** 135–150.

Grégoire, V., Daisne, J. F., Geets, X., and Levendag, P. (2003a). "Selection and delineation of target volumes in head and neck tumors: beyond ICRU definition," *Rays* **28,** 217–224.

Grégoire, V., Coche, E., Cosnard, G., Hamoir, M., and Reychler, H. (2003b). "Selection and delineation of lymph node target volumes in head and neck conformal and intensity-modulated radiation therapy," pp. 69–90 in *Clinical Target Volumes in Conformal and Intensity Modulated Radiation Therapy. A Clinical Guide to Cancer Treatment*, Grégoire, V., Scalliet, P., and Ang, K. K., Eds. (Springer, Berlin).

Grégoire, V., Levendag, P., Ang, K. K., Bernier, J., Braaksma, M., Budach, V., Chao, C., Coche, E., Cooper, J. S., Cosnard, G., Eisbruch, A., El-Sayed, S., Emami, B., Grau, C., Hamoir, M., Lee, N., Maingon, P., Muller, K., and Reychler, H. (2003c). "CT-based delineation of lymph node levels and related CTVs in the node-negative neck: DAHANCA, EORTC, GORTEC, NCIC, RTOG consensus guidelines," *Radiother. Oncol.* **69,** 227–236.

Grégoire, V. P., Scalliet, P., and Ang, K. K., Eds. (2003d). *Clinical Target Volumes in Conformal and Intensity Modulated Radiation Therapy. A Clinical Guide to Cancer Treatment* (Springer, Berlin).

Grégoire, V., Eisbruch, A., Hamoir, M., and Levendag, P. (2006). "Proposal for the delineation of the nodal CTV in the node-positive and the post-operative neck," *Radiother. Oncol*. **79,** 15–20.

Grégoire, V., Haustermans, K., and Lee, J. (2009). "Molecular image-guided radiotherapy using positron emission tomography," pp. 271–286 in *Basic Clinical Radiobiology*, Joiner, M., and van der Kodel, A., Eds. (Hodder Arnold, London).

Gueulette, J., Blattmann, H., Pedroni, E., Coray, A., De Coster, B. M., Mahy, P., Wambersie, A., and Goitein, G. (2005). "Relative biologic effectiveness determination in mouse intestine for scanning proton beam at Paul Scherrer Institute, Switzerland. Influence of motion," *Int. J. Radiat. Oncol. Biol. Phys*. **62,** 838–845.

Gunderson, L. L., Haddock, M. G., Gervza, P. A., and Nelson, H. (2003). "Rectal and anal cancers in conformal radiotherapy planning: Selection and delineation of lymph node areas," pp. 187–204 in *Clinical Target Volumes in Conformal and Intensity Modulated Radiation Therapy. A Clinical Guide to Cancer Treatment*, Grégoire, V., Scalliet, P., and Ang, K. K., Eds. (Springer, Berlin).

Hall, E. J., and Wuu, C. S. (2003). "Radiation-induced second cancers: The impact of 3D-CRT and IMRT," *Int. J. Radiat. Oncol. Biol. Phys.* **56,** 83–88.

Hardcastle, N., Metcalfe, P., Ceylan, A., and Williams, M. J. (2007). "Multileaf collimator end leaf leakage: Implications for wide-field IMRT," *Phys. Med. Biol*. **52,** N493–N504.

Harms, W. B., Low, D. A., Wong, J. W., and Purdy, J. A. (1998). "A software tool for the quantitative evaluation of 3D dose calculation algorithms," *Med. Phys.* **25,** 1830–1836.

Hartmann-Siantar, C. L., Chandler, W. P., Weaver, K. A., Albright, N. W., Verhey, L. J., Hornstein, S. M., Cox, L. J., Rathkopf, J. A., and Svatos, M. M. (1996). "Validation and performance assessment of the Peregrine all-particle Monte Carlo code for photon beam therapy," *Med. Phys*. **23,** 1128 (abstract).

Heath, E., Seuntjens, J., and Sheikh-Bagheri, D. (2004). "Dosimetric evaluation of the clinical implementation of the first commercial IMRT Monte Carlo treatment planning system at 6 MV," *Med. Phys*. **31,** 2771–2779.

Henson, B. S., Inglehart, M. R., Eisbruch, A., and Ship, J. A. (2001). "Preserved salivary output and xerostomia-related quality of life in head and neck cancer patients receiving parotid-sparing radiotherapy," *Oral Oncol*. **37,** 84–93.

Higgins, P. D., Alaei, P., Gerbi, B. J., and Dusenbery, K. E. (2003). "In vivo diode dosimetry for routine quality assurance in IMRT," *Med. Phys.* **30,** 3118–3123.

Hillier, F. S., and Lieberman, G. J. (2005). *Introduction to Operations Research* (McGraw-Hill, New York).

Holmes, T., and Mackie, T. R. (1994). "A comparison of three inverse treatment planning algorithms," *Phys. Med. Biol.* **39,** 91–106.

Holmes, T., Mackie, T. R., Simpkin, D., and Reckwerdt, P. (1991). "A unified approach to the optimization of brachytherapy and external beam dosimetry," *Int. J. Radiat. Oncol. Biol. Phys*. **20,** 859–873.

Hong, L., Hunt, M., Chui, C., Spirou, S., Forster, K., Lee, H., Yahalom, J., Kutcher, G. J., and McCormick, B. (1999). "Intensity-modulated tangential beam irradiation of the intact breast," *Int. J. Radiat. Oncol. Biol. Phys.* **44,** 1155–1164.

Huq, M. S., Das, I. J., Steinberg, T., and Galvin, J. M. (2002). "A dosimetric comparison of various multileaf collimators," *Phys. Med. Biol*. **47**, N159–N170.

Huzjan, R., Sala, E., and Hricak, H. (2005). "Magnetic resonance imaging and magnetic resonance spectroscopic imaging of prostate cancer," *Nat. Clin. Pract. Urol*. **2,** 434–442.

IAEA (2000). International Atomic Energy Agency. *Absorbed Dose Determination in External Beam Radiotherapy: An International Code of Practice for Dosimetry Based on Absorbed Dose to Water*. IAEA TRS-398 (Intenational Atomic Energy Agency, Vienna).

IAEA (2004). International Atomic Energy Agency. *Commissioning and Quality Assurance of Computerized Planning Systems for Radiation Treatment of Cancer*, IAEA TRS-430 (International Atomic Energy Agency, Vienna).

IAEA (2007). International Atomic Energy Agency. *Specification and Acceptance Testing of Radiotherapy Treatment Planning Systems*. IAEA TECDOC-1540 (International Atomic Energy Agency, Vienna).

Ibbott, G. (2009). "QA for clinical dosimetry, with emphasis on clinical trials," pp. 577–604 in *Clinical Dosimetry Measurements in Radiotherapy*, Rogers,

D. W. O., and Cygler, J. E., Eds. (American Association of Physicists in Medicine, College Park, MD).

Ibbott, G. S., Molineu, A., and Followill, D. S. (2006). "Independent evaluations of IMRT through the use of an anthropomorphic phantom," *Tech. Canc. Res. Treat*., **5,** 481–487.

ICRU (1978). International Commission on Radiation Units and Measurements. *Dose Specification for Reporting External Beam Therapy with Photons and Electrons*. ICRU Report 29 (International Commission on Radiation Units and Measurements, Bethesda, MD).

ICRU (1985). International Commission on Radiation Units and Measurements. *Dose and Volume Specification for Reporting Intracavitary Therapy in Gynecology.* ICRU Report 38 (International Commission on Radiation Units and Measurements, Bethesda, MD).

ICRU (1993). International Commission on Radiation Units and Measurements. *Prescribing, Recording and Reporting Photon Beam Therapy.* ICRU Report 50 (International Commission on Radiation Units and Measurements, Bethesda, MD).

ICRU (1999). International Commission on Radiation Units and Measurements. *Prescribing, Recording and Reporting Photon Beam Therapy (Supplement to ICRU Report 50).* ICRU Report 62 (International Commission on Radiation Units and Measurements, Bethesda, MD).

ICRU (2004). International Commission on Radiation Units and Measurements. *Prescribing, Recording and Reporting Electron Beam Therapy.* ICRU Report 71, *J. ICRU* Vol. **4**(1) (Oxford University Press, Oxford).

ICRU (2007). International Commission on Radiation Units and Measurements. *Prescribing, Recording and Reporting Proton-Beam Therapy.* ICRU Report 78, *J. ICRU* Vol. **7**(2) (Oxford University Press, Oxford).

IMRTCWG (2001). "NCI IMRT Collaborative Working Group: intensity modulated radiation therapy: Current status and issues of interest," *Int. J. Radiat. Oncol. Biol. Phys.* **51,** 880–914.

Jabbari, S., Kim, H. M., Feng, M., Lin, A., Tsien, C., Elshaikh, M., Terrell, J. E., Murdoch-Kinch, C., and Eisbruch, A. (2005). "Matched case-control study of quality of life and xerostomia after intensity modulated radiotherapy or standard radiotherapy for head-and-neck cancer: Initial report," *Int. J. Radiat. Oncol. Biol. Phys*. **63,** 725–731.

Jaffray, D. A., Drake, D. G., Moreau, M., Martinez, A. A., and Wong, J. W. (1999). "A radiographic and tomographic imaging system integrated into a medical linear accelerator for localization of bone and soft-tissue targets," *Int. J. Radiat. Oncol. Biol. Phys*. **45,** 773–789.

Jager, P. L., de Korte, M. A., Lub-de Hooge, M. N., van Waarde, A., Koopmans, K. P., Perik, P. J., and de Vries, E. G. E. (2005). "Molecular imaging: what can be used today," *Cancer Imaging* **5**, S27–S32.

Jeraj, R., and Keall, P. (1999). "Monte Carlo-based inverse treatment planning," *Phys. Med. Biol*. **44,** 1885–1896.

Jeraj, R., and Keall, P. (2000). "The effect of statistical uncertainty on inverse treatment planning based on Monte Carlo dose calculation," *Phys. Med. Biol.* **45,** 3601–3613.

Jeraj, R., Mackie, T. R., Balog, J., Olivera, G., Pearson, D., Kapatoes, J., Ruchala, K., and Reckwerdt, P. (2004). "Radiation characteristics of helical tomotherapy," *Med. Phys*. **31,** 396–404.

Jiang, S. B., and Ayyangar, K. M. (1998). "On compensator design for photon beam intensity modulated conformal therapy," *Med. Phys*. **25,** 668–675.

Jones, B. (2009). "Modeling carcinogenesis after radiotherapy using Poisson statistics: implications for IMRT, protons and ions," *J. Radiol. Prot*. **29,** A143–A157.

Jursinic, P. A., and Nelms, B. E. (2003). "A 2-D diode array and analysis software for verification of intensity modulated radiation therapy delivery," *Med. Phys*. **30,** 870–879.

Kapatoes, J. M., Olivera, G. H., Reckwerdt, P. J., Fitchard, E. E., Schloesser, E. A., and Mackie, T. R. (1999). "Delivery verification in sequential and helical tomotherapy," *Phys. Med. Biol*. **44,** 1815–1841.

Kapatoes, J. M., Olivera, G. H., Ruchala, K. J., Reckwerdt, P. J., Smilowitz, J. S., Balog, J. P., Keller, H., and Mackie, T. R. (2001a). "A feasible method for clinical delivery verification and dose reconstruction in tomotherapy," *Med. Phys*. **28,** 528–542.

Kapatoes, J. M., Olivera, G. H., Balog, J. P., Keller, H., Reckwerdt, P. J., and Mackie, T. R. (2001b). "On the accuracy and effectiveness of dose reconstruction for tomotherapy," *Phys. Med. Biol*. **46,** 943–966.

Keall, P. (2004). "4-dimensional computed tomography imaging and treatment planning," *Semin. Radiat. Oncol.* **14,** 81–90.

Kellerer, A. M., and Rossi, H. H. (1972). "The theory of dual action of radiation," *Curr. Top. Radiat. Res. Q.* **8,** 85–158.

Kelly, C. T. (1999). *Iterative Methods for Optimization*. (Society for Industrial and Applied Mathematics, Philadelphia).

Kestin, L. L., Sharpe, M. B., Frazier, R. C., Vicini, F. A., Yan, D., Matter, R. C., Martinez, A. A., and Wong, J. W. (2000). "Intensity modulation to improve dose uniformity with tangential breast radiotherapy: Initial clinical experience," *Int. J. Radiat. Oncol. Biol. Phys.* **48**, 1559–1568.

Khoo, V. S., Oldham, M., Adams, E. J., Bedford, J. L., Webb, S., and Brada, M. (1999). "Comparison of intensity-modulated tomotherapy with stereotactically guided conformal radiotherapy for brain tumors," *Int. J. Radiat. Oncol. Biol. Phys.* **45,** 415–425.

Kim, J. O., Siebers, J. V., Keall, P. J., Arnfield, M. R., and Mohan, R. (2001). "A Monte Carlo study of radiation transport through multileaf collimators," *Med. Phys*. **28,** 2497–2506.

Kissick, M. W., Boswell, S. A., Jeraj, R., and Mackie, T. R. (2005). "Confirmation, refinement, and extension of a study in intrafraction motion interplay with sliding jaw motion," *Med. Phys*. **32,** 2346–2350.

Klein, E. E., Gerber, R., Zhu, X. R., Oehmke, F., and Purdy, J. A. (1998). "Multiple machine implementation of enhanced dynamic wedge," *Int. J. Radiat. Oncol. Biol. Phys.* **40**, 977–985.

Klein, E. E., Hanley, J., Bayouth, J., Yin, F.-F., Simon, W., Dresser, S., Serago, C., Aguirre, F., Ma, L., Arjomandy, B., Liu, C., Sandin, C., and Holmes, T. (2009). "Task Group 142 report: Quality assurance of medical accelerators," *Med. Phys.* **36,** 4197–4212.

Knöös, T., Kristensen, I., and Nilsson, P. (1998). "Volumetric and dosimetric evaluation of radiation treatment plans: radiation conformity index," *Int. J. Radiat. Oncol. Biol. Phys.* **42,** 1169–1176.

Knöös, T., Wieslander, E., Cozzi, L., Brink, C., Fogliata, A., Albers, D., Nyström, H., and Lassen, S. (2006). "Comparison of dose calculation algorithms for treatment planning in external photon beam therapy for clinical situations," *Phys. Med. Biol.* **51,** 5785–5807.

Kung, J. H., Chen, G. T. Y., and Kuchnir, F. K. (2000). "A monitor unit verification calculation in intensity modulated radiotherapy as a dosimetry quality assurance," *Med. Phys*. **27,** 2226–2230.

Kutcher, G. J., and Burman, C. (1991). "Calculation of complication probability factors for non-uniform normal tissue irradiation: The effective volume method," *Int. J. Radiat. Oncol. Biol. Phys*. **16,** 1623–1630.

Kutcher, G. J., Burman, C., Brewster, L., Goitein, M., and Mohan, R. (1991). "Histogram reduction method for calculating complication probabilities for three-dimensional treatment planning evaluations," *Int. J. Radiat. Oncol. Biol. Phys.* **21,** 137–146.

Kutcher, G. J., Coia, L., Gillin, M., Hanson, W. F., Leibel, S., Morton, R. J., Palta, J. R., Purdy, J. A., Reinstein, L. E., Svensson, G. K., Weller, M., and Wingfield, L. (1994). "Comprehensive QA for radiation oncology: Report of AAPM Radiation Therapy Committee Task Group 40," *Med. Phys.* **21,** 581–618.

Lahanas, M., Schreibmann, E., and Baltas, D. (2003). "Multiobtective inverse planning for intensity modulated radiotherapy with constraint-free gradient-based optimization algorithms," *Phys. Med. Biol.* **48,** 2843–2871.

Langen, K. M., Zhang, Y., Andrews, R. D., Hurley, M. E., Meeks, S. L., Poole, D. O., Willoughby, T. R., and Kupelian, P. A. (2005). "Initial experience with megavoltage (MV) CT guidance for daily prostate alignments," *Int. J. Radiat. Oncol. Biol. Phys*. **62,** 1517–1524.

Lattanzi, J., McNeeley, S., Donnelly, S., Palacio, E., Hanlon, A., Schultheiss, T. E., and Hanks, G. E. (2000). "Ultrasound-based stereotactic guidance in prostate cancer-quanitification or organ motion and set-up errors in external beam radiation therapy," *Comput. Aided Surg*. **5,** 289–295.

Laub, W. U., and Wong, T. (2003). "The volume effect of detectors in the dosimetry of small fields used in IMRT," *Med. Phys*. **30,** 341–347.

Lea, D. E. (1947). *Actions of Radiation on Living Cells* (Cambridge University Press, Cambridge).

Lee, J. A., Geets, X., Grégoire, V., and Bol, A. (2008). "Edge-preserving filtering of images with low photon counts," *IEEE Trans. Pattern Anal. Mach. Intell.* **30,** 1014–1027.

Lee, N., Xia, P., Quivey, J. M., Sultanem, K., Poon, I., Akazawa, C., Akazawa, P., Weinberg, V., and Fu, K. K. (2002). "Intensity-modulated radiotherapy in the treatment of nasopharyngeal carcinoma: An update of the UCSF experience," *Int. J. Radiat. Oncol. Biol. Phys*. **53,** 12–22.

Lee, N., Puri, D. R., Blanco, A. I., and Chao, K. S. C. (2007). "Intensity-modulated radiation therapy in head and neck cancers: an update," *Head Neck* **29,** 387–400.

Létourneau, D., Gulam, M., Yan, D., Oldham, M., and Wong, J. W. (2004). "Evaluation of a 2D diode array for IMRT quality assurance," *Radiother. Oncol.* **70,** 199–206.

Levegrün, S., Ton, L., and Debus, J. (2001). "Partial irradiation of the brain," *Semin. Radiat. Oncol.* **11,** 259–267.

Leybovich, L. B., Sethi, A., and Dogan, N. (2003). "Comparison of ionization chambers of various volumes for IMRT absolute dose verification," *Med. Phys*. **30,** 119–123.

Libby, B., Siebers, J., and Mohan, R. (1999). "Validation of Monte Carlo generated phase-space descriptions of medical linear accelerators," *Med. Phys*. **26,** 1476–1483.

Lind, B. K., Mavroidis, P., Hyödynmaa, S., and Kappas, C. (1999). "Optimization of the dose level for a given treatment plan to maximize the complication-free tumor cure," *Acta Oncol*. **38,** 787–798.

Ling, C. C., Burman, C., Chui, C. S., Kutcher, G. J., Leibel, S. A., LoSasso, T., Mohan, R., Bortfeld, T., Reinstein, L., Spirou, S., Wang, X. H., Wu, Q., Zelefsky, M., and Fuks, Z. (1996). "Conformal radiation treatment of prostate cancer using inversely-planned intensity-modulated photon beams produced with dynamic multileaf collimation," *Int. J. Radiat. Oncol. Biol. Phys.* **35,** 721–730.

Ling, C. C., Humm, J., Larson, S., Amols, H., Fuks, Z., Leibel, S., and Koutcher, J. A. (2000). "Towards multidimensional radiotherapy (MD-CRT): Biological imaging and biological conformality," *Int. J. Radiat. Oncol. Biol. Phys.* **47,** 551–560.

Litzenberg, D. W., Moran, J. M., and Fraass, B. A. (2002). "Incorporation of realistic delivery limitations into dynamic multileaf collimation," *Med. Phys.* **29,** 810–820.

Liu, H. H., Mackie, T. R., and McCullough, E. C. (1997a). "A dual source photon beam model used in convolution/superposition dose calculations for clinical megavoltage x-ray beams," *Med. Phys*. **24,** 1960–1974.

Liu, H. H., Mackie, T. R., and McCullough, E. C. (1997b). "Calculating output factors for photon beam radiotherapy using a convolution/superposition method based on a dual source photon beam model," *Med. Phys*. **24,** 1975–1985.

Liu, H. H., McCullough, E. C., and Mackie, T. R. (1998). "Calculating dose distributions and wedge factors for photon treatment fields with dynamic wedges based on a convolution/superposition method," *Med. Phys*. **25,** 56–63.

Liu, H. H., Mackie, T. R., and McCullough, E. C. (2000). "Modeling photon output caused by backscattered radiation into the monitor chamber from collimator jaws using a Monte Carlo technique," *Med. Phys*. **27,** 737–744.

LoSasso, T., Chui, C. S., and Ling, C. C. (1998). "Physical and dosimetric aspects of a multileaf collimation system used in the dynamic mode for implementing intensity modulated radiotherapy," *Med. Phys*. **25,** 1919–1927.

LoSasso, T., Chui, C. S., and Ling, C. C. (2001). "Comprehensive quality assurance for the delivery of intensity modulated radiotherapy with a multileaf collimator used in the dynamic mode," *Med. Phys.* **28,** 2209–2219.

Lovelock, D. M. J., Chui, C. S., and Mohan, R. (1995). "A Monte Carlo model of photon beams used in radiation therapy," *Med. Phys*. **22,** 1387–1394.

Low, D. A., and Dempsey, J. F. (2003). "Evaluation of the gamma dose distribution comparison method," *Med. Phys.* **30,** 2455–2464.

Low, D. A., Chao, K. S. C., Mutic, S., Gerber, R. L., Perez, C. A., and Purdy, J. A. (1998a). "Quality assurance of serial tomotherapy for head and neck patient treatments," *Int. J. Radiat. Oncol. Biol. Phys*. **42,** 681–692.

Low, D. A., Harms, W. B., Mutic, S., and Purdy, J. A. (1998b). "A technique for the quantitative evaluation of dose distributions," *Med. Phys.* **25,** 656–661.

Low, D. A., Mutic, S., Dempsey, J. F., Gerber, R. L., Bosch, W. R., Perez, C. A., and Purdy, J. A. (1998c). "Quantitative dosimetric verification of an IMRT planning and delivery system," *Radiother. Oncol.* **49,** 305–316.

Low, D. A., Sohn, J. W., Klein, E. E., Markman, J., Mutic, S., and Dempsey, J. F. (2001). "Characterization of a commercial multileaf collimator used for intensity modulated radiation therapy," *Med. Phys*. **28,** 752–756.

Lu, W., Chen, M.-L., Olivera, G. H., Ruchala, K. J., and Mackie, T. R. (2004). "Fast free-form deformable registration via calculus of variations," *Phys. Med. Biol.* **49,** 3067–3087.

Lyman, J. T. (1985). "Complication probability as assessed from dose-volume histograms," *Radiat. Res.* **104,** S13–S19.

Lyman, .J. T., and Wolbarst, A. B. (1989). "Optimization of radiation therapy, IV: A dose–volume histogram reduction algorithm," *Int. J. Radiat. Oncol. Biol. Phys*. **17,** 433–436.

Ma, C.-M. C., and Paskalev, K. (2006). "In-room CT techniques for image-guided radiation therapy," *Med. Dosim*. **31,** 30–39.

Ma, C.-M., Mok, E., Kapur, A., Pawlicki, T., Findley, D., Brain, S., Forster, K., and Boyer, A. L. (1999). "Clinical implementation of a Monte Carlo treatment planning system," *Med. Phys*. **26,** 2133–2143.

Mackie, T. R. (1990). "Applications of the Monte Carlo method in radiotherapy," in *The Dosimetry of Ionizing Radiation*, Vol. III, Kase, K. R., Bjarngard, B. E., and Attix, F. H., Eds. (Academic Press, San Diego).

Mackie, T. R. (2006). "History of tomotherapy," *Phys. Med. Biol.* **51,** R427–R453.

Mackie, T. R., and Tomé, W. A. (2008). "Advanced image-guided external beam radiotherapy," in *Radiation Oncology Advances*, Bentzen, S. M., Harari, P. M., Tomé, W. A., and Mehta, M. P., Eds. (Springer, New York).

Mackie, T. R., Scrimger, J. W., and Battista, J. J. (1985). "A convolution method of calculating dose for 15-MV x rays," *Med. Phys*. **12,** 188–196.

Mackie, T. R., Bielajew, A. F., Rogers, D. W. O., and Battista, J. J. (1988). "Generation of photon energy deposition kernels using the EGS4 Monte Carlo code," *Phys. Med. Biol*. **33,** 1–20.

Mackie, T. R., Holmes, T. W., Swerdloff, S., Reckwerdt, P. J., Deasy, J. O., Yang, J., Paliwal, B. R., and Kinsella, T. J. (1993). "Tomotherapy: A new concept in the delivery of dynamic conformal radiotherapy," *Med. Phys*. **20,** 1709–1719.

Mackie, T. R., Reckwerdt, P., and Papanikolaou, N. (1995). "3-D photon beam dose algorithms," in *3-D Radiation Therapy Planning and Conformal Therapy*, Purdy, J. A., and Emami, B., Eds. (Medical Physics Publishing, Madison, WI).

Mackie, T. R., Reckwerdt, P., and McNutt, T. (1996). "Photon beam dose computations," in *Teletherapy: Present and Future*, Mackie, T. R., and Palta, J. R., Eds. (American Association of Physicists in Medicine, College Park, MD).

Mackie, T. R., Balog, J., Ruchala, K., Shepard, D., Aldridge, S., Fitchard, E., Reckwerdt, P., Olivera, G., McNutt, T., and Mehta, M. (1999). "Tomotherapy," *Semin. Radiat. Oncol*. **9,** 108–117.

Mackie, T. R., Olivera, G. H., Reckwerdt, P. J., and Shepard, D. M. (2000). "Convolution/superposition photon dose algorithm," pp. 39–56 in *General Practice of Radiation Oncology Physics in the 21st Century*, Shiu, A., and Mellenberg, D., Eds. (American Association of Physicists in Medicine, College Park, MD).

Mackie, T. R., Reckwerdt, P. J., Olivera, G. H., Shepard, D., and Zachman, J. (2001). "The convolution algorithm in IMRT," pp. 179–190 in *3-D Conformal and Intensity Modulated Radiation Therapy*, Purdy, J., Grant, W., III, Palta, J., Butler, B., and Perez, C., Eds. (Advanced Medical, Madison, WI).

Mackie, T. R., Olivera, G. H., Kapatoes, J. M., Ruchala, K. J., Balog, J. P., Tomé, W. A., Hui, S., Kissick, M., Wu, C., Jeraj, R., Reckwerdt, P. J., Harari, P., Ritter, M., Forrest, L., Welsh, J., and Mehta, M. P. (2003). "Helical tomotherapy," pp. 247–284 in *Intensity-Modulated Radiation Therapy: The State of the Art*, Palta, J., and Mackie, T. R., Eds. (American Association of Physicists in Medicine, College Park, MD).

Mageras, G. S., and Mohan, R. (1993). "Application of fast simulated annealing to optimization of conformal radiation treatments," *Med. Phys*. **20,** 639–647.

Mageras, G. S., and Yorke, E. (2004). "Deep inspiration breath hold and respiratory gating strategies for

reducing organ motion in radiation treatment," *Semin. Radiat. Oncol.* **14,** 65–75.

Martel, M. K., Ten Haken, R. K., Hazuka, M. B., Turrisi, A. T., Fraass, B. A., and Lichter, A. S. (1994). "Dose–volume histogram and 3-D treatment planning evaluation of patients with pneumonitis," *Int. J. Radiat. Oncol. Biol. Phys*. **28,** 575–581.

Martens, C., De Wagter, C., and De Neve, W. (2000). "The value of the PinPoint ion chamber for characterization of small field segments used in intensity-modulated radiotherapy," *Phys. Med. Biol.* **45,** 2519–2530.

McCurdy, B. M., Luchka, K., and Pistorius, S. (2001). "Dosimetric investigation and portal dose image prediction using an amorphous silicon electronic portal imaging device," *Med. Phys.* **28,** 911–924.

McKenzie, A. L. (2000). "How should breathing motion be combined with other errors when drawing margins around the clinical target volumes?" *Br. J. Radiol.* **73,** 973–977.

McKenzie, A. L., van Herk, M., and Mijnheer, B. (2000). "The width of margins in radiotherapy treatment plans," *Phys. Med. Biol*. **45,** 3331–3342.

McKenzie, A. L., van Herk, M., and Mijnheer, B. (2002). "Margins for geometric uncertainty around organs at risk in radiotherapy," *Radiother. Oncol.* **62,** 299–307.

McNutt, T. R., Mackie, T. R., Reckwerdt, P., and Paliwal, B. R. (1996). "Modeling dose distributions from portal dose images using the convolution/superposition method," *Med. Phys.* **23,** 1381–1392.

Mell, L. K., Roeske, J. C., and Mundt, A. J. (2003). "A survey of intensity-modulated radiation therapy use in the United States," *Cancer* **98,** 204–211.

Mell, L. K., Mehrotra, A. K., and Mundt, A. J. (2005). "Intensity-modulated radiation therapy use in the U.S. in 2004," *Cancer* **104,** 1296–1303.

Mohan, R. (1996). "Intensity-modulation in radiotherapy," in *Teletherapy: Present and Future*, Palta, J., and Mackie, T. R., Eds. (American Association of Physicists in Medicine, College Park, MD).

Mohan, R., and Bortfeld, T. (2006). "The potential and limitations of IMRT: A physicist's point of view," in *Image-Guided IMRT*, Bortfeld, T., Schmidt-Ullrigh, R., De Neve, W., and Wazer, D., Eds. (Springer, Heidelberg).

Mohan, R., Chui, C., and Lidofsky, L. (1985). "Energy and angular distributions of photons from medical linear accelerators," *Med. Phys*. **12,** 592–597.

Mohan, R., Zhang, X., Wang, H., Kang, Y., Wang, X., Liu, H., Ang, K. K., Kuban, D., and Dong, L. (2005). "Use of deformed intensity distributions for on-line modification of image-guided IMRT to account for interfractional anatomic changes," *Int. J. Radiat. Oncol. Biol. Phys*. **61,** 1258–1266.

Moiseenko, V., Battista, J., and Van Dyk, J. (2002). "Normal tissue complication probabilities: Dependence on choice of biolgoical model and dose–volume histogram reduction scheme," *Int. J. Radiat. Oncol. Biol. Phys*. **78,** 948–950.

Moran, J. M., and Xia, P. (2006). "QA-QC of IMRT: American perspective," pp. 129–141 in *Image-Guided IMRT*, Bortfeld, T., Schmidt-Ullrich, R., DeNeve, W., and Wazer, D. E., Eds. (Springer, Berlin).

Moran, J. M., Roberts, D. A., Nurushev, T. S., Antonuk, L. E., El-Mohri, Y., and Fraass, B. A. (2005). "An active matrix flat panel dosimeter (AMFPD) for in-phantom dosimetric measurements," *Med. Phys.* **32,** 466–472.

Muench, P. J., Meigooni, A. S., Nath, R., and McLaughlin, W. L. (1991). "Photon energy dependence of the sensitivity of radiochromic film and comparison with silver halide and LiF TLDs used for brachytherapy dosimetry," *Med. Phys*. **18,** 769–775.

Munro, T. R., and Gilbert, C. W. (1961). "The relation between tumor lethal doses and radiosensitivity of tumour cells," *Br. J. Radiol*. **34,** 246–251.

Murphy, M. J., Chang, S., Gibbs, I., Quynh-Tu, L., Martin, D., and Kim, D. (2001). "Image-guided radiosurgery in the treatment of spinal metastases," *Neurosurg. Focus* **11,** 1–7.

Nair, D. G. (2005). "About being BOLD," *Brain Res. Rev.* **50,** 229–243.

Nahum, A. E. (2007). "Monte Carlo based patient dose computation," in *Handbook of Radiotherapy Physics: Theory and Practice*, Mayles, P., Nahum, A. E., and Rosenwald, J.-C., Eds. (CRC Press, Boca Raton, FL).

Niemierko, A. (1997). "Reporting and analyzing dose distributions: A concept of equivalent uniform dose," *Med Phys*. **24,** 103–110.

Niemierko, A. (1999). "A generalized concept of equivalent uniform dose (EUD)," *Med. Phys*. **26,** 1100 (abstract).

Niemierko, A., and Goitein, M. (1991). "Calculation of normal tissue complication probability and dose–volume histogram reduction schemes for tissues with a critical element architecture," *Radiother. Oncol.* **20,** 166–176.

Niemierko, A., and Goitein, M. (1993). "Modeling of normal tissue response to radiation: The critical volume model," *Int. J. Radiat. Oncol. Biol. Phys*. **25,** 135–145.

Oelfke, U., Nill, S., and Wilkens, J. J. (2006). "Physical optimization," pp. 289–298 in *Image-Guided IMRT*, Bortfeld, T., Schmidt-Ulrich, R., De Neve, W., and Wazer, D., Eds. (Springer, Heidelberg).

Olch, A. J. (2002). "Dosimetric performance of an enhanced dose range radiographic film for intensity-modulated radiation therapy quality assurance," *Med. Phys.* **29,** 2159–2168.

Olivera, G. H., Shepard, D. M., Ruchala, K., Zachman, J., Fitchard, E. E., and Mackie, T. R. (1999). "Tomotherapy," in *Modern Technology of Radiation Oncology*, Van Dyk, J., Ed. (Medical Physics Publishing, Madison, WI).

O'Sullivan, B., Wunder, J., and Pisters, P. W. T. (2003). "Target description for radiotherapy of soft tissue sarcoma," pp. 205–227 in *Clinical Target Volumes in Conformal and Intensity Modulated Radiation Therapy—A Clinical Guide to Cancer Treatement*, Grégoire, V., Scalliet, P., and Ang, K. K., Eds. (Springer, Berlin).

Otto, K. (2008). "Volumetric modulated arc therapy: IMRT in a single gantry arc," *Med. Phys.* **35,** 310–317.

Ozyigit, G., and Chao, K. (2002). "Clinical experience of head-and-neck cancer IMRT with serial tomotherapy," *Med. Dosim*. **27,** 91–98.

Paddick, I. (2000). "A simple scoring ratio to index the conformity of radiosurgical treatment plans," *J. Neurosurg.* **93,** 219–222.

Palta, J. R., Kin, S., Li, L. G., and Liu, C. (2003). "Tolerance limits and action levels for planning and delivery of IMRT," pp. 593–612 in *Intensity-Modulated Radiation Therapy: The State of the Art*, Palta, J., and Mackie, T. R., Eds. (American Association of Physicists in Medicine, College Park, MD).

Papanikolaou, N., Mackie, T. R., Meger-Wells, C., Gehring, M., and Reckwerdt, P. (1993). "Investigation of the convolution method for polyenergetic spectra," *Med. Phys*. **20,** 1327–1336.

Parker, B. C., Shiu, A. S., Maor, M. H., Lang, F. F., Liu, H. H., White, R. A., and Antolak, J. A. (2002). "PTV margin determination in conformal SRT of intracranial lesions," *J. Appl. Clin. Med. Phys.* **3,** 176–189.

Partridge, M., Ebert, M., and Hesse, B.-M. (2002). "IMRT verification by three-dimensional dose reconstruction from portal beam measurements," *Med. Phys.* **29,** 1847–1858.

Pasma, K. L., Kroonwijk, M., Quint, S., Visser, A. G., and Heijmen, B. J. M. (1999). "Transit dosimetry with an electronic portal imaging device (EPID) for 115 prostate cancer patients," *Int. J. Radiat. Oncol. Biol. Phys*. **45,** 1297–1303.

Poltinnikov, I., Fallon, K., Xiao, Y., Reiff, J., Curran, W., Jr., and Werner-Wasik, M. (2005). "Combination of longitudinal and circumferential three-dimensional esophageal dose distribution predicts acute esophagitis in hypofractionated reirradiation of patients with non-small-cell lung cancer treated in stereotactic body frame," *Int. J. Radiat Oncol. Biol. Phys*. **62,** 652–658.

Raaymakers, B. W., Raaijmakers, A. J. E., Kotte, A. N. T. J., Jette, D., and Lagendijk, J. J. W. (2004). "Integrating a MRI scanner with a 6 MV radiotherapy accelerator: Dose deposition in a transverse magnetic field," *Phys. Med. Biol*. **49,** 4109–4118.

Ramsey, C. R., Langen, K. M., Kupelian, P. A., Scaperoth, D. D., Meeks, S. L., Mahan, S. L., and Seibert, R. M. (2006). "A technique for adaptive image-guided helical tomotherapy for lung cancer," *Int. J. Radiat. Oncol. Biol. Phys*. **64,** 1237–1244.

Rancati, T., Gagliardi, G., Cattaneo, G. M., Cozzarini, C., Fellin, G., Girelli, G., Sanguineti, G., Vavassori, V., Valdagni, R., and Fiorino, C. (2003). "Late rectal bleeding: fitting clinical data with different NTCP models," *Int. J. Radiat. Oncol. Biol. Phys.* **57**, S392 (abstract).

Renner, W. D., O'Connor, T. P., and Bermudez, N. M. (1989). "An algorithm for design of beam compensators," *Int. J. Radiat. Oncol. Biol. Phys*. **17,** 227–234.

Roeske, J. C., Forman, J. D., Mesina, C. F., He, T., Pelizzari, C. A., Fontenla, E., Vijayakumar, S., and Chen, G. T. (1995). "Evaluation of changes in the size and location of the prostate, seminal vesicles, bladder, and rectum during a course of external beam radiation therapy," *Int. J. Radiat. Oncol. Biol. Phys.* **33,** 1321–1329.

Rogers, D. W. O., Faddegon, B. A., Ding, G. X., Ma, C.-M., Wei, J., and Mackie, T. R. (1995). "BEAM: A Monte Carlo code to simulate radiotherapy treatment units," *Med. Phys*. **22,** 503–524.

Romeijn, H. E., Dempsey, J. F., and Li, J. G. (2004). "A unifying framework for multi-criteria fluence map optimization models," *Phys. Med. Biol.* **49,** 1991–2013.

Sánchez-Doblado, F., Hartmann, G. H., Pena, J., Capote, R., Paiusco, M., Rhein, B., Leal, A., and Lagares, J. I. (2007). "Uncertainty estimation in intensity-modulated radiotherapy absolute dosimetry verification," *Int. J. Radiat. Oncol. Biol Phys.* **68,** 301–310.

Saw, C. B., Ayyangar, K. M., Zhen, W., Thompson, R. B., and Enke, C. A. (2001). "Quality assurance procedures for the peacock system," *Med. Dosim*. **26,** 83–90.

Schubert, L. K., Westerly, D. C., Tomé, W. A., Mehta, M. P., Soisson, E. T., Mackie, T. R., Ritter, M. A., Khuntia, D., Harari, P. M., and Paliwal, B. R. (2009). "A comprehensive assessment by tumor site of patient setup using daily MVCT imaging from more than 3,800 helical tomotherapy treatments," *Int. J. Radiat. Oncol. Biol. Phys.* **73,** 1260–1269.

Schultheiss, T. E., Kun, L. E., Ang, K. K., and Stephens, L. C. (1995). "Radiation response of the central nervous system," *Int. J. Radiat. Oncol. Biol. Phys*. **31,** 1093–1112.

Seppenwoolde, Y., and Lebesque, J. V. (2001). "Partial irradiation of the lung," *Semin. Radiat. Oncol.* **11,** 247–258.

Seppenwoolde, Y., Shirato, H., Kitamura, K., Shimizu, S., van Herk, M., Lebesque, J. V., and Miyasaka, K. (2002). "Precise and real-time measurement of 3D tumor motion in lung due to breathing and heartbeat, measured during radiotherapy," *Int. J. Radiat. Oncol. Biol. Phys.* **53,** 822–834.

Sharpe, M. B., Miller, B. M., Yan, D., and Wong, J. W. (2000). "Monitor unit settings for intensity modulated beams delivered using a step-and-shoot approach," *Med. Phys.* **27,** 2719–2725.

Shepard, D. M., Earl, M. A., Li, X. A., Naqvi, S., and Yu, C. (2002). "Direct aperture optimization: A turnkey solution for step-and-shoot IMRT," *Med. Phys*. **29,** 1007–1018.

Sherouse, G. W., Thorn, J., Novins, K., Margolese-Malin, L., and Mosher, C. (1989). "/usr/planning: A portable 3D radiotherapy treatment design system," *Med. Phys*. **16**, 466 (abstract).

Sherouse, G. W., Novins, K., and Chaney, E. L. (1990). "Computation of digitally reconstructed radiographs for use in radiotherapy treatment design," *Int. J. Radiat. Oncol. Biol. Phys*. **18,** 651–658.

Shipley, W. U., Tepper, J. E., Prout, G. R., Verhey, L. J., Mendiondo, O. A., Goitein, M., Koehler, A. M., and Suit, H. D. (1979). "Proton radiation as boost therapy for localized prostatic carcinoma," *JAMA* **241,** 1912–1915.

Siebers, J. V., Keall, P. J., Nahum, A. E., and Mohan, R. (2000). "Converting absorbed dose to medium to absorbed dose to water for Monte Carlo based photon beam dose calculations," *Phys. Med. Biol*. **45,** 983–995.

Siochi, R. A. C. (1999). "Minimizing static intensity modulation delivery time using an intensity solid paradigm," *Int. J. Radiat. Oncol. Biol. Phys*. **43,** 671–680.

Soares, C. G., Trichter, S., and Devic, S. (2009). "Radiochromic film," pp. 759–815 in *Clinical Dosimetry Measurements in Radiotherapy*, Rogers, D. W. O., and Cygler, J. E., Eds. (American Association of Physicists in Medicine, College Park, MD).

Spirou, S. V., and Chui, C. S. (1994). "Generation of arbitrary intensity profiles by dynamic jaws or multileaf collimators," *Med. Phys*. **21,** 1031–1041.

Spirou, S. V., and Chui, C. S. (1998). "A gradient inverse planning algorithm with dose–volume constraints," *Med. Phys*. **25,** 321–333.

Steel, G. G. (1993). *Basic Clinical Radiobiology* (Edward Arnold, London).

Sternick, E. S., Bleier, A. R., Carol, M. P., Curran, B. H., Holmes, T. W., Kania, A. A., Lalonde, R., and Larson, L. S. (1997). "Intensity modulated radiation therapy: What photon energy is best?" pp. 418–419 in *Proceedings of the XII International Conference on the Use of Computers in Radiation Therapy*, Leavitt, D. D., and Starkschall, G., Eds. (Medical Physics Publishing, Madison, WI).

Stroom, J. C., de Boer, H. C. J., Huizinga, H., and Visser, A. G. (1999a). "Inclusion of geometrical uncertainties in radiotherapy treatment planning by means of coverage probability," *Int. J. Radiat. Oncol. Biol. Phys.* **43,** 905–919.

Stroom, J. C., Koper, P. C. M., Korevaar, G. A., van Os, M., Janssen, M., de Boer, H. C. J., Levendag, P. C., and Heijmen, B. J. M. (1999b). "Internal organ motion in prostate cancer patients treated in prone and supine treatment position," *Radiother. Oncol.* **51,** 237–248.

Suit, H. D., Shalek, R. J., and Wette, R. (1965). "Radiation response of C3H mouse mammary carcinoma sensitivity evaluated in terms of radiation sensitivity," pp. 514–530 in *Cellular Radiation Biology* (Williams and Wilkins, Baltimore, MD).

Ten Haken, R. K., Balter, J. M., Marsh, L. H., Robertson, J. M., and Lawrence, T. S. (1997). "Potential benefits of eliminating planning target volume expansions for patient breathing in the treatment of liver tumors," *Int. J. Radiat. Oncol. Biol. Phys.* **38,** 613–617.

Thames, H. D., Withers, H. R., Peters, L. J., and Fletcher, G. H. (1982). "Changes in early and late radiation responses with altered dose fractionation: implications for dose-survival relationships," *Int. J. Radiat. Oncol. Biol. Phys*. **8,** 219–226.

Thilmann, C., Zabel, A., Milker-Zabel, S., Schlegel, W., Wannenmacher, M., and Debus, J. (2003). "Number and orientation of beams in inversely planned intensity-modulated radiotherapy of the female breast and the parasternal lymph nodes," *Am. J. Clin. Oncol.* **26,** e136–e143.

Timmerman, R. D. (2008). "An overview of hypofractionation and introduction to this issue of Seminars in Radiation Oncology," *Semin. Radiat. Oncol.* **18,** 215–222.

Ting, J. (2006). "Commissioning and dosimetric quality assurance," pp. 186–197 in *Intensity Modulated Radiation Therapy: A Clinical Perspective*, Mundt, A. J., and Roeske, J. C., Eds. (BC Decker, Hamilton, Ontario).

Tomsej, M., Marchesi, V., and Aletti, P. (2005). "Validation of IMRT treatments in head and neck cancer through a European multicentric dosimetry study," *Radiother. Oncol.* **76,** S40 (abstract).

Travis, L. B., Curtis, R. E., and Boice, J. D., Jr. (1996). "Late effects of treatment for childhood Hodgkin's disease," *N. Engl. J. Med*. **335,** 352–353.

Uematsu, M., Fukui, T., Shioda, A., Tokumitsu, H., Takai, K., Kojima, T., Asai, Y., and Kusano, S. (1996). "A dual computed tomography linear accelerator unit for stereotactic radiation therapy: A new approach without cranially fixated stereotactic frames," *Int. J. Radiat. Oncol. Biol. Phys*. **35,** 587–592.

UICC (2002). International Union Against Cancer. *TNM Classification of Malignant Tumors*, 6th ed., Sobin, L. H., and Wittekind, C., Eds. (Wyley-Liss and Sons, New York).

Van Dyk, J., Barnett, R. B., Cygler, J. E., and Shragge, P. C. (1993). "Commissioning and quality assurance of treatment planning computers," *Int. J. Radiat. Oncol. Biol. Phys.* **26,** 261–273.

Van Esch, A., Vanstraelen, B., Verstraete, J., Kutcher, G., and Huyskens, D. (2001). "Pre-treatment dosimetric verification by means of a liquid-filled electronic portal imaging device during dynamic delivery of intensity modulated treatment fields," *Radiother. Oncol*. **60,** 181–190.

Van Esch, A., Depuydt, T., and Huyskens, D. P. (2004). "The use of an aSi-based EPID for routine absolute dosimetric pre-treatment verification of dynamic IMRT fields," *Radiother. Oncol.* **71,** 223–234.

van Herk, M. (2004). "Errors and margins in radiotherapy," *Semin. Radiat. Oncol.* **14,** 52–64.

van Herk, M., Bruce, A., Kroes, A. P., Shouman, T., Touw, A., and Lebesque, J. V. (1995). "Quantification of organ motion during conformal radiotherapy of the prostate by three dimensional image registration," *Int. J. Radiat. Oncol. Biol. Phys.* **33,** 1311–1320.

van Herk, M., Remeijer, P., Rasch, C., and Lebesque, J. V. (2000). "The probability of correct target dosage: Dose-population histograms for deriving treatment margins in radiotherapy," *Int. J. Radiat. Oncol. Biol. Phys.* **47,** 1121–1135.

van Herk, M., Remeijer, P., and Lebesque, J. V. (2002). "Inclusion of geometric uncertainties in treatment plan evaluation," *Int. J. Radiat. Oncol. Biol. Phys.* **52,** 1407–1422.

van Herk, M., Witte, M., van der Geer, J., Schneider, C., and Lebesque, J.V. (2003). "Biologic and physical fractionation effects of random geometric errors," *Int. J. Radiat. Oncol. Biol. Phys.* **57,** 1460–1471.

Vassiliev, O. N., Titt, U., Kry, S. F., Pönisch, F., Gillin, M. T., and Mohan, R. (2006). "Monte Carlo study of photon fields from a flattening filter-free clinical accelerator," *Med. Phys*. **33,** 820–827.

Verellen, D., and Vanhavere, F. (1999). "Risk assessment of radiation-induced malignancies based on whole-body equivalent dose estimates for IMRT treatment in the head and neck region," *Radiother. Oncol*. **53,** 199–203.

Wang, J. Z., and Li, X. A. (2003). "Evaluation of external beam radiotherapy and brachytherapy for localized prostate cancer using equivalent uniform dose," *Med. Phys*. **30,** 34–40.

Wang, X.-H., Mohan, R., Jackson, A., Leibel, S. A., Fuks, Z., and Ling, C. C. (1995). "Optimization of intensity-modulated 3D conformal treatment plans based on biological indices," *Radiother. Oncol*. **37,** 140–152.

Wang, H., Dong, L., Lii, M. F., Lee, A. L., de Crevoisier, R., Mohan, R., Cox, J. D., Kuban, D. A., and Cheung, R. (2005). "Implementation and validation of a three-dimensional deformable registration algorithm for targeted prostate cancer radiotherapy," *Int. J. Radiat. Oncol. Biol. Phys*. **61,** 725–735.

Warkentin, B., Steciw, S., Rathee, S., and Fallone, B. G. (2003). "Dosimetric IMRT verification with a flat-panel EPID," *Med. Phys*. **30,** 3143–3155.

Webb, S. (1992). "Optimization by simulated annealing of three-dimensional, conformal treatment planning for radiation fields determined by a multileaf collimator. II. Inclusion of two-dimensional modulation of the x-ray intensity," *Phys. Med. Biol*. **37,** 1689–1704.

Webb, S. (1993). *The Physics of Three-Dimensional Therapy: Conformal Therapy, Radiosurgery and Treatment Planning* (Institute of Physics, Bristol).

Webb, S. (1999). "Conformal intensity-modulated radiotherapy (IMRT) delivered by robotic linac—testing IMRT to the limit?" *Phys. Med. Biol*. **44,** 1639–1654.

Webb, S. (2000). "Conformal intensity-modulated radiotherapy (IMRT) delivered by robotic linac—conformality versus efficiency of dose delivery," *Phys. Med. Biol*. **45,** 1715–1730.

Webb, S. (2003). "The physical basis of IMRT and inverse planning," *Br. J. Radiol.* **76,** 678–689.

Weeks, K. J., Arora, V. R., Leopold, K. A., Light, K. L., King, S. C., Ray, S. K., Sontag, M. R., and Smith, K. D. (1994). "Clinical use of a concomitant boost technique using a gypsum compensator," *Int. J. Radiat. Oncol. Biol. Phys.* **30,** 693–698.

WHO (2000). World Health Organization. *International Classification of Disease for Oncology*, 3rd ed., (ICD-O-3), from the proceedings of WHO 2000 (World Health Organization, Geneva).

Wiezorek, T., Banz, N., Schwedas, M., Scheithauer, M., Salz, H., Georg, D., and Wendt, T. G. (2005). "Dosimetric quality assurance for intensity-modulated radiotherapy feasibility study for a filmless approach," *Strahlenther. Onkol.* **181,** 468–474.

Williams, P. C. (2003). "IMRT: delivery techniques and quality assurance," *Br. J. Radiol*. **76,** 766–776.

Williams, P. C., and Hounsell, A. R. (2001). "X-ray linkage considerations for IMRT," *Br. J. Radiol*. **74,** 98–100.

Williamson, J. F., and Thomadson, B. R., Eds. (2007). "Quality assurance for radiation therapy," *Int. J. Radiat. Oncol. Biol. Phys.* **71,** S1–S214.

Winkler, P., Zurl, B., Guss, H., Kindl, P., and Stuecklschweiger, G. (2005). "Performance analysis of a film dosimetric quality assurance procedure for IMRT with regard to the employment of quantitative evaluation methods," *Phys. Med. Biol.* **50**, 643–654.

Withers, H. R. (1986). "Predicting late normal tissue responses," *Int. J. Radiat. Oncol. Biol. Phys.* **12,** 693–698.

Withers, H. R., and Thames, H. D. (1988). "Dose fractionation and volume effects in normal tissues and tumor," *Am. J. Clin. Oncol.* **11,** 313–329.

Withers, H. R., Taylor, J. M., and Maciejewski, B. (1988). "Treatment volume and tissue tolerance," *Int. J. Radiat. Oncol. Biol. Phys.* **14,** 751–759.

Wong, J. R., Grimm, L., Uematsu, M., Oren, R., Cheng, C. W., Merrick, S., and Schiff, P. (2005). "Image-guided radiotherapy for prostate cancer by CT-linear accelerator combination: Prostate movements and dosimetric considerations," *Int. J. Radiat. Oncol. Biol. Phys.* **61,** 561–569.

Wu, Q., Mohan, R., Niemierko, A., and Schmidt-Ullrich, R. (2002). "Optimization of intensity-modulated radiotherapy plans based on the equivalent uniform dose," *Int. J. Radiat. Oncol. Biol. Phys.* **52,** 224–235.

Wu, V. W. C., Sham, J. S. T., and Kwong, D. L. W. (2004). "Inverse planning in three-dimensional conformal and intensity-modulated radiotherapy of mid-thoracic oesophageal cancer," *Br. J. Radiol.* **77,** 568–572.

Xia, P., and Verhey, L. J. (2001). "Delivery systems of intensity-modulated radiotherapy using conventional multileaf collimators," *Med. Dosim.* **26,** 169–177.

Xiao, Y., Galvin, J., Hossain, M., and Valicenti, R. (2000). "An optimized forward-planning technique for intensity modulated radiation therapy," *Med. Phys*. **27,** 2093–2099.

Xiao, Y., Straube, W., Bosch, W., Timmerman, R., and Galvin, J. (2007) "Dosimetric evaluation of heterogeneity corrections for RTOG 0236: Hypofractionated radiotherapy of inoperable stage I/II non-small cell lung cancer," *Int. J. Radiat. Oncol. Biol. Phys.* **69,** S46–S47.

Xing, L., and Chen, G. T. Y. (1996). "Iterative algorithms for inverse treatment planning," *Phys. Med. Biol*. **41,** 2107–2123.

Yan, D., Wong, J. W., Vicini, F., Michalski, J., Pan, C., Frazier, A., Horwitz, E., and Martinez, A. (1997). "Adaptive modification of treatment planning to minimize the deleterious effects of treatment setup errors," *Int. J. Radiat. Oncol. Biol. Phys.* **38,** 197–206.

Yan, D., Jaffray, D. A., and Wong, J. W. (1999). "A model to accumulate fractionated dose in a deforming organ," *Int. J. Radiat. Oncol. Biol. Phys.* **44,** 665–675.

Yan, Y., Papanikolaou, N., Weng, X., Penagaricano, J., and Ratanatharathorn, V. (2005). "Fast radiographic film calibration procedure for helical tomotherapy intensity modulated radiation therapy dose verification," *Med. Phys.* **32,** 1566–1570.

Yoda, K., and Aoki, Y. (2003). "A multiportal compensator system for IMRT delivery," *Med. Phys*. **30,** 880–886.

Yorke, E. D. (2003). "Biological indices for evaluation and optimization of IMRT," in *Teletherapy: Present and Future*, Palta, J., and Mackie, T. R., Eds. (American Association of Physicists in Medicine, College Park, MD).

Yu, C. X. (1995). "Intensity-modulated arc therapy with dynamic multileaf collimation: An alternative to tomotherapy," *Phys. Med. Biol*. **40,** 1435–1449.

Zefkili, S., Tomsej, M., Aletti, P., Bidault, F., Bridier, A., Marchesi, V., and Marcié, S. (2004). "Recommendations for a head and neck IMRT quality assurance protocol," *Cancer Radiothérapie* **8,** 364–379.

Zelefsky, M. J., Crean, D., Mageras, G. S., Lyass, O., Happersett, L., Ling, C. C., Leibel, S. A., Fuks, Z., Bull, S., Kooy, H. M., van Herk, M., and Kutcher, G. J. (1999). "Quantification and predictors of prostate position variability in 50 patients evaluated with multiple CT scans during conformal radiotherapy," *Radiother. Oncol.* **50,** 225–234.

Zelefsky, M. J., Fuks, Z., Hunt, M., Yamada, Y., Marion, C., Ling, C. C., Amols, H., Venkatraman, E. S., and Leibel, S. A. (2002). "High-dose intensity modulated radiation therapy for prostate cancer: early toxicity and biochemical outcome in 772 patients," *Int. J. Radiat. Oncol. Biol. Phys.* **53,** 1111–1116.

Zhang, M., Moiseenko, V., and Liu, M. (2006). "PTV margin for dose escalated radiation therapy of prostate cancer with daily on-line realignment using internal fiducial markers: Monte Carlo approach and dose population histogram (DPH) analysis," *J. Appl. Clin. Med. Phys.* **25,** 38–49.

Zhang, T., Jeraj, R., Keller, H., Lu, W., Olivera, G. H., McNutt, T. R., Mackie, T. R., and Paliwal, B. (2004). "Treatment plan optimization incorporating respiratory motion," *Med. Phys*. **31,** 1576–1586.

Zhang, T., Chi, Y., Meldolesi, E., and Yan, D. (2007). "Automated delineation of on-line head-and-neck computed tomography images toward on-line adaptive radiotherapy," *Int. J. Radiat. Oncol. Biol. Phys*. **68,** 522–530.

Zhu, T. C., and Saini, A. S. (2009). "Diode dosimetry for megavoltage electron and photon beams," in *Clinical Dosimetry Measurements in Radiotherapy*, Rogers, D. W. O., and Cygler, J. E., Eds. (American Association of Physicists in Medicine, College Park, MD).

Zhu, X. R., Jursinic, P. A., Grimm, D. F., Lopez, F., Rownd, J. J., and Gillin, M. T. (2002). "Evaluation of Kodak EDR2 film for dose verification of intensity modulated radiation therapy delivered by a static multileaf collimator," *Med. Phys*. **29,** 1687–1692.

OXFORD JOURNALS
OXFORD UNIVERSITY PRESS

JOURNAL OF THE ICRU

Previous reports available from Oxford University Press

Mammography - Assessment of Image Quality
Report no. 82, 2009
Quantitative Aspects of Bone Densitometry
Report no. 81, 2009
Dosimetry Systems for Use in Radiation Processing
Report no. 80, 2008
Receiver Operating Characteristic Analysis in Medical Imaging
Report no. 79, 2008
Prescribing, Recording, and Reporting Proton-Beam Therapy
Report no. 78, 2007
Elastic Scattering of Electrons and Positrons
Report no. 77, 2007
Measurement Quality Assurance for Ionizing Radiation Dosimetry
Report no. 76, 2006
Sampling for Radionuclides in the Environment
Report no. 75, 2006
Patient Dosimetry of X Rays used in Medical Imaging
Report no. 74, 2005
Stopping of Ions Heavier Than Helium
Report no. 73, 2005
Dosimetry of Beta Rays and Low-Energy Photons for Brachytherapy with Sealed Sources
Report no. 72, 2004
Prescribing, Recording, and Reporting Electron Beam Therapy
Report no. 71, 2004
Image Quality in Chest Radiography
Report no. 70, 2003
Direct Determination of the Body Content of Radionuclides
Report no. 69, 2003
Retrospective Assessment of Exposures to Ionising Radiation
Report no. 68, 2002
Absorbed Dose Specification in Nuclear Medicine
Report no. 67, 2002
Determination of Operational Dose Equivalent Quantities for Neutrons
Report no. 66, 2001
Quantities, Units and Terms in Radioecology
Report no. 65, 2001
Dosimetry of High Energy Photon Beams based on Standards of Absorbed Dose to Water
Report no. 64, 2001
Nuclear Data for Neutron and Proton Radiotherapy and for Radiation Protection
Report no. 63, 2000
Prescribing, Recording and Reporting Photon Beam Therapy (Supplement to ICRU Report 50)
Report no. 62, 1999
Tissue Substitutes, Phantoms and Computational Modelling in Medical Ultrasound
Report no. 61, 1998
Fundamental Quantities and Units for Ionizing Radiation
Report no. 60, 1998
Clinical Proton Dosimetry—Part I: Beam Production, Beam Delivery and Measurement of Absorbed Dose
Report no. 59, 1998
Dose and Volume Specification for Reporting Interstitial Therapy
Report no. 58, 1997
Conversion Coefficients for Use in Radiological Protection Against External Radiation
Report no. 57, 1998
Dosimetry of External Beta Rays for Radiation Protection
Report no. 56, 1997
Secondary Electron Spectra from Charged Particle Interactions
Report no. 55, 1995
Medical Imaging—The Assessment of Image Quality
Report no. 54, 1995
Gamma-Ray Spectrometry in the Environment
Report no. 53, 1994
Particle Counting in Radioactivity Measurement
Report no. 52, 1994
Quantities and Units in Radiation Protection Dosimetry
Report no. 51, 1993
Prescribing, Recording and Reporting Photon Beam Therapy
Report no. 50, 1993
Stopping Powers and Ranges for Protons and Alpha Particles, with Data Disk
Report no. 49D, 1993
Stopping Powers and Ranges for Protons and Alpha Particles
Report no. 49, 1993
Phantoms and Computational Models in Therapy, Diagnosis and Protection
Report no. 48, 1992
Measurement of Dose Equivalents from External Photon and Electron Radiations
Report no. 47, 1992
Photon, Electron, Proton and Neutron Interaction Data for Body Tissues, with Data Disk
Report no. 46D, 1992
Photon, Electron, Proton and Neutron Interaction Data for Body Tissues
Report no. 46, 1992
Clinical Neutron Dosimetry—Part I: Determination of Absorbed Dose in a Patient Treated by External Beams of Fast Neutrons
Report no. 45, 1989
Tissue Substitutes in Radiation Dosimetry and Measurement
Report no. 44, 1989
Determination of Dose Equivalents from External Radiation Sources - Part 2
Report no. 43, 1988
Use of Computers in External Beam Radiotherapy Procedures with High-Energy Photons and Electrons
Report no. 42, 1987
Modulation Transfer Function of Screen-Film Systems
Report no. 41, 1986
The Quality Factor in Radiation Protection
Report no. 40, 1986
Determination of Dose Equivalents Resulting from External Radiation Sources
Report no. 39, 1985
Dose and Volume Specification for Reporting Intracavitary Therapy in Gynecology
Report no. 38, 1985
Stopping Powers for Electrons and Positrons
Report no. 37, 1984
Microdosimetry
Report no. 36, 1983
Radiation Dosimetry: Electron Beams with Energies Between 1 and 50 MeV
Report no. 35, 1984
The Dosimetry of Pulsed Radiation
Report no. 34, 1982
Radiation Quantities and Units
Report no. 33, 1980
Methods of Assessment of Absorbed Dose in Clinical Use of Radionuclides
Report no. 32, 1979
Average Energy Required to Produce an Ion Pair
Report no. 31, 1979
Quantitative Concepts and Dosimetry in Radiobiology
Report no. 30, 1979
Basic Aspects of High Energy Particle Interactions and Radiation Dosimetry
Report no. 28, 1978
Neutron Dosimetry for Biology and Medicine
Report no. 26, 1977
An International Neutron Dosimetry Intercomparison
Report no. 27, 1978
Conceptual Basis for the Determination of Dose Equivalent
Report no. 25, 1976
Determination of Absorbed Dose in a Patient Irradiated by Beams of X or Gamma Rays in Radiotherapy Procedures
Report no. 24, 1976
Measurement of Absorbed Dose in a Phantom Irradiated by a Single Beam of X or Gamma Rays
Report no. 23, 1973
Measurement of Low-Level Radioactivity
Report no. 22, 1972
Radiation Protection Instrumentation and Its Application
Report no. 20, 1970
Specification of High Activity Gamma-Ray Sources
Report no. 18, 1970
Radiation Dosimetry: X rays Generated at Potentials of 5 to 150 kV
Report no. 17, 1970
Linear Energy Transfer
Report no. 16, 1970
Cameras for Image Intensifier Fluorography
Report no. 15, 1969

Please visit the web site for pricing and ordering information
www.jicru.oxfordjournals.org